Universidade do Minho
Escola de Engenharia

Seyedebrahim Hashemi Rafsanjani

High strain rate constitutive modeling for historical structures subjected to blast loading

April 2015

Universidade do Minho
Escola de Engenharia

Seyedebrahim Hashemi Rafsanjani

High strain rate constitutive modeling for historical structures subjected to blast loading

Doctoral Thesis
Civil Engineering

Work performed under the supervision of
Professor Paulo B. Lourenço
Professor Nuno Peixinho

April 2015

STATEMENT OF INTEGRITY

I hereby declare having conducted my thesis with integrity. I confirm that I have not used plagiarism or an form of falsification of results in the process of the thesis elaboration.

I further declare that I have fully acknowledged the Code of Ethical Conduct of the University of Minho.

University of Minho, _____

Full name: _____

Signature: _____

ACKNOWLEDGMENTS

The present study was fulfilled at the Department of Civil Engineering of University of Minho, under the supervision of Professor Paulo B. Lourenço, head of ISISE and Historical Masonry Structures (HMS), and direct guidance of Professor Nuno Peixinho from the Department of Mechanical Engineering. Hereby, I would like to express my gratitude for their support, useful discussions, and valuable suggestions during the past three years.

I would like to thank a number of colleagues and specialist partners for collaboration, sharing valuable insight, and giving technical supports within the all steps of the work done:

- Dr. Nuno Mendes from ISISE, Department of Civil Engineering, University of Minho, Portugal;
- Dr. Joao M. Pereira from ISISE, Department of Civil Engineering, University of Minho, Portugal;
- Professor Ali Bakhshi from Department of Civil Engineering, Sharif University of Technology, Iran;
- Professor Mohammad Ali Ghannad from Department of Civil Engineering, Sharif University of Technology, Iran;
- Dr. Sina Moallemi from Department of Civil Engineering, McMaster University, Canada;
- Dr. Maziar Partovi from TNO DIANA BV, The Netherlands;

This work was performed under the financial support of the research project CH-SECURE funded by the Portuguese Foundation of Science and Technology (FCT) and the Strategic Funding from the School of Engineering, University of Minho. This financial support is gratefully acknowledged.

Finally, my special thanks go for my family for their love and support, specially my wife, Fatima, for the love, encouragement and accompanying me to Portugal.

ABSTRACT

The work presented here was accomplished at the Department of Civil Engineering of University of Minho. This work involves detailed numerical studies intended to better understand the blast response of masonry structures, develops strain dependent constitutive material plasticity model for masonry, and addresses iso-damage curves for typical masonry infill walls in Portugal under blast with different loading conditions, which can be adopted for practical use in the case of enclosures.

A bomb explosion near a building, in addition to a great deal of casualties and losses, can cause serious effects on the building itself, such as noticeable damage on internal and external frames, collapsing walls or shutting down of critical life safety systems. Until Oklahoma City bombing in 1995, studies dealing with the blast behavior of structures were a field of limited interest in the civil engineering community. After this terrorist attack, a great deal of effort has been done to better understand the blast response of the structures and devise solutions to reduce destructive damages and casualties due to such devastative loads. Moreover, the studies on the influence of the high strain rate on mechanical characteristics of construction materials such as steel and concrete have been carried out intensively. Unfortunately, despite the high vulnerability of masonry structures against high strain rates, such investigations on masonry structures and material properties are still scarce. In this regard, conducting experiments and validating numerical models with field test data leads to a better understanding of the blast response of masonry walls and the relevance of the different masonry material properties, which, consequently, results in innovation of strengthening techniques and of assessment and design methods.

The framework of blast loading and its effect on structures is briefly revised and different expressions for prediction of blast pressure parameters are illustrated. A brief review of the recent characterization of the dynamic masonry properties, which resulted in derivation of dynamic increase factors (DIF) is presented. Performance of masonry walls against blast loading regarding experimental activities are addressed subsequently. Moreover, a series of numerical simulation of masonry structures subjected to blast loads were performed along with parametric studies to evaluate the effectiveness of most relevant parameters on the global blast response of the structures. The prominent parameters involved in parametric studies were distinguished and their effectiveness on the blast response of masonry walls is put forward. Different failure criteria have been proposed to estimate the damage level of masonry walls subjected to blast loading. The damage criteria utilized in both numerical and experimental studies are also introduced in detail.

The present study proposes a dynamic 3D interface model that includes non-associated flow rule and high strain rate effects, implemented in the finite element (FE) code ABAQUS as a user subroutine. The model capability is validated with numerical simulation of unreinforced block work masonry walls subjected to low velocity impact. The results obtained are compared with field test data and good agreement is found.

Subsequently, a comprehensive parametric analysis is accomplished with different joint tensile strengths and cohesion, and wall thickness to evaluate the effect of the parameter variations on the impact response of masonry walls.

Furthermore, a new strain rate dependent anisotropic constitutive material continuum model is developed for impact and blast applications in masonry, with validation using the high strain rate response of masonry walls. The present model, implemented in FE code ABAQUS as a user subroutine, adopted the usual approach of considering different yield criteria in tension and compression, given the different failure mechanisms. These criteria are plasticity based, obey a non-associated flow rule, are numerically stable and inexpensive, and are characterized by a few material input parameters. The analysis of two unreinforced block work masonry parapets and a masonry brick work infill wall subjected to high strain rate loads is carried out to validate the capability of the model. A comparison is done between the numerical predictions and test data, and good agreement is noticed. Next, a parametric study is conducted to evaluate the influence of the most likely dominant parameters along the three orthogonal directions and of the wall thickness on the global behavior of masonry walls.

Iso-damage curves are given for tested masonry infill walls according to three different types of typical Portuguese masonry infill walls, also with three different thicknesses. By performing multiple analyses, the pressure-impulse (P-I) diagrams are obtained under different loading conditions, which can be used for design purposes.

Finally, the new continuum plasticity model is taken into engineering applications to solve real problems. The full-scale numerical simulation of the blast response of Al-Askari holy shrine is considered to practice and validate the model capability. The numerical results including the failure of the dome, roof, minarets and side facades are well predicted compared with the reference data. Besides the real explosion, two different scenarios are also defined to estimate the most likely high strain rate response of the shrine under different explosions producing different pressure profiles.

Keywords: Blast loading; Block work masonry wall; High strain rate response; Interface model; Anisotropic continuum model; Out-of-plane behavior; Dynamic Increase Factor; Numerical simulation; Masonry infill wall; FE code ABAQUS; Pressure-Impulse diagrams; Al-Askari shrine; Engineering application.

RESUMO

O trabalho aqui apresentado foi realizado no Departamento de Engenharia Civil da Universidade do Minho. Este trabalho envolve estudos numéricos detalhados que pretendem entender melhor a resposta às explosões das estruturas de alvenaria, desenvolver modelos constitutivos para a alvenaria no âmbito da teoria da plasticidade, e abordar curvas de iso-dano para paredes típicas de alvenaria de enchimento em Portugal sob explosão com diferentes condições de carga, que possam ser usadas no projeto das ensolventes.

A explosão de uma bomba perto de um edifício, além de uma grande quantidade de vítimas e perdas materiais, pode causar efeitos graves sobre o edifício em si, tais como danos visíveis nos pórticos internos e externos, colapso de paredes ou encerramento de sistemas críticos de apoio à vida. Até ao atentado de Oklahoma City, em 1995, os estudos sobre o comportamento á explosão de estruturas eram um tema de interesse limitado na comunidade de engenharia civil. Após este ataque terrorista, um grande esforço tem sido feito para entender melhor a resposta das estruturas a explosões e para criar soluções para reduzir os danos e perdas humanas devido a essas ações devastadoras. Além disso, estudos sobre a influência da velocidade de deformação sobre as características mecânicas dos materiais de construção tais como aço e betão foram levados a cabo com grande desenvolvimento. Infelizmente, apesar da alta vulnerabilidade das estruturas de alvenaria contra as elevadas velocidades de deformação, a investigação sobre as estruturas de alvenaria e as propriedades dos seus materiais são ainda escassos. Neste sentido, a realização de experiências e a validação de modelos numéricos com os resultados de ensaios levam a uma melhor compreensão da resposta de paredes de alvenaria a explosões e premitem identificar a relevância das diferentes propriedades dos materiais de alvenaria, o que, consequentemente, resulta em inovação de técnicas de reforço e de avaliação de segurança e ferramentas de projeto.

O estado da arte sobre ações de explosão e o seu efeito sobre as estruturas é brevemente revisto, incluindo diferentes expressões para definição dos parâmetros de pressão de explosão. Uma breve revisão da recente caracterização das propriedades dinâmicas de alvenaria resultou na caracterização do fator de aumento dinâmico (DIF). Em seguida, aborda-se o desempenho de paredes de alvenaria contra ações de explosão de um ponto de vista da atividade experimental. Além disso, foi realizada uma série de simulações numéricad de estruturas de alvenaria sujeitas a ações de explosão, juntamente com estudos paramétricos, para avaliar a eficácia dos principais parâmetros sobre a resposta da explosão global das estruturas. Os parâmetros mais relevantes envolvidos em estudos paramétricos foram distinguidos e o seu efeito na resposta de paredes de alvenaria a explosões é apresentada. Vários critérios de rotura têm sido propostos para estimar o nível de dano de paredes de alvenaria sujeitas a carregamento de explosões. Os critérios utilizados nos estudos de danos, tanto numéricos quanto experimentais, são apresentados em detalhe.

O presente estudo propõe um modelo de interface 3D dinâmica que inclui regra de escoamento não-associado e efeitos da velocidade de deformação, implementado no código de elementos finitos (FE) ABAQUS como uma sub-rotina do utilizador. A capacidade do modelo é validado com simulações numéricas de paredes de alvenaria não armada submetidos a impacto a baixa velocidade. Os resultados obtidos são comparados com os dados de ensaios e boa concordância é encontrada. Subsequentemente, uma análise paramétrica abrangente é realizado com diferentes resistências à tração comum e coesão, e espessura da parede, para avaliar o efeito das variações de parâmetros em resposta a impactos nas paredes de alvenaria.

Além disso, um modelo constitutiva contínuo do material dependendo da velocidade de deformação é desenvolvido para aplicações de impacto e explosão em alvenaria, com validação usando a resposta de paredes de alvenaria a velocidades elevadas de deformação. No presente modelo, implementado no código FE ABAQUS como uma sub-rotina do utilizador, foi adotado o método habitual de considerar diferentes critérios de rotura em tração e compressão, tendo em conta os diferentes mecanismos de falha. Estes critérios são baseados na teoria da plasticidade, obedecem a uma regra de escoamento não-associado, são numericamente estáveis e de baixo custo, e são caracterizados por pouco parâmetros de entrada do material. A análise de dois parapeitos não armados de alvenaria e uma pareder de enchimento de alvenaria de tijolo submetidos a cargas de alta velocidade de deformação é realizado para validar a capacidade do modelo. A comparação é feita entre as previsões numéricas e ensaios, com bons resultados. Em seguida, é realizado um estudo paramétrico para avaliar a influência dos parâmetros dominantes mais suscetíveis ao longo das três direções ortogonais, e da espessura da parede sobre o comportamento global das paredes de alvenaria.

As curvas de iso-danos são obtidas para três tipos típicos de parede de alvenaria de enchimento em Portugal, com três espessuras diferentes. Com recurso a várias análises, os diagramas pressão-impulso (PI) são obtidos para diferentes paredes de enchimentos de alvenaria sob diferentes condições de carga, o que permite o dimensionamento em projeto corrente.

Finalmente, o novo modelo de plasticidade contínuo é utilizado em aplicações de engenharia para resolver problemas reais. A simulação numérica em escala real da resposta à explosão do santuário sagrado de Al- Askari é considerado para a prática e validação da capacidade do modelo. Os resultados numéricos, incluindo o colapso da cúpula, telhado, minaretes e fachadas laterais estão a prever bem em comparação com os dados de referência. Para além da explosão real, dois diferentes cenários são também definidos para estimar a resposta mais provável da alta taxa de deformação do santuário sob diferentes explosões, a produzir perfis de pressão diferentes.

Palavras-chave: Ações de explosão; Paredes de alvenaria; Elevada velocidade de deformação; Modelo contínuo anisotrópico; Comportamento fora do plano; Fator de aumento dinâmico; Simulação numérica; Programe MEF ABAQUS; Diagramas de pressão-impulso; Santuário Al-Askari; aplicação Engenharia.

TABLE OF CONTENTS

LIST OF TABLES

LIST OF FIGURES

Chapter 1

1 INTRODUCTION

Masonry is composed of individual units laid in and bond by mortar at bed and head joints, and has been widely used in different forms of construction, either in several parts of modern buildings or in historical structures. Due to the poor seismic performance of existing masonry structures in many earthquakes, in recent decades a series of investigations have been conducted to improve the dynamic response of such structures. Moreover, after Oklahoma City bombing in 1995, the studies dealing with the blast response of structures received increasing interest by the scientific community, given the high vulnerability of masonry structures against such destructive loads. A great deal of effort accounting for experiments and numerical simulations has been performed to better understand masonry subjected to high strain rate loads, to advance the retrofitting techniques and to update available design codes. An important objective was to reduce the structural damage of new buildings under extreme events and to enhance the blast resistance of existing structures.

A series of experimental studies in masonry panels and structures has been carried out to chracterize their blast response, including maximum deflection and failure mechanisms of collapse, and to evaluate their performance. Evaluation of structural masonry damage and fragmentation of non-retrofitted masonry walls has also been of interest in a number of studies. It is noted that the majority of existing structures were not designed with blast loading in mind. Hence, despite the large costs usually involved in laboratory tests, various retrofitting techniques have been evaluated to find effective techniques to improve the blast resistance of existing structures, aiming at the reduction of casualties and losses.

Due to the costs of laboratory tests, it is impossible to carry out a large number of tests, which would allow obtaining a comprehensive field test database, including most likely responses. Currently, given the development of computer technology, it is easy to have more detailed and accurate predictions, including dynamic response and localized damage through numerical simulations. Two common strategies have been developed for numerical simulation of masonry in the literature, namely micro strategy and macro strategy. Depending upon the required accuracy, reliability, availability and computational costs, the most suitable approaches can be selected. Only a few studies have been carried out to develop strain rate dependent constitutive material models for masonry using a micro and macro numerical approach, as done here. Here, in order to introduce the mostly used parameters in recent sensitivity studies, and to address their effectiveness on high strain rate behavior of masonry walls, a number of studies have also been performed.

1.1 OBJECTIVES

The present study aims to address several topics dealing with high strain rate loads in the dynamic response of masonry structures, including constitutive material modelling and numerical prediction of response. The first objective of this work is to review blast loading, its interaction with the structures, and introduce methods to simulate blast as pressure distribution with the time. The empirical tools to predict the blast pressure parameters and blast scaling are also presented. This work intends to propose two strain rate dependent constitutive material models for masonry. Even if some studies have

been carried out concerning this topic, a lack of suitable material models for masonry is still present.

Therefore, the second objective is to develop a dynamic interface model for micro numerical simulation of masonry walls. Regarding this study, interface elements are applied to represent the mortar behavior within numerical modeling. Given, the variation of the parameters in the stress-strain relation of masonry subjected to loading in various strain rates, the failure envelop can expand or contract. Thus, in order to apply high strain rates effects in material model, after the implementation of the model in an explicit finite element code, recognition of the most relevant parameters and the corresponding coefficients that affect the failure envelop are the main aims of this part of study.

The third objective is to develop dynamic anisotropic continuum model for macro numerical simulation of masonry walls. Here, 3D solid elements are adopted to represent the global behavior of masonry during numerical modeling. Again, the failure envelope will extend or contract during the loading process and the same procedure is adopted here: Finite element implementation, followed by a study on the definition of relevant parameters and use of the model in real applications.

The fourth objective is to present P-I diagrams for different masonry infill walls under blast and different loading conditions, which can be used as a simple tool by practitioners in preliminary design and evaluation of structural damage to establish reliable response limits and, as a result, make informed decisions.

Finally, the present study also aims to demonstrate the capacity of applying the new continuum plasticity model into an engineering application to solve a real problem. The full-scale numerical simulation of the blast response of Al-Askari holy shrine is considered to discuss the difficulties in this application and to validate the model capability. Besides the real explosion, two different scenarios are also defined to reflect the vulnerability of the mosque subjected to different sources of explosion.

1.2 OUTLINE OF THE THESIS

Besides this introductory chapter, the present manuscript includes four additional chapters, each corresponding to a particular subject related to the main topic.

Chapter 2 intends to present the available information regarding blast loading, the different mechanisms of the blast pressure distribution on an obstacle with different sizes placed in the path of shock wave propagation. In case of blast calculations, the previously developed expressions are addressed for prediction of the blast wave parameters. The chapter also gives a brief review of studies on dynamic material characteristics of masonry, namely reporting the experimentally and numerically derived dynamic increase factors (DIF) for most likely dominant parameters. In addition, this chapter reviews a series of experiments performed to estimate the blast response of masonry structures, and gives the most usual observed failure mechanisms and fracture lines distribution. Also, a number of numerical studies are put forward, as a means to introduce the parameters mostly involved in parametric studies.

Chapter 3 intends to introduce a newly developed dynamic interface model accounting for strain rate effects for numerical simulations of the structural response of masonry walls using the finite element (FE) code ABAQUS. The rate-dependent failure envelop is divided into three parts, namely tension mode, coulomb friction mode, and compressive cap mode, on the basis of the corresponding failure mechanisms. After implementing the material model into ABAQUS as a user subroutine, a micro approach is used for numerical modeling of masonry walls. The developed model is attributed to interface elements to simulate the mortar behavior between the masonry units. A comparison between numerical results and experimental data of a masonry parapet subjected to impact is performed to evaluate the performance of the proposed material model and the accuracy of the simulation in predicting the impact response and damage of masonry walls. Finally, a parametric study is carried out to discuss the effectiveness of the main parameters changes on the global behavior of masonry walls.

Chapter 4 intends to propose a novel strain rate dependent plasticity model for masonry, with validation using the high strain rate response of masonry walls. The present model, implemented in finite element code ABAQUS as a user subroutine, adopted the usual

approach of considering different yield criteria in tension and compression, given the different failure mechanisms. These criteria are plasticity based, obey a non-associated flow rule, are numerically stable and inexpensive, and are characterized by a few material input parameters. The analysis of two unreinforced block work masonry parapets and a masonry brick work infill wall subjected to high strain rate loads is carried out to validate the capability of the model. The numerical predictions are well predicted when compared with the test data. Subsequently, a parametric study is conducted to evaluate the influence of the most likely dominant parameters along the three orthogonal directions and of the wall thickness on the global behavior of masonry walls.

Chapter 5 intends to address the iso-damage curves for the masonry infill wall that was numerically simulated in chapter 4 along with three different types of typical masonry infill walls in Portugal, with three different thicknesses. The anisotropic continuum model is involved as material model in present study. Then, a large number of analyses are performed to develop the P-I diagrams for different masonry infills under blast and different loading conditions.

Chapter 6 intends to take the new anisotropic continuum model into engineering applications to solve real problems. The full-scale numerical simulation of the blast response of Al-Askari holy shrine is considered to practice and validate the model capability. The numerical results including the failure of the dome, roof, minarets and side facades are well predicted compared with the reference data. Besides the real explosion, two different scenarios are also defined to estimate the most likely high strain rate response of the shrine under different explosions producing different pressure profiles.

Chapter 7 briefly describes the conclusions and the main results obtained in the present work. The areas of future research are also suggested.

Chapter 2

2 BLAST LOADS AND STRUCTURES: A STATE OF THE ART

2.1 BLAST LOADING

2.1.1 Blast phenomenon

Blast is defined as a large-scale, rapid and sudden release of energy. Explosions can be categorized on the basis of their nature as physical (e.g. failure of a cylinder of compressed gas), nuclear (e.g. bombs dropped on Hiroshima and Nagasaki, Japan) or chemical (e.g. a mixture of nitrogen and oxygen at high temperatures) events. Explosive materials can be classified according to their physical state (solids, liquids or gases) or their sensitivity to ignition, as secondary or primary explosive.

The blast calculation is based on two parameters, the bomb size, or charge weight, W, and the stand-off distance, R, between the blast charge and the target, see Fig. 2.1.

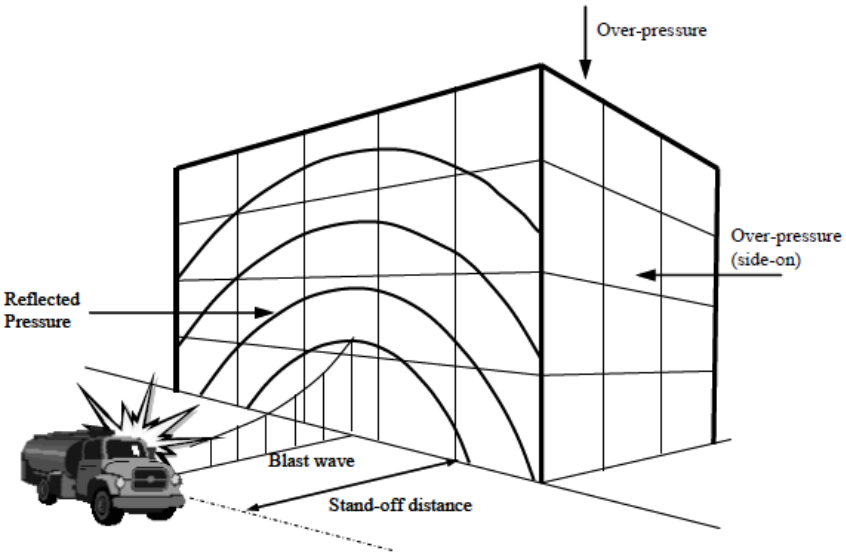

Fig. 2.1. Blast loading on a building [1].

2.1.2 Blast mechanism and pressure distribution

Depending upon the location of the blast source in the ground, the blast loading can be divided into two types (air blast and surface blast). The shock front over-pressure is different in the two burst types due to the amplification of blast waves from the ground before collision with the obstacle. Hence, the variation in burst type causes remarkable changes in calculation of over-pressure distribution with time at specific location. The characteristics of an air-blast pressure pulse are variable for three different conditions. The blast wave effects on a structure depend on the distance from the structure itself, charge weight and geometry of the structure, which results in a combination of three variables that characterize blast, namely incident over-pressure, reflected over-pressure and the drag pressure of the accompanying blast wind.

2.1.2.1 Free field air blast

Fig. 2.2 shows a typical blast pressure profile. At the arrival time, t_A, a layer of compressed air (blast wave) is created in front of the blast source containing most of the energy released by the blast. The pressure at that position immediately increases to a peak value of overpressure, P_{so}, above the ambient pressure, P_o. Then, the pressure decays to ambient level after a duration time t_d as the shock wave enlarges outward from the blast source. Shortly, the pressure behind the front decays to an under pressure,

P_{so}^{-}. Within the negative phase, a partial vacuum is formed and air is sucked in, prior to returning to ambient conditions at time $t_d + t_d^{-}$. This is also accompanied by striking suction winds carrying the debris for long distances away from the blast source. The quantity P_{so} is usually referred to as the peak side-on overpressure, incident peak overpressure or merely peak overpressure. The negative phase has a longer duration (about four times the duration of positive phase) and a lower intensity than the positive duration.

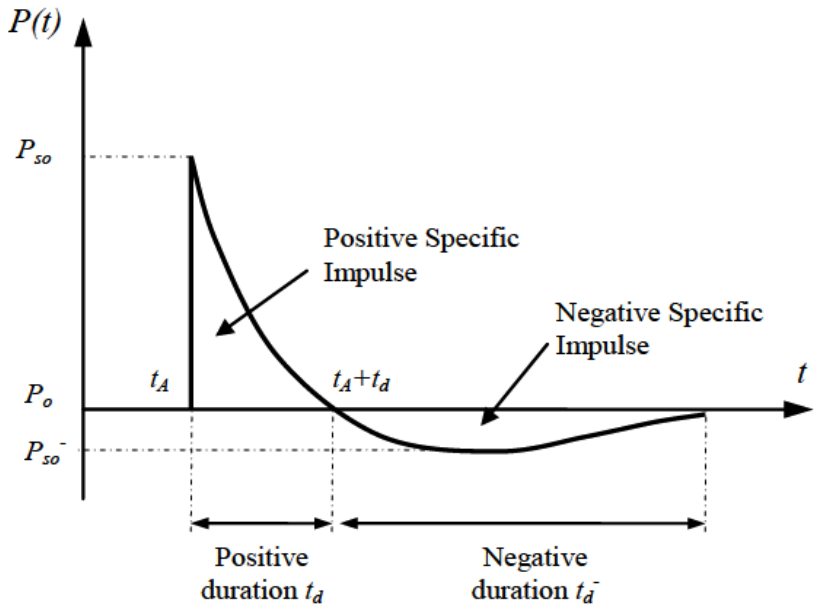

Fig. 2.2. Blast wave pressure – Time history [1].

A 3D surface of the pressure evolution in time as a function of the distance is shown in Fig. 2.3. As the stand-off distance increases, the maximum overpressure falls down and the duration of the positive-phase blast wave increases resulting in a lower-amplitude, longer-duration shock pulse.

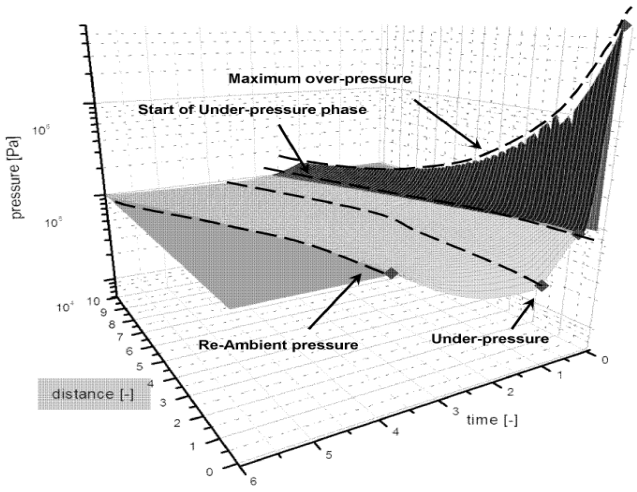

Fig. 2.3. 3D surface of the pressure evolution in time and distance function [2].

Friedlander [2, 3] proposed a formula for front shock pressure distribution that can be used in practical applications

$$P_{FR}(t) = P_{so}\cdot\left[1-\frac{t-t_A}{t_d}\right]\exp\left[-\beta\frac{t-t_A}{t_d}\right] \tag{2.1}$$

where P_{so} is the incident peak overpressure, t_d is positive phase duration, and β is the so-called wave front parameter related to a dimensionless scaled distance, ranging from 0.1 to 10. If $\beta<1$, the negative phase is important, whereas for $\beta>1$ the negative phase does not play significant role.

The following equation is used to introduce pressure distribution during time

$$P(t) = P_{SO}(1-\frac{t}{t_d})^{-\frac{t}{e^{t_o}}} \tag{2.2}$$

Here, t_d is the positive phase duration in seconds [4].

2.1.2.2 Fully reflected air blast

The blast also motivates the air to move. When a structure is placed in the path of the shock from an explosion, the interaction of the moving air with the structure impedes the air velocity, which leads to a noticeable enhancement on pressure subject to the

structure. The pressure on a structure rises very quickly to the peak reflected overpressure P_r instead of the incident peak overpressure. If the structure is very large, the decay duration of the reflected pressure pulse will be similar to the decay duration of the incident pressure pulse and the load on the structure will be similar to the history shown in Fig. 2.4.

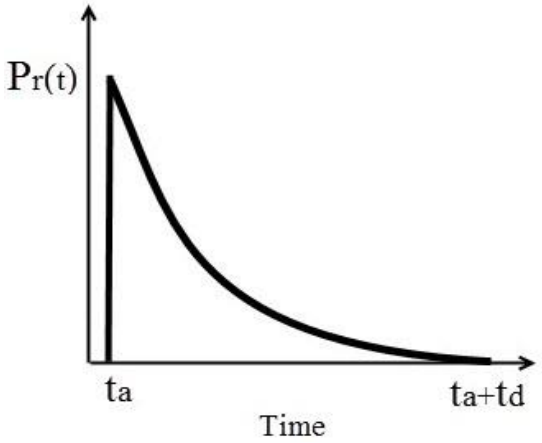

Fig. 2.4. Typical air-blast pressure distribution-
Fully reflected [5].

2.1.2.3 Reflected air blast with relief effects

If the structure is small, the reflected pressure will be relieved and the pressure will drop down to the summation of the incident pressure and the dynamic pressure loading, see Fig. 2.5. The relief starting time, t_{r1}, and the relief completion time, t_{r2}, are functions of the shock speed of the blast and the distance of the point from the closest free surface. The dynamic pressure loading is the multiplication of a drag coefficient, C_D, and the dynamic pressure, $q(t)$. The dynamic pressure is the result of drag as the air flows pass the structure. This is a different influence from the reflected pressure, where the structure ceases, or redirects, the flow of air.

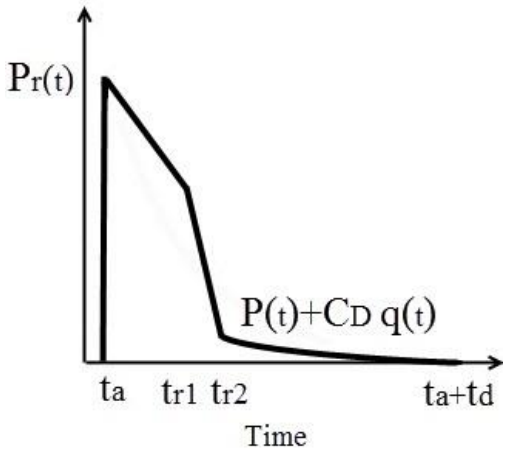

Fig. 2.5. Typical air blast pressure distribution-
Reflected with relief effects [5].

2.1.2.4 A new method for pressure distribution

Łodygowski and Sielicki [2] carried out a study to investigate the behavior of masonry walls subjected to various explosive loadings. To calculate the pressure distribution due to explosive loading, two methods are possible (numerical and empirical methods), and both were enough accurate according to these studies, see Fig. 2.6

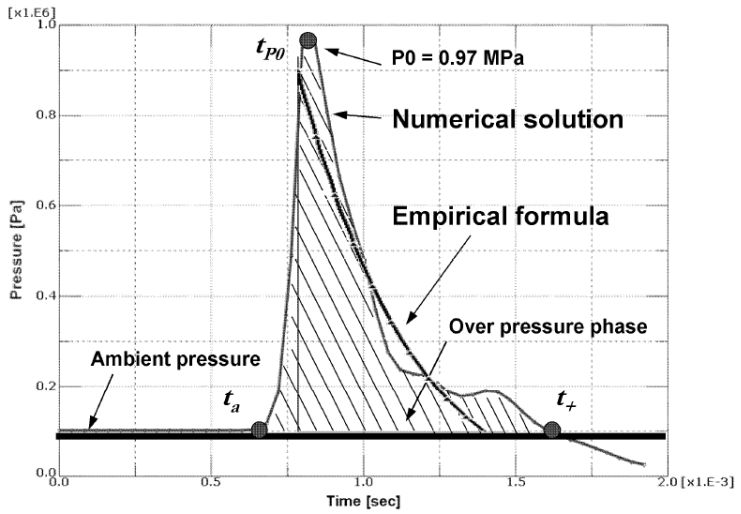

Fig. 2.6. Comparison of numerical and empirical
pressure distributions [2].

Eliminating the high computational costs, a novel method was applied to define the blast pressure distribution. According to this method, the values obtained from the curves should be multiplied by a model that describes the pressure topology in function of the position *x*, *y* parameters and α value. The α value is the distance between the

charge and the obstacle; that is, increasing the distance results in reduction of the pressure value, *P*, as

$$P(x, y, \alpha) = \frac{\alpha}{\left(x^2 + y^2 + \alpha\right)} \tag{2.3}$$

2.1.3 Prediction of blast pressure parameters and blast scaling

In recent decades, a series of investigations have been conducted to deduce formulas to predict the blast wave parameters for explosive materials. Hopkinson [6] introduced a scaling method to accurately predict air blast parameters. The Hopkinson equations for scaled stand-off distance is as follow

$$Z = \frac{R}{W^{\frac{1}{3}}} \tag{2.4}$$

Where, *R* is stand-off distance (effective distance between charge and target) (m). When the explosive charge *W* is other than TNT, the charge factor (CF) is applied to introduce the charge mass in terms of equivalent TNT mass.

The impulse of the incident overpressure concerned to the blast wave is the integrated area under the pressure-time curve. Therefore, the positive phase impulse i is defined as follow

$$i = \int_{t_A}^{t_A + t_d} P(t)dt \tag{2.5}$$

in which, $P(t)$ is over-pressure, t_A is arrival time and t_d denotes the positive phase duration, see Fig. 2.2.

These equations are used to define the free-field or fully reflected pressure pulses. Brode [7] introduced an equation for calculation of the incident peak overpressure due to spherical blast based on the scaled distance *Z*, as follow

$$P_{so} = \frac{0.975}{Z} + \frac{1.455}{Z^2} + \frac{5.85}{Z^3} - 0.019 \qquad bar \quad (0.1 < P_{so} < 10) \tag{2.6}$$

$$P_{so} = \frac{6.7}{Z^3} + 1 \qquad bar \quad (P_{so} > 10) \tag{2.7}$$

Another formulation was used by Kinney and Graham [8] to measure incident over-pressure as a function of scaled distance:

$$\frac{P_{so}}{P_o} = \frac{808\left[1 + (\frac{z}{4.5})^2\right]}{\sqrt{1 + (\frac{z}{0.048})^2}\sqrt{1 + (\frac{z}{0.32})^2}\sqrt{1 + (\frac{z}{1.35})^2}} \tag{2.8}$$

Newmark and Hansen [9] introduced also another relationship to calculate the peak overpressure for a high explosive charge detonating at the ground surface.

$$P_{so} = 6784\frac{W}{R^3} + 93(\frac{W}{R^3})^{\frac{1}{2}} \qquad bar \tag{2.9}$$

Yet another expression of peak over-pressure was introduced by Mills [10].

$$P_{so} = \frac{1772}{Z^3} - \frac{114}{Z^2} + \frac{108}{Z} \qquad kPa \tag{2.10}$$

Kinney and Graham [8] proposed also a relation for the positive phase pulse duration, t_d (milliseconds) as a function of scaled distance Z (m/Kg$^{1/3}$) as follow

$$\frac{t_d}{W^{\frac{1}{3}}} = \frac{980\left(1 + \left(\frac{z}{0.54}\right)^{10}\right)}{\left(1 + \left(\frac{z}{0.02}\right)^3\right)\left(1 + \left(\frac{z}{0.74}\right)^6\right)\sqrt{1 + \left(1 + (\frac{z}{6.9})^2\right)}} \tag{2.11}$$

When the shock wave encounters an object in its path, an incident peak over pressure is amplified by an increasing factor. Bangash [11] proposed an equation for the reflected peak overpressure P_r.

$$P_r = 2P_{so}\left\{\frac{7P_o + 4P_{so}}{7P_o + P_{so}}\right\} \tag{2.12}$$

Except for specific focusing of high intensity shock waves at near 45° incidence, these reflection factors are typically largest for normal incidence (i.e. a surface adjacent and perpendicular to the source) and diminish with the angle of obliquity.

2.1.4 Pressure-Impulse diagram

Pressure-Impulse diagrams are typically recommended by guidelines such as ASCE [12] in preliminary design and evaluation of structural damage against blast loading and to establish reliable response limits, see Fig. 2.7. A Pressure-Impulse (P-I) diagram is an iso-damage curve. In other words, each combination of pressure and impulse produces the same damage in a structural component. In most recent studies, a single degree of freedom (SDOF) model has been utilized in practice to generate the aforementioned curve. Therefore, the damage is presented in terms of displacement response. However, due to possibility that various failure modes occur, the deformation-based damage criterion does not seem to show suitable performance in predicting local damage. Shi, Hao, and Li [13] proposed a new damage criterion for RC columns based on the residual axial load-carrying capacity, since it is suitable for evaluating the shear and flexural damages. Subsequently, a simplified numerical method was introduced to generate a P-I diagram.

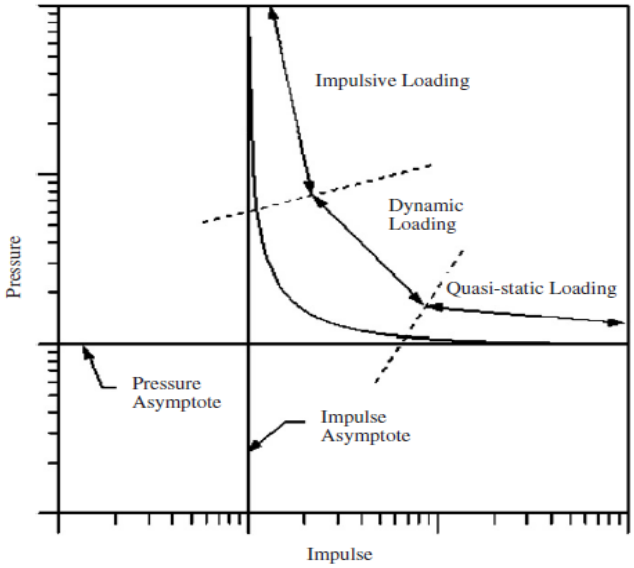

Fig. 2.7. Typical pressure-impulse curve (Primary features) [13].

According to Fig. 2.7, the horizontal axis deals with impulse values and the vertical axis presents the pressure values. The two asymptotes, one for pressure and one for impulse, define limiting values for each parameter. Loads with very short duration are called impulsive loading and the structural response induced depends on the associated impulse and not the peak pressure. This forms a vertical line that defines the minimum impulse required to reach a particular level of damage, which the curve approaches asymptotically at high pressures. On the contrary, as the load duration becomes much longer than the natural frequency of the structure, the load is considered as quasi-static loading and the response becomes insensitive to the impulse, but very sensitive to the peak pressure. The horizontal asymptote thus represents the minimum level of peak pressure required to reach that particular damage. Oswald and Wesevich [14] conducted an investigation to develop P-I diagrams for non-retrofitted and E-glass retrofitted walls made with concrete masonry units (CMU) submitted to blast loading, based on 236 open-air and shock tube tests.

2.1.5 Structural response to blast loading

The high strain rates, non-linear material behavior, uncertainties of blast load calculations and time-dependent deformations are responsible for the complexity in analyzing the dynamic response of blast-loaded structures. To establish the principles of this analysis, the structure is usually idealized as a single degree of freedom (SDOF)

system and the link between the positive duration of the blast load, t_d, load and the natural period of vibration of the structure, ω, is established.

Hence, the actual structure is replaced by an equivalent system of one concentrated mass, *M*, and one weightless spring representing the structural stiffness (i.e. *K* is the spring constant), see Fig. 2.8.

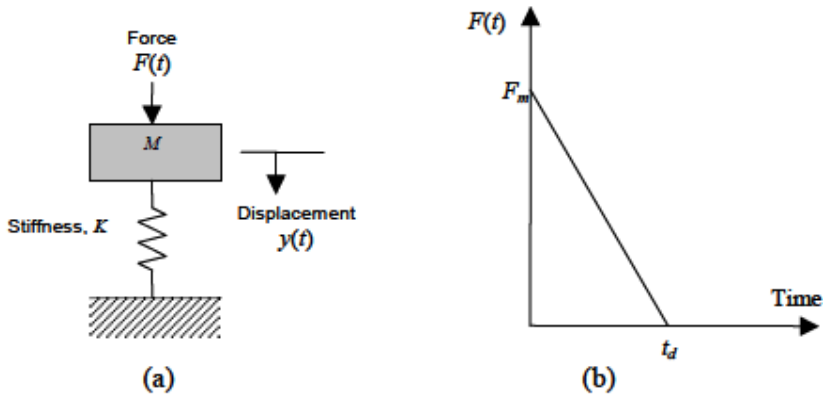

Fig. 2.8. Idealized SDOF system and idealized blast load [1].

Regarding Fig. 2.8, the idealized blast load equation having a peak force, F_M, and positive phase duration, and blast impulse equation are defined as [1]

$$F(t) = F_m\left[1-\frac{t}{t_d}\right] \qquad \text{Blast load} \qquad (2.13)$$

$$I = \frac{1}{2}F_m t_d \qquad \text{Blast impulse} \qquad (2.14)$$

The equation of motion of the un-damped elastic SDOF system for a time ranging from 0 to the positive phase duration is given as [1]

$$M\ddot{Y} + KY = F_m\left(1-\frac{t}{t_d}\right) \qquad (2.15)$$

The general solution can be expressed as

$$y(t) = \frac{F_m}{K}(1-\cos\omega t) + \frac{F_m}{Kt_d}(\frac{\sin\omega t}{\omega} - t) \qquad \text{Dynamic deflection} \qquad (2.16)$$

$$\dot{y}(t) = \frac{F_m}{K}\left[\omega\sin\omega t + \frac{1}{t_d}\left(\cos\omega t - 1\right)\right] \qquad \text{Velocity} \qquad (2.17)$$

By using above equations, the maximum dynamic deflection, y_m, and corresponding time, t_m, are obtained by setting the structural velocity equal to zero. Subsequently, the dynamic load factor, DLF, is defined as a ratio of maximum dynamic deflection to static deflection and also can be expressed in terms of $\frac{t_d}{T}$, where *T* is the natural period of vibration of the structure. The following classification of loading regime is proposed in terms of DLF factor since blast response of structures is significantly affected by dynamic load factor.

- $\omega t_d < 0.4$: Impulsive loading regime
- $\omega t_d > 40$: Quasi-static loading regime
- $0.4 < \omega t_d < 40$: Dynamic loading regime

2.2 BRIEF REVIEW OF HIGH STRAIN RATE CONSTITUTIVE MODELING

In recent years, due to the lack of dynamic material models and demand for their application in various industries, a number of investigations have been conducted to evaluate the high strain rates effects and derive constitutive models for different materials subjected to high strain rate loading. Considering the high strain rate effects, dynamic increase factors (DIFs) (i.e. a ratio of the dynamic to static parameters' values) have been introduced to define the effect of strain rates on material properties. This section aims at presenting the DIFs found in recent studies for diverse materials.

2.2.1 Study on dynamic material properties

2.2.1.1 Experimental derivation of DIF for masonry

Hao and Tarasov [15] conducted a series of dynamic uniaxial compressive tests on brick using a tri-axial static-dynamic testing machine to obtain stress-strain curves at various levels of strain rate. Hence, an adequate number of experiments were carried out and led to obtaining a variation of DIFs for the material parameters in a specific strain rate range as shown in Fig. 2.9 and Fig. 2.10 for compression.

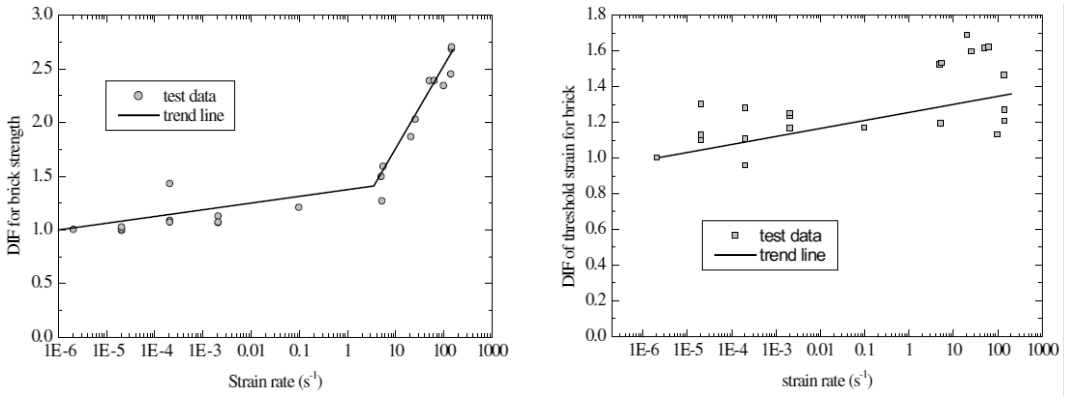

(*a*) (*b*)

Fig. 2.9. DIF for material properties of brick: (a) compressive strength; (b) compressive peak strain [15].

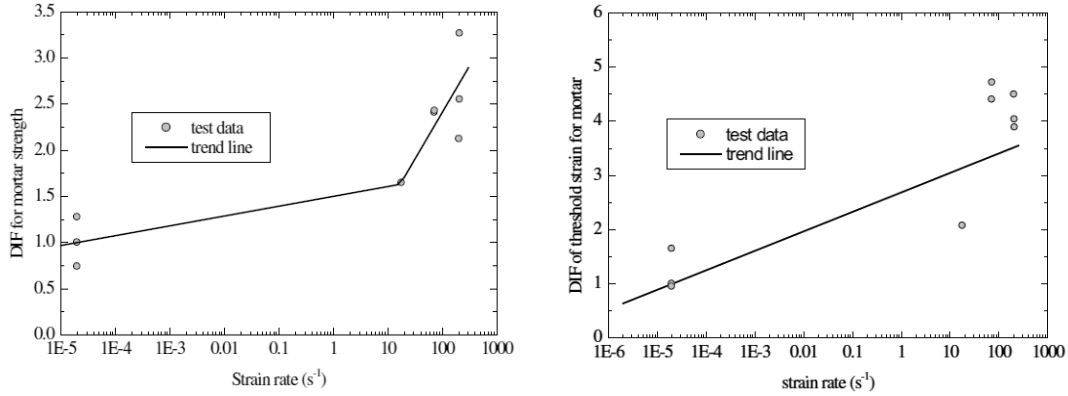

(*a*) (*b*)

Fig. 2.10. DIF for material properties of mortar: (a) compressive strength; (b) compressive peak strain [15].

The formulations of DIF for brick strength and peak strain (i.e. the strain corresponding to the peak strength) are fitted against experimental data for strain rates in a wide range

of $2\times10^{-6}\,s^{-1}-150\,s^{-1}$. The strain rate of $2\times10^{-6}\,s^{-1}$ is taken into account as the reference static strain rate. As shown in Fig. 2.9, increasing the strain rate led to an enhancement in both compressive strength and compressive threshold strain. Moreover, the strain rate influence is more significant for the strength after the strain rate of $3.2\,s^{-1}$ The experiments on brick to derive DIFs for material properties were followed by uniaxial compressive tests on mortar to study the strain rate also by Hao and Tarasov [15]. The DIF vs. strain rate curves for compressive strength and peak strain for mortar are presented in Fig. 2.10. The formulations of DIF for material properties are fitted against test data for strain rates ranging from $2\times10^{-6}\,s^{-1}$ to $150\ \ s^{-1}$. The strain rate of $2\times10^{-5}\,s^{-1}$ is considered as a reference static strain rate. It is obvious that by increasing the strain rate, both compressive strength and compressive threshold strain are enhanced. The strain rate variation is more effective on strength after the strain rate of $13\ \ s^{-1}$. The obtained expressions of this study for brick and mortar are adopted to consider the high strain rate effects in the material model presented in chapter 3.

Pereira [16] carried out a study to experimentally characterize the brick, mortar and masonry behavior at high strain rates. The expressions for DIFs of masonry parameters, see Eq. (2.18) to Eq. (2.21), in terms of strain rate were obtained under drop weight impacts loading over a wide range of strain rate and are adopted here to consider the high strain rate effects in material model presented in chapter 4. It is noted that very few results are available for this purpose and the most recent results, involving also the fracture energy and Young's modulus, were not available when developing the micro-model. It is also noted that the results of Pereira [16] in terms of stress and peak strain are consistent with those of Hao and Tarasov [15]

Regression equation for ultimate compressive strength

$$\begin{cases} 1 \quad if \quad 1E-5s^{-1} < \dot{\varepsilon} \le 3\,s^{-1} \\ 0.2798\ln\dot{\varepsilon}+0.6863 \quad if \quad 3s^{-1} < \dot{\varepsilon} \le 200\,s^{-1} \end{cases} \tag{2.18}$$

Regression equation for the Young's modulus

$$\begin{cases} 1 \quad if \quad 1E-5s^{-1} < \dot{\varepsilon} \le 1.7\,s^{-1} \\ 0.2409\ln\dot{\varepsilon}+0.8701 \quad if \quad 1.7s^{-1} < \dot{\varepsilon} \le 200\,s^{-1} \end{cases} \tag{2.19}$$

Regression equation for strain corresponding to peak compressive strength

$$\begin{cases} 1 \quad if \quad 1E-5s^{-1} < \dot{\varepsilon} \le 4s^{-1} \\ 0.0678\ln\dot{\varepsilon} + 0.9036 \quad if \quad 4s^{-1} < \dot{\varepsilon} \le 200\,s^{-1} \end{cases} \tag{2.20}$$

Regression equation for compressive fracture energy

$$\begin{cases} 1 \quad if \quad 1E-5s^{-1} < \dot{\varepsilon} \le 2\,s^{-1} \\ 0.4716\ln\dot{\varepsilon} + 0.5968 \quad if \quad 2s^{-1} < \dot{\varepsilon} \le 200\,s^{-1} \end{cases} \tag{2.21}$$

Burnett et al. [17] introduced results from dynamic tensile experiments on mortar joints using a specially designed Split Hopkinson Pressure Bar apparatus to obtain the strain rate sensitivity of tensile material properties of mortar. It was concluded that there is a remarkable dynamic enhancement of 3.1 in mortar strength at strain rate of $1s^{-1}$.

The high strain rate effect on tensile material properties of a specific type of stone found in Naples, Italy was the subject of a study by Asprone et al. [18]. Stress vs. strain curves in a wide range of strain rates from $10^{-5}\,s^{-1}$ to $50\,s^{-1}$ were presented by applying medium and high strain rate loading using a Hydro-Pneumatic Machine (HPM) and a Modified-Hopkinson bar apparatus. It was inferred that increasing the strain rate results in tensile strength enhancement up to three times, but in a tensile peak strain reduction. The DIF vs. strain rate curve for tensile strength is shown in Fig. 2.11 was also plotted to be evaluated and compared with the available DIF formulation for the materials with somewhat similar properties.

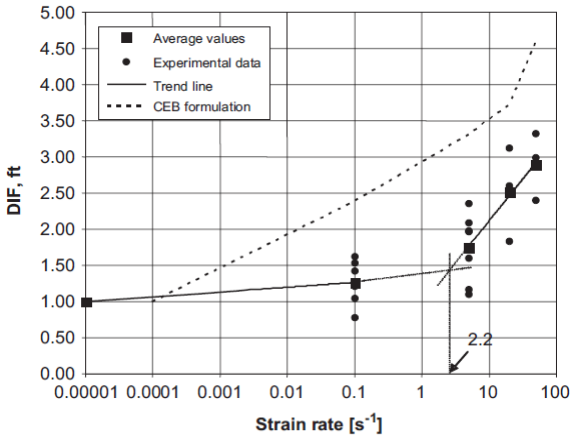

Fig. 2.11. Tuff stone tensile strength DIF vs. Strain rate experimental data [18].

In recent decades, a number of empirical relations for DIF of material properties have been proposed by the scientific community to consider the strain rate effect on concrete and to apply it during numerical analysis. Comité Euro-International du Béton [19] suggested diverse formulations of the DIF for compressive and tensile strengths, applicable in a wide range of strain rate based on experiments. The DIF of the tensile strength is given as [13]

$$DIF = \frac{f_{td}}{f_{ts}} = (\frac{\dot{\varepsilon}_d}{\dot{\varepsilon}_{ts}})^{1.016\delta} \quad for \quad \dot{\varepsilon}_d \le 30 \quad s^{-1} \tag{2.22}$$

$$DIF = \frac{f_{td}}{f_{ts}} = \beta(\frac{\dot{\varepsilon}_d}{\dot{\varepsilon}_{ts}})^{\frac{1}{3}} \quad for \quad \dot{\varepsilon}_d > 30 \quad s^{-1} \tag{2.23}$$

Where, f_{td} is the dynamic tensile strength at strain rate $\dot{\varepsilon}_d$, f_{ts} is defined as the static tensile strength at the static reference strain rate $\dot{\varepsilon}_{ts}$ ($\dot{\varepsilon}_{ts} = 3\times10^{-6}\, s^{-1}$), and $\log\beta = 7.11\delta - 2.33$. $\delta = \dfrac{1}{(10 + 6\dfrac{f_c'}{f_{co}'})}$, $f_{co}' = 10$ MPa, and f_c' is defined as uniaxial compressive strength in MPa.

In compression, the DIF is defined by [13]

$$DIF = \frac{f_{cd}}{f_{cs}} = (\frac{\dot{\varepsilon}_d}{\dot{\varepsilon}_{cs}})^{1.026\alpha} \quad for \quad \dot{\varepsilon}_d \le 30 \quad s^{-1} \tag{2.24}$$

$$DIF = \frac{f_{cd}}{f_{cs}} = \gamma(\dot{\varepsilon}_d)^{\frac{1}{3}} \quad for \quad \dot{\varepsilon}_d > 30 \quad s^{-1} \tag{2.25}$$

Where, f_{cd} is the dynamic compressive strength at strain rate $\dot{\varepsilon}_d$, f_{cs} is defined as static compressive strength at the static reference strain rate $\dot{\varepsilon}_{cs}$ ($\dot{\varepsilon}_{cs} = 3\times10^{-6}\, s^{-1}$), and $\log\gamma = 6.156\alpha - 0.49$. $\alpha = \left(5 + \dfrac{3f_{cu}}{4}\right)^{-1}$, and f_{cu} is the static cube compressive strength in MPa.

Malvar and Ross [20] proposed another DIF equation for tensile strength of concrete according to their experimental program. First, the slope variation is moved to $1 s^{-1}$ and the static reference strain rate is fixed at $10^{-6}\ s^{-1}$.

$$DIF = \frac{f_{td}}{f_{ts}} = (\frac{\dot{\varepsilon}_d}{\dot{\varepsilon}_{ts}})^{\delta} \quad for \quad \dot{\varepsilon}_d \le 1 \ \ s^{-1} \tag{2.26}$$

$$DIF = \frac{f_{td}}{f_{ts}} = \beta(\frac{\dot{\varepsilon}_d}{\dot{\varepsilon}_{ts}})^{\frac{1}{3}} \quad for \quad \dot{\varepsilon}_d > 1 \ \ s^{-1} \tag{2.27}$$

$$\delta = \frac{1}{(1+8\frac{f'_c}{f'_{co}})} \quad , \quad f'_{co} = 10\,\text{MPa}$$

Based on experimental studies on tensile dynamic behavior of existing concrete under high strain rates using modified Hopkinson bar, Asprone, Cadoni and Prota [21] verified the accuracy of CEB and Malvar formulations in predicting the DIF for tensile strength of concrete, for specific ranges of strain rate. Comparison between experimental DIFs of tensile strength and their corresponding values obtained from CEB and Malvar formulations is shown in Fig. 2.12. It was concluded the CEB formulation slightly underestimates their experimental results, whereas the Malvar formulation overestimates the experimental results in many cases.

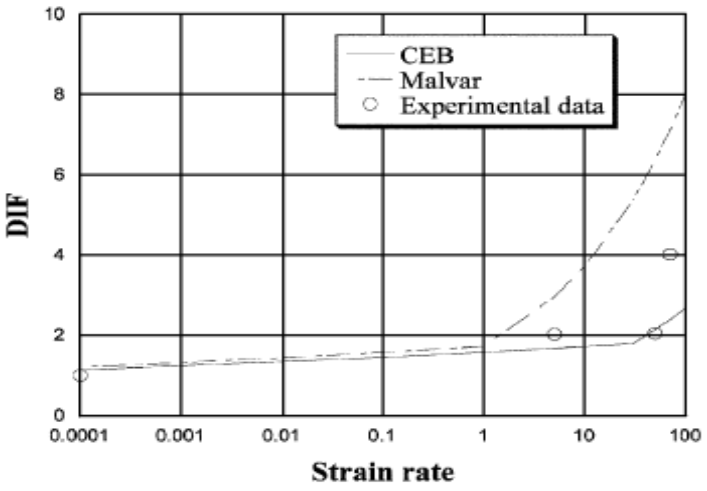

Fig. 2.12. Concrete tensile strength DIF vs. strain rate [21].

A series of experiments was performed on high-strength concrete by Ruiz et al. [22] to propose the Eq. (2.28) and Eq. (2.29) for compressive fracture energy as a bilinear function of the displacement rate. By increasing the displacement rate, the fracture energy is enhanced. The loading rate effect is more significant after the displacement rate of $7.04\times10^{2}\,mm/s$.

$$G_f = 147.5(1+0.34\dot{\delta}^{0.17}) \quad [N/m], \quad \dot{\delta} < 7.04\times10^{2}\,mm/s \tag{2.28}$$

$$G_f = -26171.6+9296.4\log\dot{\delta} \quad [N/m], \quad \dot{\delta} \geq 7.04\times10^{2}\,mm/s \tag{2.29}$$

Also, a formulation is given to measure peak load over a wide range of displacement rates, as

$$P_{\max} = 5.88(1+0.10\dot{\delta}^{0.51}) \tag{2.30}$$

Both fracture energy and peak load were measured over a wide range of loading rates. In order to apply low displacement rates, ranging from $10^{-4}\,mm/s$ to $10\,mm/s$, a servo-hydraulic machine was utilized, where for higher loading rates ($10^{2}-10^{3}\,mm/s$), a self-designed drop-weight impact machine device was used.

In order to introduce the strain rate effect on mechanical properties of steel, a model was reported in terms of strain rate by Malvar [23]. The proposed model is applicable for a wide range of strain rates from $10^{-4}s^{-1}$ to $225s^{-1}$ and could be evaluated for steel bars with different yield stresses, f_y, in MPa, ranging from 290 to 710 MPa, as

$$DIF = \left(\frac{\dot{\varepsilon}}{10^{-4}}\right)^{\alpha}, \tag{2.31}$$

$\alpha = 0.074 - 0.04\dfrac{f_y}{414}$, *for yield stress calculation*

$\alpha = 0.074 - 0.04\dfrac{f_y}{414}$, *for ultimate stress calculation*

2.2.1.2 Numerical derivation of DIF for masonry

A numerical study was performed on the numerical derivation of DIFs for strength and elasticity moduli of homogenized masonry [24]. A typical masonry unit, mortar and bond were selected to serve as a representative volume element (RVE) with detailed distinctive modeling of brick and mortar. By applying compatible displacement conditions with high strain rates on different surfaces of RVE, the equivalent stress vs. strain curves under different strain rate levels were calculated using the FE code LS-DYNA. DIF formulations for uniaxial compressive strength, uniaxial tensile strength, elastic modulus and the shear modulus as a function of strain rate in three directions are shown in Fig. 2.13.

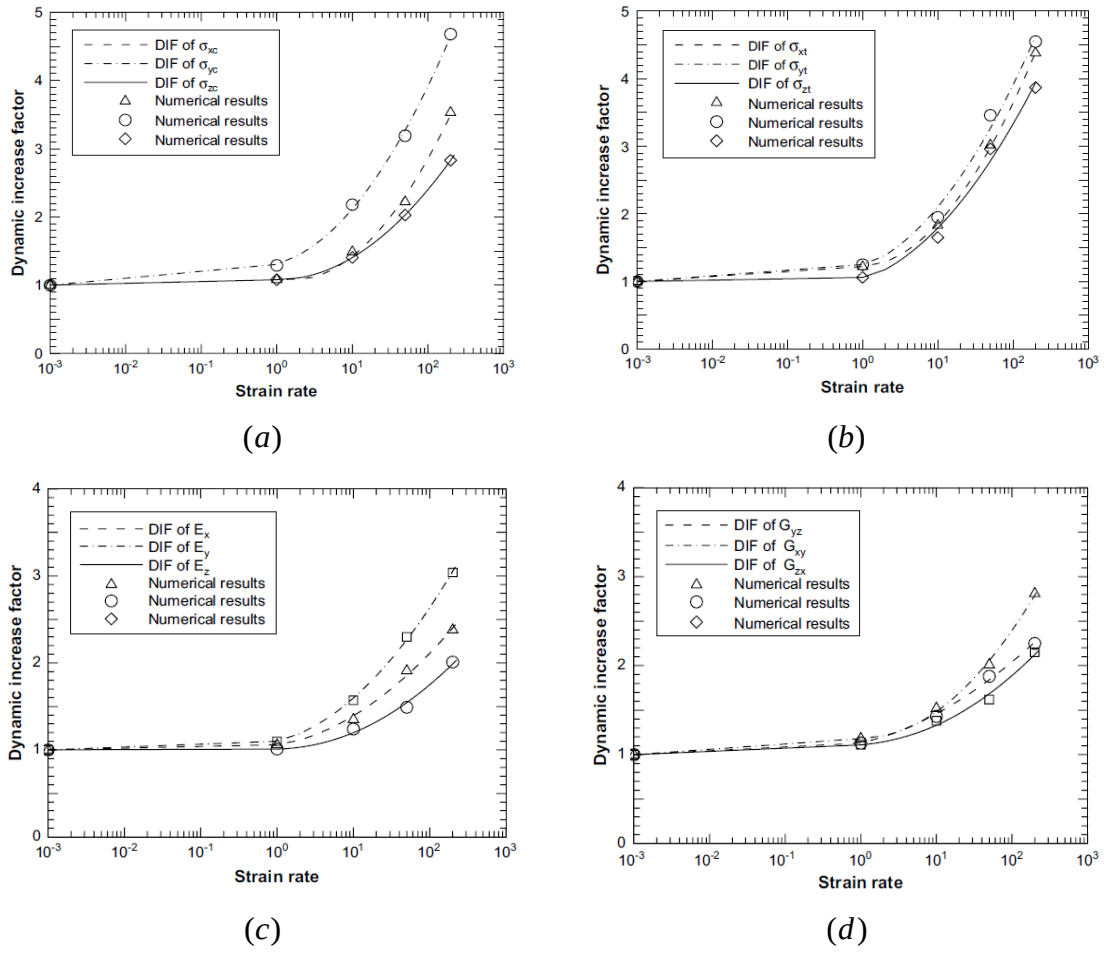

Fig. 2.13. DIF for material properties of masonry: (a) uniaxial compressive strength in the three directions; (b) uniaxial tensile strength in the three directions; (c) elastic modulus in the three directions; (d) shear modulus [24].

The DIFs were calculated in a wide range of strain rates from $10^{-3}\,s^{-1}$ to $200\,s^{-1}$. The strain rate of $10^{-3}\,s^{-1}$ was taken into account as static reference strain rate. Due to bond arrangement, the masonry properties are not equal in the three directions. The strain rate dependency is more pronounced at strain rates ranging from $10\,s^{-1}$ to $200\,s^{-1}$.

Based on the obtained DIF vs. strain rate curves for various material properties, the following conclusions were made by the authors:

- The uniaxial compressive strength, uniaxial tensile strength and the elastic modulus increase with the strain rate enhancement;
- At the same strain rate, the shear strength is slightly higher than the tensile strength, but much lower than the corresponding compressive strength;
- The quasi-static compressive strength of masonry is governed by the mortar strength;
- The compressive strength of masonry at high strain rate depends on both brick and mortar;
- The compressive peak strain is influenced more by mortar than brick.

As it is mentioned before, in order to predict the structural response accurately, using appropriate failure criteria is inevitable. Hence, DIFs are needed to govern the failure envelop. In this regard, DIFs of the parameters of the failure envelop associated with material properties at certain strain rates need to be multiplied by their respective quasi-static parameters' values to expand the failure envelop.

2.3 EXPERIMENTAL STUDIES ON THE PERFORMANCE OF MASONRY STRUCTURES TO BLAST LOADS

A series of experimental studies have been conducted to evaluate the performance and blast response of masonry structures subjected to high strain rate loading. Structural damage and fragmentation, and mechanisms of collapse have been evaluated through such investigations. The majority of existing structures were not designed with blast loading in mind and various retrofitting techniques have been evaluated to find more effective techniques to enhance the blast resistance of existing structures. This is particularly applicable for higher hazard buildings, such as governmental buildings, religious buildings and landmark buildings, and the objective is to reduce casualties and material losses. Despite the large costs usually involved in laboratory tests,

experimental data are needed to improve the previously developed analysis codes, and a review is presented next.

2.3.1 Structural masonry damage and fragmentation

2.3.1.1 Non-retrofitted walls

The formation of cracks in every horizontal mortar joint was the failure mechanism of un-grouted, unreinforced concrete masonry unit walls (CMU walls) tested by Baylot et al. [25]. These CMU walls were connected through pins to supporting frames in top and bottom, and were out-of-plane loaded. It was noted that the fully-grouted, unreinforced CMU walls failed at the mid-height mortar joint over the entire length, and rotated along the bottom edge. Additionally, in some cases, diagonal cracking and vertical cracks on both sides of the wall at the central part of the wall were also observed.

Bond failure at the mortar joint and overturning about mid-height were also reported in other tests [26], as failure mechanisms of CMU walls that were fixed at top and bottom. Eamon, Baylot, and O'Daniel [27] classified CMU wall behavior against blast loads into three failure modes that correspond to three ranges of pressure magnitude. For high pressure load, the entire wall was broken in two horizontal lines and was divided into three parts, where the bottom and top parts rotated while the central one remained vertical in a four parallel yield line mechanism, see Fig. 2.14(a). In case of moderate pressure, a horizontal crack formed at mid-height of the wall along the entire length of the wall in a typical three-hinged mechanism, see Fig. 2.14(b). In case of low pressure, the wall was divided also due to a long crack at mid-height, but no remarkable rotating was noticed, see Fig. 2.14(c).

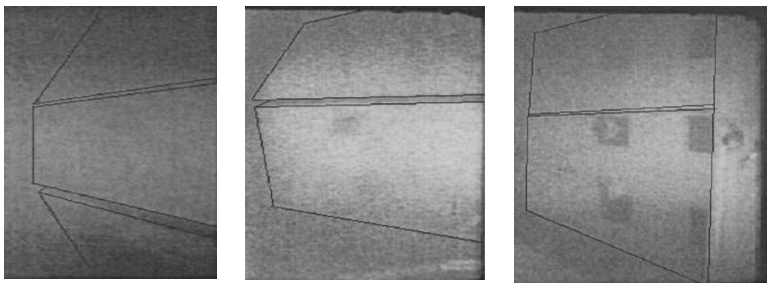

(*a*) (*b*) (*c*)

Fig. 2.14. Typical failure modes: (a) High pressure load; (b) Moderate pressure load; (c) Low pressure load [27].

The crack patterns of unreinforced masonry walls subjected to lower velocity impacts were addressed by Gilbert, Hobbs, and Molyneaux [28] in parapets supported at the bottom and side edges. Cracks patterns were classified into two groups based on the time of formation: during test and after test. During the test, the major cracks formation coincided with the peak applied force time (back face tensile zone cracks, and horizontal cracks). Primarily, the cracks at the top of the walls were detected, followed by cracks at mid-depth. Cracks at the bottom were formed much later. Finally, front face cracks occurred far from the applied force. Fig. 2.15 shows observed post-test crack patterns diagrammatically.

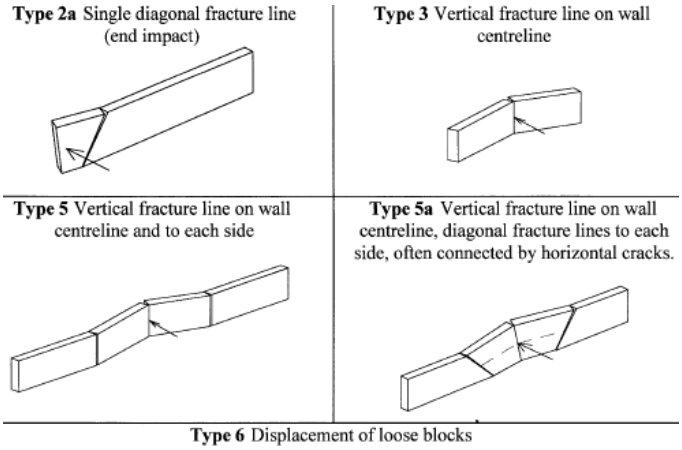

Fig. 2.15. Observed post-test failure mechanisms in parapets, supported at the bottom and sides [28].

2.3.1.2 Retrofitted walls

Baylot et al. [25] adopted three different retrofitting methods to reduce the debris hazard and improve the blast response of CMU walls, namely bonding FRP to the back of the wall, applying sprayed-on polyurea on back of the wall, and placing a sheet of steel behind the wall. Although the proposed retrofitting techniques performed acceptable in reducing damage against detonation, some improvement seemed still needed in the aforementioned methods. In the FRP case, the overlapped FRP was disconnected from the reaction structure and led to wall rotation about the bottom of the wall into the structure. Similar difficulties had occurred in utilizing polyurea technique (pulling out from reaction structure and wall rotation into the structure).

Muszynski and Purcell [29] carried out tests on retrofitted concrete masonry walls with CFRP which led to remarkable reduction in displacement. Due to pulverization of

masonry blocks, after the test the CFRP felt loose. Myers, Belarbi, and El-Domiaty [30] carried out a series of tests on masonry walls, retrofitted with GFRP rods and wide GFRP strips, subjected to a series of increasing intensity blast tests. The retrofitted wall had a reduction in debris scatter and at least a 50% increase in peak pressure resistance. Cracks formed at the bed joint of masonry wall at low stress levels but the GFRP resisted the tensile stresses, whereas the masonry resisted much of compressive stresses. Davidson et al. [31] reported the application of sprayed-on polymer retrofit for strengthening masonry walls against blast loads. The polymer layers were coated in the entire face of the walls and overlapped onto the surrounding reaction structures. It was noted that in low and moderate detonation this technique shows appropriate performance since the retrofitted walls remained intact. However, in large explosions, due to extreme energy imparted by the blast, polymer ripped across the mortar joint at mid-height of the wall and the wall sheared from its support although the polymer held much of the retrofitted wall.

2.3.2 Damage (level) criterion

It is inevitable to adopt a damage criterion that can be readily applied to categorize masonry wall behavior from test results. The design manual UFC-3-340-02 (2008) [32], which provides widely used criteria for design of blast resistant structures, proposes Table 2.1 to classify damage response of unreinforced masonry walls.

Table 2.1. Masonry damage criteria (UFC-3-340-02, 2008) [32].

Element	Yield pattern	Maximum support rotation (°)
Masonry reusable	One-way	0.5
	Two-way	0.5
Masonry non-reusable	One-way	1.0
	Two-way	2.0

Doherty et al. [33] concluded that walls would collapse if the mid-height deflection values reached the wall thickness. The US Army Corps of Engineers (USACE) [34] also proposed that deflection exceeding the wall thickness should be applied as ultimate damage criterion. Zapata and Weggel [35] presented test results on a unreinforced masonry structure subjected to blast loads. The experimental observations emphasized again that the infill walls will fail if the maximum deflection exceeds the wall thickness.

Varma et al. [36] reported a qualitative damage criterion by classification of damage in four levels based on their test observations:

- Level A - Total collapse of brick wall;
- Level B - Major translocation of brick wall – Non-repairable damage;
- Level C - Observable cracks along the RC and brickwork joints;
- Level D - Outward damage like hairline cracks along the RC and the brick wall joints. Generalized chipping of mortar linings.

2.4 NUMERICAL INVESTIGATIONS ON MASONRY STRUCTURES SUBJECTED TO BLAST LOADS

Masonry consists of units which can be bricks, adobes or blocks, and mortar joints such as clay, bitumen and cement based mortar. Despite the geometry and combination of unit and mortar materials in masonry construction, all masonry has similar characteristic of low tensile strength. The fundamental condition in achieving high accuracy during numerical modeling is accessing reliable and comprehensive knowledge of constitutive material models of masonry components. In particular, good understanding of softening (in tension, shear and compression) and hardening behavior (in compression) are required, which are undeniable features of pressure dependent materials.

The linkage between mortar and unit (unit-mortar interface) is the weakest part of the masonry assemblage and significantly affects the non-linear behavior of masonry. The potential damage in unit-mortar interface can be due to tension and shear, whereas compression action is a composite effect.

2.4.1 Strategies for numerical modeling

Micro and macro strategies have been developed for numerical modeling of masonry structures. Each strategy has its own advantages and disadvantages regarding the accuracy, computational costs, better understanding of local behavior, and user-friendly mesh generation. Regarding the use of the two strategies, each of them is valuable. If the accuracy and best understanding of local behavior is important, detailed micro modeling is more adequate. In most cases, simplified micro-modeling suffices. On the contrary, in case of avoiding high computational costs, the macro approach is more adequate.

2.4.1.1 Micro approach

The micro-modeling approach is used to consider local effects in detail. With this method more accurate representation of the behavior of a masonry structure can be obtained. This method is useful for local analysis while it is impractical for analysis of full structures due to the need for calibrating a large number of parameters and the large number of degrees of freedom. Micro modeling of individual components can also be done in two ways: detailed or simplified, see Fig. 2.16.

In detailed micro modeling the units and mortar joints are modeled by continuum elements, while unit-mortar interfaces are represented by non-continuum elements. The mechanical properties of both units and mortar joints are taken into account and the interface elements present possible failure behavior. However, in simplified micro modeling, units are represented by continuum elements which are bonded by joints that consist of mortar and two unit-mortar interfaces (upper and lower). This combination is lumped into an average zero-thickness interface element. Given the lack of Poison's ratio of mortar, some accuracy is lost.

2.4.1.2 Macro approach

Macro modeling is a very simplified method and takes into account the global behavior of the structure. In macro modeling, the global behavior of the masonry structure is governed by anisotropic homogenous continuum elements, see Fig. 2.16. It can be emphasized that macro modeling needs lower computational resources and allow easier interpretation of results than micro modeling, and provides usually gratifying accuracy.

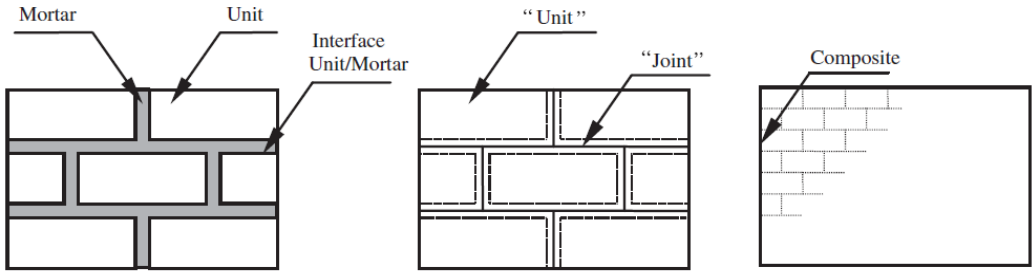

Fig. 2.16. Modeling strategies for masonry structures: (a) detailed micro-modeling; (b) simplified micro-modeling; (c) macro-modeling [37].

Marques and Lourenco, [38], in an investigation related to seismic assessment of masonry structures with using the push-over analysis, presented structural component models (macro elements) developed in recent years, which are even grosser representations. The aforementioned macro elements are presented in Fig. 2.17.

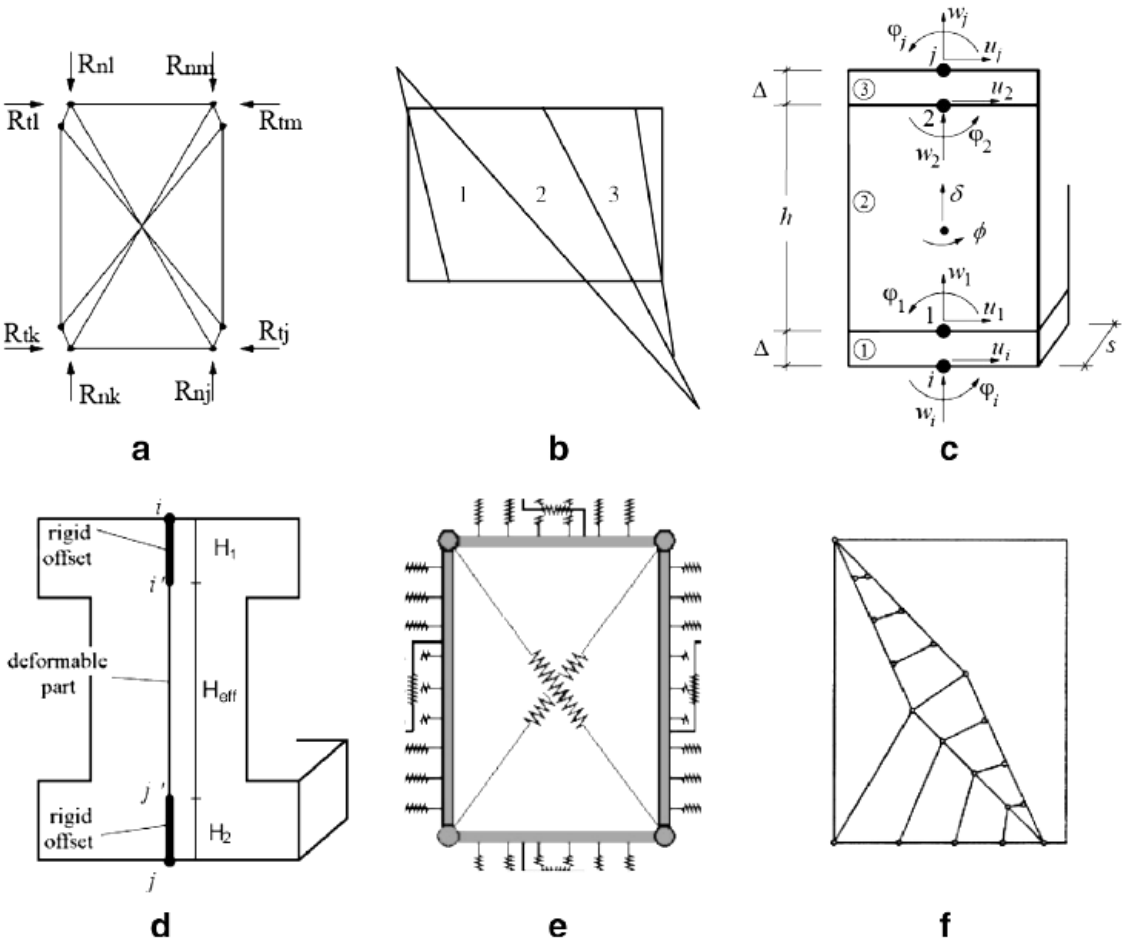

Fig. 2.17. Macro-elements of (a) variable geometry; (b) multiple fans; (c) three layers; (d) equivalent frame; (e) multiple springs; (f) strut and tie [38].

Initially, this strategy was based on two-dimensional macro elements adopted in order to perform in-plane wall analysis, assuming a "no-tension" hypothesis, see Fig. 2.17(a) and (b). Afterwards, one-dimensional macro-elements were idealized to simulate the global behavior of framed structures, see Fig. 2.17(c) and (d). Two-dimensional multiple springs, and strut and tie macro-elements (Fig. 2.17(e) and (f)) were developed to avoid the limitations inherent to inaccurate simulation of the interaction between macro-elements and weak modeling of the cracked condition of panels in the use of beam-type macro-elements, by applying a set of non-linear springs and a strut and tie model, sequentially.

2.4.2 Parameters involved in sensitivity studies

This section is dedicated to the introduction of relevant parameters used in recent sensitivity studies, and to address their effect on high strain rate behavior of masonry walls. The parameters concerning the material properties of brick and mortar, and their corresponding DIFs were adopted as input parameters in model calibration of a study that deals with model validation on the blast response of unreinforced brick masonry walls [39]. The parameters are the quasi-static strengths under uniaxial compression, uniaxial tension, tri-axial tension, and the quasi-static threshold strains under uniaxial compression and uniaxial tension, and their corresponding DIFs. Due to shortage of information regarding the strain rate effects in tension for brick and mortar, the DIFs of tensile parameters adopted were the same as in compression. A detailed micro modeling approach was adopted. According to this approach, three dimensional solid elements were used to model brick and mortar, and perfect bond was assumed between them. The commercial explicit FE code LS-DYNA was used for the purpose of numerical simulation.

The parametric study was conducted to investigate the effect of mortar and brick strength, boundary conditions and wall thickness variations on response and damage prediction of the wall. According to this study, the effect of brick and mortar strength are insignificant on the structural response under larger blast loading. However, they have a significant influence on the maximum deflection or the support rotations under smaller blast loading. Increasing the mortar and brick strength, the maximum deflection of the wall is reduced. Moreover, increasing the number of the fixed sides or wall thickness can lead to higher reduction in maximum deflection of the wall.

In another investigation by Eamon, Baylot, and O'Danie [27] for modeling CMU walls subjected to explosive loads, the following parameters were taken into account for parametric studies: top block failure pressure, block–frame contact friction, block–block contact slide-surface strength, block–block contact friction, and blast pressure. Failure mode variation was observed as well as maximum debris velocity. It was noted that for higher blast pressure cases, the analysis results are more sensitive to parameter values and failure mode is most sensitive to boundary block strength. For moderate pressure cases, contact surface interaction is also considered relevant, when compared to the reduced blast load. Frictional forces are now of a magnitude such that they may significantly affect failure shape. For low pressure blasts, mortar strength becomes

important, as this is the key factor for wall failure or survival, whereas for the higher blast loads, failure occurs regardless of mortar strength. Regarding modeling, a simplified- micro modeling approach was adopted in this study since 8 node hexahedral solid elements were utilized for units and zero thickness interface elements were applied for mortar.

The sensitivity analysis was conducted for a variety of parameters that potentially could be taken for the particular CMU walls considered in a study by Eamon [40]: Mortar joint modulus of rupture, contact friction between CMU surfaces, contact friction between the CMU and top and bottom building floors; and for the CMUs, Poisson ratio, compressive strength, tensile strength, modulus of elasticity, shear modulus, bulk modulus, and strain rate strengthening. Fig. 2.18 was presented to identify the variables affecting the wall behavior significantly at three different hazard levels.

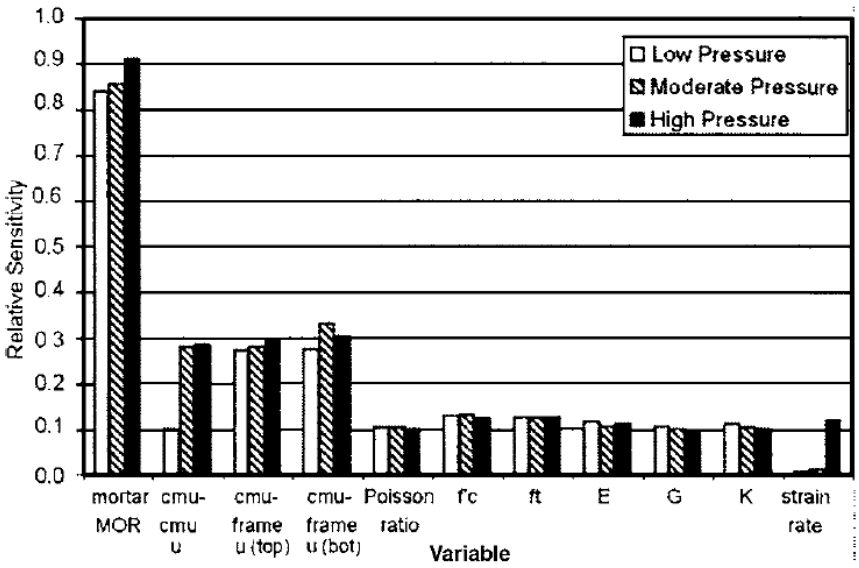

Fig. 2.18. Normalized resistance sensitivity analysis [40].

Furthermore, in an investigation by Milani and Lourenco [41] for blast analysis of enclosure masonry walls, a parametric analysis was carried out to evaluate the effectiveness of different wall thicknesses, mortar joint tensile strengths, and dynamic pressures, corresponding to blast loads (in kilograms of TNT), ranging from small to large. As expected, the maximum displacement would decrease sensibly when high-strength mortar, thicker walls or lower blast pressure would be adopted.

Chapter 3

3 A DYNAMIC COMPOSITE INTERFACE MODEL FOR MASONRY

3.1 INTRODUCTION

A few attempts have been made recently to address the micro-modeling of masonry subjected to high strain rates. One example is the plastic damage material model that was utilized to characterize the brick and mortar behavior in micro numerical simulation of blast response of unreinforced walls by Wei and Stewart [39]. The DIFs for masonry material properties derived by Hao and Tarasov [15] were adopted to include the strain rate effect during numerical analysis. The damage dependent piecewise Drucker-Prager strength criterion was presented in Fig. 3.1 and Eq. (3.1) was used for continuum modeling of brick and mortar. No interface was considered in the analysis.

$$F = a_i I_1 + \sqrt{J_2} - C_{i0}(1-D) = 0 \tag{3.1}$$

Here, I_1 is the first invariant of the stress tensor, J_2 is the second invariant of the stress deviatoric tensor, a_i, C_{io} are material parameters determined by tests, and D is a damage scalar that consists of two parts, tension and compression.

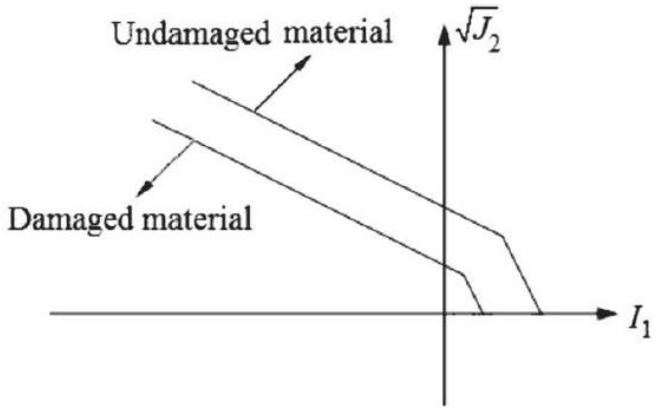

Fig. 3.1. Piecewise Drucker-Prager strength criterion for bricks and mortar in [39].

A simple rigid-perfectly plastic homogenization masonry model was developed by Milani, Lourenço, and Tralli [42] for micro numerical simulation of masonry structures subjected to out-of plane high strain rate loads. The proposed model is not only characterized by a low number of input material parameters but also numerically inexpensive and robust. The aforementioned model was assigned to a limit analysis FE thin plate triangular element. In order to obtain anisotropic masonry failure criteria, the unit cell is subdivided into a fixed number of sub-domains and layers along the thickness. A Drucker-Prager with a cap failure criterion was adopted for bricks and joints sub-domains, and a Mohr-Coulomb failure criterion with compressive linearized cap and tension cut-off was utilized for bricks-joints interfaces, see Fig. 3.2.

In the model, the following hypotheses are assumed: (a) Rigid perfectly plastic behavior of the material; (b) Strain rate insensitivity of the yield stress; (c) Negligible changes of the geometry during deformation.

This work intends to propose a newly developed dynamic interface model accounting for strain rate effects for numerical simulations of the structural response of masonry walls subjected to high strain rates using the finite element (FE) code ABAQUS. The rate-dependent failure envelop is divided into three parts, namely tension mode, coulomb friction mode, and compressive cap mode on the basis of the corresponding failure mechanisms. After implementing the material model into ABAQUS as a user

supplied subroutine, a micro approach is used for numerical modeling of masonry walls. The developed model is attributed to interface elements to simulate the joint behavior between two masonry units. A comparison between numerical results and field test data obtained by Gilbert et al. [28] is performed to evaluate the performance of the proposed material model and the accuracy of the simulation in predicting the impact response and damage of masonry walls. Finally, a parametric study is carried out to discuss the effect of the main parameters changes on the global behavior of masonry walls.

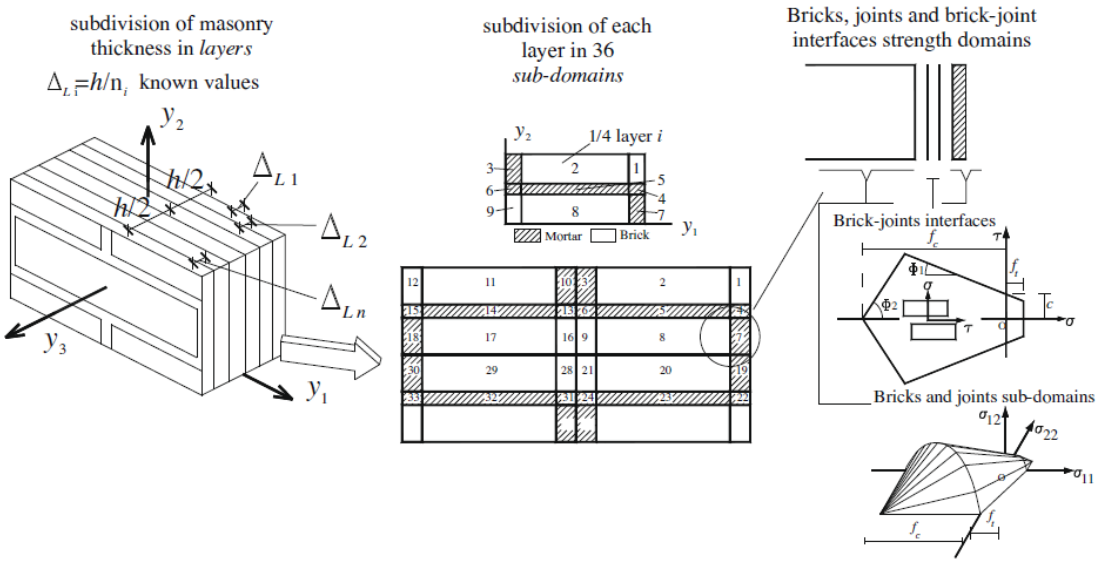

(*a*) (*b*) (*c*)

Fig. 3.2. The micro-mechanical model proposed in [42]: (a) Subdivision in layers along the thickness; (b) Subdivision of each layer in sub-domains; (c) Linearized strength domain for bricks and joints sub-domains, with Mohr-Coulomb failure criteria, and for bricks-joint.

3.2 A PLASTIC INTERFACE MODEL FOR HIGH STRAIN RATES

In the present study, a rate dependent interface model is introduced to characterize the joint behavior. Depending upon the main failure mechanisms of masonry walls, the failure envelop is divided into three parts namely, tension cut-off, Coulomb friction, and elliptical cap after [43], see Fig. 3.3. Hence, each part has its own failure criterion presented in terms of k, where the k parameter is a scalar adopted to measure the amount of softening and hardening in order to control the yield surface. For a 3D configuration, the stress vector $\boldsymbol{\sigma}=\{\sigma,\tau_s,\tau_t\}^T$, the stiffness matrix $D=diag\{k_n,k_s,k_t\}$

and the generalized strain vector $\varepsilon = \{\Delta u_n, \Delta u_s, \Delta u_t\}^T$. The subscripts n, s, t refer to the normal and the two perpendicular shear components.

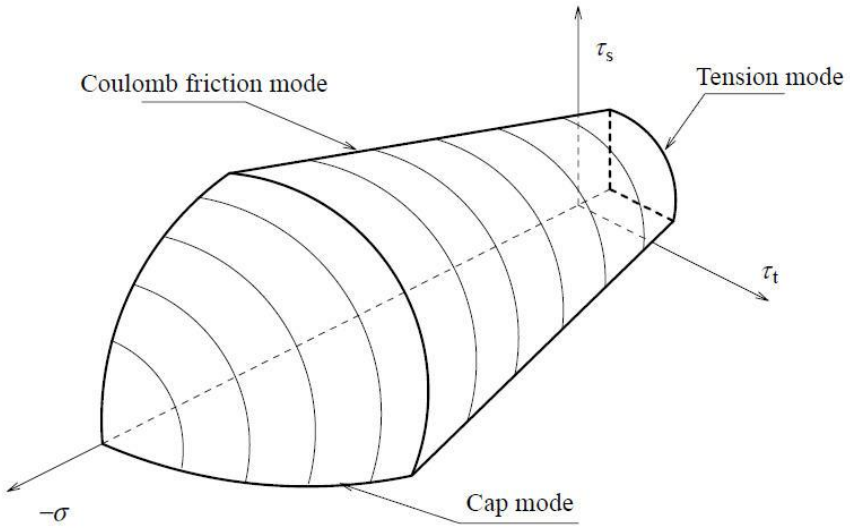

Fig. 3.3. 3D Failure envelope of the interface cap model [43].

In order to consider the high strain rate effects on the interface material model, a few dynamic increase factors (DIFs) are defined to control the failure envelop. Again, the DIF is the ratio between the dynamic and static parameters' values. These factors multiply the material parameters to expand the failure envelope at different strain rate levels.

3.2.1 Tension cut-off mode

For the tension cut-off mode, the yield function is given as follows

$$f_1(\boldsymbol{\sigma}, k_1) = \sigma - \bar{\sigma}_1(k_1) \tag{3.2}$$

where σ denotes the normal stress and k_1 is a scalar to control the yield surface by measuring the amount of softening. The yield stress value $\bar{\sigma}_1$ follows the exponential tensile softening behavior assumed in accordance with tests (Fig. 3.4) to describe the inelastic behavior and reads

$$\bar{\sigma}_1 = f_t \exp(-\frac{f_t}{G_f^I} k_1) \tag{3.3}$$

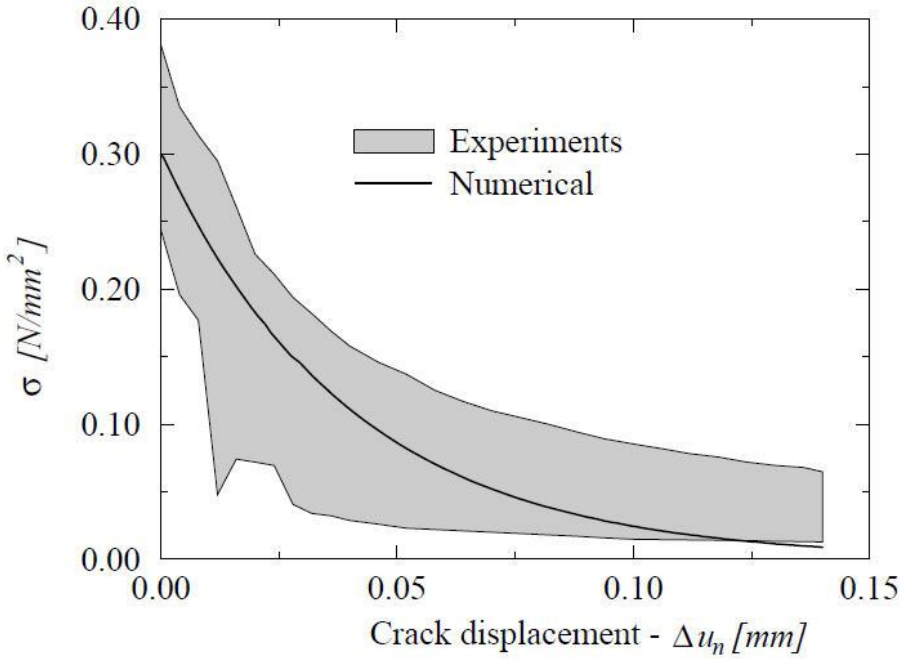

Fig. 3.4. Tensile behavior of present model vs. experimental results with f_t = 0. 30 (N/mm^2) and G_f^I = 0. 012 [Nmm/mm^2] [44].

Here, f_t is the tensile strength of the joint (usually equal to the unit-mortar interface) and G_f^I is the mode I fracture energy.

The dynamic increase factors are applied to the uniaxial tensile strength and the fracture energy to obtain

$$f_t = DIF \times f_{t_0} \tag{3.4}$$

$$G_f^I = DIF \times G_{f_0}^I \tag{3.5}$$

where, f_{t_0} and $G_{f_0}^I$ are the quasi-static strength and fracture energy under uniaxial tension, respectively.

In the case of strain softening, the scalar $\dot{k}_i$ is given, in rate form, in terms of plastic strain rate and is expressed as

$$\dot{k}_i(\boldsymbol{\sigma}, \dot{\lambda}_i) = \dot{\varepsilon}_i^{eps} = \sqrt{(\dot{\varepsilon}_i^p)^T \dot{\varepsilon}_i^p} \tag{3.6}$$

where the plastic strain rate reads $\dot{\varepsilon}_i^p = \dot{\lambda}_i \frac{\partial g_i}{\partial \boldsymbol{\sigma}}$ assuming non-associated flow rule, and $\dot{\varepsilon}^{eps}$ denotes the equivalent plastic strain rate and must always be positive. The subscript *i* refers to the label of yield surface.

Here, g_i is the non-associated plastic potential and $\dot{\lambda}_i$ is the plastic multiplier. As in mode *I*, the normal plastic relative displacement governs the softening behavior, $\dot{k}_1$ can be assumed equal to

$$\dot{k}_1(\dot{\lambda}_1) = \left|\Delta \dot{u}_n^p\right| = \dot{\lambda}_1 \tag{3.7}$$

When yielding occurs, the plastic corrector brings back the stress update to the yield surface by applying locally a Newton-Raphson method to solve the nonlinear system and updating the stress tensor and the user-defined state variables for state *n*+1. In a plasticity model, it is worth to mention that at the starting point the stress is assumed to be elastic (considering a trial value), such as $\boldsymbol{\sigma}_{n+1} = \boldsymbol{\sigma}^{trial}$, $\dot{k}_{i\,n+1} = 0$, and $\dot{\lambda}_{i\,n+1} = 0$, which is obtained by the elastic predictor. The stress update equations are given for a finite step are given by

$$\boldsymbol{\sigma}_{n+1} = \boldsymbol{\sigma}^{trial} - D\dot{\varepsilon}_{n+1}^p \tag{3.8}$$

with $\boldsymbol{\sigma}^{trial} = \boldsymbol{\sigma}_n + D\dot{\varepsilon}_{n+1}$.

For single surface plasticity, in the general case of $g = g(\boldsymbol{\sigma}, k)$, the Euler backward algorithm reduces to the non-linear set of equations with unknowns, $\boldsymbol{\sigma}_{n+1}$ components, $\dot{k}_{i\,n+1}$ and the plastic multiplier $\dot{\lambda}_{i\,n+1}$ to obtain the stress update in the presence of yielding

$$\begin{cases} D^{-1}(\boldsymbol{\sigma}_{n+1} - \boldsymbol{\sigma}^{trial}) + \dot{\varepsilon}^{p}_{i\,n+1} = 0 \\ \dot{k}_{i\,n+1} = \dot{k}_{i\,n+1}(\boldsymbol{\sigma}_{n+1}, \dot{\varepsilon}^{p}_{i\,n+1}) \\ f_{i\,n+1}\left(\boldsymbol{\sigma}_{n+1}, k_{i\,n+1}\right) = 0 \end{cases} \tag{3.9}$$

Considering $\boldsymbol{\sigma}_{n+1} = \boldsymbol{\sigma}_{n+1}(\dot{\lambda}_{i\,n+1})$ and Eq. (3.6) at the stage *n*+1, followed by substitution of these two equation in the yield criterion Eq. $(3.9)_3$ results in a non-linear expression of yield function in one variable, $f_{i\,n+1}(\dot{\lambda}_{i\,n+1}) = 0$.

For mode I, after manipulation, the stress update equation yields

$$\begin{cases} \sigma_{n+1} = \sigma^{trial} - \dot{\lambda}_{1\,n+1} k_n \\ \tau_{n+1} = \tau^{trial} \end{cases} \tag{3.10}$$

where $\tau = \sqrt{\tau_s^2 + \tau_t^2}$ is assumed for 3D configuration. The derivative with respect to $\Delta\lambda_{n+1}$ is needed for the iterative local Newton-Raphson method, given by

$$\left.\frac{\partial f_1}{\partial \dot{\lambda}_1}\right|_{n+1} = -k_n - \frac{\partial \bar{\sigma}_1}{\partial k_1} \tag{3.11}$$

3.2.2 Coulomb friction mode

In mode *II*, the Coulomb friction yield criterion reads

$$f_2(\boldsymbol{\sigma}, k_2) = \tau + \sigma \tan\phi(k_2) - \bar{\sigma}_2 \tag{3.12}$$

Here, τ and $\bar{\sigma}_2$ are given

$$\tau = \sqrt{\tau_s^2 + \tau_t^2} \tag{3.13}$$

$$\bar{\sigma}_2 = c \exp(-\frac{c}{G_f^{II}} k_2) \tag{3.14}$$

where, c denotes the cohesion of the unit-mortar interface, G_f^{II} is fracture energy in mode *II*, and ϕ denotes the friction angle. $\bar{\sigma}_2$ is the yield stress value following exponential softening behavior, based on the experiments to describe the inelastic behavior, see Fig. 3.5.

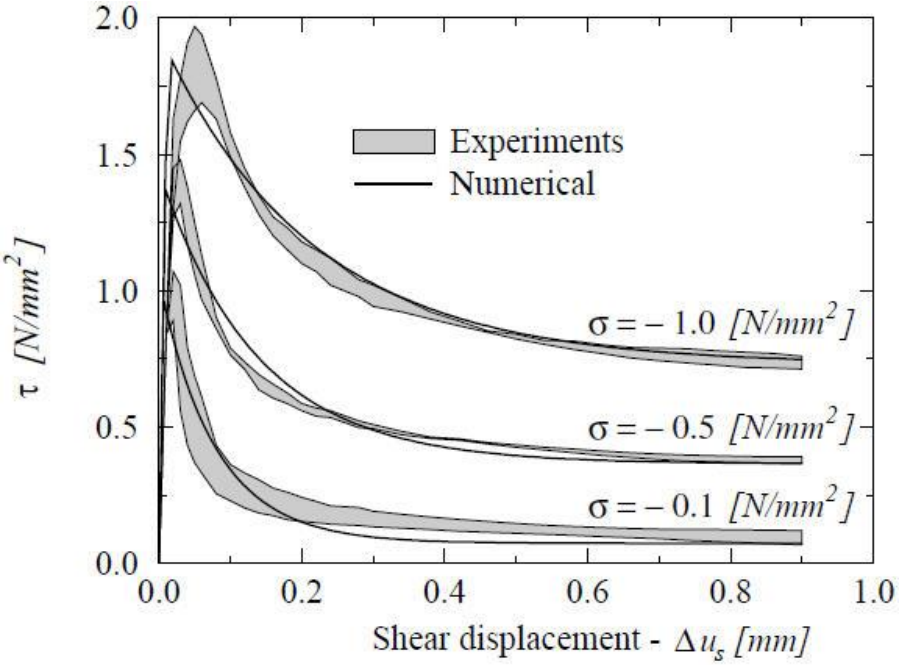

Fig. 3.5. Shear behavior of present model vs. experimental results for different confinement levels, with c = 0. 87 (N/mm^2) [45].

The dynamic increase factors are applied to the cohesion, and mode *II* fracture energy and read

$$c = DIF \times c_0 \tag{3.15}$$

$$G_f^{II} = DIF \times G_{f_0}^{II} \tag{3.16}$$

Again, here, c_0 and $G_{f_0}^{II}$ are the quasi-static cohesion and fracture energy under shear, respectively.

A non-associated plastic potential g_2 is defined as

$$g_2 = \tau + \sigma \tan\psi - c \tag{3.17}$$

Here, $\tan\psi$ is the dilatancy angle. In terms of pure shear, the shear plastic relative displacement can be assumed to control the softening behavior as

$$\dot{k}_2 = \left|\Delta \dot{u}_s^p\right| = \dot{\lambda}_2 \tag{3.18}$$

Manipulating Eq. $(3.9)_1$, the stress update equations are obtained as

$$\begin{cases} \sigma_{n+1} = \sigma^{trial} - \dot{\lambda}_{2\,n+1} k_n \tan\psi \\ \tau_{n+1} = \tau^{trial} - \dot{\lambda}_{2\,n+1} k_s \end{cases} \tag{3.19}$$

The derivative required for the iterative local Newton-Raphson method is given by

$$\left.\frac{\partial f_2}{\partial \dot{\lambda}_2}\right|_{n+1} = -k_n \tan\phi \tan\psi - k_s - \frac{\partial \bar{\sigma}_2}{\partial k_2} \tag{3.20}$$

3.2.3 Compressive cap mode

For the compressive cap mode, the yield function can be better provided in matrix notation form as

$$f_3(\boldsymbol{\sigma}, k_3) = \frac{1}{2}\boldsymbol{\sigma}^T P \boldsymbol{\sigma} + p^T \boldsymbol{\sigma} - (\bar{\sigma}_3(k_3))^2 \tag{3.21}$$

where P is the projection matrix, given by $diag\{2C_{nn}, 2C_{ss}\}$, and p is the projection vector, given by $\{C_n, 0\}^T$. Here, C_{nn} and C_n are material parameters that determine the contribution of the normal stress component to failure, assumed equal to 1 and 0, respectively (this provides a centered ellipsoid in the origin). Parameter C_{ss} governs the intersection of the ellipsoid with the shear stress axis so that the maximum shear stress τ_u is given by $\tau_u = \frac{f_m}{\sqrt{C_{ss}}}$, where f_m denotes the masonry compressive strength. It is recommended to use a value equal to 9, Lourenço [43].

The following law is used to introduce the hardening/softening behavior of masonry under uniaxial compression:

$$\bar{\sigma}_a(k_3) = \bar{\sigma}_i + (\bar{\sigma}_p - \bar{\sigma}_i)\sqrt{\frac{2k_3}{k_p} - \frac{k_3^2}{k_p^2}} \tag{3.22}$$

$$\bar{\sigma}_b(k_3) = \bar{\sigma}_p + (\bar{\sigma}_m - \bar{\sigma}_p)\left(\frac{k_3 - k_p}{k_m - k_p}\right)^2 \tag{3.23}$$

$$\bar{\sigma}_c(k_3) = \bar{\sigma}_r + (\bar{\sigma}_m - \bar{\sigma}_r)\exp\left(m\frac{k_3 - k_m}{\bar{\sigma}_m - \bar{\sigma}_r}\right) \tag{3.24}$$

with $m = 2\dfrac{\bar{\sigma}_m - \bar{\sigma}_p}{k_m - k_p}$.

Here, the subscripts *i*, *m*, *p* and *r* in the yield value and scalar *k* indicate the initial, medium, peak and residual values, respectively, providing parabolic hardening, followed by exponential softening, see Fig. 3.6.

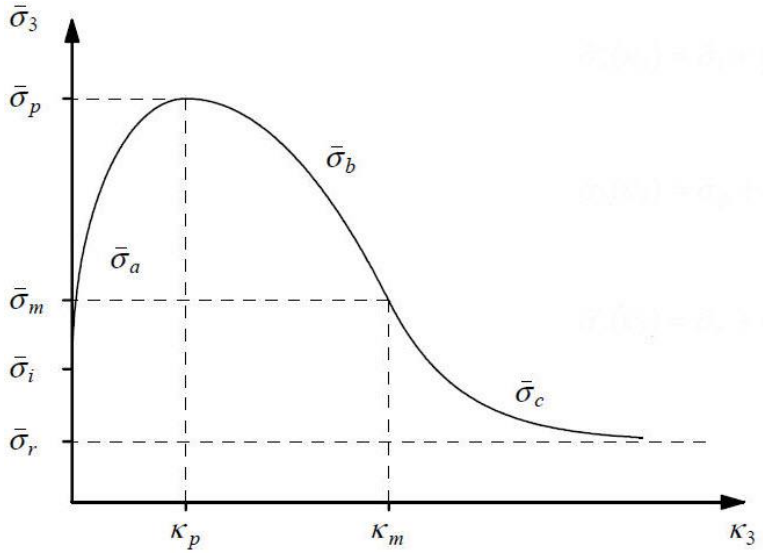

Fig. 3.6. Hardening/softening law for cap model [43].

The dynamic increase factors of uniaxial compressive strength and hardening are utilized to shift the failure envelop at different strain rates.

$$f_m = DIF \times f_{m_0} \tag{3.25}$$

$$k_m = DIF \times k_{m_0} \tag{3.26}$$

$$k_p = DIF \times k_{p_0} \tag{3.27}$$

Here, f_{m_0}, k_{p_0}, and k_{m_0} are the quasi-static strength, amount of hardening corresponding to uniaxial compressive strength and scalars defining the inelastic law. Considering an associated flow rule and strain hardening/softening hypothesis, Eq. (3.6) leads to

$$\dot{k}_3 = \dot{\lambda}_3 \sqrt{(P\boldsymbol{\sigma} + p)^T (P\boldsymbol{\sigma} + p)} \tag{3.28}$$

After manipulation of Eq. $(3.9)_1$, Lourenço [43], the stress update equation yields

$$\boldsymbol{\sigma}_{n+1} = (D^{-1} + \Delta\lambda_{3\,n+1} P)^{-1} (\varepsilon^e_{trial} - \Delta\lambda_{3\,n+1} p) \tag{3.29}$$

with $\varepsilon^e_{trial} = D^{-1}\boldsymbol{\sigma}^{trial}$.

The derivative necessary for iterative local Newton-Raphson method is given

$$\left.\frac{\partial f_3}{\partial \dot{\lambda}_3}\right|_{n+1} = \left(\frac{\partial f_3}{\partial \boldsymbol{\sigma}} + \frac{\partial f_3}{\partial k_3}\frac{\partial k_3}{\partial \boldsymbol{\sigma}}\right)^T \frac{\partial \boldsymbol{\sigma}}{\partial \dot{\lambda}_3} - h_3 \tag{3.30}$$

where,

$$\frac{\partial f_3}{\partial \boldsymbol{\sigma}} = P\boldsymbol{\sigma}_{n+1} + p \qquad \frac{\partial k_3}{\partial \boldsymbol{\sigma}} = \dot{\lambda}_{3\,n+1} \frac{P(P\boldsymbol{\sigma}_{n+1} + p)}{\sqrt{(P\boldsymbol{\sigma}_{n+1} + p)^T (P\boldsymbol{\sigma}_{n+1} + p)}}$$

$$\frac{\partial f_3}{\partial k_3} = -2\bar{\sigma}_{3\,n+1} \frac{\partial \bar{\sigma}_3}{\partial k_3} \qquad \frac{\partial \boldsymbol{\sigma}}{\partial \Delta\lambda_3} = -(D^{-1} + \dot{\lambda}_{3\,n+1} P)^{-1} (P\boldsymbol{\sigma}_{n+1} + p) \tag{3.31}$$

$$h_3 = -\frac{\partial f_3}{\partial k_3} \sqrt{(P\boldsymbol{\sigma}_{n+1} + p)^T (P\boldsymbol{\sigma}_{n+1} + p)}$$

3.2.4 A composite yield criterion

In case of yield surface violation, besides the three aforementioned modes, there are also two more possibilities at corners namely, tension/shear corner and compression/shear corner. For tension/shear corner, the tension and shear modes are assumed to be coupled because both phenomena are due to the breakage of the same bridges at micro level between the unit and mortar. Here isotropic softening is assumed which means equal degradation of strength in tension and compression. The softening scalars for composite yield surface are defined in rate form in terms of two variables $\dot{\lambda}_1$ and $\dot{\lambda}_2$, see [43] for a review on derivation of expressions and assumptions,

$$\dot{k}_1^c(\dot{\lambda}_1,\dot{\lambda}_2)=\sqrt{(\dot{\lambda}_1)^2+(\frac{G_f^I}{G_f^{II}}\frac{c}{f_t}\dot{\lambda}_2)^2} \tag{3.32}$$

$$\dot{k}_2^c(\dot{\lambda}_1,\dot{\lambda}_2)=\sqrt{(\frac{G_f^{II}}{G_f^I}\frac{f_t}{c}\dot{\lambda}_1)^2+(\dot{\lambda}_2)^2} \tag{3.33}$$

For multi surface plasticity, in the general case of $g=g(\boldsymbol{\sigma},k)$, the return mapping algorithm reduces to the following non-linear system of equations with unknowns, $\boldsymbol{\sigma}_{n+1}$ components, and user state variables $\dot{k}_{1\,n+1}$, $\dot{k}_{2\,n+1}$, $\dot{\lambda}_{1\,n+1}$, $\dot{\lambda}_{2\,n+1}$ to obtain the stress update in the presence of yielding

$$\begin{cases} D^{-1}(\boldsymbol{\sigma}_{n+1}-\boldsymbol{\sigma}^{trial})+\dot{\varepsilon}^p_{\ 1\,n+1}+\dot{\varepsilon}^p_{\ 2\,n+1}=0 \\ \dot{k}^c_{\ 1\,n+1}=\dot{k}^c_{\ 1\,n+1}(\boldsymbol{\sigma}_{n+1},\dot{\varepsilon}^p_{\ 1\,n+1},\dot{\varepsilon}^p_{\ 2\,n+1}) \\ \dot{k}^c_{\ 2\,n+1}=\dot{k}^c_{\ 2\,n+1}(\boldsymbol{\sigma}_{n+1},\dot{\varepsilon}^p_{\ 1\,n+1},\dot{\varepsilon}^p_{\ 2\,n+1}) \\ f_{1\,n+1}\left(\boldsymbol{\sigma}_{n+1},k^c_{\ 1\,n+1}\right)=0 \\ f_{2\,n+1}\left(\boldsymbol{\sigma}_{n+1},k^c_{\ 2\,n+1}\right)=0 \end{cases} \tag{3.34}$$

where $\dot{\varepsilon}^p_{\ 1\,n+1}$ and $\dot{\varepsilon}^p_{\ 2\,n+1}$ read

$$\dot{\varepsilon}^{p}_{1\,n+1} = \dot{\lambda}_{1\,n+1} \left.\frac{\partial g_1}{\partial \boldsymbol{\sigma}}\right|_{n+1} \qquad \dot{\varepsilon}^{p}_{2\,n+1} = \dot{\lambda}_{2\,n+1} \left.\frac{\partial g_2}{\partial \boldsymbol{\sigma}}\right|_{n+1} \tag{3.35}$$

Inserting Eq. (3.35) in Eq. $(3.34)_2$ and Eq. $(3.34)_3$ yields

$$\dot{k}^{c}_{1\,n+1} = \dot{k}^{c}_{1\,n+1}(\boldsymbol{\sigma}_{n+1}, \dot{\lambda}_{1\,n+1}, \dot{\lambda}_{2\,n+1}) \qquad \dot{k}^{c}_{1\,n+1} = \dot{k}^{c}_{1\,n+1}(\boldsymbol{\sigma}_{n+1}, \dot{\lambda}_{1\,n+1}, \dot{\lambda}_{2\,n+1}) \tag{3.36}$$

Considering $\boldsymbol{\sigma}_{n+1} = \boldsymbol{\sigma}_{n+1}(\dot{\lambda}_{1\,n+1}, \dot{\lambda}_{2\,n+1})$ and Eq. (3.36), followed by substitution of these equations in the yield criteria Eq. $(3.34)_4$ and Eq. $(3.34)_5$ results in non-linear expression of yield functions in two variables, $f_{1\,n+1}(\dot{\lambda}_{1\,n+1}, \dot{\lambda}_{2\,n+1}) = 0$ and $f_{2\,n+1}(\dot{\lambda}_{1\,n+1}, \dot{\lambda}_{2\,n+1}) = 0$.

For the tension/shear corner, Eq. $(3.34)_1$ is manipulated to obtain the stress update equation

$$\begin{cases} \sigma_{n+1} = \sigma^{trial} - \dot{\lambda}_{1\,n+1} k_n - \dot{\lambda}_{2\,n+1} k_n \tan\psi \\ \tau_{n+1} = \tau^{trial} - \dot{\lambda}_{2\,n+1} k_s \end{cases} \tag{3.37}$$

The Jacobian necessary for the iterative local Newton-Raphson method is given by

$$J_{n+1} = \begin{bmatrix} j_{11} & | & j_{12} \\ - & + & - \\ j_{21} & | & j_{22} \end{bmatrix} \tag{3.38}$$

where,

$$j_{11} = -k_n - \frac{\partial \bar{\sigma}_1}{\partial k^{c}_{1}} \frac{\dot{\lambda}_{1\,n+1}}{\dot{k}^{c}_{1\,n+1}} \qquad j_{12} = -k_n \tan\psi - \frac{\partial \bar{\sigma}_1}{\partial k^{c}_{1}} \left(\frac{G^{I}_{f}}{G^{II}_{f}} \frac{c}{f_t}\right)^2 \frac{\dot{\lambda}_{2\,n+1}}{\dot{k}^{c}_{1\,n+1}} \tag{3.39}$$

$$j_{21} = -k_n \tan\phi - \frac{\partial \bar{\sigma}_2}{\partial k^{c}_{2}} \left(\frac{G^{II}_{f}}{G^{I}_{f}} \frac{f_t}{c}\right)^2 \frac{\dot{\lambda}_{1\,n+1}}{\dot{k}^{c}_{2\,n+1}} \qquad j_{22} = -k_n \tan\phi \tan\psi - k_s - \frac{\partial \bar{\sigma}_2}{\partial k^{c}_{2}} \frac{\dot{\lambda}_{2\,n+1}}{\dot{k}^{c}_{2\,n+1}}$$

For the compression/shear corner, the compression and shear modes are assumed to be uncoupled. Hence, the expression of the scalar that controls the amount of hardening/softening of the compressive cap mode does not change.

After manipulation of Eq. $(3.34)_1$, the stress update equation is obtained as follows

$$\begin{cases} \sigma_{n+1} = \dfrac{\sigma^{trial} - \dot{\lambda}_{2\,n+1} k_n \tan\psi - \dot{\lambda}_{3\,n+1} k_n C_n}{1 + 2\dot{\lambda}_{3\,n+1} k_n C_{nn}} \\ \tau_{n+1} = \dfrac{\tau^{trial} - \dot{\lambda}_{2\,n+1} k_s}{1 + 2\dot{\lambda}_{3\,n+1} k_s C_{ss}} \end{cases} \tag{3.40}$$

The Jacobian necessary for the iterative local Newton-Raphson method is given by

$$J_{n+1} = \begin{bmatrix} j_{11} & | & j_{12} \\ - & + & - \\ j_{21} & | & j_{22} \end{bmatrix} \tag{3.41}$$

where,

$$j_{11} = \frac{\partial \sigma}{\partial \dot{\lambda}_2} \tan\phi + \frac{\partial \tau}{\partial \dot{\lambda}_2} - \frac{\partial \bar{\sigma}_2}{\partial k_2} \qquad j_{12} = \frac{\partial \sigma}{\partial \dot{\lambda}_3} \tan\phi + \frac{\partial \tau}{\partial \dot{\lambda}_3} \tag{3.42}$$

$$j_{21} = \left(\frac{\partial f_3}{\partial \sigma} + \frac{\partial f_3}{\partial k_3}\frac{\partial k_3}{\partial \sigma}\right)^T \frac{\partial \sigma}{\partial \dot{\lambda}_2} \qquad j_{22} = \left(\frac{\partial f_3}{\partial \sigma} + \frac{\partial f_3}{\partial k_3}\frac{\partial k_3}{\partial \sigma}\right)^T \frac{\partial \sigma}{\partial \dot{\lambda}_3} - h_3$$

in which

$$\frac{\partial \sigma}{\partial \dot{\lambda}_2} = -\frac{k_n \tan\psi}{1 + 2\dot{\lambda}_{3\,n+1} k_n C_{nn}} \qquad \frac{\partial \sigma}{\partial \dot{\lambda}_3} = -\frac{k_n C_n + 2k_n C_{nn} \sigma_{n+1}}{1 + 2\dot{\lambda}_{3\,n+1} k_n C_{nn}} \tag{3.43}$$

$$\frac{\partial \tau}{\partial \dot{\lambda}_2} = -\frac{k_s}{1 + 2\dot{\lambda}_{3\,n+1} k_s C_{ss}} \qquad \frac{\partial \tau}{\partial \dot{\lambda}_3} = -\frac{2k_s C_{ss} \tau_{n+1}}{1 + 2\dot{\lambda}_{3\,n+1} k_s C_{ss}}$$

3.2.5 Strain rate effects

A series of experiments have been carried out to characterize the material properties of brick and mortar at high strain rates, which resulted in the derivation of DIFs. Hao and Tarasov [15] conducted a series of dynamic uniaxial compressive tests on brick and mortar using a tri-axial static-dynamic testing machine, providing the following DIFs

for the material parameters at a specific range of strain rate. These tests provided also the following equations:

(1) DIF of mortar

Regression equations for the ultimate compressive strength

$$\begin{aligned} DIF &= 0.0372\ln\dot{\varepsilon} + 1.4025 \quad for \quad \dot{\varepsilon} \le 13 s^{-1} \\ DIF &= 0.3447\ln\dot{\varepsilon} + 0.5987 \quad for \quad \dot{\varepsilon} > 13 s^{-1} \end{aligned} \tag{3.44}$$

Regression equation for the strain at ultimate compressive strength

$$DIF = 0.1523\ln\dot{\varepsilon} + 2.6479 \tag{3.45}$$

Regression equation for Young's modulus

$$DIF = 0.7601 - 0.02272\ln\dot{\varepsilon} \tag{3.46}$$

(2) DIF of brick

Regression equations for the ultimate compressive strength

$$\begin{aligned} DIF &= 0.0268\ln\dot{\varepsilon} + 1.3504 \quad for \quad \dot{\varepsilon} \le 3.2 s^{-1} \\ DIF &= 0.2405\ln\dot{\varepsilon} + 1.1041 \quad for \quad \dot{\varepsilon} > 3.2 s^{-1} \end{aligned} \tag{3.47}$$

Regression equation for the strain at ultimate compressive strength

$$DIF = 0.0067\ln\dot{\varepsilon} + 1.0876 \tag{3.48}$$

Regression equations for the Young's modulus

$$\begin{aligned} DIF &= 0.0013\ln\dot{\varepsilon} + 1.0174 \quad for \quad \dot{\varepsilon} \le 7.3 s^{-1} \\ DIF &= 0.3079\ln\dot{\varepsilon} + 0.4063 \quad for \quad \dot{\varepsilon} > 7.3 s^{-1} \end{aligned} \tag{3.49}$$

Regression equations for the Poisson's ratio

$$DIF = 0.0085 \ln \dot{\varepsilon} + 1.1112 \tag{3.50}$$

No information has been reported concerned to strain rate effects on tensile and shear material properties of masonry. Hence, the DIF for material properties in tension, shear and compression is assumed here as equal. The behavior of the model under varying strain rate is evaluated in the next section.

For the implementation of the proposed dynamic interface model in ABAQUS, a FORTRAN user-subroutine was developed. Through this process, the material model is introduced by a failure criterion and the Euler backward algorithm (linear predictor-plastic corrector approach) is adopted in the stress update process. The user-subroutine VUINTER provided in ABAQUS is involved to define contact interface behavior. The interface material is assumed to be bonded to each of two contacting surfaces (slave and master surfaces).

3.3 BEHAVIOR OF THE MODEL WITH DIFFERENT STRAIN RATES

In order to illustrate the response of the developed material model in the prediction of joint behavior and appropriate implementation of user-defined subroutine in ABAQUS, simple numerical models of a rigid block and an interface element were developed and submitted to uniaxial tension, pure shear, and uniaxial compression at different strain rate levels. The numerical models and the behavior subjected to each type of loading are given in Fig. 3.7. Typical material properties are adopted for the joints, and the dynamic increase factors proposed by Hao and Tarasov [15] are used here, see Table 3.1. Comparing the default material properties, introduced as input parameters to the software, and the numerical joint behavior at different strain rate levels, full agreement between both is noticed. Hence, the material model and implementation in the user-subroutine in the FE code ABAQUS seems adequate.

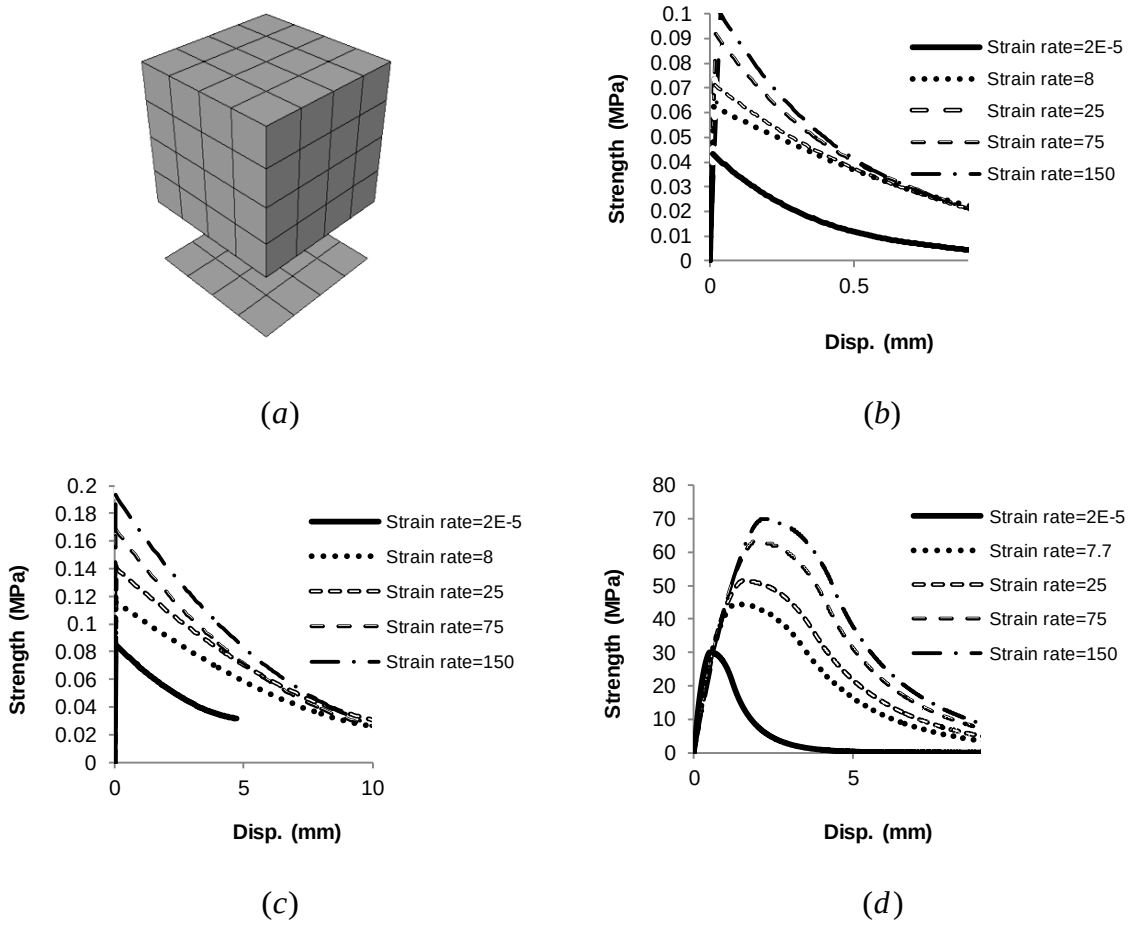

Fig. 3.7. Joint behavior at different strain rates: (a) simple numerical model; (b) uniaxial tension; (c) pure shear; (d) uniaxial compression.

Table 3.1. Material properties of joints and corresponding DIFs [15].

	Inelastic properties										**Elastic properties**	
	Tension		**Shear**				**Cap**					
	f_t *(MPa)*	G_f^I *(N/m)*	c *(MPa)*	$\tan\phi$	$\tan\psi$	G_f^{II} *(N/m)*	f_m *(MPa)*	C_{SS}	k_m *(m)*	k_p *(m)*	k_n *(N/m³)*	k_s *(N/m³)*
	0.043	17.2	0.083	0.5	0	400	30	9	1.0E-3	0.2E-3	9.26E10	5.45E10
Strain rate	DIF f_t	DIF G_f^I *(N/m)*	DIF C	-	-	DIF G_f^{II} *(N/m)*	DIF f_m	-	DIF k_m	DIF k_p	DIF k_n	DIF k_s
2E-5	1	1	1	-	-	1	1	-	1	1	1	1
8	1.48	2.96	1.48	-	-	2.96	1.48	-	2.96	2.96	0.71	0.71
25	1.71	3.14	1.71	-	-	3.14	1.71	-	3.14	3.14	0.69	0.69
75	2.10	3.31	2.10	-	-	3.31	2.10	-	3.31	3.31	0.66	0.66
150	2.33	3.40	2.33	-	-	3.40	2.33	-	3.40	3.40	0.65	0.65

3.4 NUMERICAL SIMULATION AND COMPARISON WITH EXPERIMENTAL RESULTS

The experimental data by Gilbert et al. [28] is used for validation of the developed numerical model. In this study, 21 full-scale unreinforced walls, made of bricks and blocks bonded by mortar layers at bed and head joints, were subjected to low velocity impacts with different applied impulses applied by square steel plate placed at mid-length. Two walls, namely *URP*1 and *URP*2 are considered here. These walls have clear size of $5.75\times1.15m$ and $9.15\times1.13m$, using mortar bonded concrete blockwork with dimensions of $440\times215\times200mm$ and $440\times215\times215mm$, and are constructed with two different thicknesses of $200mm$ and $215mm$, respectively. The mortar type was kept constant in both tests. The walls were placed on 12 mm thick steel plates bolted to the strong floor and jointed to the walls using epoxy. Two stiff concrete blocks served as abutments and were constructed at the extremes of the walls. The abutments were connected to the walls using epoxy mortar, precluding the rotation at edges. It was noted that these types of bonding produce fixed boundary condition at three edges. According to the test results, no serious damage was seen in both abutments, so they are assumed as rigid boundaries in the numerical simulation. The impact load was applied through a $400\times400\times50mm^3$ steel plate at mid-height of the wall. The details of the walls and dimensions are shown in Fig. 3.8. In numerical modelling, the applied load is modelled by a triangular load-time distribution with peak force of 90 KN and 110 KN reached at 22.9 msec and 25 msec, respectively, see Fig. 3.9.

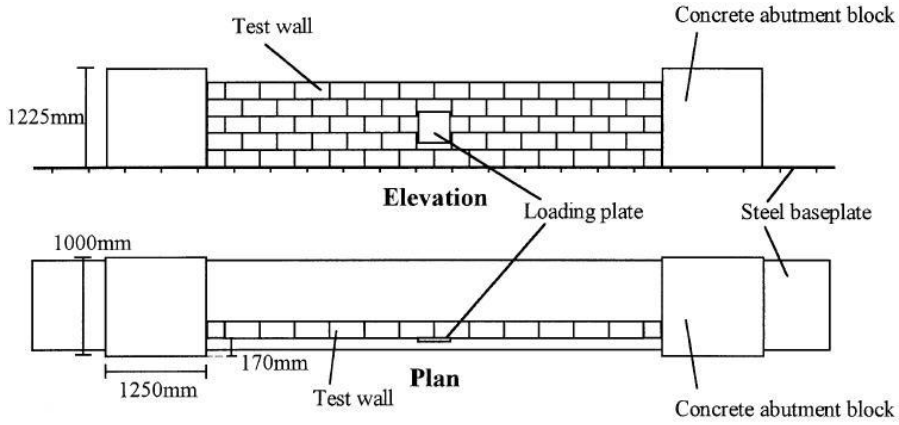

Fig. 3.8 . Geometry of masonry parapet subjected to low velocity impact [28].

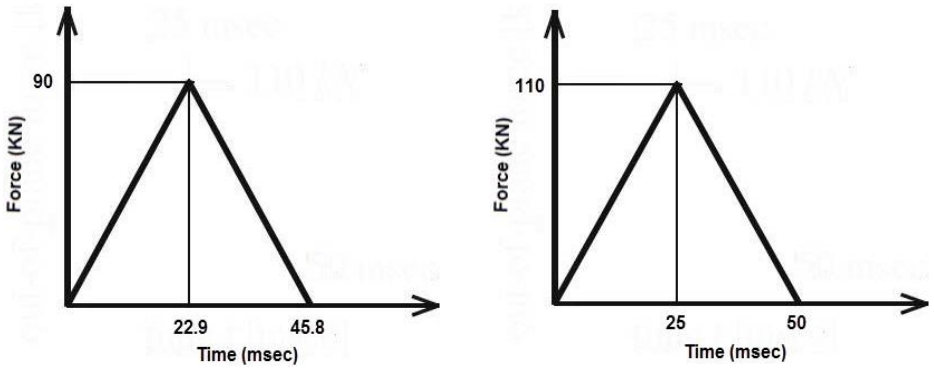

(*a*) (*b*)

Fig. 3.9. Typology of dynamic load applied to: (a) URP1; (b) URP2.

The dynamic interface model is attributed to the 3D interface elements to take into account the joint behavior during numerical simulation. Since the failure mechanisms of masonry walls subjected to high strain rate loads mostly deal with failure in joints, no serious damage is expected for the units and they were considered elastic and modeled by 3D solid elements. The finite element mesh of the wall URP1 is given in Fig. 3.10.

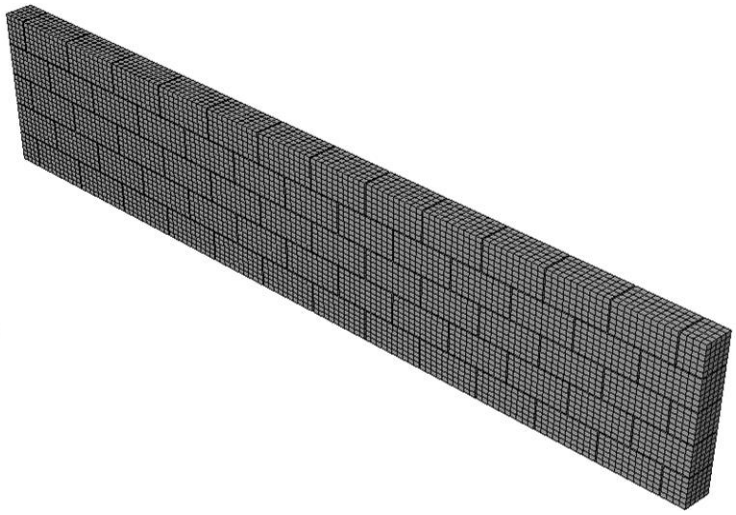

Fig. 3.10. Adopted finite element scheme (only URP1 is shown).

As shown, a fine mesh was adopted for the concrete block units. Since no experimental test data was reported on tensile material properties of mortar, the previously given tensile material properties are adopted for the joints. The material properties of the blocks, joints and their corresponding dynamic increase factors, Hao and Tarasov [15], are presented in Table 3.2, Table 3.4 and Table 3.4.

Table 3.2. Material properties of the blocks and DIFs [15, 28].

Weak concrete block		**Strong concrete block**	
$E\ (N/m^2)$	υ	$E\ (N/m^2)$	υ
1.65E10	0.2	2.88E10	0.2
DIF E	DIF υ	DIF E	DIF υ
1.74	1.15	1.74	1.15

Table 3.3. Elastic material properties of the joints and DIFs [15, 28].

k_n (N/m^3)	k_s (N/m^3)
9.26E10	5.456E10

Table 3.4. Inelastic material properties of the joints and DIFs [15, 28].

Tension		**Shear**				**Cap**			
f_t (MPa)	G_f^I (N/m)	c (MPa)	$\tan\phi$	$\tan\psi$	G_f^{II} (N/m)	$f_m\ (MPa)$	C_{SS}	$k_m\ (m)$	$k_p\ (m)$
0.043	17.2	0.083	0.5	0.0	400	8.6	9	0.30E-3	0.06E-3

It is noted that the tensile strength of masonry can vary significantly according to the materials adopted (unit and mortar), and for this reason a parametric analysis is carried out later in this work. As an example, the Eurocode 6 EN 1996-1-1:2005 provides values for the flexural strength of masonry ranging from 0.05 to 0.20 MPa. A comparison between the predicted wall response and experimental test data is carried out using crack patterns and deflection, to evaluate the accuracy of the simulations. Fig. 3.11 and Fig. 3.12 show the observed crack patterns of both tested parapets, URP1 and URP2 subjected to out of plane impact loads. The deformations of the parapets recorded at the maximum deflections are also presented in Fig. 3.13 and Fig. 3.14. According to the simulations, it is noted that vertical cracks were formed over the entire height of the parapet URP1 at the center and to each side, and both right and left parts rotated inside. Moreover, the cracks are distributed along the length of the parapet, see Fig. 3.13.

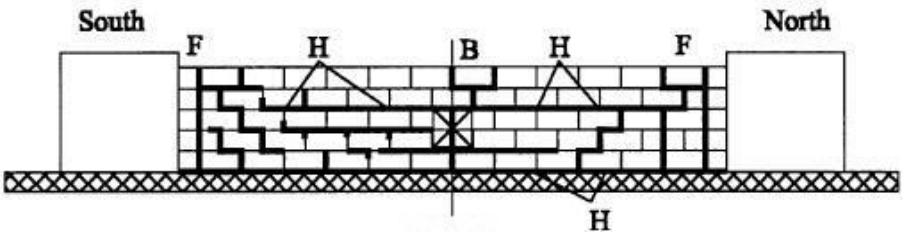

Fig. 3.11. Observed crack patterns in test - URP1 [28].

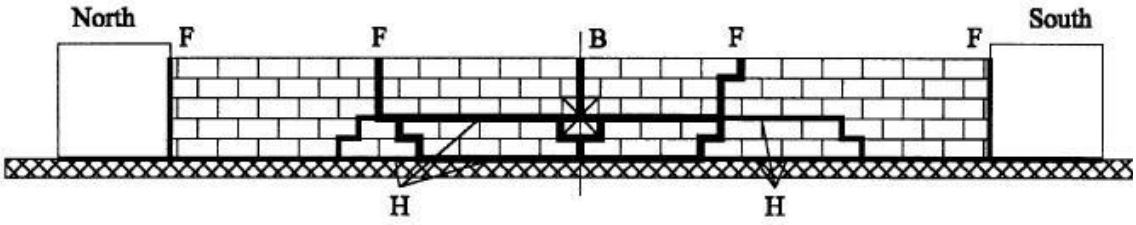

Fig. 3.12. Observed crack patterns in test - URP2 [28].

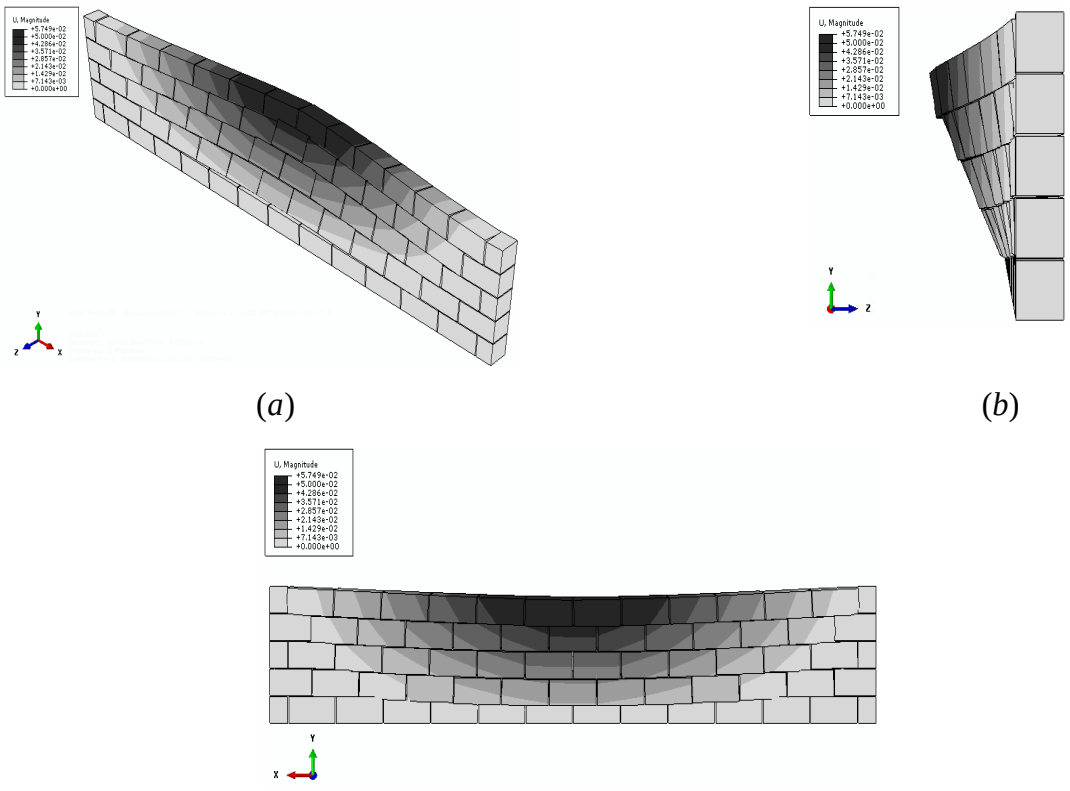

(*a*) (*b*)

(*c*)

Fig. 3.13. Deformation of URP1 at maximum deflection: (a) perspective; (b) side view; (c) back face.

For the wall URP2, besides a vertical fracture line that occurred at the center over the entire height of the wall, diagonal fractures, distributed around the centerline in both

sides, were observed connected to horizontal cracks, see Fig. 3.14. Some horizontal cracks are noticed in joints at lower levels. It is evident that increasing the length of the wall, reduces the effect of the boundaries and cracks localize close to the impact zone. Adequate agreement in the failure modes is apparent between the tests and simulations.

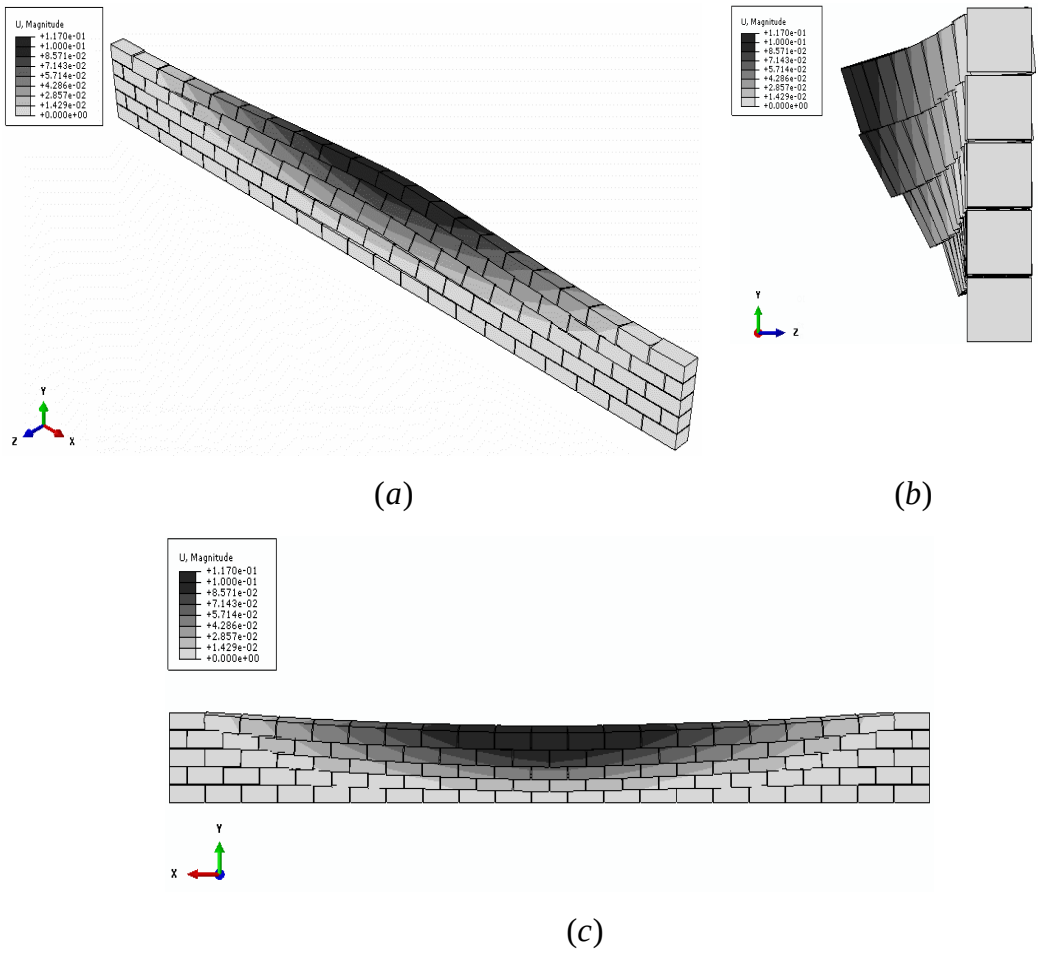

Fig. 3.14. Deformation of URP2 at maximum deflection: (a) perspective; (b) side view; (c) back face.

Next, a comparison is made for the displacement vs. time response of the walls. The displacements are recorded at the points located at mid-height and 580 mm above the base, offset by 500 mm and 250 mm to the left of the centerline, respectively. As shown in Fig. 3.15, the numerical models can simulate the high strain rate response of the walls including magnitude of peak displacement and post-peak trend close to the observed test results. Here it is noted that for wall URP1 there is a pronounced built up of stiffness found in response due to the inertial forces and acceleration of movement. For the wall URP2, The numerical response is shifted to the origin because the experimental result by the authors does not show the initial acceleration of movement.

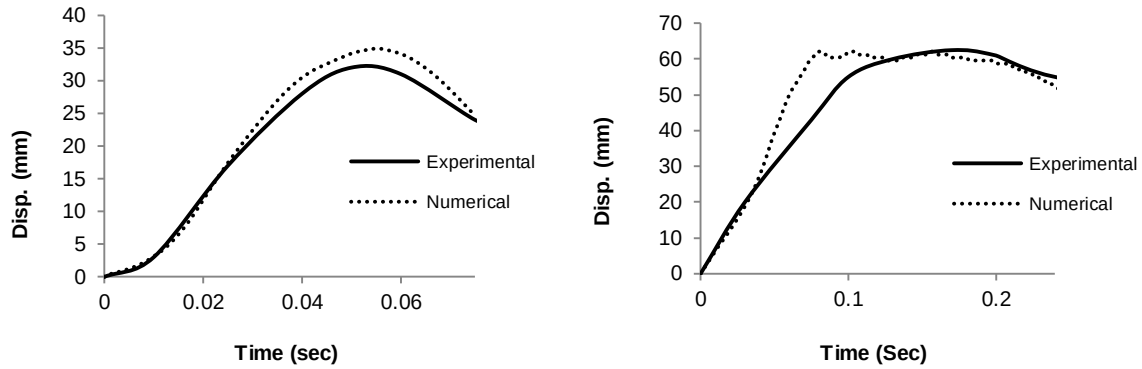

(*a*) (*b*)

Fig. 3.15. Displacement vs. time response of the wall: (a) URP1; (b) URP2.

3.5 PARAMETRIC STUDIES

The wall URP1, shown in the previous section is now adopted in parametric studies to investigate the influence of the variation of the parameters, namely material properties of the joint and wall thickness, on the strain rate response of masonry walls. The effects of the parameters are evaluated by comparing the maximum deflections and crack patterns with the reference (experimental) response.

3.5.1 Influence of material properties

Three values of tensile strength, cohesion, and dilatancy angle are used distinctly to investigate the effectiveness of material properties of the joint, as summarized in Table 3.5. The strength values are given an extreme change (dividing and multiplying by a factor 4), while for the dilatancy small values are considered, in opposition to zero (assumed as default value).

Table 3.5. Material properties of the joints.

Material parameter	**Type 1**	**Type 2**	**Type 3**
f_t *(MPa)*	0.011	0.043	0.172
Material parameter	**Type 1**	**Type 2**	**Type 3**
c *(MPa)*	0.021	0.083	0.332
Material parameter	**Type 1**	**Type 2**	**Type 3**
$\tan\psi$	0.1	0.0	0.2

Only one parameter is changed for each analysis, using Type 2 values as reference values. The displacement-time responses of the masonry wall for three different types of tensile strength and cohesion are presented in Fig. 3.16 and Fig. 3.17, respectively.

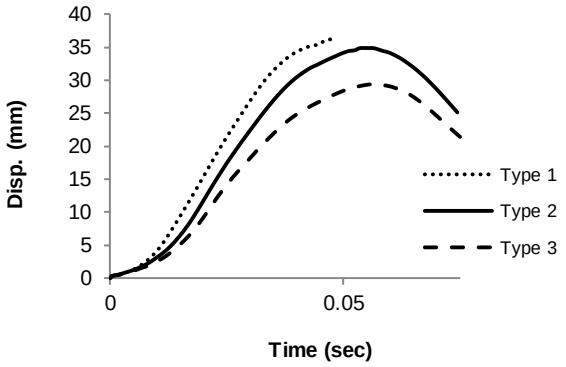

(*a*)

Fig. 3.16 . Displacement vs. time responses of the wall URP1 with three different values of tensile strength.

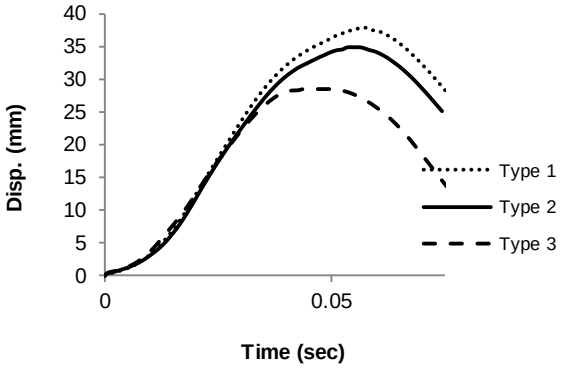

(*b*)

Fig. 3.17. Displacement vs. time responses of the wall URP1 with three different values of cohesion.

Comparing the above diagrams for the masonry wall with three values of tensile strength and cohesion, it is noted that reducing the tensile strength or cohesion leads to an increase in deflection of the wall, as expected. Also, increasing the tensile strength results in a noticeable reduction in initial stiffness. Hence, the effect of tensile strength seems more relevant than of cohesion for this wall. No changes could be found in the damage mechanism, so the different results are not shown.

The dilatancy angle takes into account the uplift when a unit slides over another unit. Dilatancy produces a vertical displacement (if the structure is unrestrained) or a normal stress built-up (if the structure is restrained). The dilatancy angle degrades with the normal confining pressure and plastic shear slipping increases. For practical purposes, it is recommend to adopt a zero value, Lourenço [43], in order to avoid locking in restrained quasi-static calculations. Fig. 3.18 shows the displacement-time responses of the masonry wall with three types of dilatancy angle subjected to low velocity impact. It is observed that when the dilatancy angle changes from 0.2 to zero, the deflection of the wall increases 1.75 times so that it can be concluded that the influence of the dilatancy on deflection is extremely large for high strain rate loading, even for the relatively unconfined wall shown. It is of interest to mention that the failure mode also changes.

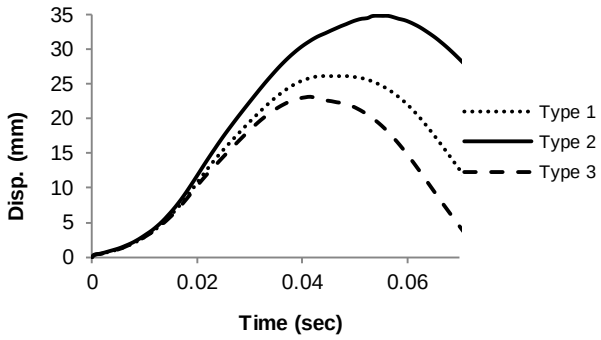

Fig. 3.18. Displacement vs. time responses of the wall URP1 with three different types of dilatancy angle.

As shown in Fig. 3.19, when the dilatancy angle tends to zero, shear slipping grows considerably with a much more localized failure mode (note the opening of the masonry joint between the first and second masonry courses). For a (small) non-zero dilatancy angle, a more homogeneous response of the wall is found.

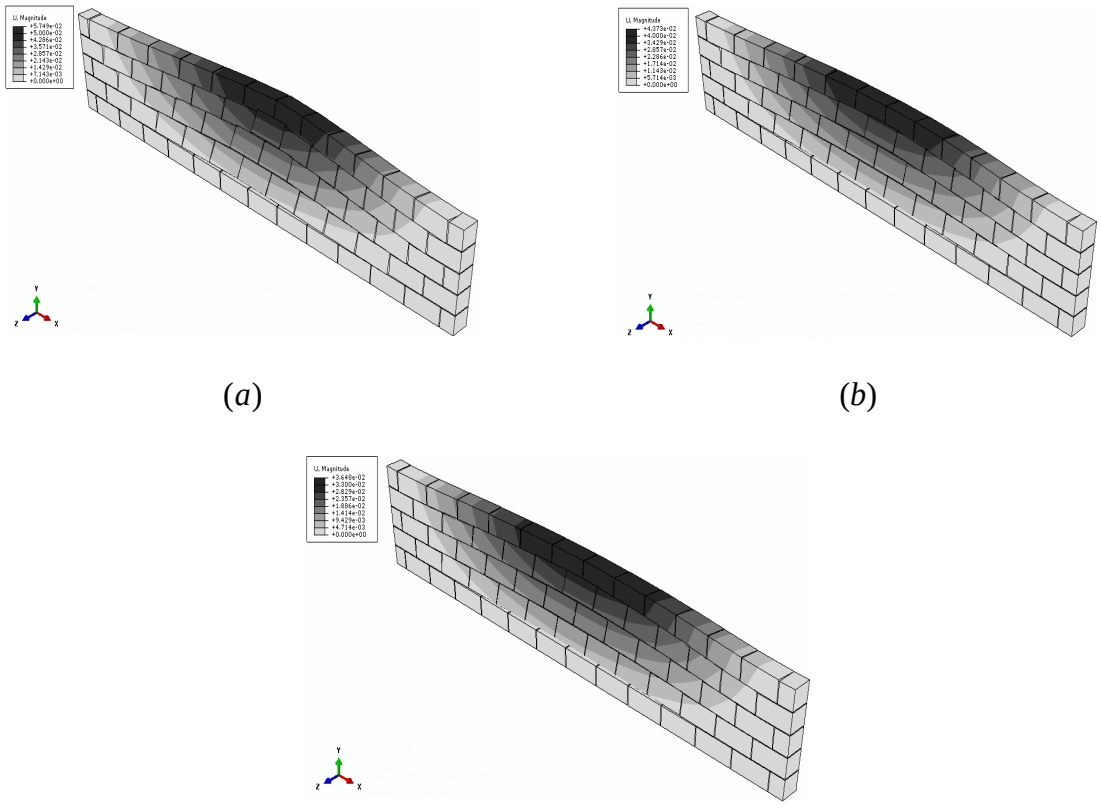

(*a*) (*b*)

(*c*)

Fig. 3.19. 3D view of deformation of URP1 at maximum deflection with three different dilatancy angle: (a) $\tan\psi = 0$; (b) $\tan\psi = 0.1$; (c) $\tan\psi = 0.2$.

3.5.2 Influence of wall thickness

Fig. 3.20 shows the displacement-time diagrams of the masonry wall with three wall thicknesses. The reference material properties of mortar and block are applied in the walls. The numerical results indicate that the wall with wall thickness $200mm$ has the maximum deflection, as expected. The growth of deflection is almost 2.3 times with the decrease of the wall thickness. This in opposition with a quasi-static elastic calculation, where this deformation would be proportional to the bending stiffness (in this case, this would be a maximum difference $1.5^3 = 3.4$). It is also noted that the most common used criterion for structural collapse is when the maximum deflection exceeds the wall thickness, Wei and Stewart [39], meaning that the wall with a minimum thickness of 250 mm would be required for the present load. Again, it is noted that no changes could be found in the damage mechanism, so the results are not shown.

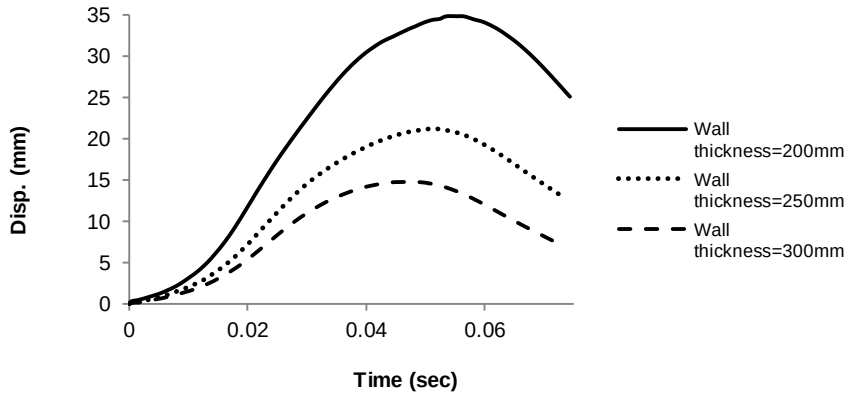

Fig. 3.20. Displacement vs. time responses of the wall URP1 with three wall thicknesses: t=200mm; t=250mm; t=300mm.

3.5.3 Influence of strain rate dependency

It is also of interest to compare a model with strain rate dependency, labeled A, (i.e. making each integration point to have a different strength, given by its own strain rate and velocity) with a model where the properties are assumed identical in all integration points, and equal to the properties of the integration point situated at mid height, labeled B. Fig. 3.21 and Fig. 3.22 show the results of the analyses. As noted, using the same properties in all integration points results in a slight decrease in displacement vs. time response; however, the changes are negligible.

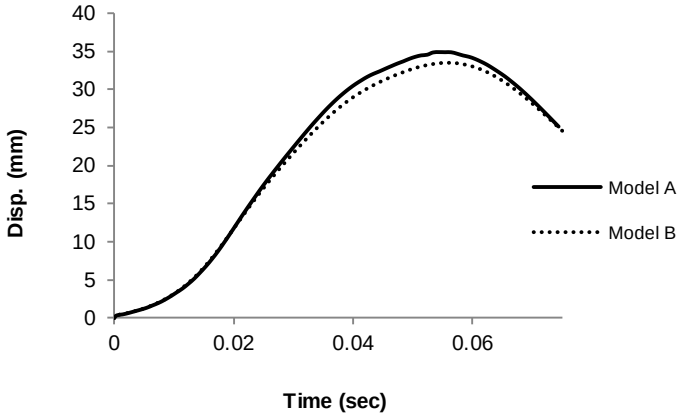

Fig. 3.21. Displacement vs. time responses of the wall URP1 for two different approaches:
(a) different properties in integration points;
(b) identical properties in integration points.

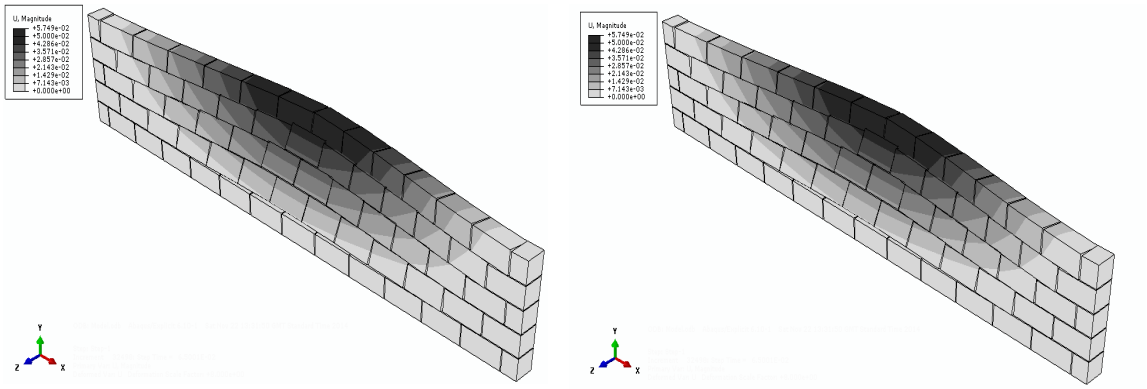

(*a*) (*b*)

Fig. 3.22. Crack patterns of URP1 at ultimate deflection for two different approaches: different properties in integration points (a) perspective; identical properties in integration points (b) perspective.

Moreover, the changes on crack distribution can be ignored. Fig. 3.23 and Fig. 3.24 give the results of the analyses, including the displacement vs. time trend, and the failure mechanism in case of applying the double of the original impulse. As shown, the changes between the analyses are more escalated. This demonstrates that a simplified assumption, not including a proper point-wise dependency of material properties according to the actual strain rate is not recommended.

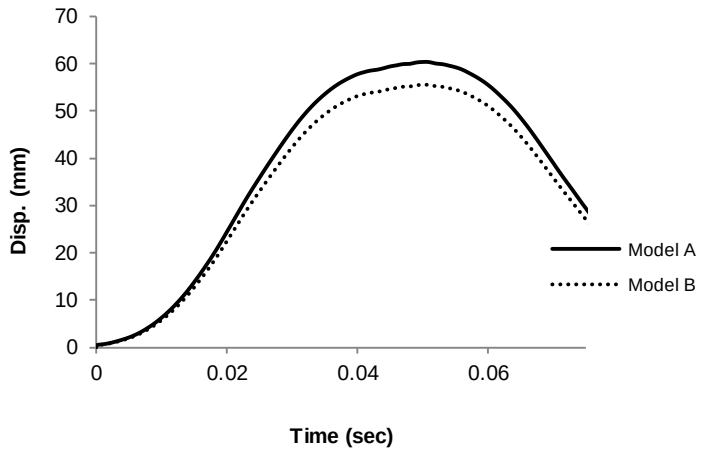

Fig. 3.23. Displacement vs. time responses of the wall URP1 for two different approaches against double applied impulse: (a) different properties in integration points; (b) identical properties in integration points.

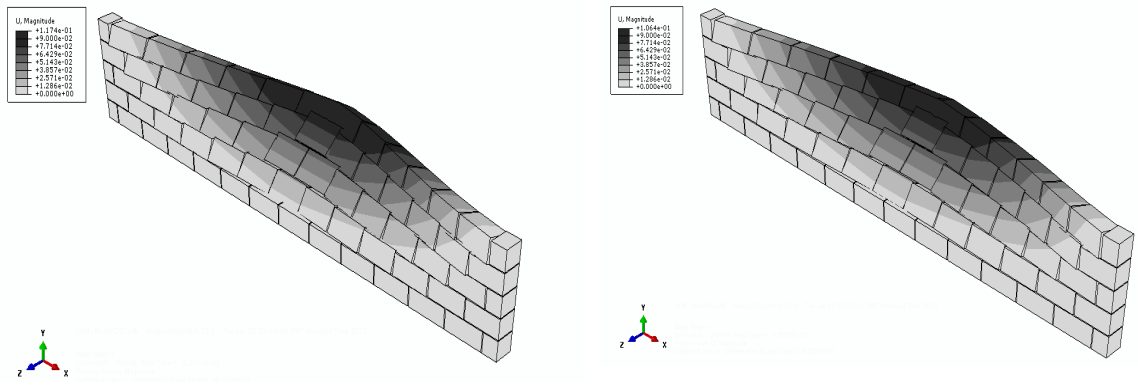

(*a*) (*b*)

Fig. 3.24. Crack patterns of URP1 at ultimate deflection for two different approaches against different applied impulse: different properties in integration points (a) perspective; identical properties in integration points (b) perspective.

3.6 FINAL REMARKS

The present study aims at developing a rate dependent dynamic interface model for the numerical simulation of masonry structures using a micro-modeling approach. The 3D interface model is implemented as a user-defined subroutine in the finite element code ABAQUS. The adequacy of the material model to replicate measured dynamic increase factors measures experimentally is demonstrated by applying various uniaxial loading conditions. A comparison between numerical predictions and experimental test data of two full scale masonry walls is carried out, including displacement-time response diagrams and failure mechanisms. It can be inferred from the numerical results that the

model can predict the maximum deflection and failure mode over the entire length of the walls, with good agreement.

Finally, a sensitivity analysis is conducted to evaluate the influence of the material properties of the joint and wall thickness on response of the walls. It is concluded that the influence of tensile strength on the maximum displacement-time response of the walls is significant, much more than the cohesion. Regarding to dilatancy angle, it is noted that the use of a zero dilatancy in case of a localized impact load leads to localized failure with shear sliding between the blocks, which can make it not realistic for many applications. Finally, it was found that an increase of the wall thickness can decrease the maximum deflection, as expected, but the changes obtained for fast impact are significantly different than the changes in stiffness obtained in a linear elastic calculation. Evaluation of the influence of strain rate dependency is also carried out. It is noted that considering the same properties in all integration points results in a slight reduction in displacement vs. time response and negligible changes on failure mode for low strain rates. At higher strain rates, the changes are more intensified and the use of a proper point-wise dependency of material properties according to the actual strain rate, as done here, is recommended.

Chapter 4

4 A STRAIN RATE DEPENDENT ANISOTROPIC CONTINUUM MODEL FOR MASONRY

4.1 INTRODUCTION

Using the appropriate constitutive material model in macro-models to analyse the masonry structures built with a large number of units and joints is indispensable and improves the reliability of the predictions. A series of studies have been carried out to propose the suitable material models for a wide range of materials including masonry for numerical analysis of structures. No attempts seem to have been made to simulate large scale masonry structures subjected to blast loading before 2006. Wei and Hao [24] defined a continuum damage model with strain rate effect based on homogenization techniques. In this regard, a masonry unit with detailed distinctive brick and mortar was considered as a representative volume element. The application of various compatible displacement conditions on the RVE surfaces led to the derivation of stress vs. strain curves in principal directions. Plotting the ultimate strength in the $I_1 - \sqrt{J_2}$ plane, the

equivalent strength envelop was obtained at different strain rate levels, see Fig. 4.1. This failure envelop is divided in four parts. A compressive cap was used since masonry can also fail under tri-axial compression.

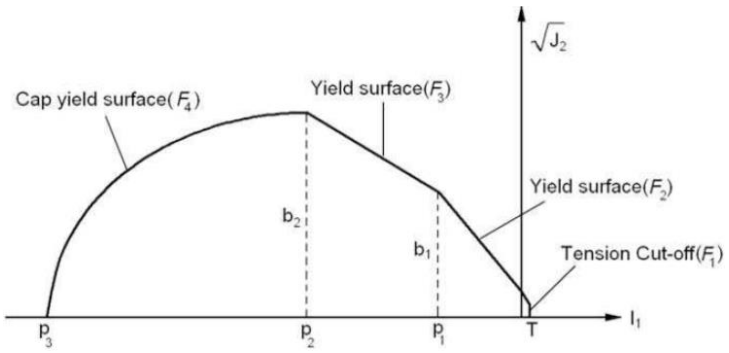

Fig. 4.1 . Strength envelope for masonry in $I_1 - \sqrt{J_2}$ space [24].

The following expressions were presented as failure criteria for the four parts:

$$F_1 = I_1 - T = 0 \tag{4.1}$$

$$F_i = \alpha_i I_1 + \sqrt{J_2} - c_i = 0, \quad i = 2,3 \tag{4.2}$$

$$F_4 = (I_1 - P_2)^2 + R^2 J_2 - (P_2 - P_3)^2 = 0 \tag{4.3}$$

where, T is the material tensile strength, I_1 is the first invariant of the hydrostatic stress tensor, J_2 is the second invariant of deviatoric stress tensor, and α, R, P_2 and P_3 are surface parameters.

A newly developed dynamic anisotropic constitutive material continuum model is proposed here for impact and blast applications in masonry, with validation using high strain rate response of masonry walls. The present model adopted the usual approach of considering different yield criteria in tension and compression, given the different failure mechanisms. These criteria are plasticity based, obey a non-associated flow rule, are numerically stable and inexpensive, and are characterized by a few material input parameters. The continuum model, developed as a user-defined subroutine, is implemented into ABAQUS and attributed to 3D solid elements to simulate the masonry behavior. The macro approach is involved in the numerical modeling of

masonry parapets and a masonry infill wall, and is combined with a dynamic explicit method. The results obtained are compared with test data to evaluate the accuracy of the proposed material model to numerically predict the structural damage and response of masonry walls subjected to high strain rate loads. Finally, a parametric study is conducted to evaluate the influence of the main parameters along the three orthogonal directions and the influence of the wall thickness on the global behavior of masonry walls.

4.2 AN ANISOTROPIC CONTINUUM MODEL FOR HIGH STRAIN RATES

A plastic dynamic continuum model is presented, which obeys a non-associated flow rule, to characterize the masonry behavior at high strain rates. The newly developed model benefits from the advantages of a powerful representation of anisotropic material behavior (i.e. different hardening/softening behavior is defined along each material axis) and follows the previously used approach of making a composite yield surface considering individual inelastic criteria in tension and compression to model the orthotropic material behavior, see Lourenço [43] for a review. The proposed model is composed of three Rankine type yield criteria in tension, using pairs of normal and shear stresses, and a Hill type yield criterion in compression, see Fig. 4.2.

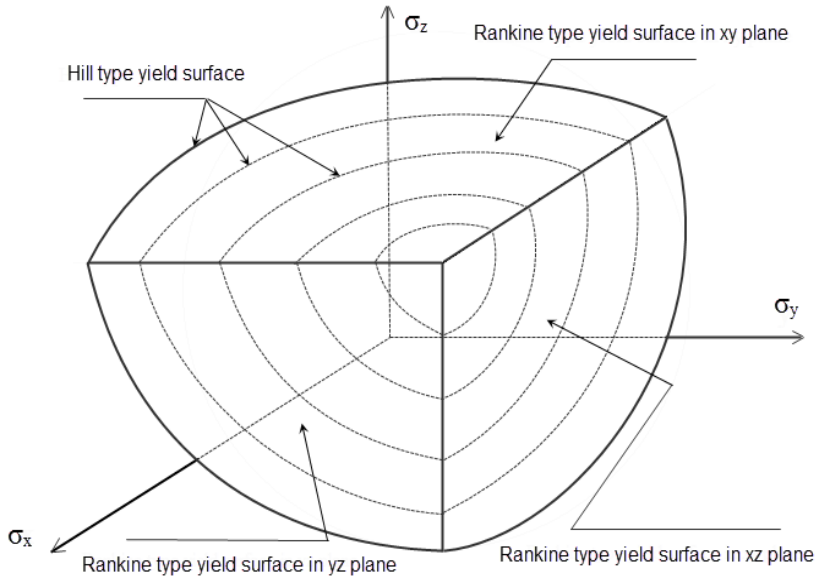

Fig. 4.2. Proposed composite yield surface with different strength values for tension and compression along each material axis.

The formulation is presented in the 3D stress space, with six stress components. For a 3D configuration, the stress vector, strain vector, and the compliance matrix are given as

$$\sigma = \left\{\sigma_x, \sigma_y, \sigma_z, \tau_{xy}, \tau_{yz}, \tau_{xz}\right\}^T \tag{4.4}$$

$$\varepsilon = \left\{\varepsilon_x, \varepsilon_y, \varepsilon_z, \gamma_{xy}, \gamma_{yz}, \gamma_{xz}\right\}^T \tag{4.5}$$

$$C = D^{-1} = \begin{bmatrix} \frac{1}{E_x} & \frac{-\upsilon_{xy}}{E_y} & \frac{-\upsilon_{zx}}{E_z} & 0 & 0 & 0 \\ & \frac{1}{E_y} & \frac{-\upsilon_{zy}}{E_z} & 0 & 0 & 0 \\ & & \frac{1}{E_z} & 0 & 0 & 0 \\ & & & \frac{1}{2G_{xy}} & 0 & 0 \\ & \textit{Sym.} & & & \frac{1}{2G_{yz}} & 0 \\ & & & & & \frac{1}{2G_{xz}} \end{bmatrix} \tag{4.6}$$

where, σ is the stress vector and ε is the strain vector. C denotes the compliance matrix and D is the symmetric orthotropic elasticity matrix. For an orthotropic material, the three symmetry planes namely *xy*, *yz*, and *xz* include nine independent elastic moduli. E_i and G_{jk} (i = *x*, *y* or *z* and *jk* = *xy*, *yz* or *xz*) are the three Young's moduli and three shear moduli, respectively, and υ_{jk} are the three Poisson's ratio.

4.2.1 Tensile mode

Considering the high strain effects on the continuum material model, the dynamic increase factors (DIFs), which are the ratio of dynamic to static parameters' values, are applied to the most likely dominant material parameters to expand or to contract the failure envelope at different strain rates. The orthotropic Rankine type yield criteria for tension in *xy*, *yz*, and *xz* symmetric planes, labeled now as i = 1, 2, and 3 respectively,

are introduced in terms of $k_{t,i}$, stress components, and α_i. The parameter k_t is a scalar to control the composite yield surface by measuring the amount of softening in the each material axes and is a measure of the inelastic process. The parameter α controls the shear stress contribution to failure, which is assumed, for simplicity, to be constant. Also, the subscripts *x*, *y*, *z* refer to the material axes.

In the following equations, the subscript *i* refers to the yield surface label.

$$f_1 = \frac{(\sigma_x - \bar{\sigma}_{tx}(k_{t,1})) + (\sigma_y - \bar{\sigma}_{ty}(k_{t,1}))}{2} + \sqrt{\left[\frac{(\sigma_x - \bar{\sigma}_{tx}(k_{t,1})) - (\sigma_y - \bar{\sigma}_{ty}(k_{t,1}))}{2}\right]^2 + \alpha_1 \tau^2_{xy}}$$
$$\alpha_1 = \frac{f_{tx} f_{ty}}{\tau_u^2} \tag{4.7}$$

$$f_2 = \frac{(\sigma_y - \bar{\sigma}_{ty}(k_{t,2})) + (\sigma_z - \bar{\sigma}_{tz}(k_{t,2}))}{2} + \sqrt{\left[\frac{(\sigma_y - \bar{\sigma}_{ty}(k_{t,2})) - (\sigma_z - \bar{\sigma}_{tz}(k_{t,2}))}{2}\right]^2 + \alpha_2 \tau^2_{yz}}$$
$$\alpha_2 = \frac{f_{ty} f_{tz}}{\tau_u^2} \tag{4.8}$$

$$f_3 = \frac{(\sigma_x - \bar{\sigma}_{tx}(k_{t,3})) + (\sigma_z - \bar{\sigma}_{tz}(k_{t,3}))}{2} + \sqrt{\left[\frac{(\sigma_x - \bar{\sigma}_{tx}(k_{t,3})) - (\sigma_z - \bar{\sigma}_{tz}(k_{t,3}))}{2}\right]^2 + \alpha_3 \tau^2_{xz}}$$
$$\alpha_3 = \frac{f_{tx} f_{tz}}{\tau_u^2} \tag{4.9}$$

The yield values follow exponential tensile softening rules, with different fracture energies along each axis, and are expressed as

$$\bar{\sigma}_{tx}(k_{t,i}) = f_{tx} \exp(-\frac{h f_{tx}}{G_{ftx}} k_{t,i})$$
$$\bar{\sigma}_{ty}(k_{t,i}) = f_{ty} \exp(-\frac{h f_{ty}}{G_{fty}} k_{t,i}) \tag{4.10}$$
$$\bar{\sigma}_{tz}(k_{t,i}) = f_{tz} \exp(-\frac{h f_{tz}}{G_{ftz}} k_{t,i})$$

Here, f_{tx}, f_{ty}, and f_{tz} are the material uniaxial tensile strength, and G_{ftx}, G_{fty}, G_{ftz} are

the material tensile fracture energy along the material axes. The parameter h denotes the equivalent length and is associated with the area of an element by, see [46], by

$$h = \alpha_h \sqrt{A_e} = \alpha_h \left(\sum_{\xi=1}^{\eta_\xi} \sum_{\eta=1}^{\eta_\eta} \det(J) w_\xi w_\eta \right)^{1/2} \tag{4.11}$$

in which α_h is a modification factor and is assumed equal to $\sqrt{2}$ for linear elements, see [47]. w_ξ and w_η are the weight factors in Gaussian integration rule. In order to eliminate the snap-back at constitutive level, in case of large element size, to obtain a pronounced step in brittle failure, the following condition is required to be satisfied, see Rots [47],

$$h \leq \frac{G_{fti} E_i}{f_{ti}^2} \tag{4.12}$$

In case of violation of this condition for any of the material axes, the respective tensile strength f_{ti} is revised to

$$f_{ti} = \left(\frac{G_{fti} E_i}{h} \right)^{1/2} \tag{4.13}$$

The expressions for the Rankine type yield criteria can be recast in a matrix form as

$$f_i = \left(\tfrac{1}{2} \xi_i^T P_{t,i} \xi_i \right)^{1/2} + \tfrac{1}{2} \pi_i^T \xi_i \tag{4.14}$$

where, ξ_i is the reduced stress vector and reads

$$\xi_i = \sigma - \eta_i \tag{4.15}$$

The back stress vector η_i reads

$$\eta_1 = \left\{\bar{\sigma}_{tx}(k_{t,1}), \bar{\sigma}_{ty}(k_{t,1}), 0, 0, 0, 0\right\}^T$$
$$\eta_2 = \left\{0, \bar{\sigma}_{ty}(k_{t,2}), \bar{\sigma}_{tz}(k_{t,2}), 0, 0, 0\right\}^T \tag{4.16}$$
$$\eta_3 = \left\{\bar{\sigma}_{tx}(k_{t,3}), 0, \bar{\sigma}_{tz}(k_{t,3}), 0, 0, 0\right\}^T$$

The projection matrix $P_{t,i}$ reads

$$P_{t,1} = \begin{bmatrix} 1/2 & -1/2 & 0 & 0 & 0 & 0 \\ & 1/2 & 0 & 0 & 0 & 0 \\ & & 0 & 0 & 0 & 0 \\ & & & 2\alpha_1 & 0 & 0 \\ & Sym. & & & 0 & 0 \\ & & & & & 0 \end{bmatrix} \quad P_{t,2} = \begin{bmatrix} 0 & 0 & 0 & 0 & 0 & 0 \\ & 1/2 & -1/2 & 0 & 0 & 0 \\ & & 1/2 & 0 & 0 & 0 \\ & & & 0 & 0 & 0 \\ & Sym. & & & 2\alpha_2 & 0 \\ & & & & & 0 \end{bmatrix} \quad P_{t,3} = \begin{bmatrix} 1/2 & 0 & -1/2 & 0 & 0 & 0 \\ & 0 & 0 & 0 & 0 & 0 \\ & & 1/2 & 0 & 0 & 0 \\ & & & 0 & 0 & 0 \\ & Sym. & & & 0 & 0 \\ & & & & & 2\alpha_3 \end{bmatrix}$$

(4.17)

The projection vector π_i reads

$$\pi_1 = \left\{1, 1, 0, 0, 0, 0\right\}^T$$
$$\pi_2 = \left\{0, 1, 1, 0, 0, 0\right\}^T \tag{4.18}$$
$$\pi_3 = \left\{1, 0, 1, 0, 0, 0\right\}^T$$

Involving the high strain rate effects, the DIFs are applied to the uniaxial tensile strength and the fracture energy along the material axes to obtain

$$f_{tj} = DIF \times f_{tj_0} \tag{4.19}$$

$$G_{ftj} = DIF \times G_{ftj_0} \tag{4.20}$$

where, f_{tj_0} and G_{ftj_0} are the quasi-static strength and fracture energy under uniaxial tension in different directions, respectively. The subscript *j* refers to the material axis *x*, *y* and *z*.

The non-associated plastic potential g_i is considered as

$$g_i = (\tfrac{1}{2}\xi_i^T P_{g,i}\xi_i)^{1/2} + \tfrac{1}{2}\pi_i^T \xi_i \tag{4.21}$$

Here, the projection matrix $P_{g,i}$ to represent the Rankine plastic flow is given as

$$P_{g,1} = \begin{bmatrix} \frac{1}{2} & -\frac{1}{2} & 0 & 0 & 0 & 0 \\ & \frac{1}{2} & 0 & 0 & 0 & 0 \\ & & 0 & 0 & 0 & 0 \\ & & & 2 & 0 & 0 \\ & Sym. & & & 0 & 0 \\ & & & & & 0 \end{bmatrix} \quad P_{g,2} = \begin{bmatrix} 0 & 0 & 0 & 0 & 0 & 0 \\ & \frac{1}{2} & -\frac{1}{2} & 0 & 0 & 0 \\ & & \frac{1}{2} & 0 & 0 & 0 \\ & & & 0 & 0 & 0 \\ & Sym. & & & 2 & 0 \\ & & & & & 0 \end{bmatrix} \quad P_{g,3} = \begin{bmatrix} \frac{1}{2} & 0 & -\frac{1}{2} & 0 & 0 & 0 \\ & 0 & 0 & 0 & 0 & 0 \\ & & \frac{1}{2} & 0 & 0 & 0 \\ & & & 0 & 0 & 0 \\ & Sym. & & & 0 & 0 \\ & & & & & 2 \end{bmatrix}$$

(4.22)

In case of strain softening to describe the inelastic behavior, the scalar $\dot{k}_{t,i}$ is given, in rate form, in terms of maximum principal plastic strain, recast in a matrix form, and expressed as

$$\dot{k}_{t,i} = (\tfrac{1}{2}(\dot{\varepsilon}^p)^T Q_i \dot{\varepsilon}^p)^{1/2} + \tfrac{1}{2}\pi_i^T \dot{\varepsilon}^p \tag{4.23}$$

where

$$Q_1 = \begin{bmatrix} \frac{1}{2} & -\frac{1}{2} & 0 & 0 & 0 & 0 \\ & \frac{1}{2} & 0 & 0 & 0 & 0 \\ & & 0 & 0 & 0 & 0 \\ & & & \frac{1}{2} & 0 & 0 \\ & Sym. & & & 0 & 0 \\ & & & & & 0 \end{bmatrix} \quad Q_2 = \begin{bmatrix} 0 & 0 & 0 & 0 & 0 & 0 \\ & \frac{1}{2} & -\frac{1}{2} & 0 & 0 & 0 \\ & & \frac{1}{2} & 0 & 0 & 0 \\ & & & 0 & 0 & 0 \\ & Sym. & & & \frac{1}{2} & 0 \\ & & & & & 0 \end{bmatrix} \quad Q_3 = \begin{bmatrix} \frac{1}{2} & 0 & -\frac{1}{2} & 0 & 0 & 0 \\ & 0 & 0 & 0 & 0 & 0 \\ & & \frac{1}{2} & 0 & 0 & 0 \\ & & & 0 & 0 & 0 \\ & Sym. & & & 0 & 0 \\ & & & & & \frac{1}{2} \end{bmatrix}$$

(4.24)

After manipulation, Eq. (4.23) reduces to the following particularly simple expression

$$\dot{k}_{t,i} = \dot{\lambda}_{t,i} \tag{4.25}$$

in which $\dot{\lambda}_{t,i}$ is the plastic multiplier rate.

When the trial stress violates the yield surface, the plastic corrector brings back the stress update to the yield surface. Having the stress updating equations and failure

criteria, a non-linear system of equations with several unknowns is established and solved by using an iterative Newton-Raphson method. Using the return mapping algorithm results in updating the stress vector and user-state variables in every integration point during the iterations at each increment. In a plasticity model, assuming the elastic stress value in the first iteration, a trial value is assumed for stress such as $\sigma_{n+1} = \sigma^{trial}$, $\dot{k}_{t\,n+1} = 0$, and $\dot{\lambda}_{t\,n+1} = 0$, which is obtained by the elastic predictor. The unknowns of the nonlinear system of equations that arise in this update procedure are the stress components, $\dot{k}_{t\,n+1}$ and $\dot{\lambda}_{t\,n+1}$. The stress update equations for a finite step are given by

$$\sigma_{n+1} = \sigma^{trial} - D\dot{\varepsilon}^{p}_{n+1} \tag{4.26}$$

with $\sigma^{trial} = \sigma_n + D\dot{\varepsilon}_{n+1}$. The stress update equations can be easily obtained from the set of non-linear seven equations system

$$\begin{cases} D^{-1}(\sigma_{n+1} - \sigma^{trial}) + \dot{\lambda}_{t,i\,n+1} \left.\dfrac{\partial g_i}{\partial \sigma}\right|_{n+1} = 0 \\ f_{i\,n+1} = (\tfrac{1}{2}\xi^{T}_{i\,n+1} P_{t,i\,n+1} \xi_{i\,n+1})^{1/2} + \tfrac{1}{2}\pi^{T}\xi_{i\,n+1} = 0 \end{cases} \tag{4.27}$$

The Jacobian required for the iterative local Newton-Raphson method is obtained as

$$J_{i\,n+1} = \begin{bmatrix} D^{-1} + \dot{\lambda}_{t,i\,n+1}\dfrac{\partial^2 g_i}{\partial \sigma^2} & | & \dfrac{\partial g_i}{\partial \sigma} + \dot{\lambda}_{t,i\,n+1}\dfrac{\partial^2 g_i}{\partial \sigma \partial k_{t,i}} \\ - & + & - \\ \left(\dfrac{\partial f_i}{\partial \sigma}\right)^{T} & | & \dfrac{\partial f_i}{\partial k_{t,i}} \end{bmatrix} \tag{4.28}$$

where

$$\frac{\partial f_i}{\partial \sigma} = \frac{P_{t,i}\xi_{i\,n+1}}{2(\tfrac{1}{2}\xi^{T}_{i\,n+1}P_{t,i}\xi_{i\,n+1})^{1/2}} + \tfrac{1}{2}\pi \qquad \frac{\partial g_i}{\partial \sigma} = \frac{P_{g,i}\xi_{i\,n+1}}{2(\tfrac{1}{2}\xi^{T}_{i\,n+1}P_{g,i}\xi_{i\,n+1})^{1/2}} + \tfrac{1}{2}\pi \tag{4.29}$$

$$\frac{\partial f_i}{\partial k_{t,i}} = -(\frac{\partial f_i}{\partial \sigma})^T \frac{\partial \eta_i}{\partial k_{t,i}} \qquad \frac{\partial^2 g_i}{\partial \sigma \partial k_{t,i}} = -\frac{\partial^2 g_i}{\partial \sigma^2}\frac{\partial \eta_i}{\partial k_{t,i}}$$

$$\frac{\partial \eta_1}{\partial k_{t,1}} = \{\frac{\partial \bar{\sigma}_{tx}(k_{t,1})}{\partial k_{t,1}}, \frac{\partial \bar{\sigma}_{ty}(k_{t,1})}{\partial k_{t,1}}, 0, 0, 0, 0\}^T \qquad \frac{\partial \eta_2}{\partial k_{t,2}} = \{0, \frac{\partial \bar{\sigma}_{ty}(k_{t,2})}{\partial k_{t,2}}, \frac{\partial \bar{\sigma}_{tz}(k_{t,2})}{\partial k_{t,2}}, 0, 0, 0\}^T$$

$$\frac{\partial \eta_3}{\partial k_{t,3}} = \{\frac{\partial \bar{\sigma}_{tx}(k_{t,3})}{\partial k_{t,3}}, 0, \frac{\partial \bar{\sigma}_{tz}(k_{t,3})}{\partial k_{t,3}}, 0, 0, 0\}^T$$

$$\frac{\partial^2 g_i}{\partial \sigma^2} = \frac{P_{g,i}}{2(\frac{1}{2}\xi_{i\,n+1}^T P_{g,i}\xi_{i\,n+1})^{1/2}} - \frac{P_{g,i}\xi_{i\,n+1}\xi_{i\,n+1}^T P_{g,i}}{4(\frac{1}{2}\xi_{i\,n+1}^T P_{g,i}\xi_{i\,n+1})^{3/2}}$$

However, the gradient of the plastic potential in Eq. (4.29) is not defined for the entire stress domain. As shown in Fig. 4.2, the intersection of three perpendicular Rankine type yield surfaces defines one apex and three edges, in which the numerical algorithm is not stable. Lourenço [43] implemented a simple algorithm to solve the difficulty dealing with non-defined gradient in the apex and edges. For the apex regime, the three shear stress components, namely τ_{xy}, τ_{yz}, and τ_{xz} are equal to zero. Independently of the trial stress, the stress update is assumed to return to the apex, which is sufficient to fulfill $f_{1\,n+1} = 0$, $f_{2\,n+1} = 0$, and $f_{3\,n+1} = 0$, given by

$$\sigma_{n+1} = \left\{\bar{\sigma}_{tx}(\max(k_{t,1}, k_{t,3})), \bar{\sigma}_{ty}(\max(k_{t,1}, k_{t,2})), \bar{\sigma}_{tz}(\max(k_{t,2}, k_{t,3})), 0, 0, 0\right\}^T \tag{4.30}$$

The following non-linear equation is then obtained to update the softening scalar, $\dot{k}_{t,i}$

$$F(\dot{k}_{t,i\,n+1}) = \dot{k}_{t,i\,n+1} - (\frac{1}{2}(\dot{\varepsilon}_{n+1}^p)^T Q_i \dot{\varepsilon}_{n+1}^p)^{1/2} - \frac{1}{2}\pi_i^T \dot{\varepsilon}_{n+1}^p \tag{4.31}$$

with $\dot{\varepsilon}_{n+1}^p = D^{-1}(\sigma^{trial} - \sigma_{n+1})$.

Along the three edges, for the intersection between the 3 and 2 planes, labeled *A*, $\tau_{xy} = 0$. $\tau_{yz} = 0$ is assumed for the intersection of 1 and 3 surfaces, labeled *B*, and $\tau_{xz} = 0$ is assumed for the intersection between the 1 and 2 surfaces, labeled *C*.

For the edges *A*, *B*, and *C*, the stress update for each return mapping is then given by

$$\sigma_{A\,n+1} = \left\{ \bar{\sigma}_{tx}(k_{t,1}), \bar{\sigma}_{ty}(k_{t,1}), \sigma_z^{trial}, 0, \tau_{yz}^{trial}, \tau_{xz}^{trial} \right\}^T$$
$$\sigma_{B\,n+1} = \left\{ \sigma_x^{trial}, \bar{\sigma}_{ty}(k_{t,2}), \bar{\sigma}_{tz}(k_{t,2}), \tau_{xy}^{trial}, 0, \tau_{xz}^{trial} \right\}^T \tag{4.32}$$
$$\sigma_{C\,n+1} = \left\{ \bar{\sigma}_{tx}(k_{t,3}), \sigma_y^{trial}, \bar{\sigma}_{tz}(k_{t,3}), \tau_{xy}^{trial}, \tau_{yz}^{trial}, 0 \right\}^T$$

The non-linear equations, used to update the softening scalars for the edges *A*, *B*, and *C*, are expressed as, where the subscribe j refers to the edge label,

$$F_j(\dot{k}_{t,i\,n+1}) = \dot{k}_{t,i\,n+1} - (\tfrac{1}{2}(\dot{\varepsilon}_{n+1}^p)^T Q_i \dot{\varepsilon}_{n+1}^p)^{1/2} - \tfrac{1}{2}\pi_i^T \dot{\varepsilon}_{n+1}^p \tag{4.33}$$

4.2.2 Compression mode

In the present study, a rotated centered ellipsoid shape Hill type yield criterion is adopted, in the full 3D stress space with six stress components, to characterize the masonry behavior in compression. Using matrix notation, the orthotropic Hill type yield criterion is expressed in a cube root matrix form more compatible for numerical implementation, and is given as follows

$$f_4 = (\tfrac{1}{2}\sigma^T P_c \sigma)^{1/3} - \bar{\sigma}_c(k_c) \tag{4.34}$$

where the scalar k_c measures the amount of hardening/softening along the material axes, and the yield value $\bar{\sigma}_c$ reads as the product of the yield value along the three material axes with subscripts *x*, *y* and *z*,

$$\bar{\sigma}_c(k_c) = \sqrt[3]{\bar{\sigma}_{cx}(k_c)\bar{\sigma}_{cy}(k_c)\bar{\sigma}_{cz}(k_c)} \tag{4.35}$$

The projection matrix P_c reads

$$P_c = \begin{bmatrix} G'+H' & -H' & -G' & 0 & 0 & 0 \\ & F'+H' & -F' & 0 & 0 & 0 \\ & & F'+G' & 0 & 0 & 0 \\ & & & 2N' & 0 & 0 \\ & Sym. & & & 2L' & 0 \\ & & & & & 2M' \end{bmatrix} \tag{4.36}$$

in which, $G' = \left[\frac{\bar{\sigma}_{cx}\bar{\sigma}_{cy}}{\bar{\sigma}_{cz}} + \frac{\bar{\sigma}_{cy}\bar{\sigma}_{cz}}{\bar{\sigma}_{cx}} - \frac{\bar{\sigma}_{cx}\bar{\sigma}_{cz}}{\bar{\sigma}_{cy}} \right]$, $F' = \left[\frac{\bar{\sigma}_{cx}\bar{\sigma}_{cz}}{\bar{\sigma}_{cy}} + \frac{\bar{\sigma}_{cx}\bar{\sigma}_{cy}}{\bar{\sigma}_{cz}} - \frac{\bar{\sigma}_{cy}\bar{\sigma}_{cz}}{\bar{\sigma}_{cx}} \right]$,

$H' = \left[\frac{\bar{\sigma}_{cy}\bar{\sigma}_{cz}}{\bar{\sigma}_{cx}} + \frac{\bar{\sigma}_{cx}\bar{\sigma}_{cz}}{\bar{\sigma}_{cy}} - \frac{\bar{\sigma}_{cx}\bar{\sigma}_{cy}}{\bar{\sigma}_{cz}} \right]$, $N' = \bar{\sigma}_{cz}\gamma_{xy}$, $L' = \bar{\sigma}_{cx}\gamma_{yz}$, and $M' = \bar{\sigma}_{cy}\gamma_{xz}$.

The parameters γ_{xy}, γ_{yz}, and γ_{xz} are used to control the shear stress contribution to failure and are given by $\gamma_{xy} = \frac{f_{mx} f_{my}}{\tau_u^{\,2}}$, $\gamma_{yz} = \frac{f_{my} f_{mz}}{\tau_u^{\,2}}$, and $\gamma_{xz} = \frac{f_{mx} f_{mz}}{\tau_u^{\,2}}$. f_{mx}, f_{my}, and f_{mz} are the material uniaxial compressive strengths along the material axes and τ_u is the material pure shear strength.

Following the parabolic-exponential compressive hardening/softening rules to describe the inelastic behavior of masonry along each material axis, the subsequent law is involved as

$$\bar{\sigma}_a(k_c) = \bar{\sigma}_i + (\bar{\sigma}_p - \bar{\sigma}_i)\sqrt{\frac{2k_c}{k_p} - \frac{k_c^2}{k_p^2}} \tag{4.37}$$

$$\bar{\sigma}_b(k_c) = \bar{\sigma}_p + (\bar{\sigma}_m - \bar{\sigma}_p)\left(\frac{k_c - k_p}{k_m - k_p} \right)^2 \tag{4.38}$$

$$\bar{\sigma}_f(k_c) = \bar{\sigma}_r + (\bar{\sigma}_m - \bar{\sigma}_r)\exp\left(m\frac{k_c - k_m}{\bar{\sigma}_m - \bar{\sigma}_r} \right) \tag{4.39}$$

with $m = 2\frac{\bar{\sigma}_m - \bar{\sigma}_p}{k_m - k_p}$.

Here, the subscripts *i*, *m*, *p* and *r* in the yield value and scalar *k* indicate the initial, medium, peak and residual values, respectively, providing parabolic hardening, followed by exponential softening, see Fig. 4.3.

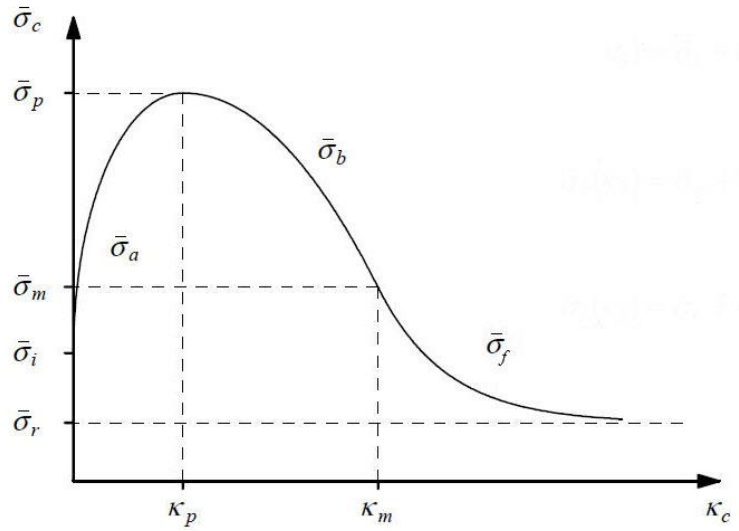

Fig. 4.3. Hardening/softening law for cap mode [43].

The dynamic increase factors of uniaxial compressive strength and hardening are utilized to shift the failure envelop at different strain rates.

$$f_{mj} = DIF \times f_{mj_0} \tag{4.40}$$

$$G_{fcj} = DIF \times G_{fcj_0} \tag{4.41}$$

$$k_p = DIF \times k_{p_0} \tag{4.42}$$

Here, f_{mj_0}, G_{fcj_0}, and k_{p_0} refer to the quasi-static compressive strength, fracture energy, and amount of hardening corresponding to uniaxial compressive strength and scalars defining the inelastic law. The subscript *j* refers to the material axis.

Considering an associated flow rule and work hardening/softening hypothesis, this yields to the particularly simple equation

$$\dot{k}_c = \frac{1}{\bar{\sigma}_c} \sigma^T \dot{\varepsilon}^p = \dot{\lambda}_c \tag{4.43}$$

The return mapping algorithm reduces to following non-linear set of seven equations with seven unknowns, σ_{n+1} components and the plastic multiplier $\dot{\lambda}_{c\,n+1}$

$$\begin{cases} D^{-1}(\sigma_{n+1}-\sigma^{trial})+\dot{\lambda}_{c\,n+1}\left.\dfrac{\partial f_4}{\partial \sigma}\right|_{n+1}=0 \\ f_{4\,n+1}=(\tfrac{1}{2}\sigma_{n+1}^{T}P_{c\,n+1}\sigma_{n+1})^{1/3}-\bar{\sigma}_{c\,n+1}=0 \end{cases} \tag{4.44}$$

The Jacobian necessary for the iterative local Newton-Raphson method is given

$$J_{n+1}=\begin{bmatrix} D^{-1}+\dot{\lambda}_{c\,n+1}\dfrac{\partial^2 f_4}{\partial \sigma^2} & | & \dfrac{\partial f_4}{\partial \sigma}+\dot{\lambda}_{c\,n+1}\dfrac{\partial^2 f_4}{\partial \sigma \partial k_c} \\ - & + & - \\ \left(\dfrac{\partial f_4}{\partial \sigma}\right)^{T} & | & \dfrac{\partial f_4}{\partial k_c} \end{bmatrix} \tag{4.45}$$

where,

$$\frac{\partial f_4}{\partial \sigma}=\frac{P_c\sigma_{n+1}}{3(\frac{1}{2}\sigma_{n+1}^{T}P_c\sigma_{n+1})^{2/3}} \qquad \frac{\partial^2 f_4}{\partial \sigma^2}=\frac{P_c}{3(\frac{1}{2}\sigma_{n+1}^{T}P_c\sigma_{n+1})^{2/3}}-\frac{2P_c\sigma_{n+1}\sigma_{n+1}^{T}P_c}{9(\frac{1}{2}\sigma_{n+1}^{T}P_c\sigma_{n+1})^{5/3}}$$

$$\frac{\partial^2 f_4}{\partial \sigma \partial k_c}=\frac{\frac{\partial P_c}{\partial k_c}\sigma_{n+1}}{3(\frac{1}{2}\sigma_{n+1}^{T}P_c\sigma_{n+1})^{2/3}}-\frac{(\sigma_{n+1}^{T}\frac{\partial P_c}{\partial k_c}\sigma_{n+1})P_c\sigma_{n+1}}{9(\frac{1}{2}\sigma_{n+1}^{T}P_c\sigma_{n+1})^{5/3}} \tag{4.46}$$

$$\frac{\partial f_4}{\partial k_c}=\frac{\sigma_{n+1}^{T}\frac{\partial P_c}{\partial k_c}\sigma_{n+1}}{6(\frac{1}{2}\sigma_{n+1}^{T}P_c\sigma_{n+1})^{2/3}}-\frac{\partial \bar{\sigma}_c}{\partial k_c} \qquad \frac{\partial \bar{\sigma}_c}{\partial k_c}=\frac{\frac{\partial \bar{\sigma}_{cx}}{\partial k_c}\bar{\sigma}_{cy}\bar{\sigma}_{cz}+\bar{\sigma}_{cx}\frac{\partial \bar{\sigma}_{cy}}{\partial k_c}\bar{\sigma}_{cz}+\bar{\sigma}_{cx}\bar{\sigma}_{cy}\frac{\partial \bar{\sigma}_{cz}}{\partial k_c}}{3\bar{\sigma}_c^{\,2}}$$

4.2.3 A composite yield criterion

Regarding the different facets of multiscale plasticity, the different four yield criteria in uncoupled tension and compression regimes are combined in a composite yield surface. As noted in Fig. 4.4, given the different yield surfaces in tension and compression, the stress domain is divided into different divisions. Despite the possibility of location of

the trial stress on apex or three different edges beyond the yield surface, once the trial stress violates the yield surface, depending upon its spot, a number of yield surfaces become active.

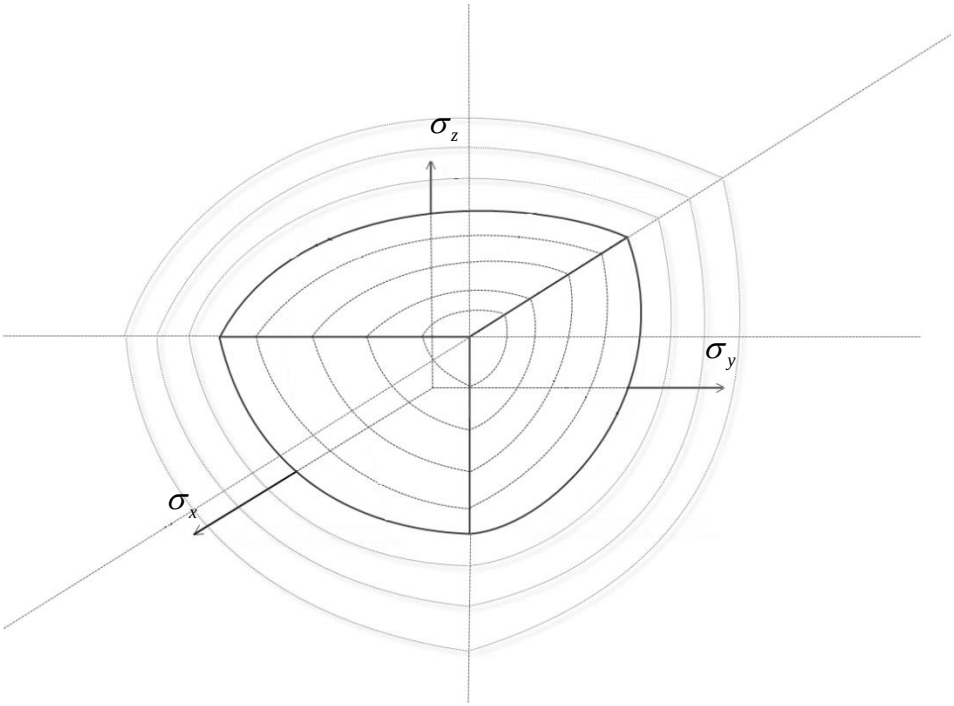

Fig. 4.4. Different divisions beyond the yield surface.

The Euler backward algorithm reduces to the following non-linear system of seven to ten equations with seven to ten unknowns, σ_{n+1} components and one to four plastic multipliers $\dot{\lambda}_{t,i\,n+1}$, and $\dot{\lambda}_{c\,n+1}$, depending on where the trial stress is located

$$\begin{cases} D^{-1}(\sigma_{n+1}-\sigma^{trial})+\dot{\lambda}_{t,i\,n+1}\left.\dfrac{\partial g_i}{\partial\sigma}\right|_{n+1}+\dot{\lambda}_{c\,n+1}\left.\dfrac{\partial f_4}{\partial\sigma}\right|_{n+1}=0 \\ f_{i\,n+1}=(\tfrac{1}{2}\xi^T_{i\,n+1}P_{t,i\,n+1}\xi_{i\,n+1})^{1/2}+\tfrac{1}{2}\pi^T\xi_{i\,n+1}=0 \\ f_{4\,n+1}=(\tfrac{1}{2}\sigma^T_{n+1}P_{c\,n+1}\sigma_{n+1})^{1/3}-\bar{\sigma}_{c\,n+1}=0 \end{cases} \tag{4.47}$$

The jacobian necessary for the iterative local Newton-Raphson method is presented

$$J_{n+1}=\begin{bmatrix} D^{-1}+\dot{\lambda}_{t,i\,n+1}\dfrac{\partial^2 g_i}{\partial\sigma^2}+\dot{\lambda}_{c\,n+1}\dfrac{\partial^2 f_4}{\partial\sigma^2} & | & \dfrac{\partial g_i}{\partial\sigma}+\dot{\lambda}_{t,i\,n+1}\dfrac{\partial^2 g_i}{\partial\sigma\partial k_{t,i}} & | & \dfrac{\partial f_4}{\partial\sigma}+\dot{\lambda}_{c\,n+1}\dfrac{\partial^2 f_4}{\partial\sigma\partial k_c} \\ - & + & - & + & - \\ \left(\dfrac{\partial f_i}{\partial\sigma}\right)^T & | & \dfrac{\partial f_i}{\partial k_{t,i}} & | & 0 \\ - & + & - & + & - \\ \left(\dfrac{\partial f_4}{\partial\sigma}\right)^T & | & 0 & | & \dfrac{\partial f_4}{\partial k_c} \end{bmatrix} \tag{4.48}$$

The matrix dimensions are 7×7 to 10×10 and all the terms are given in Eq. (4.29) and Eq. (4.46).

4.2.4 Strain rate effects

The expressions for DIFs of masonry parameters in terms of strain rate, obtained by Pereira [16] under drop weight impacts loading over a wide range of strain rate, are adopted here. Given the lack of information associated with the tensile material properties of masonry with increasing strain rates, identical DIFs are assumed for material properties both in tension and compression. The following parameters are those to which the DIFs are applied to: f_{tx}, f_{ty}, f_{tz}, $G_{ft,x}$, $G_{ft,y}$, $G_{ft,z}$, f_{mx}, f_{my}, f_{mz}, $G_{fc,x}$, $G_{fc,y}$, $G_{fc,z}$, k_p, E_x, E_y, and E_z.

In order to implement the proposed dynamic continuum model in ABAQUS, a VUMAT user-defined subroutine, including the material model and the procedure to update the stress vector and the state variables.

4.3 VALIDATION OF THE CONSTITUTIVE MODEL

4.3.1 Masonry parapets under low velocity impact

In the present study, the use of the dynamic continuum model for numerical analysis of masonry structures is validated by comparing the numerical results with test data of two parapets, namely URP1 and URP2, as done in the previous chapter. The two full-scale unreinforced mortar bonded concrete blockwork masonry parapets are subjected to low velocity impacts with different applied impulses, applied by square steel plate located at

mid-length [28]. The information concerned to the loading, the details of the walls and dimensions are given in the previous chapter. The applied load is simulated by a triangular load-time distribution with peak force of 90 KN and 110 KN reached at 22.9 msec and 25 msec, respectively, see Fig. 4.5.

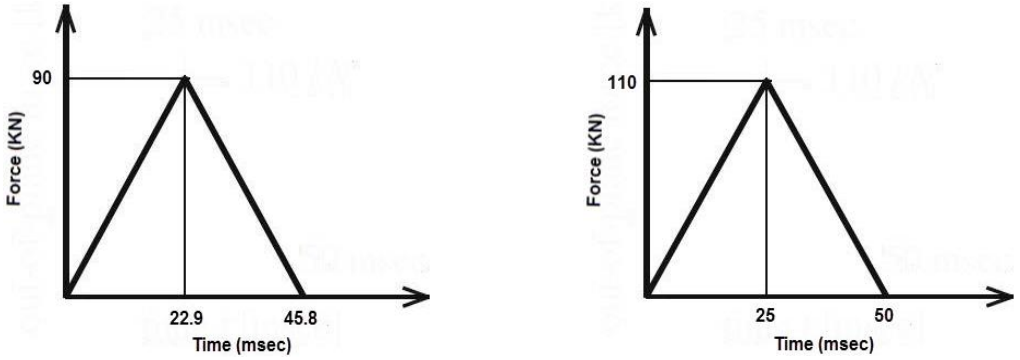

(*a*) (*b*)

Fig. 4.5. Typology of dynamic load applied to: (a) URP1; (b) URP2.

For numerical analysis, the rate dependent composite plasticity model is attributed to eight-node linear bricks (reduced integration degenerated solid elements) to consider the masonry behavior along different material axes. A regular fine mesh of cubic elements is used in numerical analysis. There are a total of 3024, and 4788 elements in the numerical models of the walls URP1 and URP2, respectively. The adopted finite element scheme of the wall URP1 is presented in Fig. 4.6. The *x*, *y*, *z* axes are along the horizontal, vertical and thickness directions, respectively.

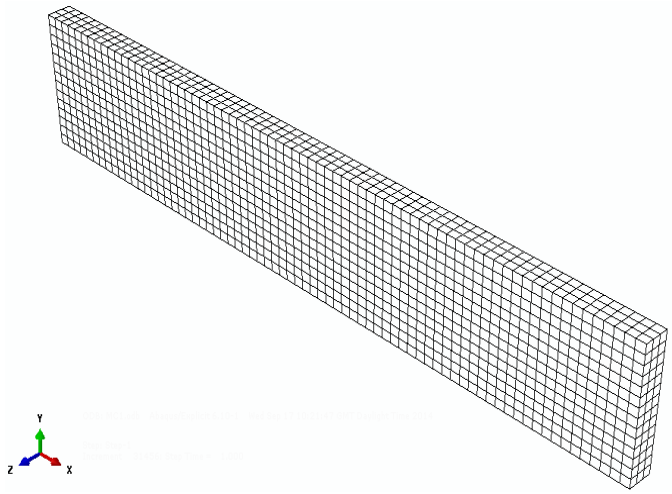

Fig. 4.6. Adopted finite element scheme (URP1 is shown).

No tests were done to characterize the masonry properties, so the values in Table 4.1 and Table 4.2 are obtained from [48]. The material properties are introduced as input parameters in numerical simulations.

Table 4.1. Elastic material properties for masonry parapets.

Wall	**Elastic properties**			
	E_x *(GPa)*	E_y *(GPa)*	E_z *(GPa)*	υ
URP1	4.5	1.8	2.8	0.2
URP2	4.5	1.8	7.9	0.2

Table 4.2. Inelastic material properties for masonry parapets.

Wall	**Tension**						**Compression**						
	f_{tx} *(MPa)*	f_{ty} *(MPa)*	f_{tz} *(MPa)*	G_{ftx} *(N/m)*	G_{fty} *(N/m)*	G_{ftz} *(N/m)*	f_{mx} *(MPa)*	f_{my} *(MPa)*	f_{mz} *(MPa)*	G_{fcx} *(N/m)*	G_{fcy} *(N/m)*	G_{fcz} *(N/m)*	k_p
URP1	0.130	0.043	1.230	3.12	0.52	72	21.5	8.6	12.3	22580	13760	19740	3.2E-3
URP2	0.130	0.043	3.740	3.12	0.52	217	21.5	8.6	37.4	22580	13760	26050	3.2E-3

Comparison of results

The predicted impact responses of the walls, URP1 and URP2, accounts for the out-of-plane displacement vs. time responses and the observed failure lines. The displacement is recorded at the point placed at mid height, and 580 mm above the base. The maximum principal plastic strain is adopted as the indicator of the crack distribution. The numerical results are compared to test data to estimate the accuracy of the predictions. As shown in Fig. 4.7, the simulated magnitude of peak displacement and the pre-peak and post-peak trends are close to the observed test responses. Though weaker concrete blocks were used in construction of URP1 and the wall thickness is lower, the wall URP2 moves much further given the different applied force-time distribution. Also, the longer length of URP2 has a significant influence in increasing

the out-of-plane displacement. Here it is noted that for wall URP1 there is a pronounced built up of stiffness found in response due to the inertial forces and acceleration of movement. For the wall URP2, the numerical response is shifted to the origin because the experiment does not show the initial acceleration of movement, which is possibly due to unexpected data acquisition difficulties. The slight reduction observed in displacement vs. time trends is due to the rocking back of the local sections bounded by diagonal cracks connected with the horizontal fracture lines over the length of the wall.

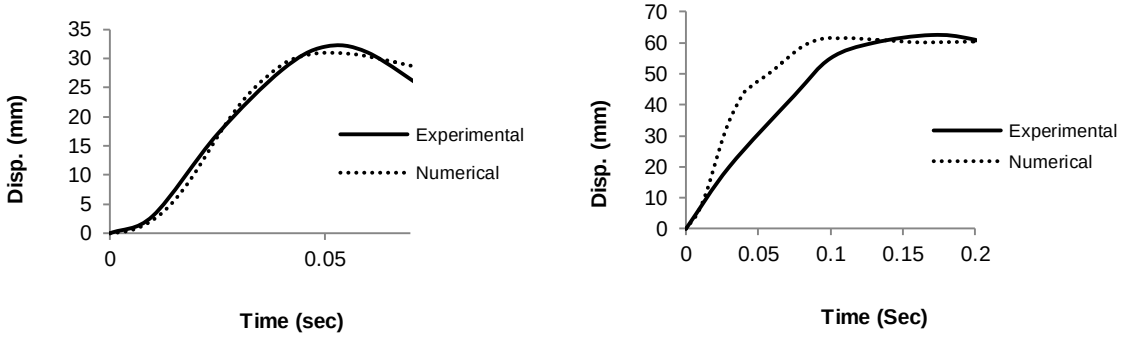

(*a*) (*b*)

Fig. 4.7. Displacement vs. time response of the wall: (a) URP1; (b) URP2.

The observed damages and fragmentation of the parapets against applied force-time history are addressed in Fig. 4.8 and Fig. 4.9.

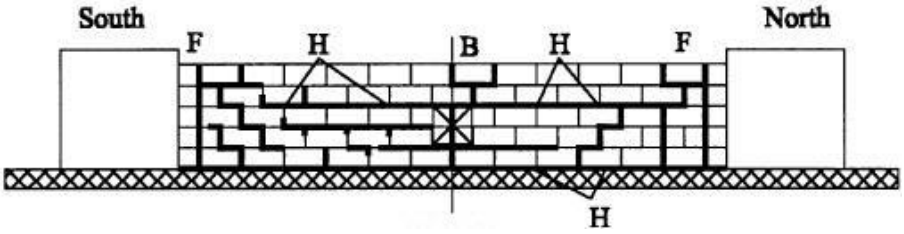

Fig. 4.8. Observed crack patterns in test – URP1 [28].

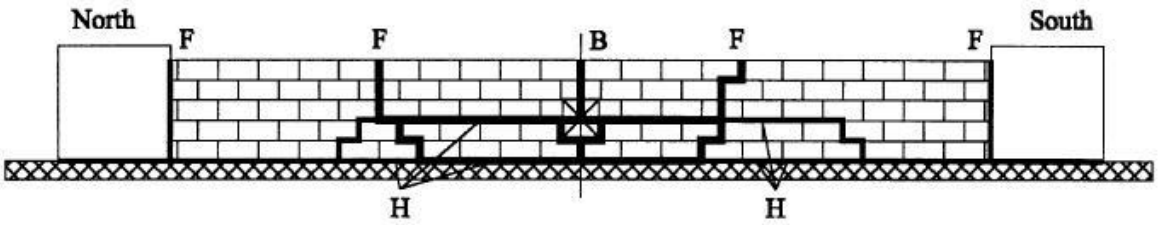

Fig. 4.9. Observed crack patterns in test - URP2 [28].

Fig. 4.10 and Fig. 4.11 show the predicted behavior of the parapets including the deformed mesh and the front and back face crack distribution at ultimate deflection loaded with out-of-plane impact. Regarding the predictions, for URP1, the escalation of cracks is noted close to the impact zone along with the front and back face diagonal tensile fracture lines at both sides. The vertical cracks are formed on wall centerline and to each side. The horizontal cracks are also distributed at lower levels along the length of the parapet, see Fig. 4.10.

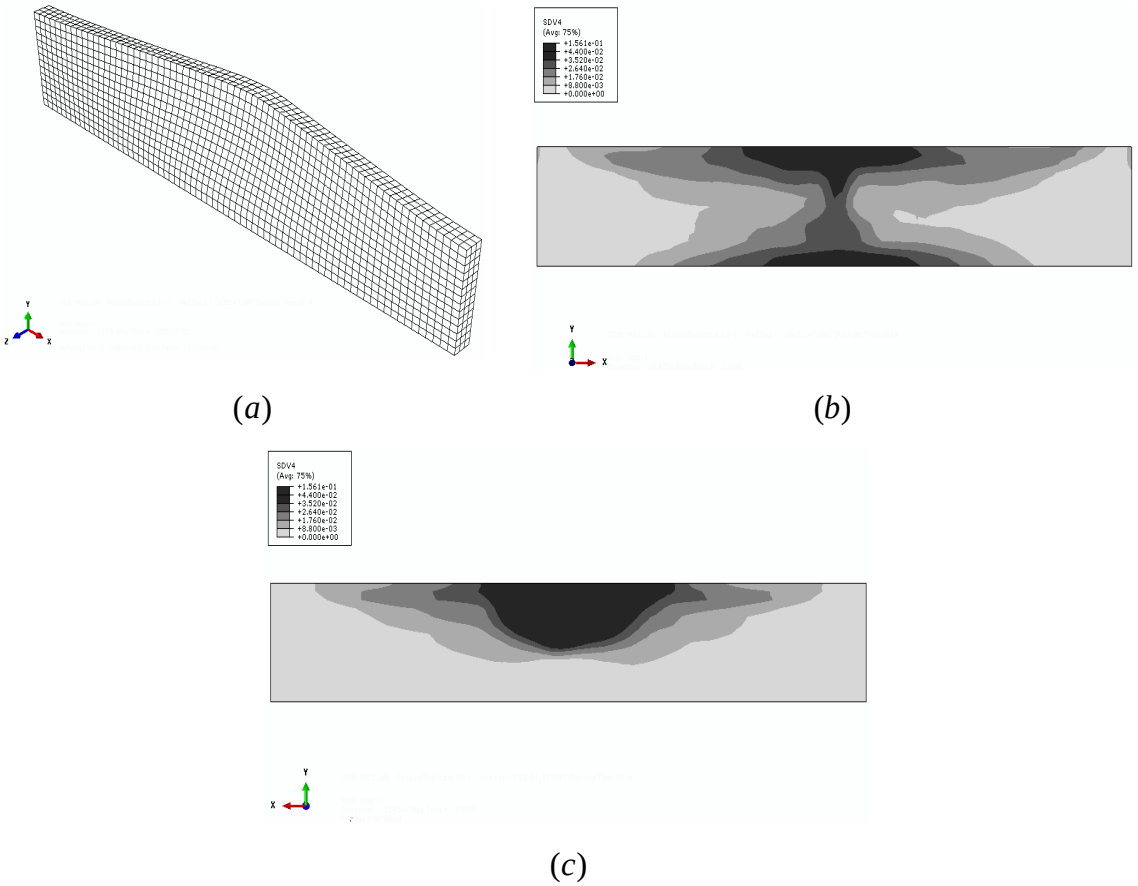

Fig. 4.10. Results of the analysis of URP1 at ultimate deflection: (a) deformed mesh; maximum principal plastic strain at the (b) front and (c) back face.

The diagonal tensile fracture lines are also detected in both sides, often connected by the horizontal cracks to each side. The horizontal cracks formed at the lower levels lead both right and left parts to rotate inside, see Fig. 4.11. Tracking the crack formation with loading, initially, cracks at the top of the walls were observed, followed by cracks at mid-height. Cracks at the bottom occurred much later, and at last, front face cracks

were formed far from the impact zone. As noted, the predictions dealing with the simulated crack patterns are reasonably close to the test response.

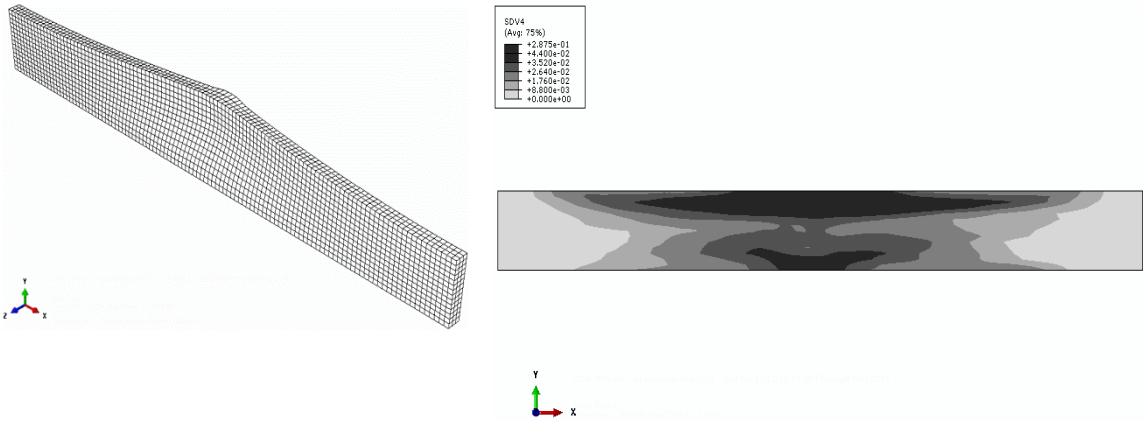

(*a*) (*b*)

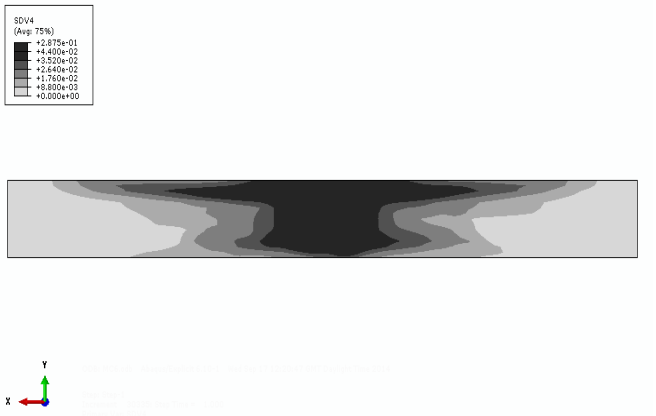

(*c*)

Fig. 4.11. Results of the analysis of URP2 at ultimate deflection: (a) deformed mesh; maximum principal plastic strain at the (b) front and (c) back face.

4.3.2 Masonry infill wall under blast

The full-scale macro numerical simulation of the tested unreinforced masonry infill wall is carried out to estimate the blast response including the displacement vs. time trend and the failure mechanisms. The masonry infill is composed of a reinforced concrete (RC) frame with a masonry panel inside. The masonry panel has a clear size of $5.75\times1.15m$, and is constructed with a single leaf of $30\times20\times15cm$ brick with 15 mm of M5 plaster cover on both sides, see Fig. 4.12.

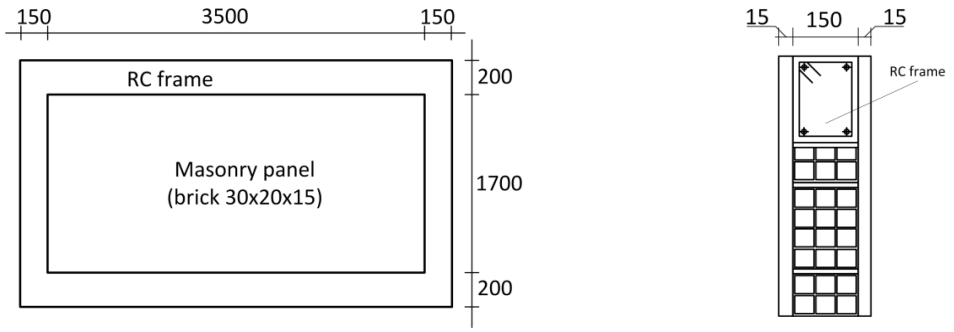

(*a*) (*b*)

Fig. 4.12. Masonry specimens: (a) geometry; (b) schematics (dimensions in mm) [16].

Again, the masonry infill is considered as a homogeneous continuum. The RC frame is bolted to the steel structure that serves as support in 11 places along the perimeter. Since no serious damage was observed in RC frame during the post-test visual inspection, the RC frame is considered as rigid boundary precluding the rotation at four edges. Thus, only the masonry panel is simulated, and perfect connection is considered between the panel and the RC frame. The applied pressure-time history recorded by oscilloscope during the test has a peak pressure of 149 kPa reached at 6 msec. Subsequently, it continues to reach 119 kPa at 17.5 msec and decays to the ambient pressure, see Fig. 4.13.

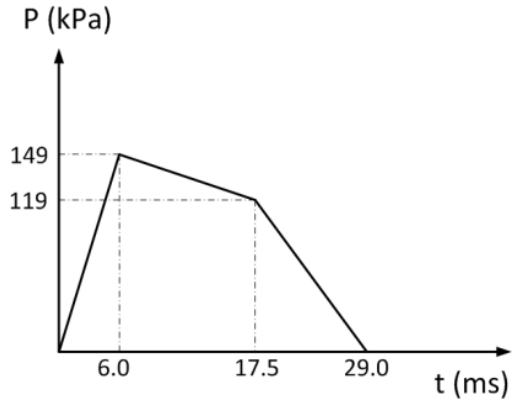

Fig. 4.13. Applied pressure-time history [16].

The dynamic plasticity model is attributed to the regular fine mesh of eight-node solid elements with reduced integration to simulate the orthogonal masonry behavior with different inelastic behavior along each material axis. There are a total of 1848 elements in the numerical model of the masonry infill. The adopted finite element scheme of the

masonry infill wall is shown in Fig. 4.14. Here, The *x*, *y*, *z* axes are along the horizontal, vertical and thickness directions, respectively.

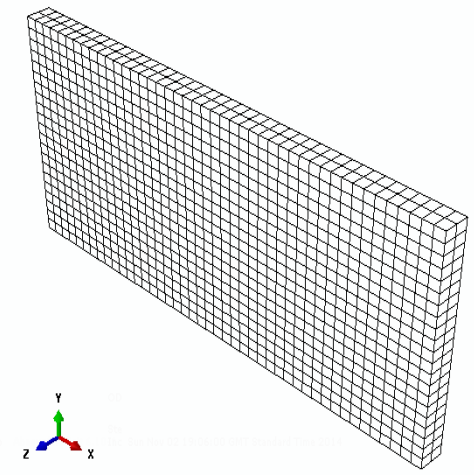

Fig. 4.14. Adopted finite element scheme.

The material properties of masonry obtained from the experiments by Pereira [49] served as quasi-static reference mechanical characteristics for the calibration of input parameters, see Table 4.3 and Table 4.4. Moreover, the expressions for DIFs obtained by Pereira [16] are adopted to provide the strain rate dependency of composite yield surface.

Table 4.3. Elastic material properties for masonry infill wall.

Elastic properties			
E_x *(GPa)*	E_y *(GPa)*	E_z *(GPa)*	υ
2.00	1.81	4.43	0.2

Table 4.4. Inelastic material properties for masonry infill wall.

Tension						**Compression**						
f_{tx} *(MPa)*	f_{ty} *(MPa)*	f_{tz} *(MPa)*	G_{ftx} *(N/m)*	G_{fty} *(N/m)*	G_{ftz} *(N/m)*	f_{mx} *(MPa)*	f_{my} *(MPa)*	f_{mz} *(MPa)*	G_{fcx} *(N/m)*	G_{fcy} *(N/m)*	G_{fcz} *(N/m)*	k_p
0.340	0.100	0.385	8.2	1.2	11.2	1.75	1.50	3.85	2000	2400	6160	0.93E-3

Comparison of results

The numerical predictions of the out-of-plane behavior of masonry infill wall subjected to large detonation include the displacement vs. time trend and the post-test observed crack patterns. Regarding the test data, the masonry panel behaves as a plate constrained in four edges and the maximum displacement is obtained at mid-height. Therefore, in numerical simulation, the maximum displacement is recorded at the point placed at the center of the panel. The maximum principal plastic strain is involved to indicate the crack distribution. As shown in Fig. 4.15, comparing the numerical results with the test data, the maximum displacement is well predicted. The pre-peak trend is rather well predicted up to the 10 mm in deformation, but after this instant the test curve progressively changes the slope due to the initiation of the crack formation. In post-peak region, given the rocking back of the local sections bounded by diagonal fracture lines connected with the horizontal cracks, a noticeable reduction is noted that causes a residual deformation at the end of the test. Depending upon the numerical predictions, the reduction in post-peak is observed, but still there is a slight difference in residual deformations compared to the test response. Ignoring the negative phase of applied pressure protocol and escalation of the cracks can partly justify the differences. Here it is noted that for the masonry infill wall there is a pronounced built up of stiffness found in response due to the inertial forces and acceleration of movement, giving the high quality data acquisition adopted in tests.

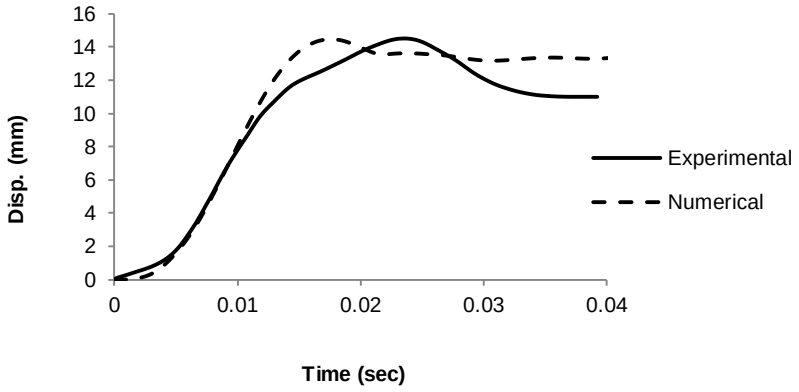

Fig. 4.15. Displacement vs. time response of the masonry infill wall.

The damages and fragmentation of the tested masonry infill wall subjected to blast loading are presented in Fig. 4.16.

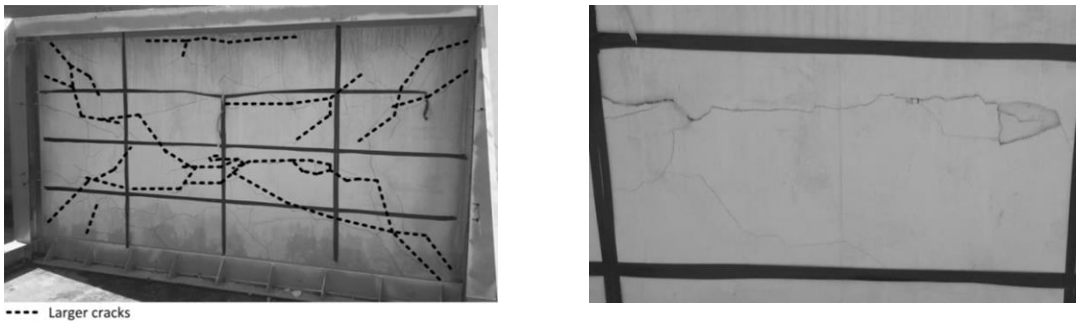

(*a*) (*b*)

Fig. 4.16. Damaged wall after blast test: (a) full panel; (b) zoom on the center of the panel (2nd row and 3rd column quadrant, from bottom-left) [16].

Fig. 4.17 shows the numerically simulated response of the masonry infill in terms of deformed mesh and the back face crack distribution at ultimate deflection. Regarding the predictions, there is a concentration of the horizontal fractures lines at mid-height over the entire length of the wall connected to the diagonal tensile cracks spreading to the corners. Tracking the crack formation with loading, initially, horizontal cracks are formed at the center of the wall, followed by the diagonal cracks close to the corners, which occurred much later. As noted, the results concerning the crack patterns are replicated close to the test data.

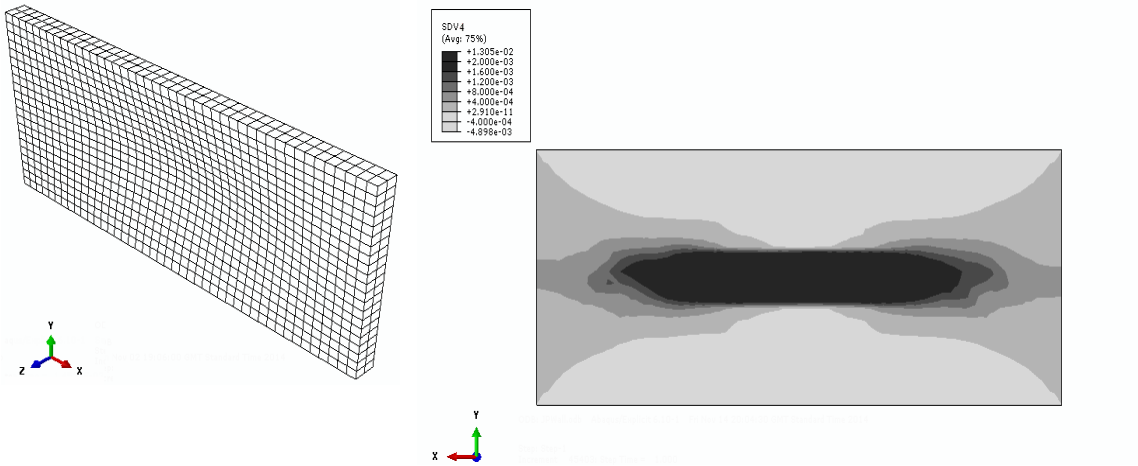

(*a*) (*b*)

Fig. 4.17. Results of the analysis of masonry infill wall at ultimate deflection:
(a) deformed mesh; (b) maximum principal plastic strain at the back face.

4.4 PARAMETRIC STUDIES

The wall URP1, used for validation, is considered in this section to carry out a parametric study to estimate the influence of changes in the most dominant parameters including the tensile strengths along different material axes on the impact response of the masonry walls, by comparing the displacement vs. time evolution and the crack formation with the reference response. Normally, the masonry is controlled by tension, not compression. However, it is also of interest to evaluate the effectiveness of compressive properties on high strain rate response of a masonry structure. Thus, the tested masonry infill wall, adopted for validation, is adopted to study the influence of variation in the uniaxial compressive strength and Young's modulus along each material axis on high strain rate response of masonry infills under blast over a specified range of scaled stand of distance, Z. Moreover, a mesh sensitivity analysis is carried out to evaulate the influece of further refinement in the mesh along the thickness direction.

4.4.1 Masonry parapet under impact

4.4.1.1 Influence of tensile strength

As mentioned before, masonry is constructed with individual units bonded in courses by mortar layers, in staggered configuration. Consequently, besides the scatter usually found in masonry properties, the masonry tensile strength varies significantly along the different material axes. Hence, the influence of the tensile strengths at different directions on impact behavior and damage level of the masonry parapets is evaluated in this parametric study. Each subsequent graph gives the displacement vs. time evolution of the walls with different tensile strengths along the material axes, considering an extreme range of values. The given range of each material parameter is selected in accordance with the typical range of values addressed in literature to enable the author to evaluate the possible changes in blast response of masonry infill wall in reasonable range of values, see e.g. [48, 50]. As shown in Fig. 4.18 to Fig. 4.20, increasing the tensile strength in each direction reduces the maximum displacement; however, the influence of tensile strength is much more significant in *y* and *z* directions, but lower in *x* direction. This can be justified by considering that the wall thickness and loading direction are along the *z* direction that results in the frequent activation of Rankine type yield surface in *xy* plane of composite yield surface, whereas the length of the wall is

along the *x* direction and this reduces the possibility of activation of the Rankine type yield surface in *yz* plane.

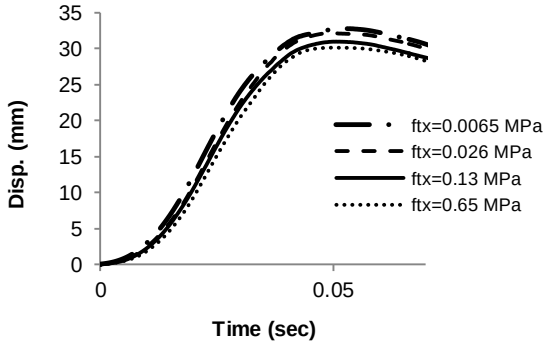

Fig. 4.18 . Displacement vs. time diagram of URP1with different tensile strengths in *x* direction.

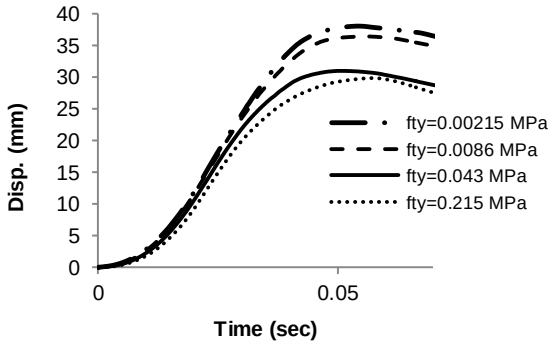

Fig. 4.19. Displacement vs. time diagram of URP1with different tensile strengths in *y* direction.

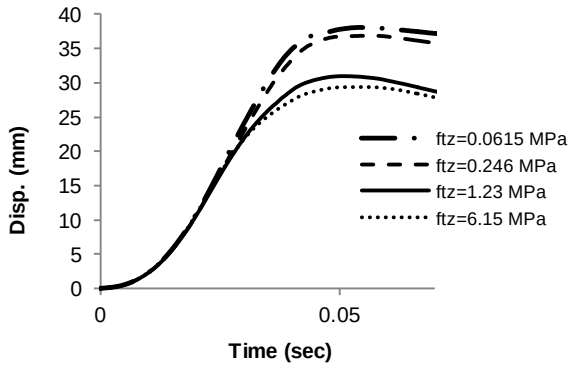

Fig. 4.20. Displacement vs. time diagram of URP1with different tensile strengths in *z* direction.

Comparing the crack distribution of the wall for parameter variation in the *x* direction, it can be inferred that tensile strength changes do not affect the crack patterns, see Fig. 4.21. As noted in Fig. 4.22 and Fig. 4.23, the reduction of tensile strength in *y* or *z* direction does not effectively change the governing failure mechanisms, but rises the magnitude of maximum principal plastic strain at integration points close to the centerline at both sides, which indicates the intensification of localized cracks in this zone.

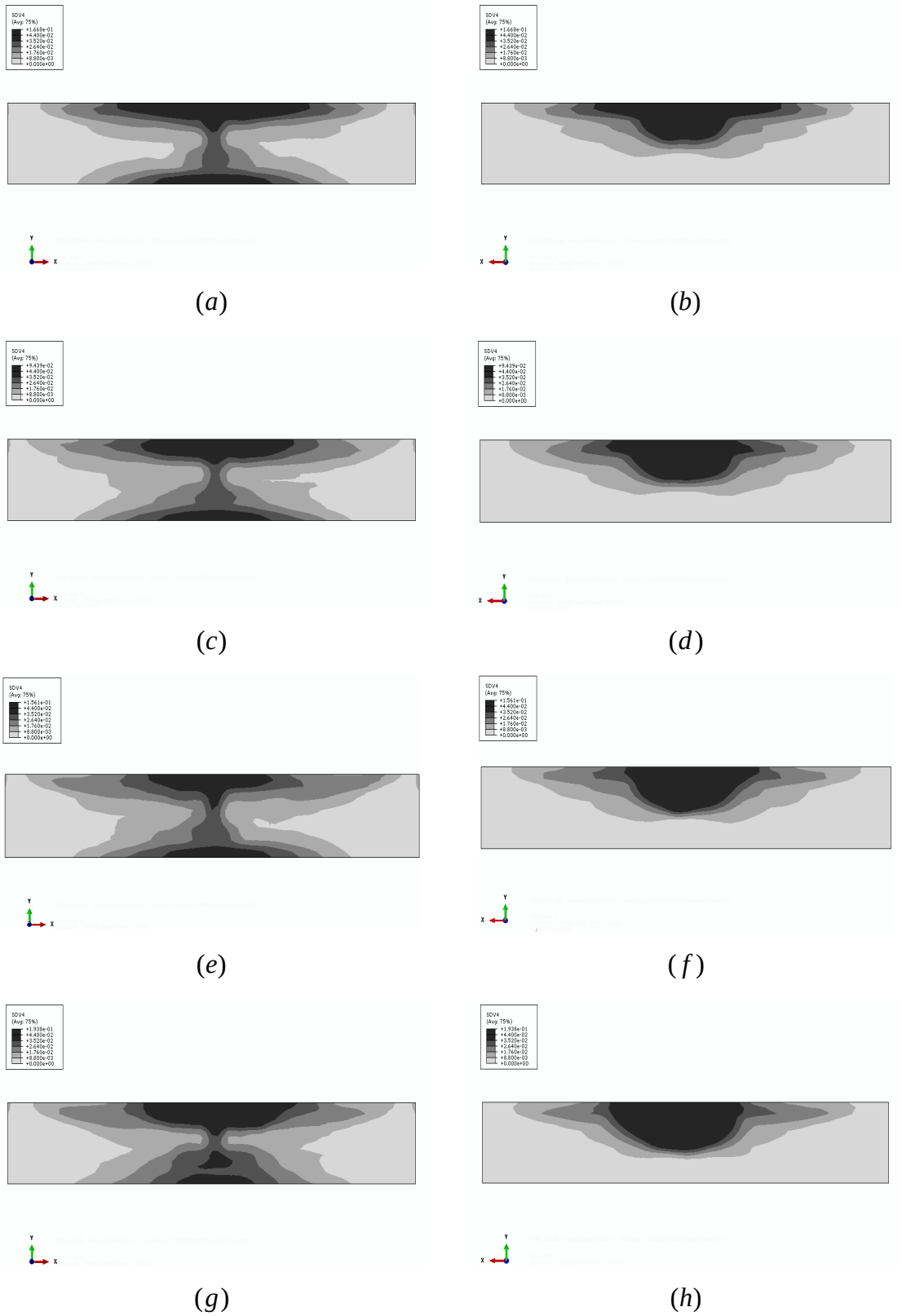

Fig. 4.21. Crack patterns of URP1 at ultimate deflection with three different tensile strength along *x* material axis: f_{tx}=0.0065 MPa (a) front and (b) back face; f_{tx}=0.026 MPa (c) front and (d) back face; f_{tx}=0.13 MPa (e) front and (f) back face; f_{tx}=0.65 MPa (g) front and (h) back face.

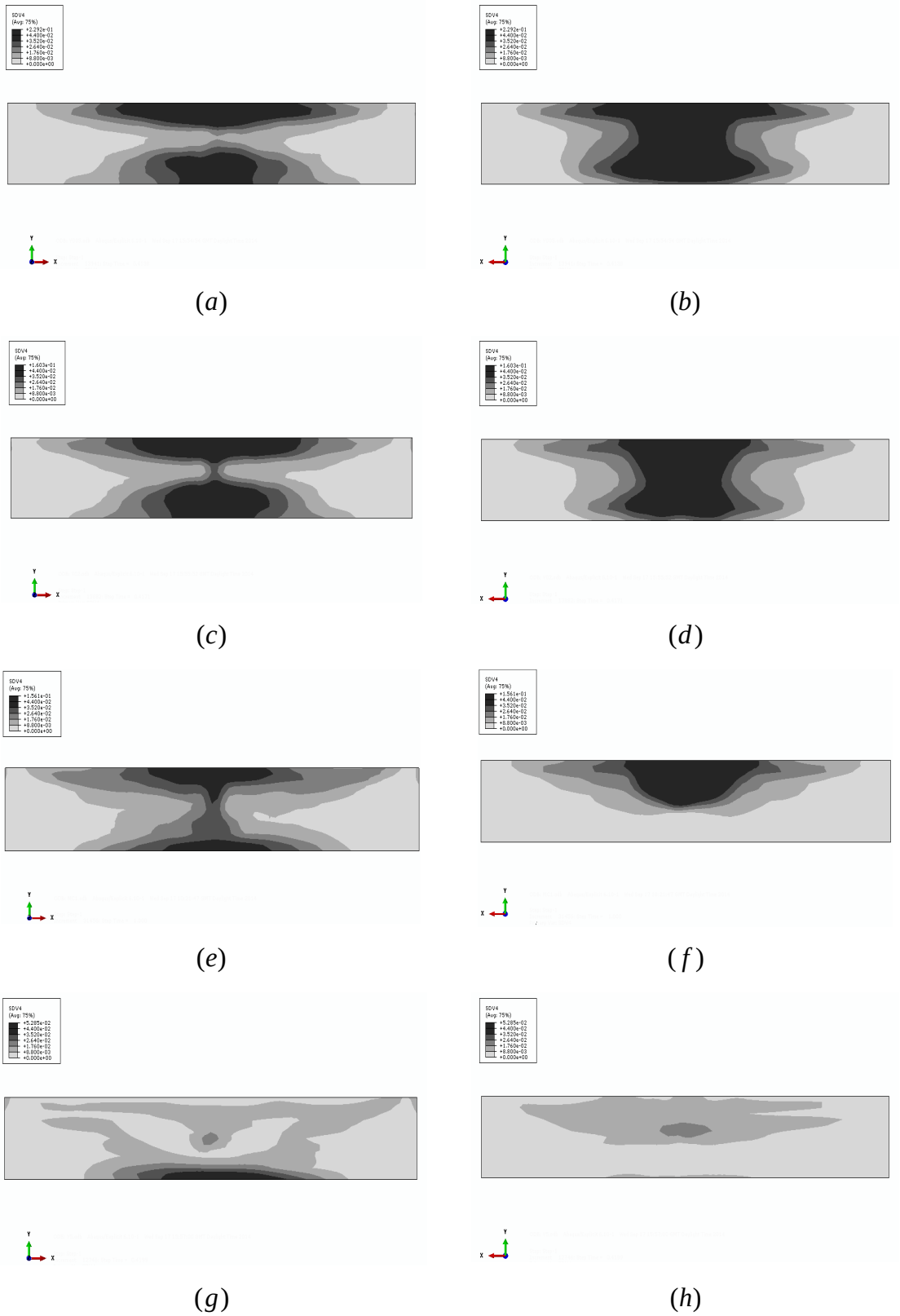

Fig. 4.22. Crack patterns of URP1 at ultimate deflection with three different tensile strength along *y* material axis: f_{ty}=0.00215 MPa (a) front and (b) back face; f_{ty}=0.0086 MPa (c) front and (d) back face; f_{ty}=0.043 MPa (e) front and (f) back face; f_{ty}=0.215 MPa (g) front and (h) back face.

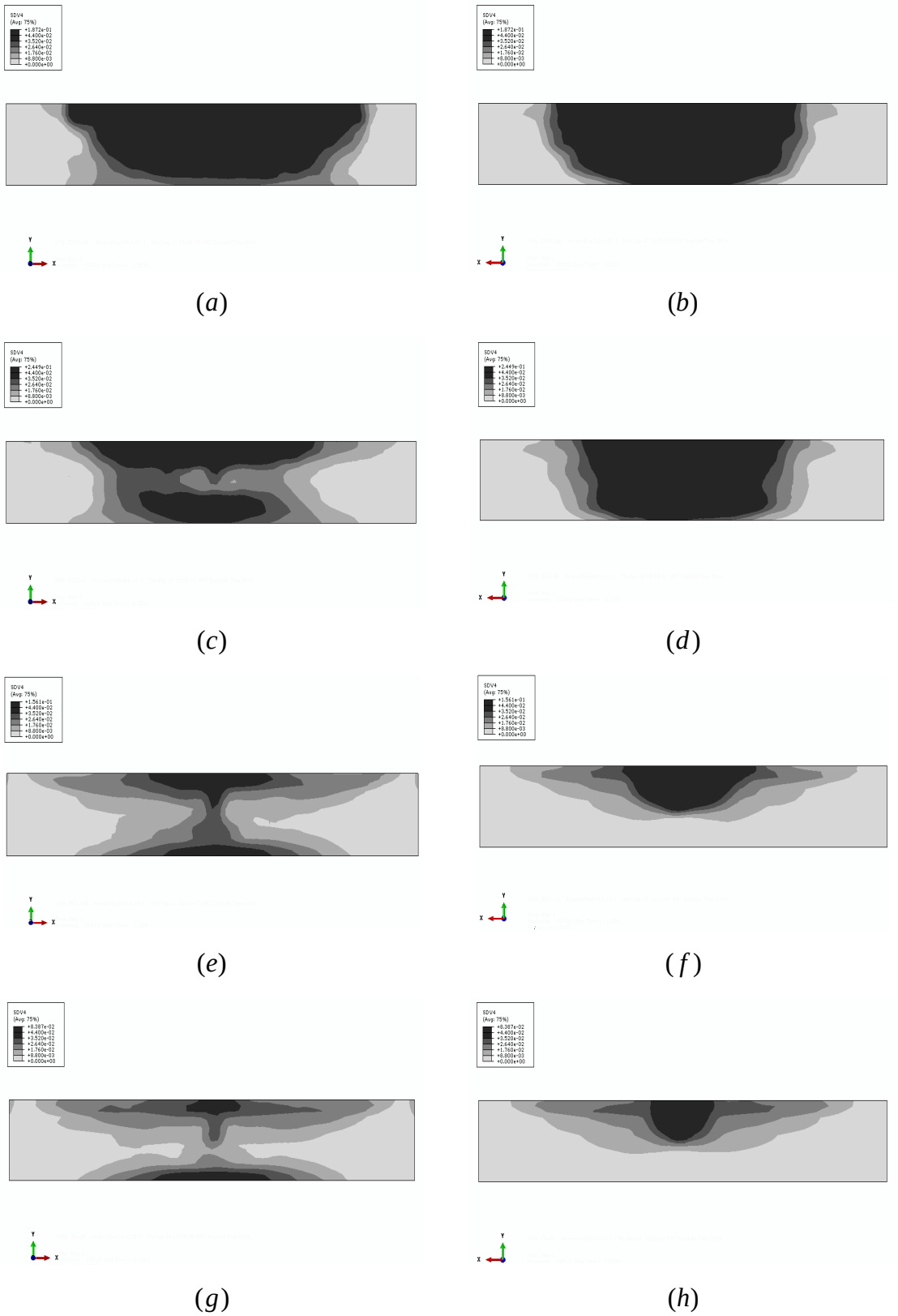

Fig. 4.23. Crack patterns of URP1 at ultimate deflection with three different tensile strength along *z* material axis: f_{tz}=0.0615 MPa (a) front and (b) back face; f_{tz}=0.246 MPa (c) front and (d) back face; f_{tz}=1.23 MPa (e) front and (f) back face; f_{tz}=6.15 MPa (g) front and (h) back face.

4.4.1.2 Influence of wall thickness

Three different types of wall thicknesses of 200 mm, 250 mm, and 300 mm are applied to evaluate the effect of wall thickness. The reference masonry material properties are adopted in the three walls. It is noted that the wall with the thickness of 200 mm has the maximum deflection. As expected, the growth of the wall thickness, almost 1.5 times, causes an evident reduction of up to 2.7 times in maximum displacement of the wall, see Fig. 4.24.

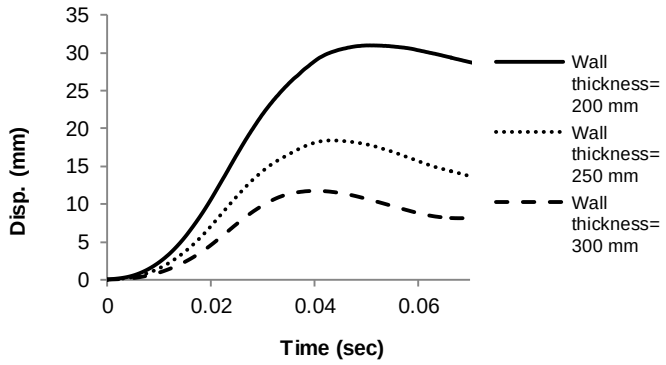

Fig. 4.24. Displacement vs. time responses of the wall URP1 with three wall thicknesses: (a) t=200mm; (b) t=250mm; (c) t=300mm.

Again, this in opposition with a quasi-static elastic calculation, where this deformation would be proportional to the bending stiffness (in this case, this would be a maximum difference $1.5^3 = 3.4$). Fig. 4.25 shows that decreasing the wall thickness, and thus lowering the out-of-plane bending stiffness of the wall, results in growth of the damage and fragmentation over the entire length of the wall.

Afterwards, a comparison is performed between the results of the micro and macro modeling of the masonry parapet with different wall thicknesses to evaluate the similarity of them, see Fig. 4.26. As shown, a good agreement is noted between the results of walls up to 0.03 sec. After this time, the slope reduction starts for macro modelled walls due to failure growing. Moreover, the difference between the curves rises by increasing the wall thickness. Assuming the elastic blocks in micro modelling, using different expressions for DIFs of material properties for two different modelling strategies and low accuracy of the macro approach compared with micro approach can justify the differences.

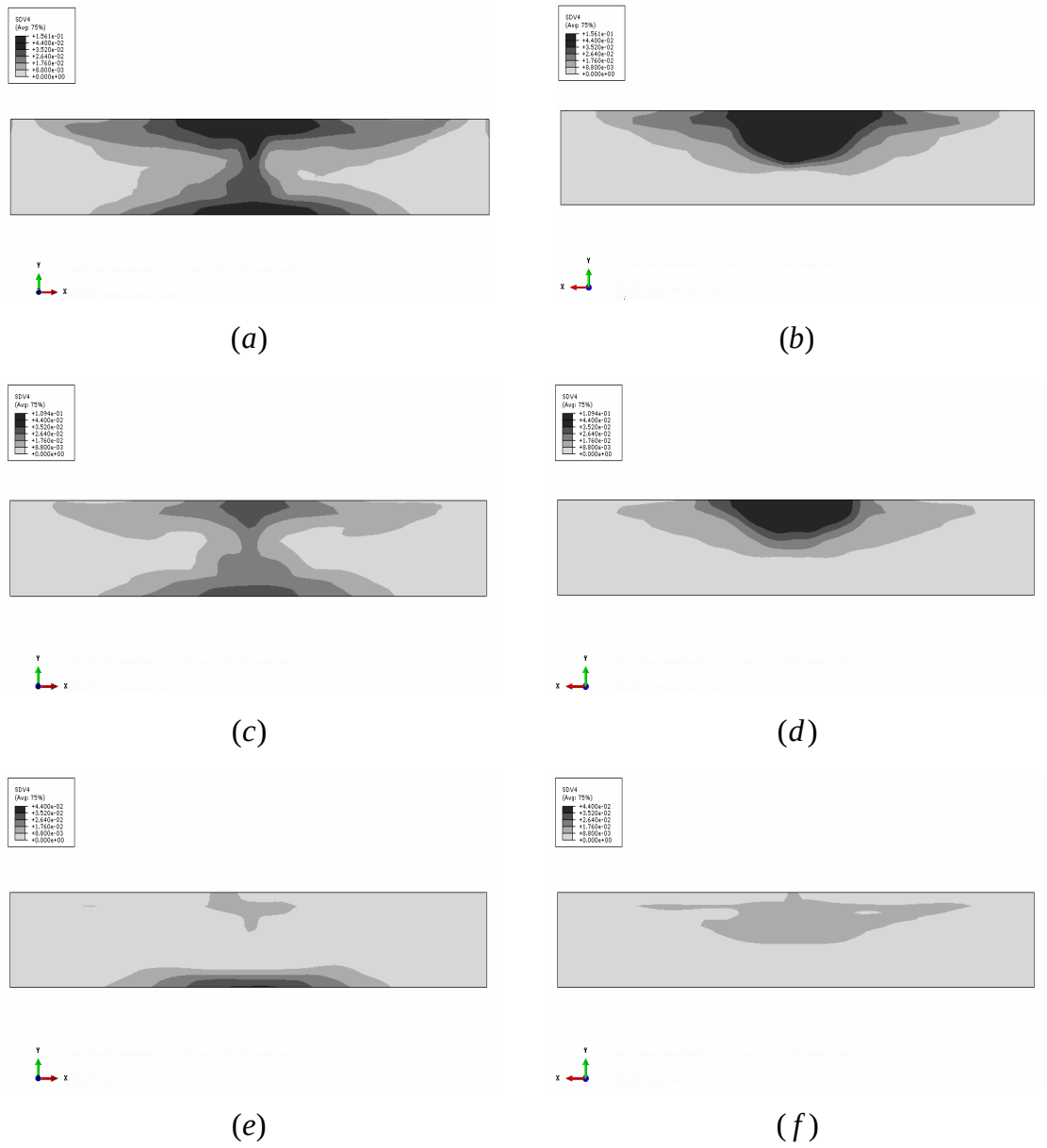

(*a*) (*b*)

(*c*) (*d*)

(*e*) (*f*)

Fig. 4.25. Crack patterns of URP1 at ultimate deflection with three different wall thicknesses: t=200 mm (a) front and (b) back face; t=250 mm (c) front and (d) back face; t=300 mm (e) front and (f) back face.

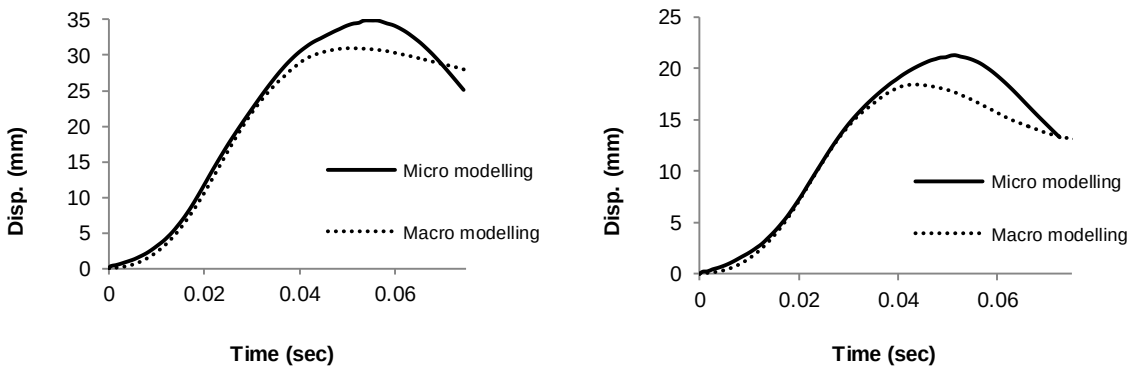

(*a*) (*b*)

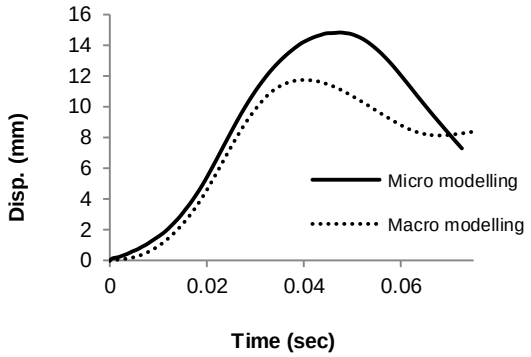

(*c*)

Fig. 4.26. Comparison between the results of the micro and macro modeling of the masonry parapet with three wall thicknesses: (a) t=200 mm; (b) t=250 mm; (c) t=300 mm.

4.4.1.3 Influence of strain rate dependency

One aspect that is of interest is to compare a model with strain rate dependency, labeled A, (i.e. making each integration point to have a different strength, given by its own strain rate and velocity) with a model where the properties are assumed identical in all integration points, and equal to the properties of the integration point situated at mid height, labeled B. The results of the analysis, shown in Fig. 4.27 and Fig. 4.28 indicate that by adopting the same properties in all integration points the displacement vs. time trend is slightly reduced, but the response is very similar.

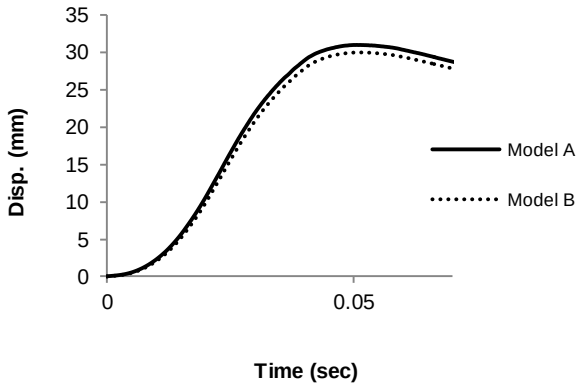

Fig. 4.27. Displacement vs. time responses of the wall URP1 for two different approaches: (a) different properties in integration points; (b) identical properties in integration points.

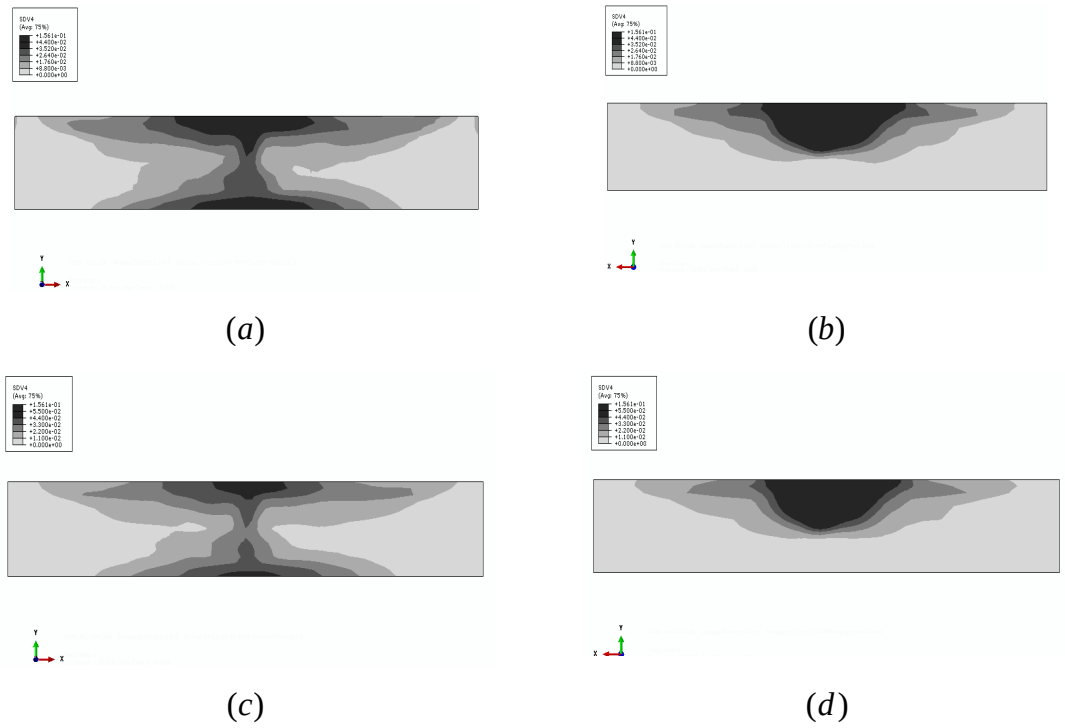

Fig. 4.28. Crack patterns of URP1 at ultimate deflection for two different approaches: different properties in integration points (a) front and (b) back face; identical properties in integration points (c) front and (d) back face.

Additionally, the changes on fracture line distribution are imperceptible. If higher strain rates occur, by applying the double of the original impulse, the changes between the analyses, including the displacement vs. time response, and the failure mode, are more intensified, see Fig. 4.29 and Fig. 4.30. This demonstrates that a simplified assumption, not including a proper point-wise dependency of material properties according to the actual strain rate is not recommended.

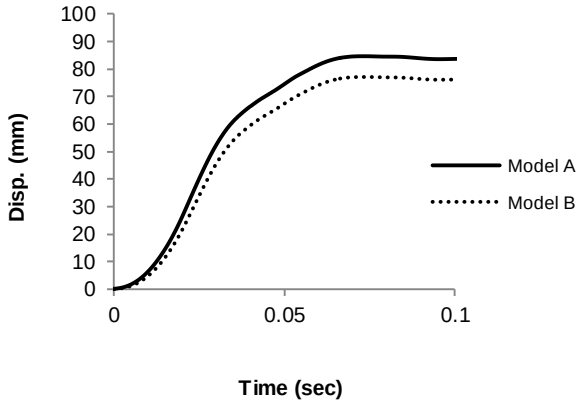

Fig. 4.29. Displacement vs. time responses of the wall URP1 for two different approaches against double applied impulse: (a) different properties in integration points; (b) identical properties in integration points.

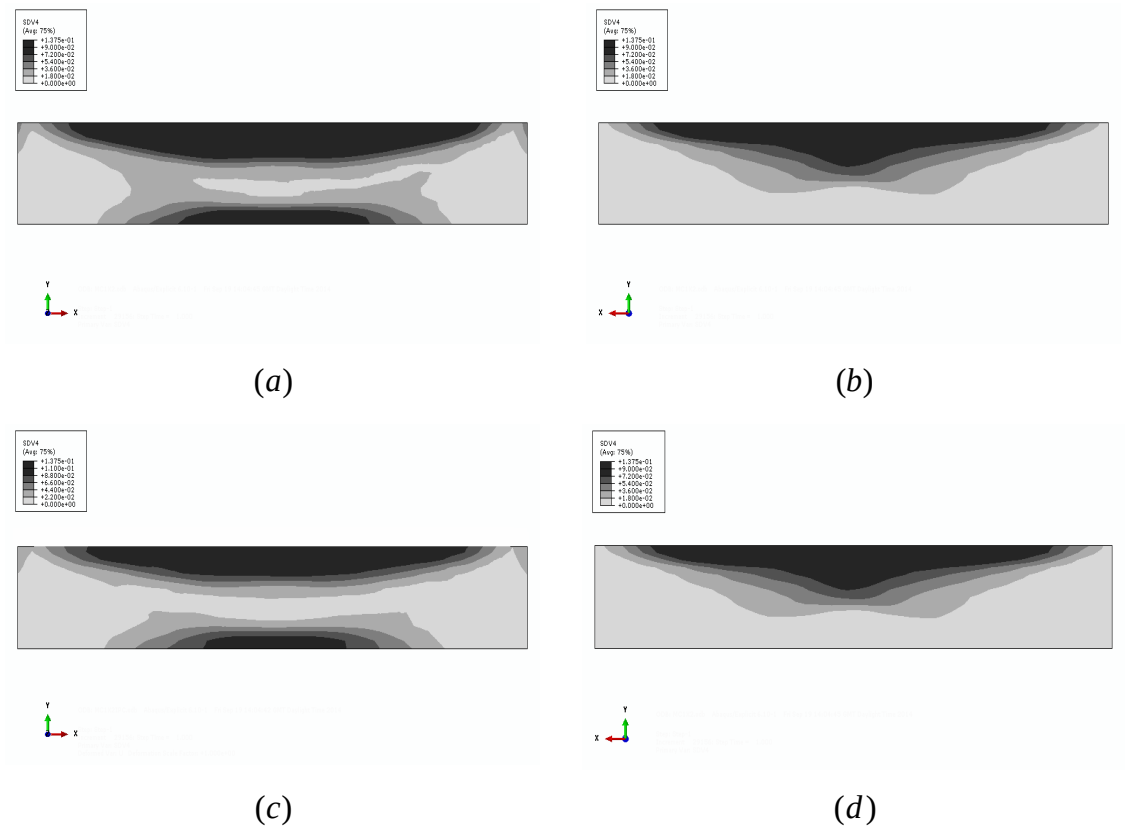

(*a*) (*b*)

(*c*) (*d*)

Fig. 4.30. Crack patterns of URP1 at ultimate deflection for two different approaches against different applied impulse: different properties in integration points (a) front and (b) back face; identical properties in integration points (c) front and (d) back face.

4.4.2 Masonry infill wall under blast

4.4.2.1 Influence of compressive strength and Young's modulus

The triangular shape loading protocol shown in Fig. 4.31 is applied on the masonry infill. Here, t_d is the positive phase duration and P is the overpressure.

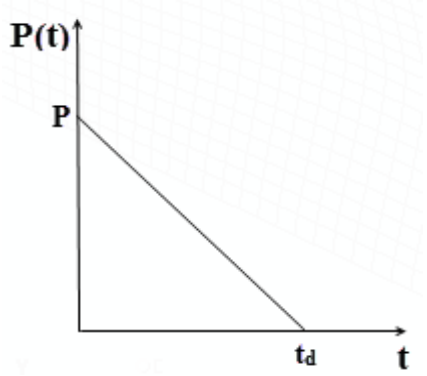

Fig. 4.31. Typology of the dynamic applied load.

The side-on overpressure, reflected overpressure and positive phase duration are calculated using the below expressions.

$$P_{so} = \frac{1772}{Z^3} - \frac{114}{Z^2} + \frac{108}{Z} \tag{4.48}$$

$$P_r = 2P_{so}\left\{\frac{7P_o + 4P_{so}}{7P_o + P_{so}}\right\} \tag{4.49}$$

$$\frac{t_d}{W^{\frac{1}{3}}} = \frac{980(1+\left(\frac{z}{0.54}\right)^{10})}{(1+\left(\frac{z}{0.02}\right)^{3})(1+\left(\frac{z}{0.74}\right)^{6})\sqrt{1+\left(1+(\frac{z}{6.9})^2\right)}} \tag{4.50}$$

The given range of each material parameter is presented in Table 4.5. The certain range of each material parameter is selected with respect to the typical range of values addressed in literature to evaluate the most likely changes in blast response of masonry infill wall in reasonable range of values, see e.g. [16].

Table 4.5. The range of each material parameter in parametric study.

Material parameter	**Min**	**Mid**	**Max**
f_{mx} *(MPa)*	1.75	3.5	7
f_{my} *(MPa)*	1.5	3	6
f_{mz} *(MPa)*	3.85	7.7	15.4
E_x *(GPa)*	2	4	8
E_y *(GPa)*	1.81	3.62	7.24
E_z *(GPa)*	4.43	8.86	17.72

By conducting several numerical simulations, the maximum displacement vs. Z responses of masonry infill for each parameter over a given range are obtained, see Fig. 4.32. As noted, reducing the parameter Z results in increasing the maximum displacement for all parameters. Its growth rate also rises significantly at lower amounts of Z, specially for $Z \leq 3$. For each parameter, independent of the parameter Z, enhancing its amount causes a reduction in maximum displacement. Furthermore, the differences between the different amounts of each parameter grow significantly for $Z \leq 3$.

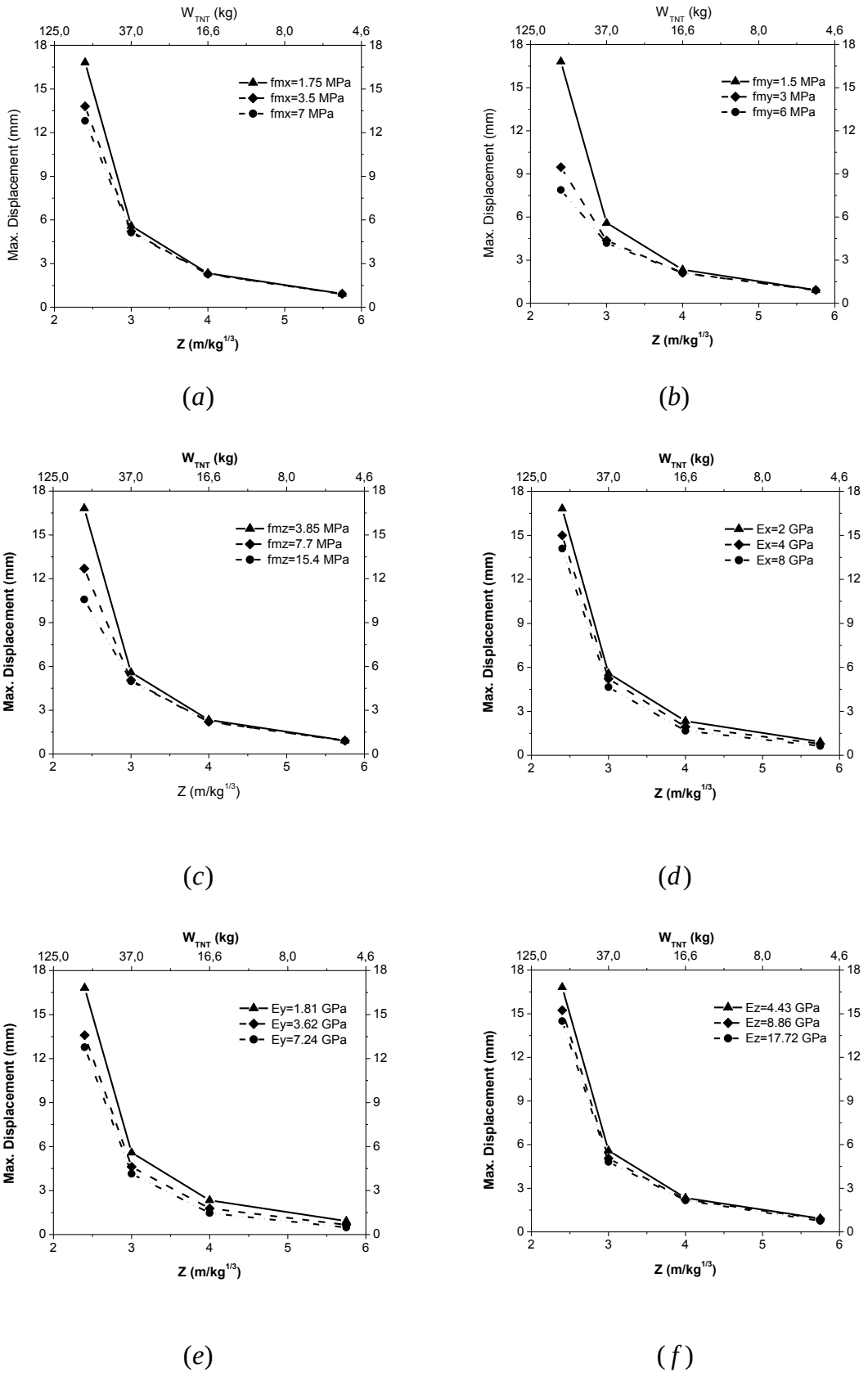

Fig. 4.32. Parametric study on the material properties of masonry infills under blast: uniaxial compressive strength along (a) *x* axis, (b) *y* axis, (c) *z* axis; Young's modulus along (d) *x* axis, (e) *y* axis, (f) *z* axis.

Fig. 4.32(a), (b), (c) show the influence of the variation of compressive strength along different material axes on maximum displacement at different strain rates. The compressive strength in *y* direction governs significantly the maximum displacement, much more than the *x* and *z* direction. The variation of the compressive strength in three directions changes slightly the maximum displacement for $Z > 3$. However, for $Z \leq 3$, the changes become clearer, more for f_{my} and less for f_{mz}. Fig. 4.32(d), (e), (f) show the effect of the changes of Young's modulus on maximum displacement at different strain rates. It is noted that the influences of Young's modulus in *y* direction is higher compared with the influence of Young's modulus in *x* and *z* directions over the given range of Z. Moreover, in three directions, decreasing the parameter Z leads to increase the changes in maximum displacement between different amounts of Young's modulus.

4.4.2.2 Mesh sensitivity

A mesh sensitivity analysis is conducted to study the sensitivity of the results with respect to the mesh size along the thickness direction. The analysis of the masonry infill wall with finite element meshes refined by a factor 1.5 in thickness direction is carried out. The comparative results of the analyses with coarser and finer meshes are shown in Fig. 4.34 and Fig. 4.34. As noted, the difference between the displacement vs. time responses is negligible and the crack patterns remain unchanged. Hence, the results can be considered mesh insensitive and no further refinement in the mesh along the thickness direction is required. It can be justified given adopting a fracture energy based regularization in present study that incorporates an equivalent length, *h*, in the material model which is dealing with the area of an element.

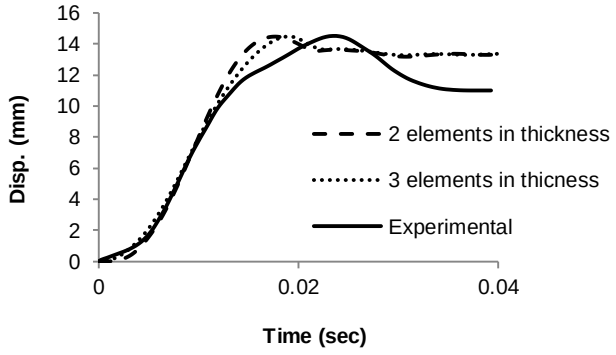

Fig. 4.33. Displacement vs. time responses of the masonry infill wall with different mesh sizes.

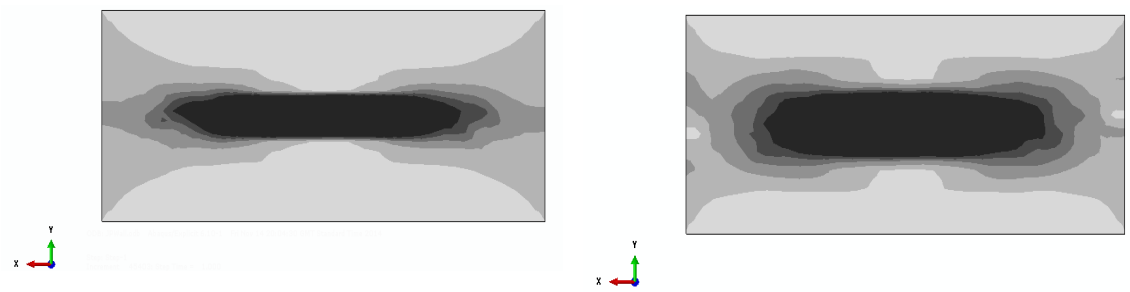

(*a*) (*b*)

Fig. 4.34. The results of the analyses of the masonry infill wall with different mesh sizes: Crack patterns at ultimate deflection (a) two elements in thickness direction; (b) three elements in thickness direction.

4.5 FINAL REMARKS

The present study introduces a novel dynamic anisotropic continuum model for the simulation of masonry structures under high strain rates. The composite plasticity model is implemented as a user-defined subroutine in the finite element code ABAQUS, in the context of 3D solid elements to simulate the masonry behavior. The numerical simulation of high strain rate responses of two full scale masonry parapets and a masonry infill wall is carried out to evaluate the performance and validity of the proposed model and the results are compared with test reference values. The numerical simulations accounting for the maximum deflection and crack patterns over the entire length of the wall are well replicated when compared with test data.

A parametric study is also performed to study the effectiveness of the most likely main properties on impact response of a masonry parapet and blast response of a masonry infill wall. As noted, the influence of tensile strength on maximum deflection and crack patterns of the masonry wall is much more significant in *y* and *z* directions, but less in *x* direction. The *x*, *y*, *z* axes are along the horizontal, vertical and thickness directions, respectively. The reduction of tensile strength in *y* or *z* direction leads to a localized failure close to the impact zone. As expected, increasing the wall thickness decreases the maximum deflection and damage, but the changes obtained for fast impact are significantly different from the changes in stiffness obtained in a linear elastic calculation. Another aspect is the evaluation of the influence of strain rate dependency. It is concluded that considering the same properties in all integration points causes a slight decrease in displacement vs. time trend and imperceptible changes on crack distribution for low strain rates. At higher strain rates, the changes are significant and

the use of a proper point-wise dependency of material properties according to the actual strain rate, as done here, is recommended.

Regarding the evaluation of the effectiveness of the uniaxial compressive strength and Young's modulus along each material axis on high strain rate response of masonry infills made with hollow clay tiles under blast over a specified range of scaled stand of distance, Z, reducing the parameter Z results in increasing the maximum displacement for all parameters. Its growth rate also rises significantly at lower amounts of Z, specially for $Z \leq 3$. For each parameter, independent of the parameter Z, enhancing its amount causes a reduction in maximum displacement. Furthermore, the differences between the different amounts of each parameter grow significantly for $Z \leq 3$. The compressive strength in *y* direction governs significantly the maximum displacement, much more than the *x* and *z* direction. The variation of the compressive strength in three directions changes slightly the maximum displacement for $Z > 3$. However, for $Z \leq 3$, the changes become clearer, more f_{my} and less f_{mz}. It is noted that the influence of Young's modulus in *y* direction is higher compared with the influence of Young's modulus in *x* and *z* directions over the given range of Z. Finally, a mesh sensitivity analysis is conducted to study the sensitivity of the results with respect to the mesh, demonstrating that further refinement in the mesh along the thickness direction is not required.

Chapter 5

5 DESIGN RULES FOR MASONRY INFILL WALLS SUBJECTED TO EXPLOSIVE LOADS

5.1 INTRODUCTION

The masonry envelop is considered highly vulnerable against blast loading due to the possibility of human losses, irreparable damages and fragmentation on the structures. There are only a studies dealing with the blast response of masonry structures, and the majority of them do not address infills.

Still, in recent years, a series of damage response limits have been proposed based on numerical and experimental studies to evaluate the damage level of masonry structures subjected to blast loading. Pressure-Impulse diagrams typically are recommended by guidelines such as ASCE [12] in preliminary design and evaluation of structural damage against blast loading and to establish reliable response limits, see Fig. 5.1. A Pressure-Impulse diagram is an iso-damage curve. In other words, each combination of pressure and impulse produces the same damage in a structure component.

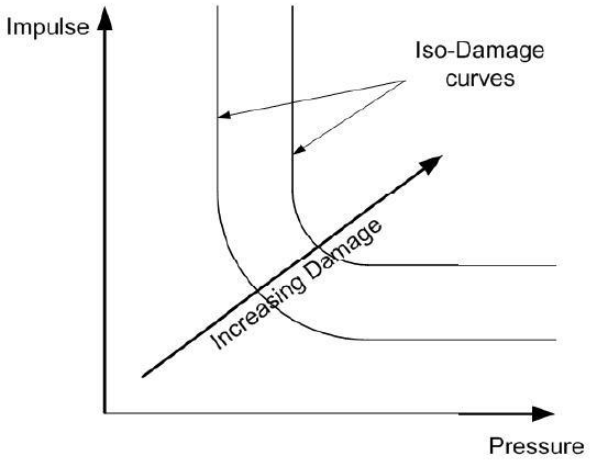

Fig. 5.1. Generic pressure-impulse diagram.

As noted in Fig. 5.1, the horizontal axis deals with impulse values and the vertical axis presents the pressure values. The two asymptotes, one for pressure and one for impulse, define limiting values for each parameter. Loads with very short duration are called impulsive loading and the structural response induced depends on the associated impulse and not the peak pressure. This forms a vertical line that defines the minimum impulse required to reach a particular level of damage, which the curve approaches asymptotically at high pressures. On the contrary, as the load period becomes longer than the natural frequency, the load is considered as quasi-static loading and the response becomes insensitive to the impulse, but very sensitive to the peak pressure. The horizontal asymptote thus represents the minimum level of peak pressure required to reach that particular damage. Oswald and Wesevich [14] conducted an investigation to develop P-I diagrams for non-retrofitted and E-glass retrofitted walls made with concrete masonry units (CMU) submitted to blast loading, based on 236 open-air and shock tube tests. Still, the field is still open as an area of future research to develop reliable and accurate damage criteria.

The present study aims to propose iso-damage curves for different types of typical masonry infill walls in Portugal. First, using the newly developed three-dimensional strain rate dependent plasticity model, the P-I diagrams for the tested masonry infill wall presented in the previous chapter are derived with three different wall thicknesses. Then, performing multiple analyses, the pressure-impulse diagrams are obtained for three different types of typical Portuguese unreinforced masonry infills and one type of masonry infill reinforced with two different reinforcement solutions under different loading conditions.

5.2 ISO-DAMAGE CURVES FOR TESTED MASONRY INFILL WALL

Masonry damage criteria (Table 5.1) are defined by UFC-3-340-02 (2008) (i.e. two levels of damage are defined, namely reusable and non-reusable in accordance with the maximum support rotation of the wall). Then, using the validated model from the previous chapter, the iso-damage curves are derived for the masonry infill by performing simulations of masonry infill subjected to blast loading with different impulses and different reflected over pressures.

Table 5.1. Masonry damage criteria (UFC-3-340-02, 2008) [32].

Element	Yield pattern	Maximum support rotation (º)
Masonry Reusable	One-way	0.5
	Two-way	0.5
Masonry Non-reusable	One-way	1.0
	Two-way	2.0

Three different wall thicknesses of 140 mm, 180 mm, and 230 mm are considered here composed of one single leaf brick with different thicknesses of 110 mm, 150 mm and 200 mm, with two layers of M5 plaster on both sides with a total thickness of 30 mm. Even if plaster is not normally considered in structural masonry applications, for an accidental load such as blast, it seems reasonable to consider it. In numerical modeling, the applied load is modeled with triangular shape pressure-time history with peak pressure at the beginning, decay during the positive phase, and stops acting after t_d, see Fig. 4.31.

The P-I diagrams for three different wall thicknesses are shown in Fig. 5.2. The damage curves of the panel in case of the three different wall thicknesses, for each damage level, are given in Fig. 5.3. As noted, for each damage level, increasing the wall thickness, the damage curve moves further from the origin. Additionally, the difference between the damage levels grows by increasing the wall thickness, and the difference is more significant in quasi-static loading than the dynamic loading and impulsive loading sections. According to developed P-I diagrams, the tested masonry infill wall with thickness of 140 mm is severely devastated and considered non-reusable under the blast with reflected overpressure of 175 kPa and impulse of 3 kPa.s while this wall with thickness of 180 mm under the same loading conditions is seriously damaged but taken into account as reusable. Furthermore, the masonry infill wall with the

thickness of 230 mm is slightly damaged and even does not violate the reusable damage level under the same loading conditions.

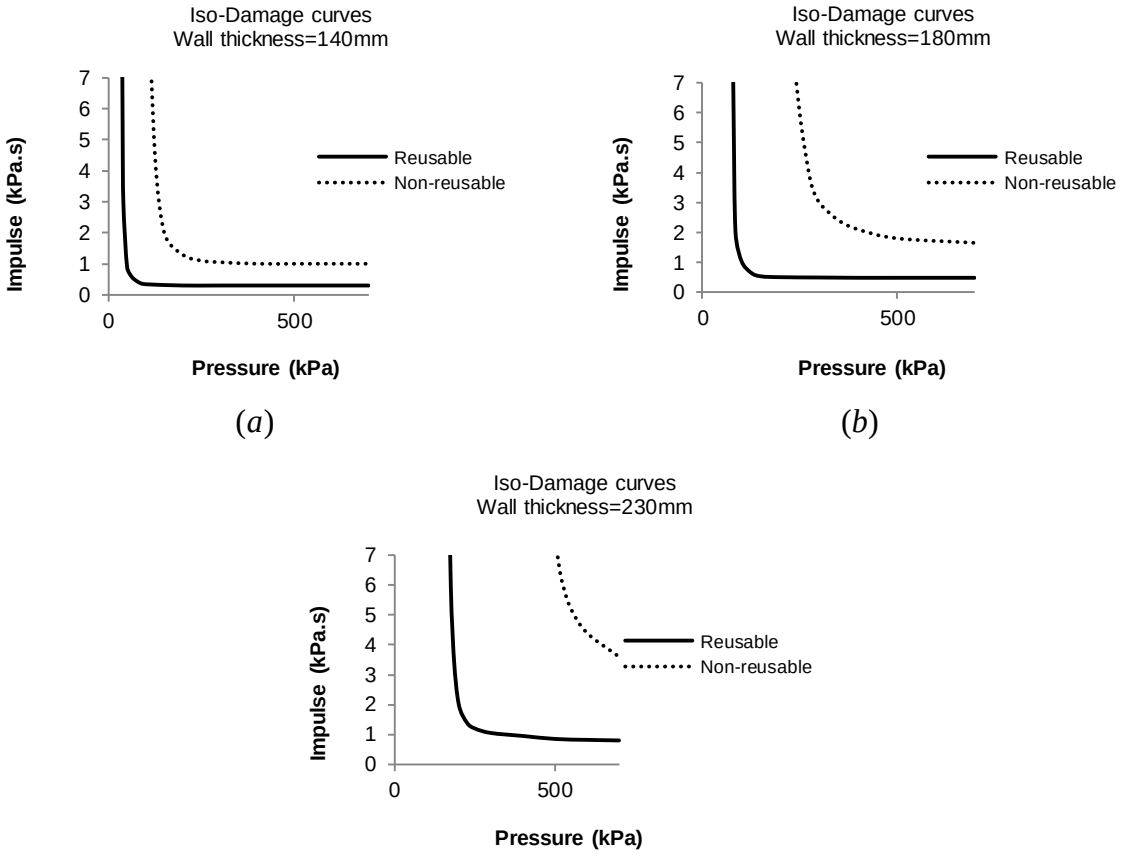

Fig. 5.2. P-I diagram for the wall: (a) 140 mm; (b) 180 mm; (c) 230 mm.

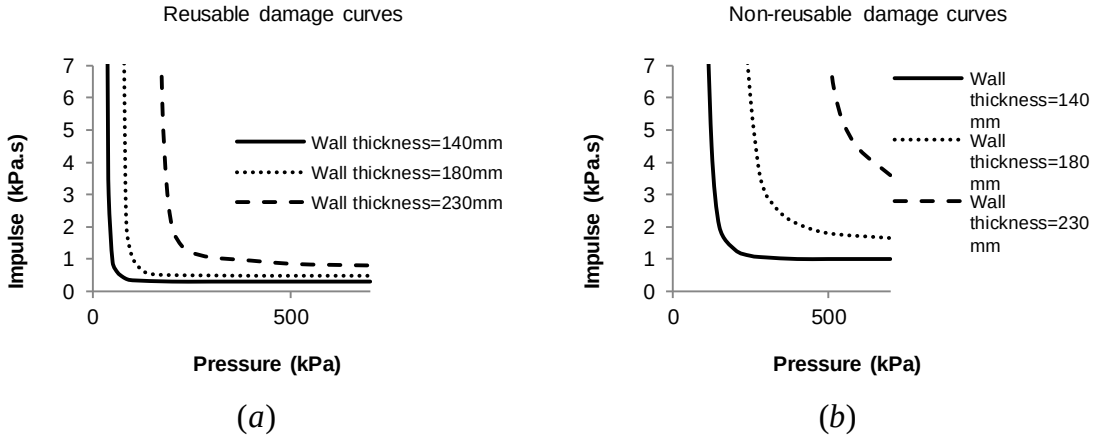

Fig. 5.3. The comparative P-I diagrams between three different wall thicknesses for the wall: (a) Reusable; (b) Non-reusable.

5.3 P-I DIAGRAMS FOR TYPICAL PORTUGUESE MASONRY INFILLS

5.3.1 Unreinforced masonry infills

The three most typical Portuguese masonry infill walls are considering in the present study, [51]. The three brickwork masonry infills are labeled A, B and C, and have clear size of $4.5\times3m$, $4.2\times3m$, and $5.8\times3m$, respectively. The wall A is a solid wall with no openings, while the wall B has one opening, and the wall C has two openings, see Fig. 5.4.

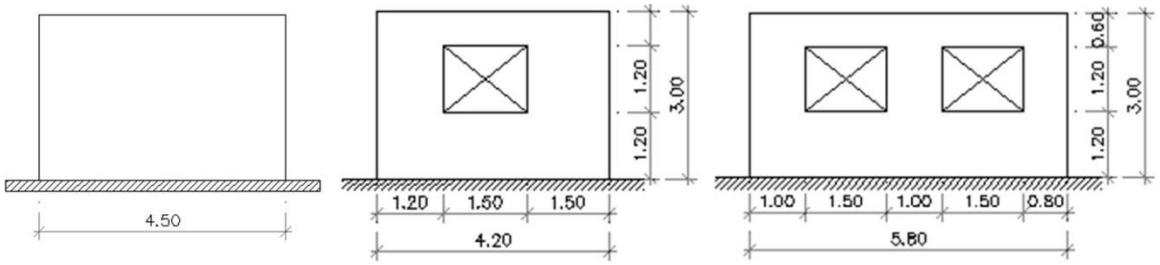

(*a*) (*b*) (*c*)

Fig. 5.4. Geometry of three different types of masonry infill walls subjected to blast loading: (a) Type A; (b) Type B; (c) Type C [51].

The hollow clay tiles with dimensions of $30\times20\times11cm$, $30\times20\times15cm$, and $30\times20\times20cm$ are assumed in a single leaf brick inside the concrete frames. Even if most enclosures are double leaf, they are often not connected or are weakly connected. Therefore, for each type of masonry infill, three different thicknesses of 110 mm, 150 mm, and 200 mm are studied, making a total of nine different masonry infills. As usual in structural design, the influence of plaster, if any, is not considered here. A total of nine different masonry infills are involved in this part of study, with three different geometries and three different thicknesses. For developing the P-I diagrams for each masonry infill, several simulations of the wall subjected to blast loading with different levels of pressures and impulses are performed. The triangular shape applied pressure-time history involved in numerical modeling is given in Fig. 4.31. The proposed anisotropic continuum model is applied here to represent the orthotropic masonry behavior. The quasi-static material properties for masonry derived by Pereira [49] are adopted as input parameters in numerical simulations and given in Table 5.2 and Table 5.3. The expressions for DIFs obtained by Pereira [16] are used to apply the high strain rate effects to enlarge the composite yield surface.

Table 5.2. Elastic material properties for masonry infill walls.

Elastic properties			
E_x *(GPa)*	E_y *(GPa)*	E_z *(GPa)*	υ
2.00	1.81	4.43	0.2

Table 5.3. Inelastic material properties for masonry infill walls.

Tension						**Compression**						
f_{tx} *(MPa)*	f_{ty} *(MPa)*	f_{tz} *(MPa)*	G_{ftx} *(N/m)*	G_{fty} *(N/m)*	G_{ftz} *(N/m)*	f_{mx} *(MPa)*	f_{my} *(MPa)*	f_{mz} *(MPa)*	G_{fcx} *(N/m)*	G_{fcy} *(N/m)*	G_{fcz} *(N/m)*	k_p
0.340	0.100	0.385	8.2	1.2	11.2	1.75	1.50	3.85	2000	2400	6160	0.93E-3

Similar boundary conditions are assumed as in previous infill simulation, and the only the masonry panel constrained at four edges is simulated. Again, a regular fine mesh of cubic elements with reduced integration is used in numerical analysis. The adopted finite element schemes of the three different types of walls with thickness of 150 mm are presented in Fig. 5.5.

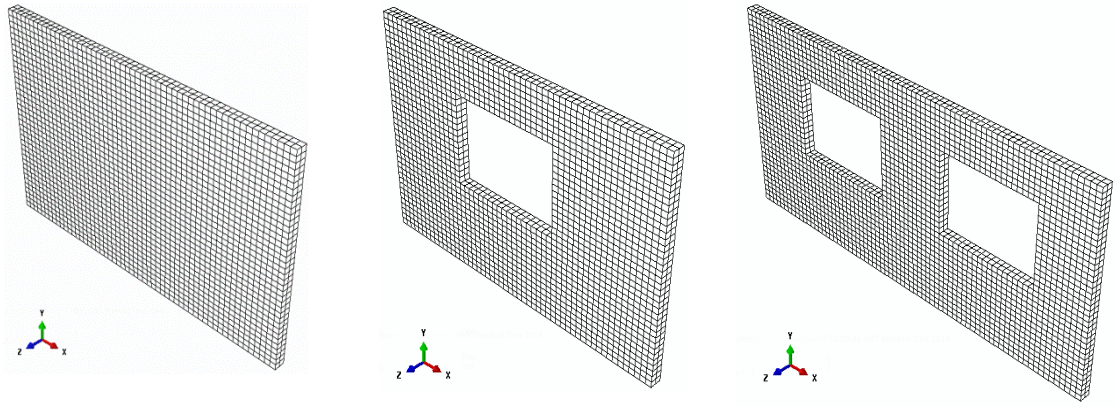

(*a*) (*b*) (*c*)

Fig. 5.5. Adopted finite element scheme of the wall with thickness of 150 mm: (a) Type A; (b) Type B; (c) Type C.

Fig. 5.6 shows the obtained pressure-impulse diagrams of panel type A with different wall thicknesses under study. Moreover, the comparative P-I diagrams between three different wall thicknesses for the wall type A at both levels of damage are given in Fig. 5.7. As expected, the panel with higher thickness is able to accommodate somewhat larger loading profiles and have the non-reusable and the reusable curves further away. Regarding Fig. 5.7, for each damage level, the differences between the diagrams become clearer by increasing the wall thickness, and the differences are much more significant in quasi-static loading, when compared with the dynamic loading and impulsive loading sections.

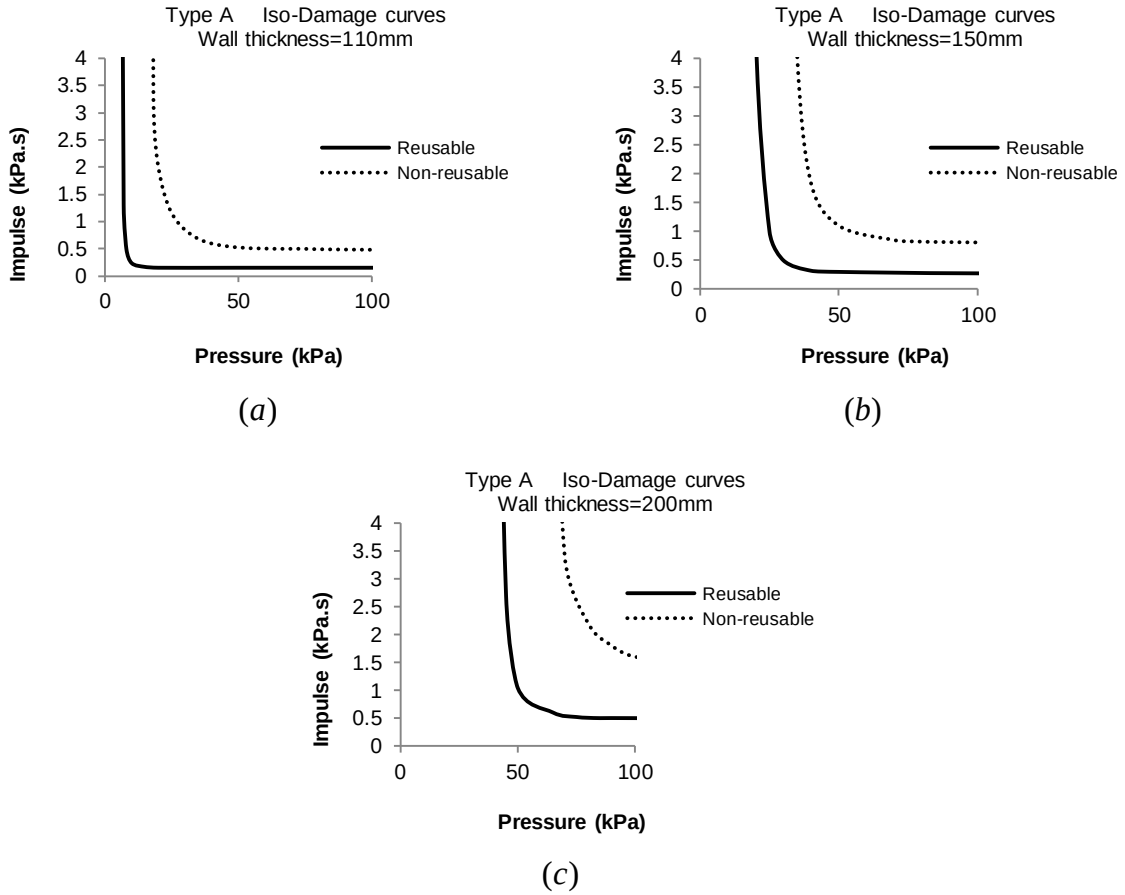

Fig. 5.6. P-I diagram for the wall type A: (a) 110 mm; (b) 150 mm; (c) 200 mm.

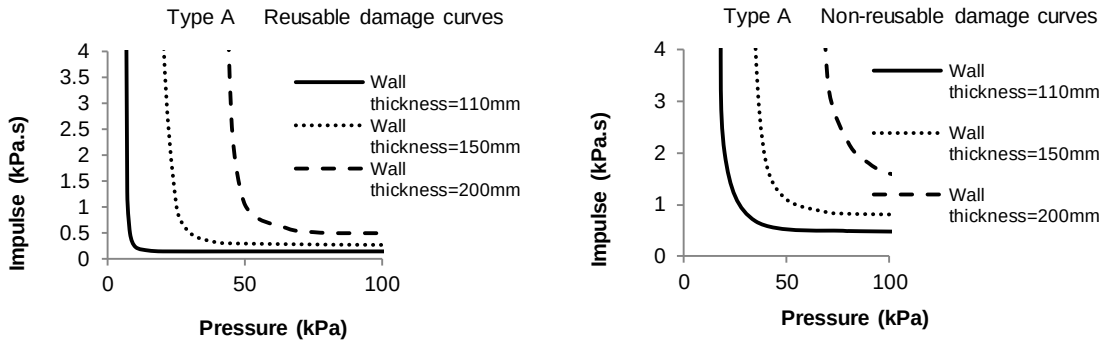

(*a*) (*b*)

Fig. 5.7. The comparative P-I diagrams between three different wall thicknesses for the wall type A: (a) Reusable; (b) Non-reusable.

The obtained pressure-impulse diagrams of panel type B and type C with different wall thicknesses are shown in Fig. 5.8 and Fig. 5.9, respectively.

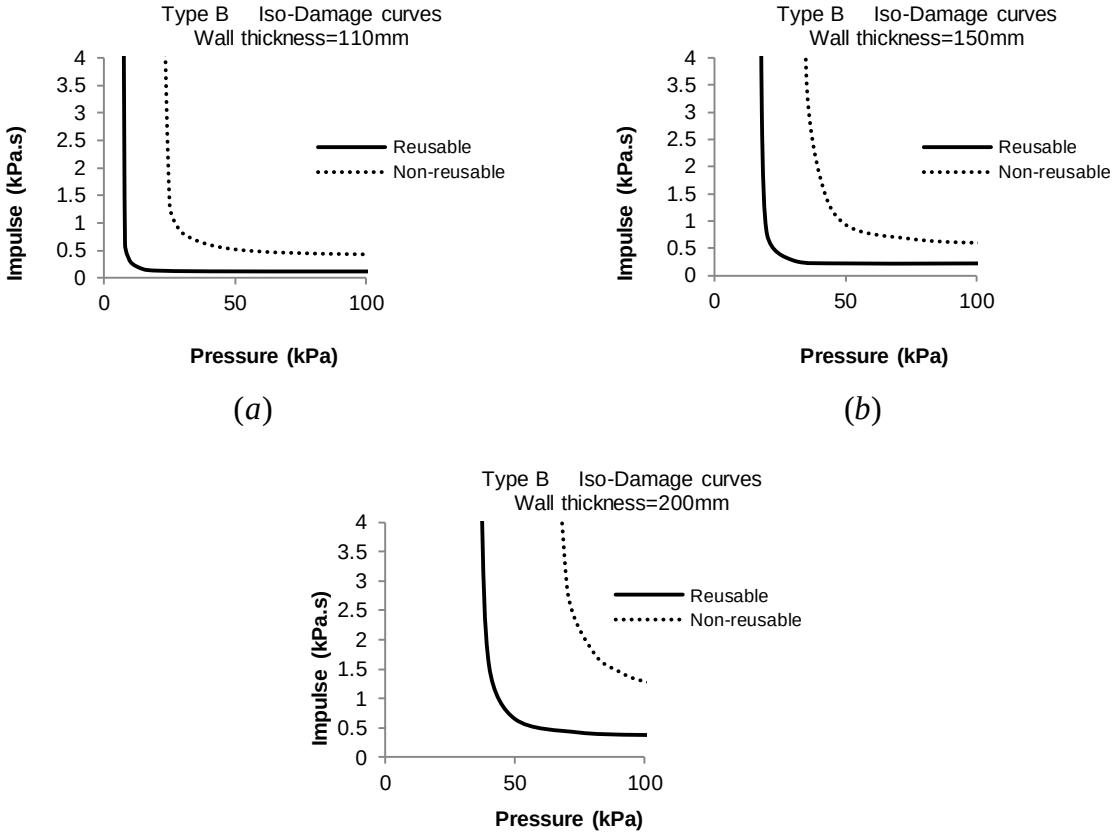

(*a*) (*b*)

(*c*)

Fig. 5.8. P-I diagram for the wall type B: (a) 110 mm; (b) 150 mm; (c) 200 mm.

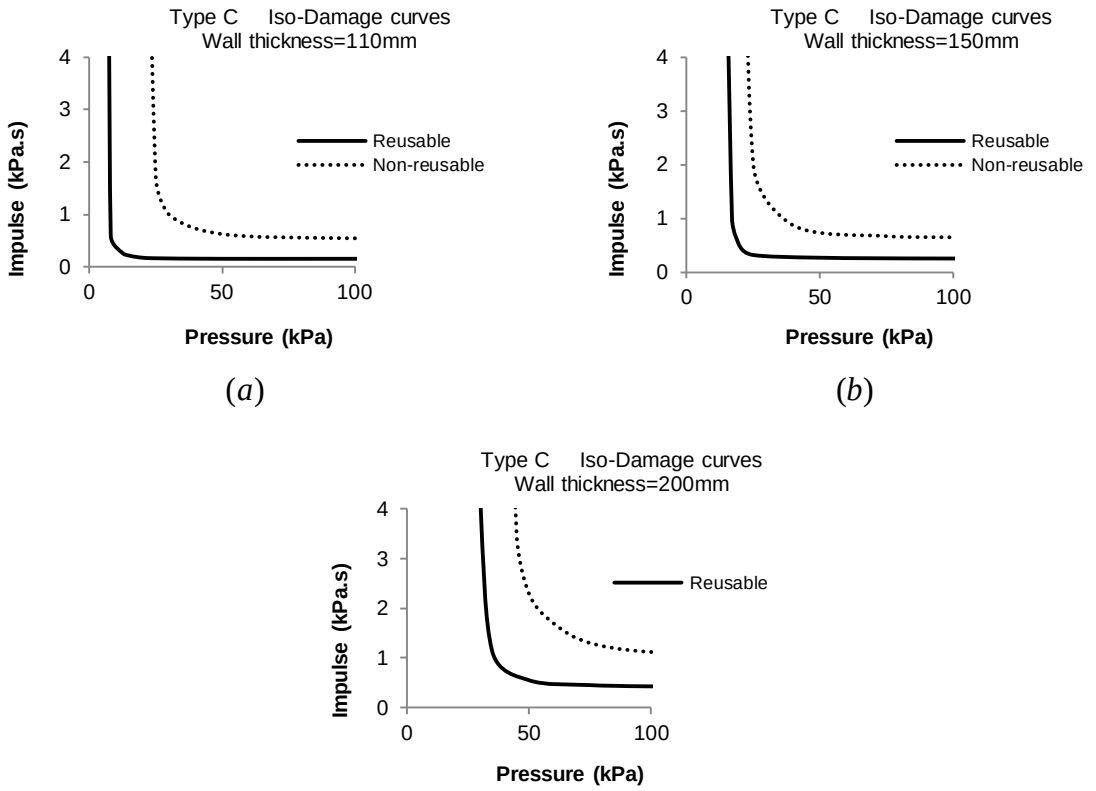

Fig. 5.9. P-I diagram for the wall type C: (a) 110 mm; (b) 150 mm; (c) 200 mm.

Also, the comparative P-I diagrams between three different wall thicknesses for the wall type B and C at both levels of damage are given in Fig. 5.10 and Fig. 5.11.

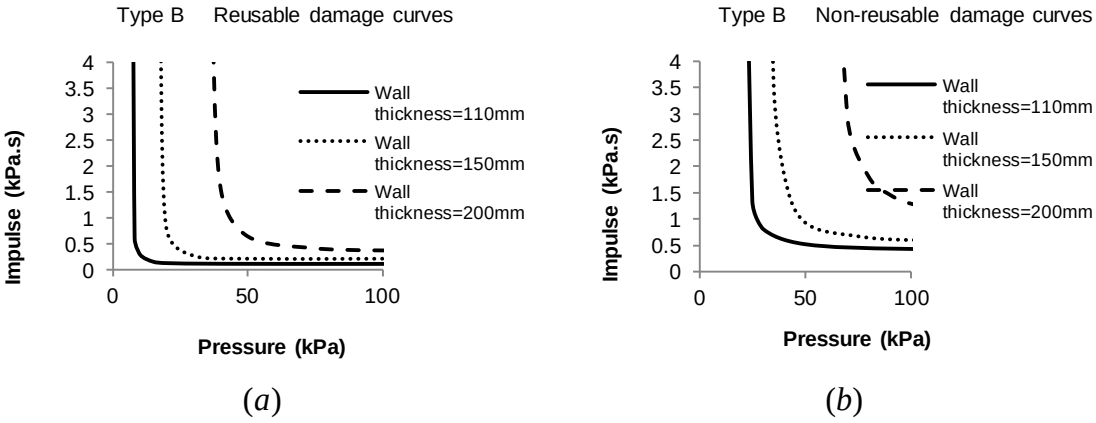

Fig. 5.10. The comparative P-I diagrams between three different wall thicknesses for the wall type B: (a) Reusable; (b) Non-reusable.

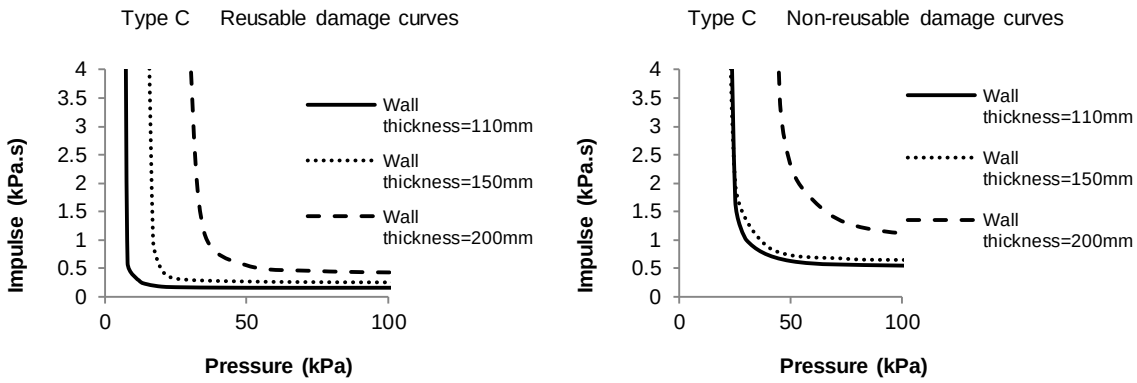

(*a*) (*b*)

Fig. 5.11. The comparative P-I diagrams between three different wall thicknesses for the wall type C: (a) Reusable; (b) Non-reusable.

As shown, for the walls type B and C, at smaller thicknesses, increasing the wall thickness changes the damage levels slightly, while for higher thickness, it moves the damage levels further away; however, the differences between the P-I diagrams are less apparent.

The P-I diagrams are compared as well between the three wall types for three wall thicknesses at both damage levels, see Fig. 5.12 to Fig. 5.14. For the wall thicknesses of 110 mm and 150 mm, no noticeable change is noticed between the P-I diagrams of three wall types for both damage levels, while the changes between the iso-damage curves of three types of wall are significant for the wall thickness of 200 mm at non-reusable level, much more than the reusable level.

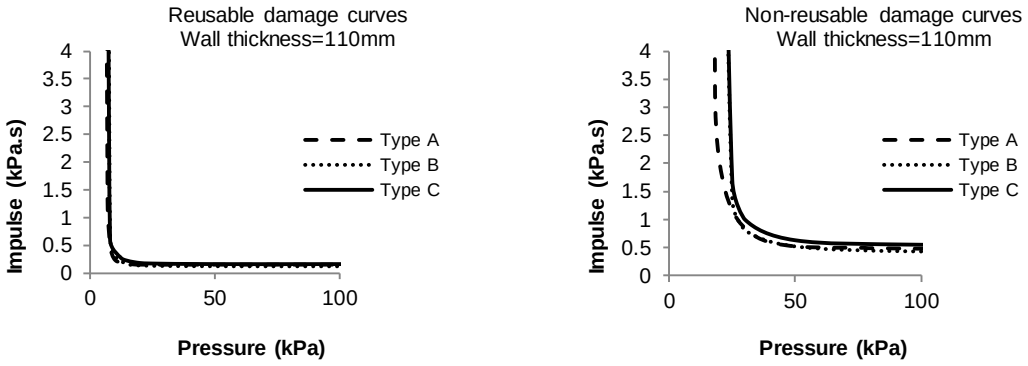

(*a*) (*b*)

Fig. 5.12. The comparative P-I diagrams between the three wall types for the wall thickness of 110 mm: (a) Reusable; (b) Non-reusable.

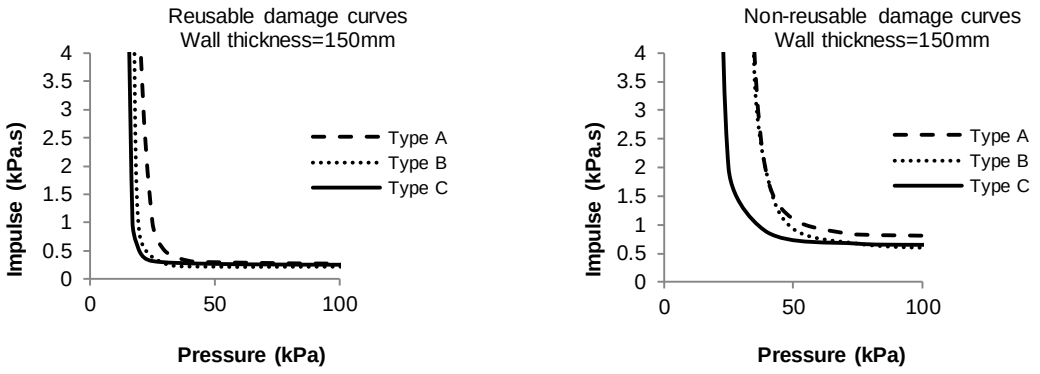

(*a*) (*b*)

Fig. 5.13. The comparative P-I diagrams between the three wall types for the wall thickness of 150 mm: (a) Reusable; (b) Non-reusable.

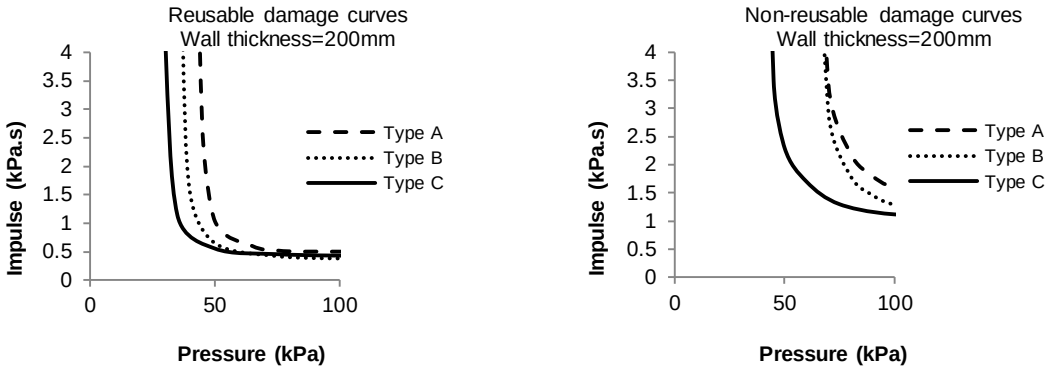

(*a*) (*b*)

Fig. 5.14. The comparative P-I diagrams between the three wall types for the wall thickness of 200 mm: (a) Reusable; (b) Non-reusable.

5.3.2 Reinforced masonry infills

The reinforcement solutions are normally used in construction of different structures like masonry and concrete to improve their seismic responses including the ductility and energy dissipation, and prevent the structural collapse at large deflections. Two different masonry reinforcement solutions are involved in present study to obtain P-I diagrams for reinforced masonry infill walls. These reinforcement solutions have been also used previously for explosive action mitigation, see e.g. [16]. Although it is possible to make a thicker wall using a large amount of reinforcement to reach the desirable performance, this study aims to have the thinnest possible wall reinforced with minimum amount of reinforcement. Hence, the unreinforced wall type A (solid) with no openings and thickness of 110 mm is adopted for this study. The first solution, namely JAR is a

prefabricated bed joint reinforcement using the BEKAERT MURFOR RND 4/50 to increase the strength of masonry and the integrity of construction. JAR solution consists of two parallel wires with a clear distance of 50 mm from each other. The parallel wires are embedded in every two horizontal joints, see Fig. 5.15. Each wire has a cross section area of 12.57 mm^2. The distance between each wire and the closest wall surface is selected equal to 30 mm which should be more than or equal to 20 mm.

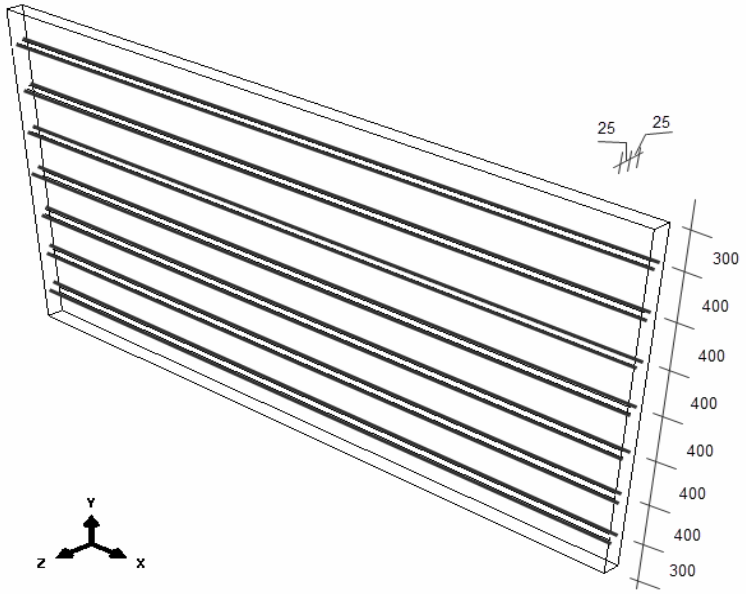

Fig. 5.15. Geometry of the BJR reinforcement solution

The second solution, namely RAR is an external reinforcing mesh using BEKAERT – ARMANET ϕ1.05 mm 12.7×12.7 mm. Two reinforcement grids with a clear distance of 120 mm are embedded in both sides of the wall in plaster layers with a total thickness of 30 mm. Due to large computational cost dealing with the large number of grid elements, the original solution is not used and instead the grid size is changed resulting in significant analysis time. Therefore, an equivalent reinforcement grid is adopted here, composed of reinforcement bars with cross section areas of 3.46 mm^2 and openings with clear size of 88.9×88.9 mm, see Fig. 5.16. For each solution, the reinforcement is discretized with 2-node linear 3D truss elements in numerical analysis. The elastic-perfectly plastic model is attributed to the truss elements to simulate the reinforcement behavior.

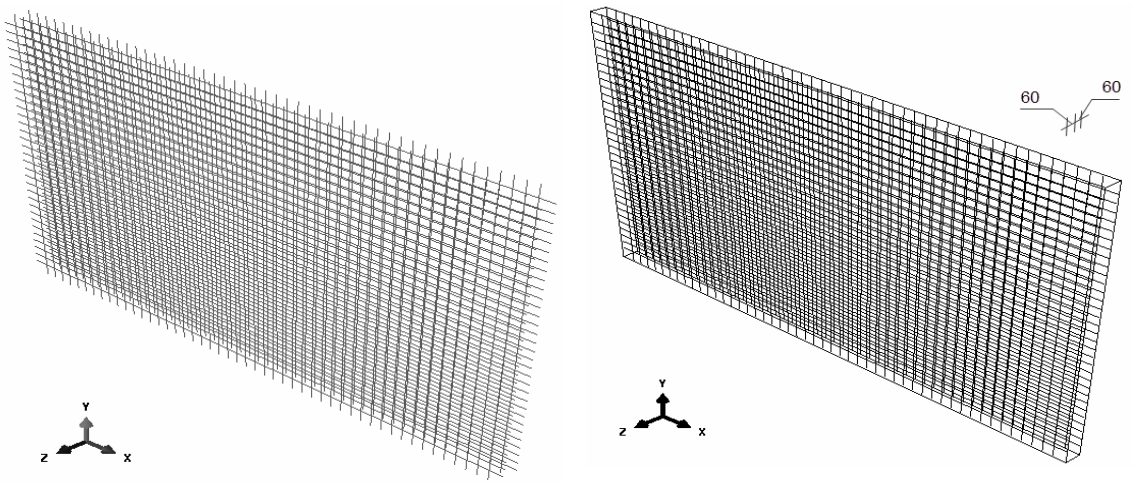

(*a*) (*b*)

Fig. 5.16. EMR reinforcement solution: (a) geometry ; (b) reinforcement grid

The static mechanical characteristics of reinforcement are given in product datasheets, see ANNEX A. Since no information was reported on high strain rate mechanical properties of reinforcement, a DIF of 1.23, recommended by UFC-3-340-02, (2008) for tensile strength of reinforcement steel is used, [32]. The material properties of reinforcement are presented in Table 5.4.

Table 5.4. Material properties of reinforcement and DIFs.

Parameter	**static**	**DIF**
f_y *(MPa)*	320	1.23
E (GPa)	210	1

The P-I diagrams for the solid wall reinforced with two different reinforcement solutions are shown in Fig. 5.17. As expected, involving the reinforcement solutions shifts damage levels further away from the origin for both solutions. It means that the wall is able to more resist against high intensity impulsive loading.

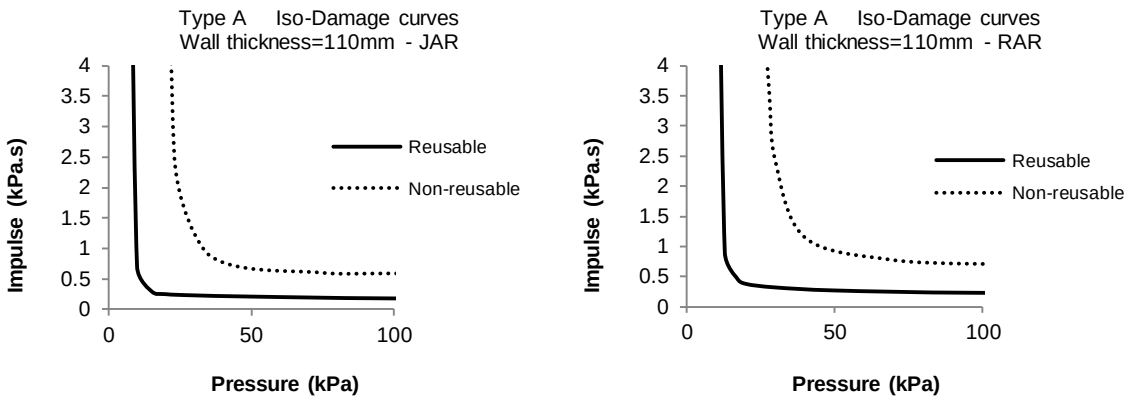

(*a*) (*b*)

Fig. 5.17. The P-I diagrams for the reinforced masonry infill wall: (a) bed joint reinforcement; (b) external reinforcement mesh.

However, when referring to Fig. 5.18, in case of using the JAR solution, no advantages can be considered for such weak masonry infill with large panel given a very slight change on the reusable level. The results for the RAR solution are much better than the bed joint reinforcement. As a result, excluding the price factor, the external reinforcement mesh is preferred to reinforce the masonry infill walls in case of large impulsive loading. URM is the abbreviation of unreinforced masonry wall.

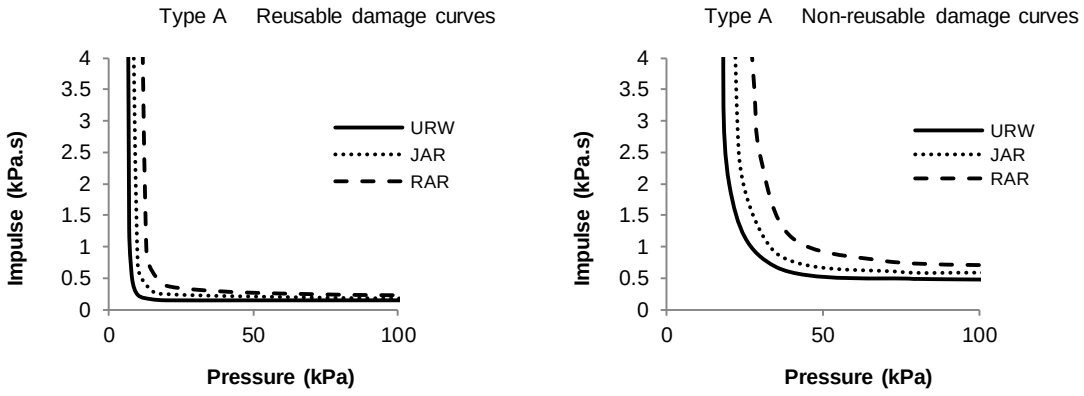

(*a*) (*b*)

Fig. 5.18. The comparative P-I diagrams between different reinforcement solutions: (a) Reusable; (b) Non-reusable.

Additionally, for each damage level, the differences between the damage curves become more significant in quasi-static loading than the dynamic loading and impulsive loading regimes.

According to developed P-I diagrams, the unreinforced masonry infill wall and the one reinforced with JAR solution is severely devastated and considered non-reusable under the blast with reflected overpressure of 35 kPa and impulse of 1 kPa.s while the wall reinforced with RAR solution under the same loading conditions is seriously damaged but taken into account as reusable.

5.4 FINAL REMARKS

The present study addresses the pressure-impulse diagrams for different types of typical masonry infill walls with three different thicknesses. Using a novel dynamic anisotropic plasticity model in FE code ABAQUS, several numerical simulations of the tested masonry infill under blast with different pressures and impulses are carried out to obtain P-I diagrams over a wide range of strain rate. Then, a large number of analyses are performed to develop the iso-damage curves for three different types of typical Portuguese masonry infills under blast with various loading conditions. It is noted that the thicker panel is able to accommodate somewhat larger loading profiles and have the iso-damage curves further away. Additionally, for the wall type A (solid), for each damage level, the differences between the P-I diagrams of wall thicknesses become clearer by increasing the wall thickness, and the differences are more significant in quasi-static loading than in the dynamic and impulsive loading sections. For the walls type B(one window opening) and C (two windows opening), at lower thicknesses, increasing the wall thickness changes the damage levels slightly, while for higher thickness, it moves the damage levels further away. Also, it can be concluded that the changes between the iso-damage curves of three types of wall are significant for the wall thickness of 200 mm at non-reusable level, much more than the reusable level. Finally, performing multiple analyses, the pressure-impulse diagrams are obtained for the wall type A reinforced with two different reinforcement solutions under different loading conditions. As expected, involving the reinforcement solutions shifts damage levels further away from the origin for both solutions, but the results for the external reinforcement mesh solution are much better than the bed joint reinforcement, and excluding the price factor, the external reinforcement mesh is considered more preferable to reinforce the masonry infill walls in case of large impulsive loading.

Chapter 6

6 ENGINEERING APPLICATION: CASE STUDY- "AL-ASKARI" HOLY SHRINE IN SAMARRA, IRAQ

6.1 INTRODUCTION

The concept of terrorism is controversial. Political and emotional reasons raise complexities in its precise definition. In general, terrorism is defined as a pre-planned, deliberate and criminal act of violence against targets including civilians, infrastructures, public services, and information, by militant hardline subnational forces usually seeking to create terror and influence the people, and perpetrated for a religious, political, or ideological goal. Depending upon the detonating charge weight, blast site situation and site crowd, the terrorist attacks can bring a wide range of casualties and material losses. Nearly, 12 000 deaths were reported by terrorist attacks in 2011. Over 50 percent of them were civilians and unfortunately 755 of victims were children [52]. Recently, due to the political issues, religious conflicts, and instability of the region, a number of militant hardline forces such as AL-QAEDA and ISIS have been announced

in Middle East and settled mainly in Afghanistan, Iraq, Pakistan and Syria, resulting in rising terrorism and violence in this region, and also Europe. It is worth to mention that the aforementioned militant groups have been conducting a series of suicide bombings as one of the most frequently used terrorist attack types against historical holy shrines, and different cultural heritage sites in Middle East.

The main objective of this study is to demonstrate the possibility of advanced numerical tool for the analysis of full masonry structures under blast load, as a means to understand damage and loading level, assess residual capacity, assess vulnerability and define strengthening measures. Needless to say, an example of how the models can be used to solve real engineering problems is a valuable complement for this study. In this chapter, full-scale numerical simulation of one prominent target in case of religious conflict, namely Al-Askari holy shrine, a world cultural heritage site located in Samarra, Iraq is carried out to present an engineering application of the continuum model developed. In order to extend the application to practice, two different scenarios are also considered to study possible damages of the shrine under terrorist attacks with different loading conditions.

6.2 DESCRIPTION OF THE CASE STUDY

The Islamic cultural heritage site of Al-Askari holy shrine is situated in Samarra, 125 km from Baghdad, in Iraq surrounded by the ancient city walls of Samarra. The Al-Askari shrine is home to the burial chambers of Ali al-Hadi and Hassan al-Askari, the 10^{th} and 11^{th} of Shi'a Imams, respectively. Considered as one of the Shi'a holiest shrines in the world, it has become a popular pilgrimage destination for millions of religious visitors seeking the intercession of the Imams. The site built in 944 A.D includes historic building with surrounding walls on all sides and was constructed with adobe bricks bond by mud mortar at head and bed joints. Besides the main building, there are two minarets on the left and east side of the North façade and a dome located at the top of the building, see Fig. 6.1. No information was available in literature regarding the geometry of dome and minarets except the diameter of the dome which was reported by Northedge [53]. Hence, in this study, several geometrical parameters used in Imam Ali shrine in Najaf, Iraq must be estimated. The minarets have the height of 31 m from the base with the thickness of 0.4 m and variable diameter of 4 m to 3 m along the height from the bottom.

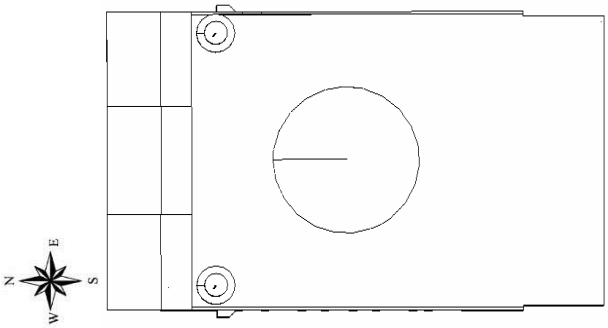

(*a*)

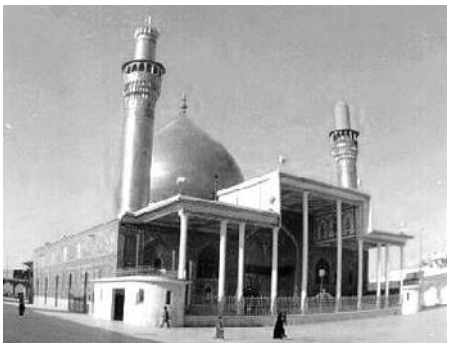

(*b*)

(*c*)

Fig. 6.1. The Al-Askari holy shrine: (a) top view schematic; (b) North and East facades; (c) South and West facades.

The most complex structural part to build was the bulbous type discontinuous double-shell dome. The dome has three main components, namely external shell, internal shell, and drum [54]. The external shell is what appears from outside. The instructions provided by Ashkani et al. [54] are followed to draw the complex external shell geometry, see Fig. 6.2.

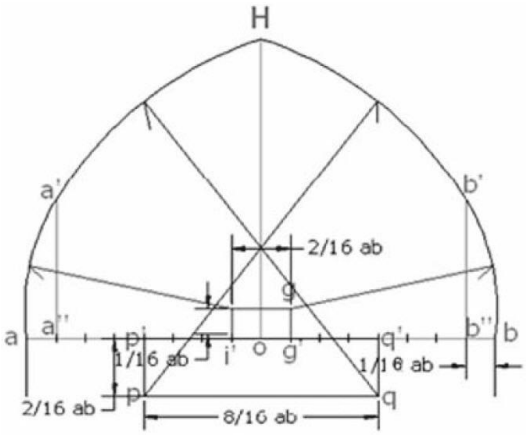

Fig. 6.2. Geometry of bulbous shape external shell [54].

This dome has a height of 16 m, an exterior diameter of 16.3 m and variable thickness of 0.8 m to 0.2 m from its base to the tip to decrease the weight of the shell, see Fig. 6.3(a). Comparing to the external shell, the internal shell has a simpler geometric shape to cover the internal chamber. It has a height of 5 m and an exterior diameter of 14.6 m. The thickness also varies from 0.6 m at its bottom to 0.15 m in the tip, see Fig. 6.3(b). The drum is located beneath the shells with 12 openings with a height of 5 m and a large thickness of 1.45 m to transfer and neutralize the forces from the shells to the lower parts. Each opening has a size of 1.5×2.7 m.

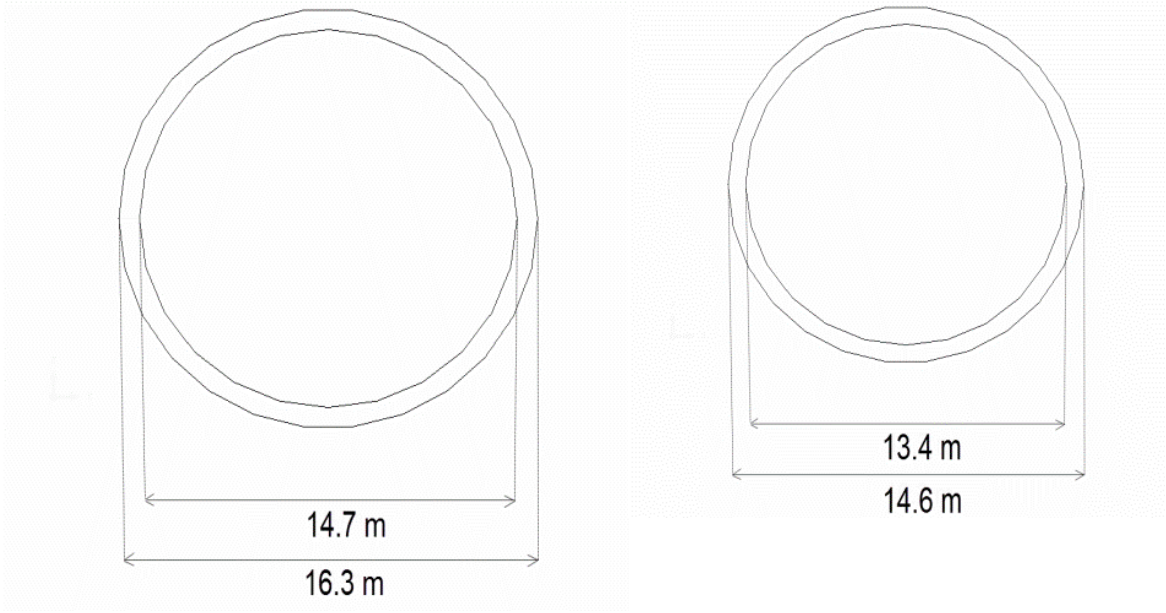

(*a*) (*b*)

Fig. 6.3. Cross section of the shell: (a) external shell; (b) internal shell.

The adopted geometry of the shrine is shown in Fig. 6.4 more in detail. The South façade has a thickness of 0.35 m and a height of 9 m. The East façade consists of two bodies as well as the West facade. The bottom part has the height of 9 m, and the top part has the height 1.5 m, with a thickness of 0.35 m. The North façade has also two bodies with the height of 10.5 m for bottom part and 4 m for upper part.

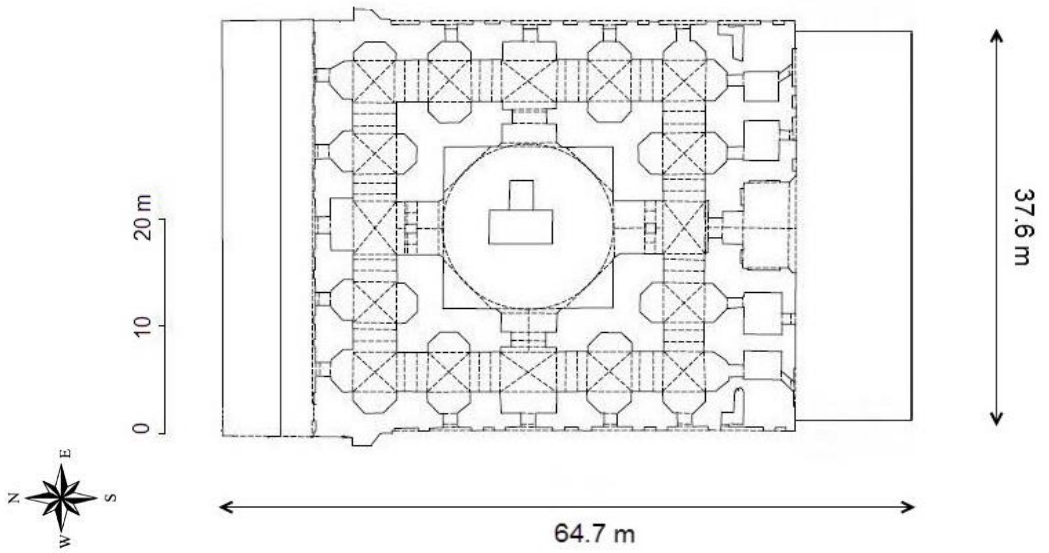

(*a*)

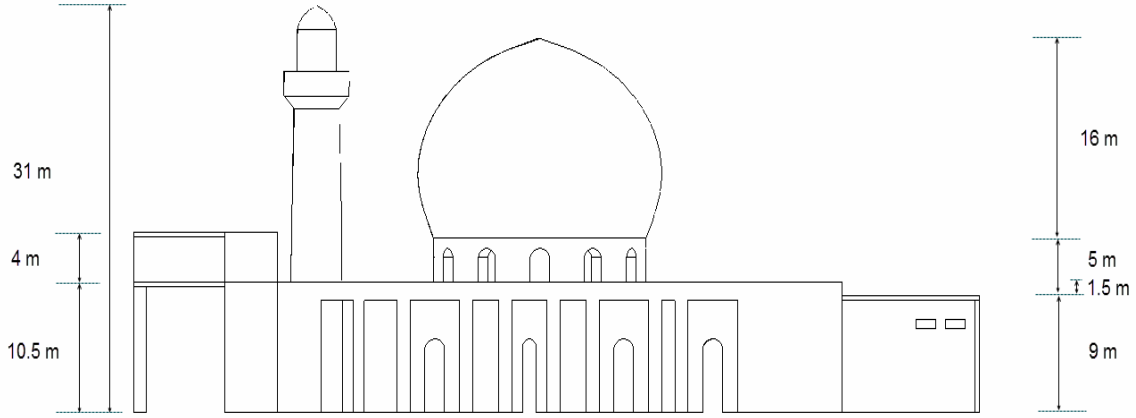

(*b*)

Fig. 6.4. The adopted geometry of Al-Askari shrine: (a) plan [53]; (b) West side view.

The Al-Askari shrine was the target of a terrorist attack using a large quantity of explosive charge (200 kg TNT) placed at the top of the dome in February, 2006 [55], given the easy access and presence of scaffolding during conservation works. In the present study, this terrorist attack refers to the scenario A, see Fig. 6.5. The explosion destroyed the dome due to its weakness to resist the high strain rate very large load. The debris from the entire external dome fell on the roof and damaged it. The external shell was totally destroyed and, approximately, more than the half of the inner dome collapsed inside the mosque, with large pieces scattered on the floor [56]. Also, the detonation significantly devastated the East and West facades, see Fig. 6.6.

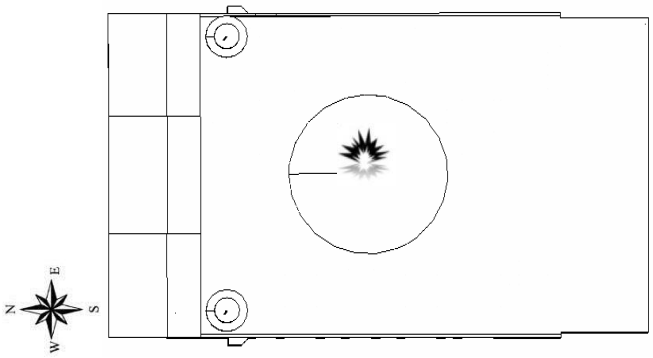

Fig. 6.5. Scenario A - location of the explosive charge.

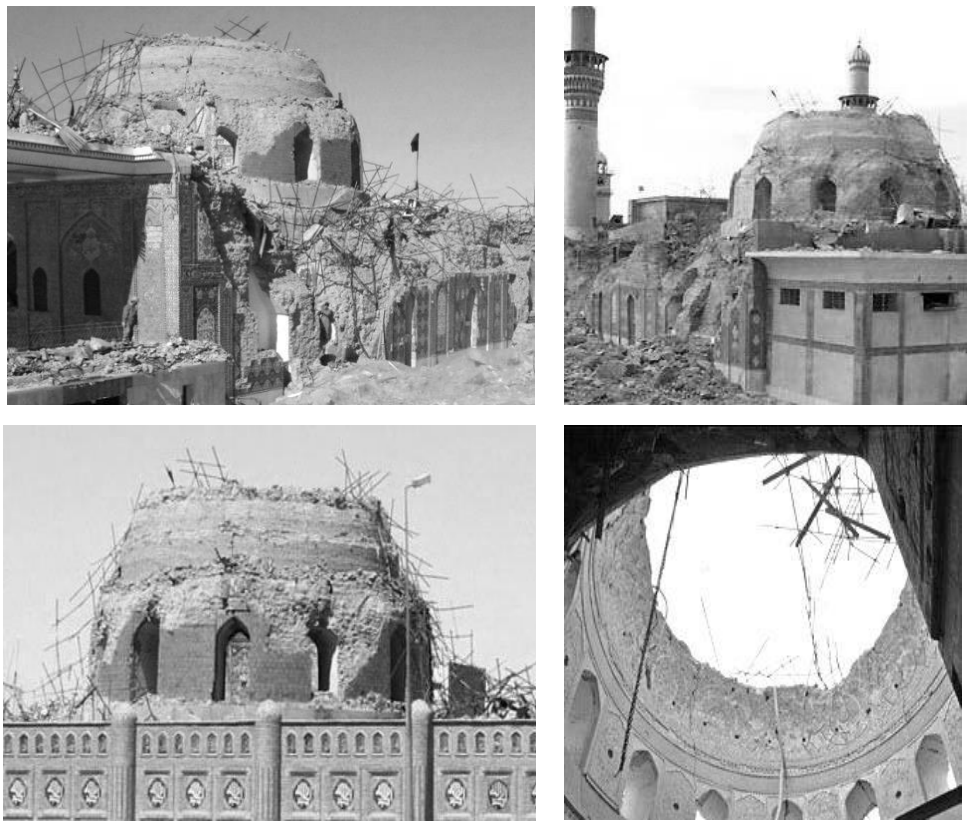

Fig. 6.6. The shrine after the explosion: different views.

Two different scenarios, labeled B and C are considered also to reflect the vulnerability of the mosque subjected to different sources of explosion. Given that the shrine is bordered by walls at all sides and security gates have been stationed after the explosion in 2006, there is a low probability to bring a high capacity of explosive charge such as car or van size close to the shrine. However, in the present study, to extend the engineering application of the model to practice, besides the portable luggage size IED (Improved Explosive Devices) containing 20 kg TNT as delivery system of scenario B, a car size IED with 500 kg TNT is taken into account as delivery system for scenarios

C. The explosions for these extra scenarios are assumed to occur at the West side, 5 m from the façade and at mid-length of it, see Fig. 6.7.

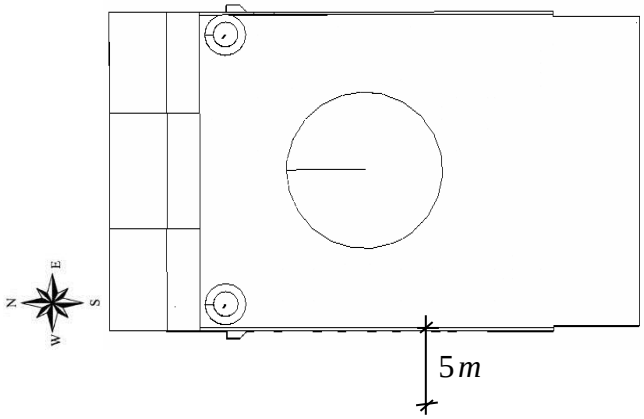

Fig. 6.7. Scenarios B and C - location of three different explosive charges on the West side.

6.3 NUMERICAL MODELLING AND COMPARISON WITH REFERENCE DATA

6.3.1 FE model (mesh and load)

The numerical models are built using the FE code ABAQUS with Explicit solver, as discussed in the chapter 4. Only the structural parts of the mosque are included in analysis and non-structural parts such as glazing systems, frames and occupants are not involved in modeling. The lower ends of the walls are assumed fixed to the ground. All the structural parts are discretized with solid elements. For numerical analysis, the plasticity model is attributed to eight-node linear bricks (reduced integration, hourglass control) and four-node linear tetrahedron to consider the masonry behavior along different material axes. There are a total of 116481 elements in the numerical model of shrine. The shrine schematic and adopted FE scheme of it are presented in Fig. 6.8 and Fig. 6.9. Several damage criteria have been proposed to classify the damage on the masonry panels. The damage criterion defined by UFC-3-340-02 (2008) [32] is adopted in present study to categorize the damage on the unreinforced masonry walls in terms of the maximum support rotation of the wall, see Table 6.1.

Table 6.1. Masonry damage criteria (UFC-3-340-02, 2008) [32].

Element	Yield pattern	Maximum support rotation (º)
Masonry Reusable	One-way	0.5
	Two-way	0.5
Masonry Non-reusable	One-way	1.0
	Two-way	2.0

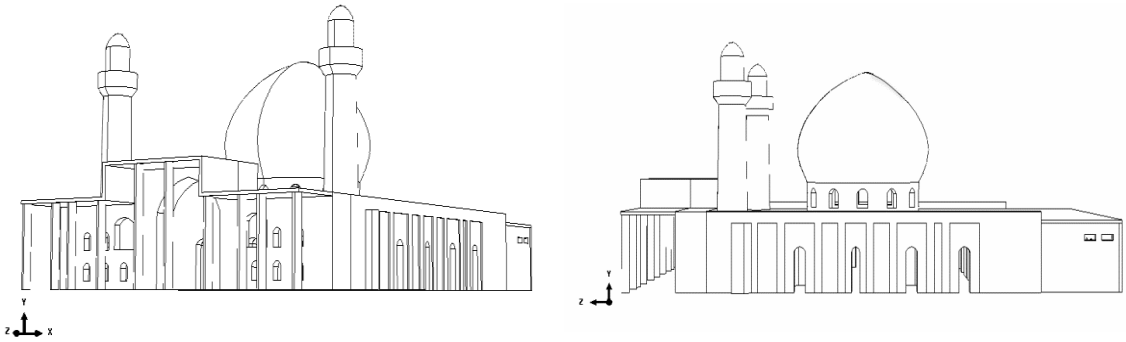

(*a*) (*b*)

Fig. 6.8. Shrine schematic: (a) perspective; (b) West side view.

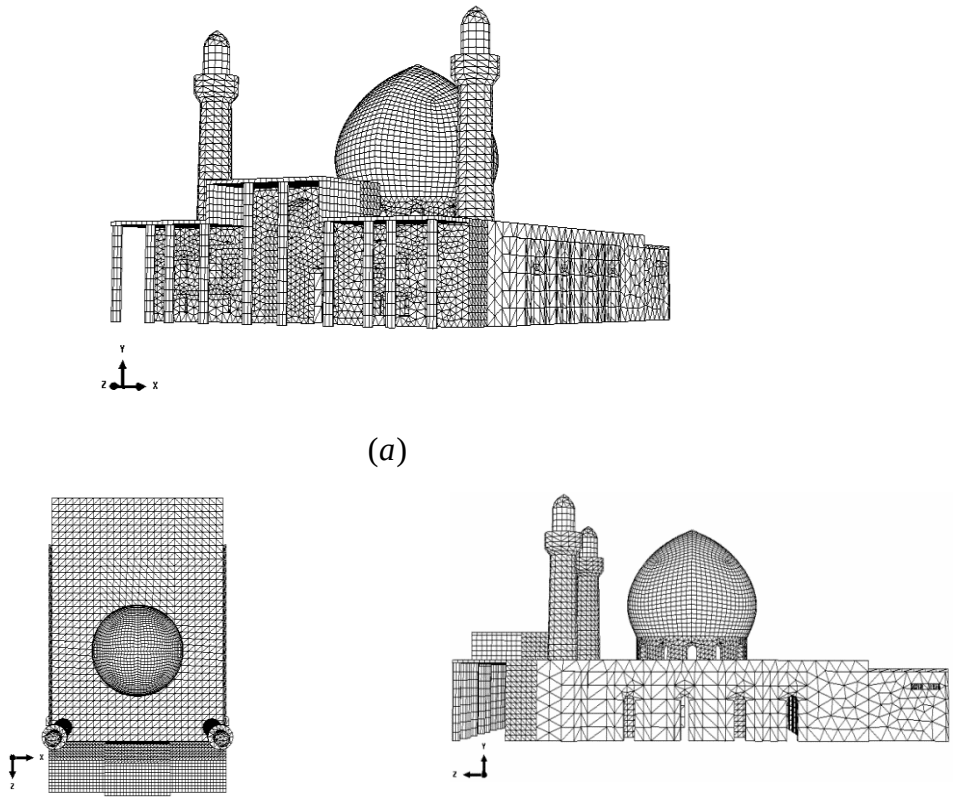

(*a*)

(*b*) (*c*)

Fig. 6.9. Adopted FE scheme of the shrine: (a) perspective; (b) top view; (c) West side view.

No tests have been conducted to characterize the behavior of materials used in shrine construction. Therefore, typical material properties for clay adobe brick and mortar behavior are used, which are reported in literature and widely used [57, 58]. The obtained material properties are introduced as input parameters for local axes in numerical simulations, see Table 6.2 and Table 6.3. The subscripts *x*, *y*, *z* refer to the material axes along the horizontal, vertical and thickness directions, respectively. The expressions for DIFs obtained by Pereira [16] are also used to provide the strain rate dependency of the composite yield surface.

Table 6.2. Elastic material properties for Al-Askari shrine [57, 58].

Elastic properties			
E_x *(GPa)*	E_y *(GPa)*	E_z *(GPa)*	υ
0.812	1.450	0.812	0.2

Table 6.3. Inelastic material properties for Al-Askari shrine [57, 58].

Tension						**Compression**						
f_{tx} *(MPa)*	f_{ty} *(MPa)*	f_{tz} *(MPa)*	G_{ftx} *(N/m)*	G_{fty} *(N/m)*	G_{ftz} *(N/m)*	f_{mx} *(MPa)*	f_{my} *(MPa)*	f_{mz} *(MPa)*	G_{fcx} *(N/m)*	G_{fcy} *(N/m)*	G_{fcz} *(N/m)*	k_p
0.120	0.025	0.120	2.88	0.30	2.88	0.812	1.450	0.812	1300	2320	1300	0.67E-3

Keeping the problem as pure Lagrangian formulation, the blast loads are applied as pressure profiles. This study adopts the expressions below to estimate the pressure profile parameters such as side-on overpressure, P_{so}, reflected overpressure, P_r, positive phase duration, t_d, and blast wave front velocity, *U*, to calculate the arrival time using the scaled stand-off distance, $Z = \frac{R}{W^{1/3}}$, and charge weight, *W*. The definition of blast loading and blast calculation is thoroughly addressed in chapter 2.

$$P_{so} = \frac{1772}{Z^3} - \frac{114}{Z^2} + \frac{108}{Z} \tag{6.1}$$

$$P_r = 2P_{so}\left\{\frac{7P_o + 4P_{so}}{7P_o + P_{so}}\right\} \tag{6.2}$$

$$\frac{t_d}{W^{\frac{1}{3}}} = \frac{980(1+(Z)^{10})}{(1+\left(\frac{Z}{0.02}\right)^3)(1+\left(\frac{Z}{0.74}\right)^6)\sqrt{1+\left(1+(\frac{Z}{6.9})^2\right)}} \tag{6.3}$$

$$U = \sqrt{\frac{6P_{so} + 7P_o}{7P_o}}.a_o \tag{6.4}$$

Here, P_o denotes the atmospheric pressure, which is equal 1 bar, a_o is the ambient sound velocity and is equal to 343 m/sec in dry air at 20 °C and *R* is stand of distance. Owing to the large size of the mosque and its long length, different pressure profiles are defined to apply on different zones in order to keep the blast load distribution close to reality. For scenario A, eight zones (*P*1, *P*2, *P*3, *P*4, *P*5, *P*6, *P*7 and *P*8), having different stand-off distances (*R*1, *R*2, *R*3, *R*4, *R*5, *R*6, *R*7 and *R*8) are defined, see Fig. 6.10. Regarding the North, South, East and West sides, the stand-off distances is measured at one meter distance from the edge into the surface itself [59]. Throughout the façades, the pressure profiles are taken into account as constant (*P*5, *P*6 and *P*7). As the explosive charge was exactly located on the dome, the stand-off distances of the zones related to the dome need to be assumed. Here, the *R*1 and *R*2 are assumed equal to 11 m and 20 m, respectively. For each zone, the pressure profile is calculated using the relative charge weight, *W*, and stand-off distance, *R*, that acts on it, see Fig. 6.11. The maximum pressure obtained is almost 1 MPa and highly depends on the distance from the explosive charge.

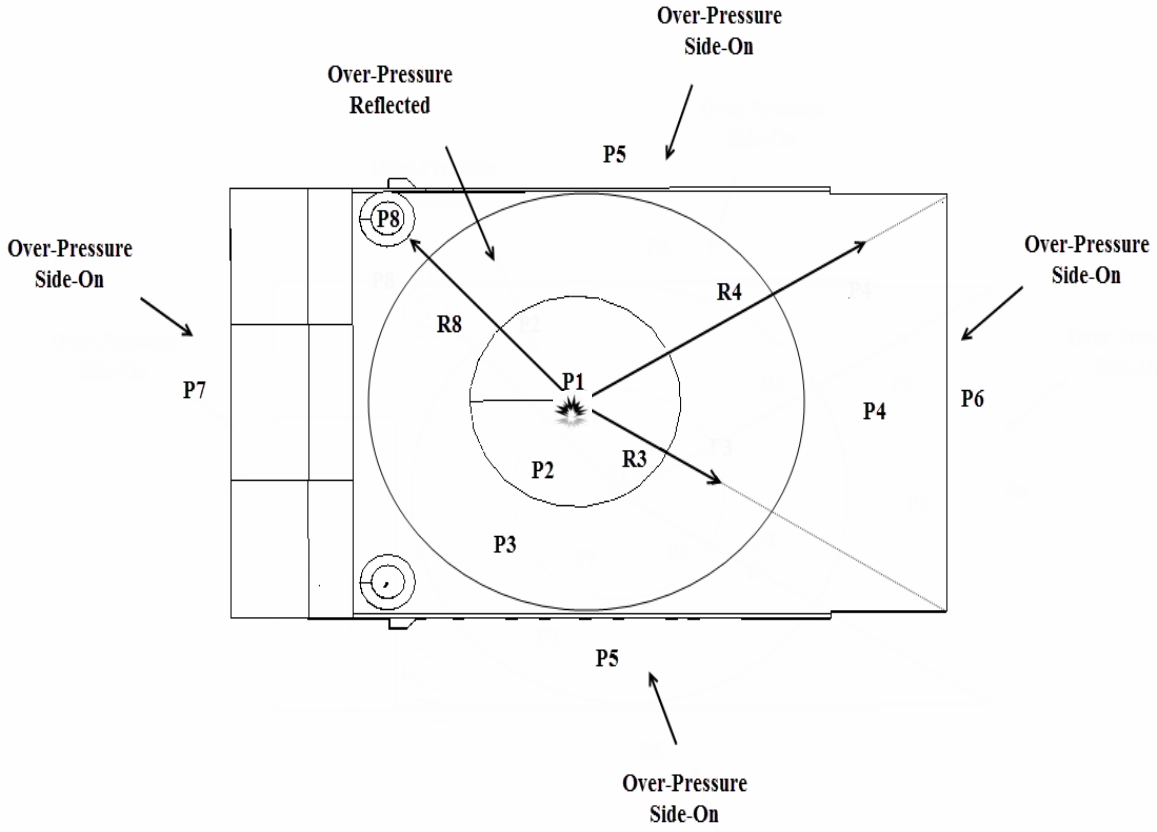

(*a*)

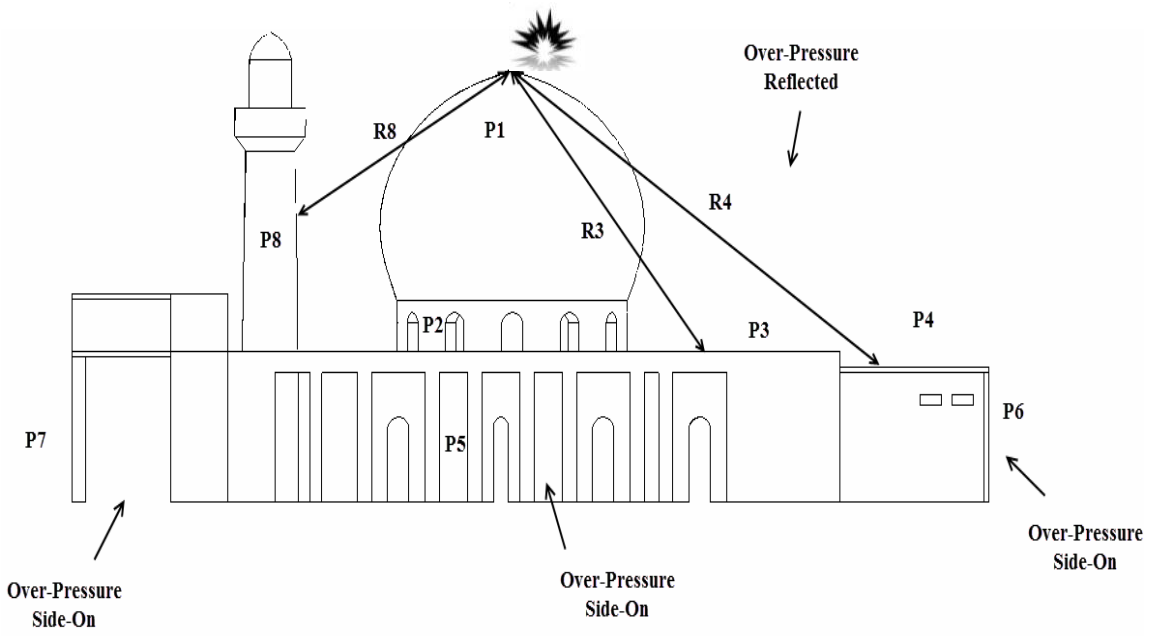

(*b*)

Fig. 6.10. Blast pressure distribution - Scenarios A: (a) top view; (b) side view.

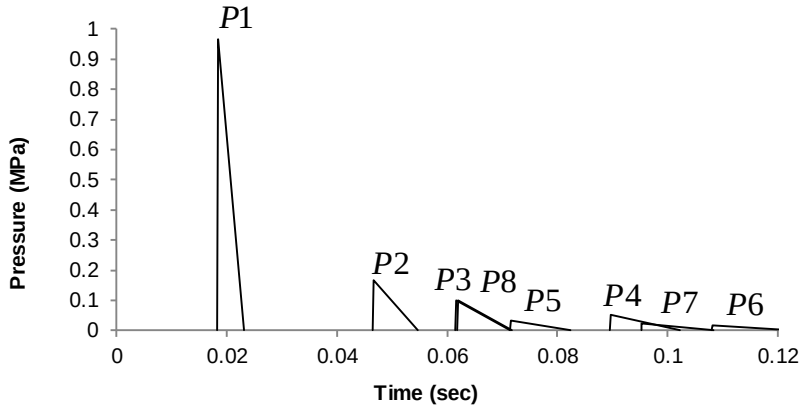

Fig. 6.11. Scenario A - pressure profiles.

For scenarios B and C, four zones, namely *L*1, *L*2, *L*3 and *L*4, having different stand-off distances (*R*1, *R*2, *R*3 and *R*4) are given, see Fig. 6.12. Regarding the pressure profiles, for each scenario, the pressure profiles are calculated for different zones, see Fig. 6.13 to Fig. 6.14. For each of North side, South side and roof, the pressure profile is uniformly distributed over the entire surface (*L*3 and *L*4).

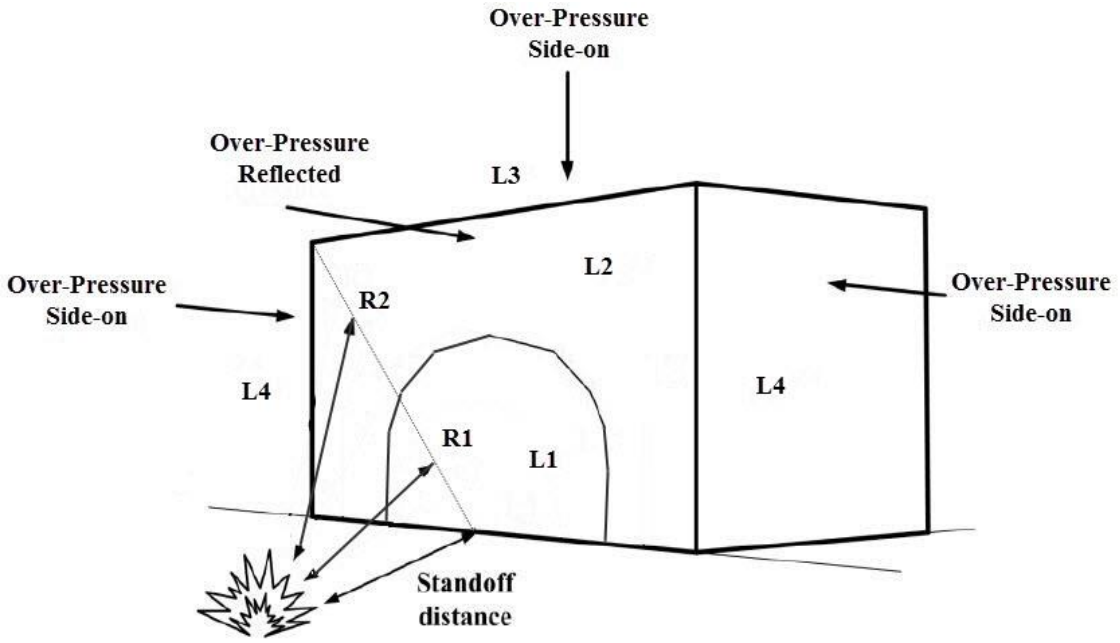

Fig. 6.12. Blast pressure distribution - Scenarios B and C.

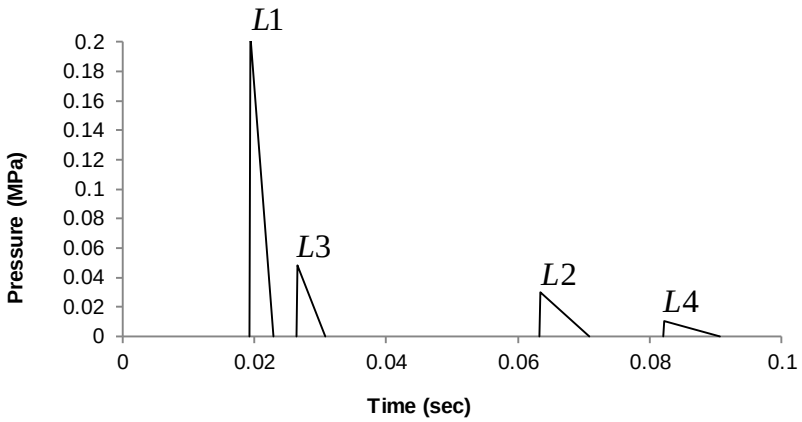

Fig. 6.13. Scenario B - pressure profiles.

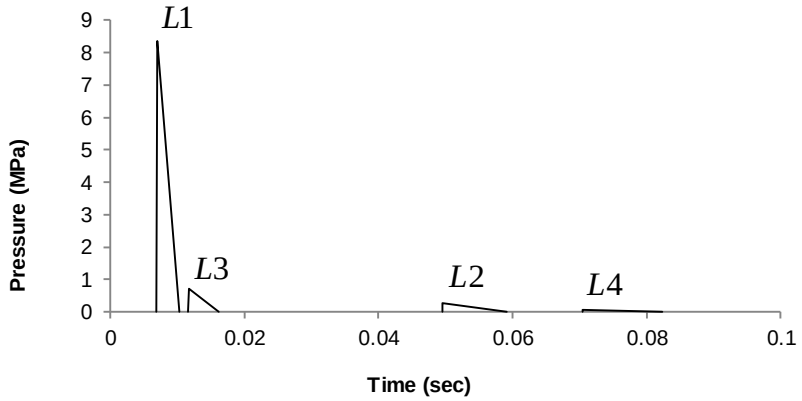

Fig. 6.14. Scenario C - pressure profiles.

6.3.2 Results and discussion

Scenario A

According to scenario A, an explosion with an approximate charge weight of 200 Kg TNT occurred at the top of the dome and led to severe damage of the dome, roof and failure of the East and West side facades. After defining the pressure profiles to distribute on different zones of the shrine in accordance with the arrival times; shown in Fig. 6.11, the dome which is closest to the explosion is initially loaded and unloaded in a very short time interval before loading other parts. The dome still continues to move after unloading due to the structural inertial forces. Next, the blast pressure respectively distributes to the roof, minarets, and side facades. For all scenarios, the analyses start once the blast wave touches the closest panel. Fig. 6.15 and Fig. 6.16 show time history of the crack distribution and deformed mesh for the shrine, using contour plots.

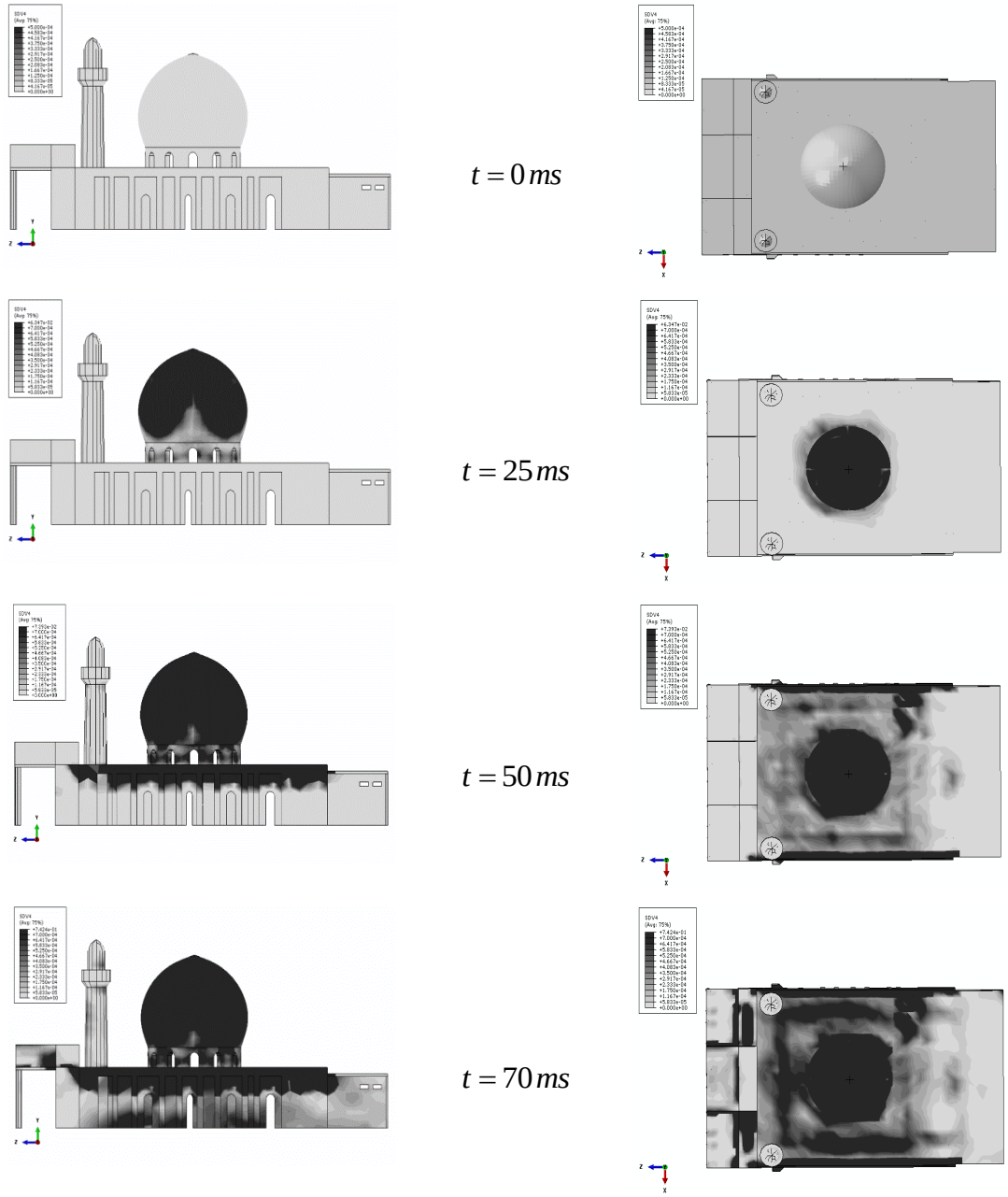

Fig. 6.15. Results of the analysis of the shrine – scenario A: time history of maximum principal plastic strain (a) West side view; (b) top view.

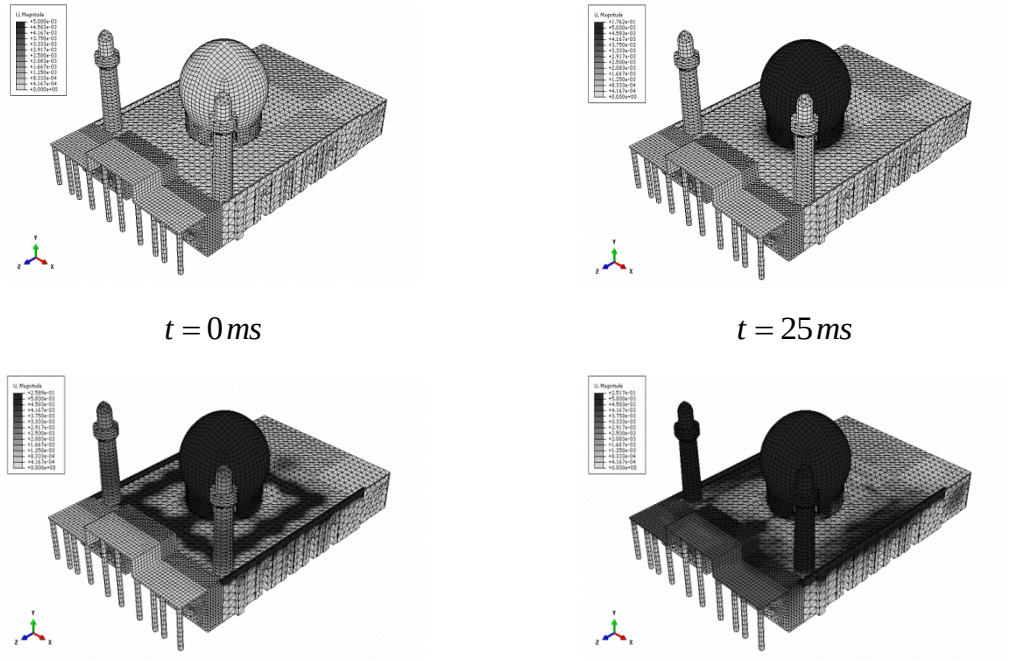

$t = 0\,ms$ $t = 25\,ms$

$t = 50\,ms$ $t = 70\,ms$

(a) (b)

Fig. 6.16. Incremental deformed mesh for the shrine – scenario A

The level of loading seems high enough for this structure to show the severe non-linearity of the masonry behavior and consequently intense crack formation. As noted, failure begins from the top of the dome, instantly encompasses upper part of it and spreading to the bottom of the dome around the openings. Afterwards, failure distributes on the roof and spreads to the minarets, and East and West side facades. In side facades, the concentration of cracks occurs at the top, over the length of the facades. The rest of the structure where the maximum principal plastic strain stays zero, remains in elastic regime. A qualitative evaluation of the damage level of the external dome is carried out as no damage criteria have been proposed for domes. However, considering the maximum displacements in different directions of the key point of the external dome can be useful to estimate the damage level. As shown in Fig. 6.17, the external dome has a large vertical displacement of 201 mm at key point. Comparing this amount with 200 mm thickness of the external dome, and taking into account the severe cracking distributed on it, collapse of external dome is certain, thus well predicting the observed damage.

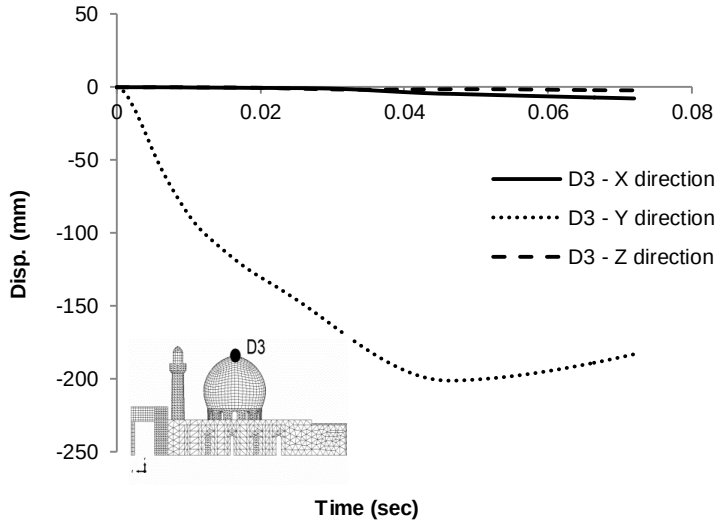

Fig. 6.17. Displacement vs. time response at key point of external dome – scenario A.

Regarding the damage level of minarets, besides limited cracking distributed on minarets, low values for support rotation around the global *x* direction are obtained, see Fig. 6.18. Hence, low damage level of minarets was obtained, which is again confirmed by their actual performance in the blast.

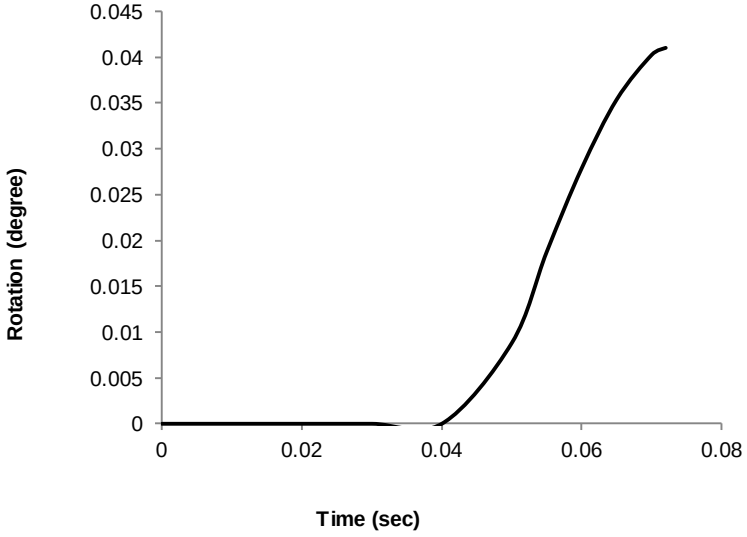

Fig. 6.18. Rotation at the support vs. time response of minarets: around x direction – scenario A.

As shown in Fig. 6.19, once the blast waves reach the West façade, it starts to move rapidly and increasingly. Each curve progressively changes the slope after 50 msec due

to the initiation of crack formation. The maximum displacement on the side façade located at point D1, reaches 111 mm at 70 msec, see Fig. 6.19(a). Analysis of the support rotations shows that the maximum support rotation occurred at point R1 in side facade and reaches 0.6^0 at 70 msec that indicates the level of loading is high enough to move further the side facade and raise the support rotation to reach the reusable damage level defined by UFC-3-340-02 (2008), see Fig. 6.19(b). Again, the large damage observed in the simulation was also found as consequence of the attack.

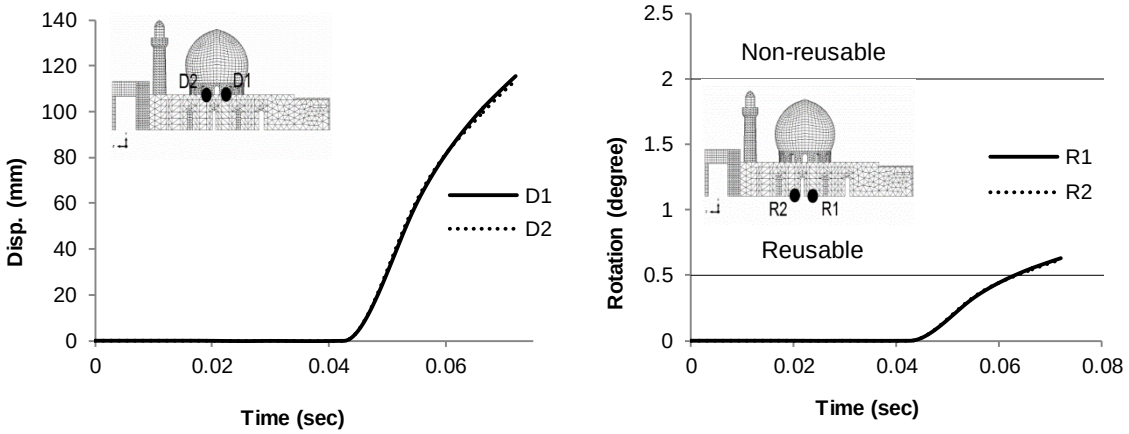

(*a*) (*b*)

Fig. 6.19. Results of the analysis of West façade – scenario A: (a) displacement vs. time response in x direction; (b) rotation at the support vs. time response around z direction.

Scenario B

As mentioned before, besides the real explosion analyzed before, a different explosion is assumed to occur with a portable luggage size IED with an explosive charge weight of 20 kg TNT placed at 5 m from the West side façade and at mid-length of it. Fig. 6.20 and Fig. 6.21 show the time history of maximum principal plastic strain and deformed mesh of the shrine. Since the scenarios B and C mostly damage the West side façade, only the West side and top views are given in the images. The failures start from the west façade and instantly spread over its length. As noted, the load resulting from the explosion mainly damages the upper part of the West side facade. The lower thickness of the upper end of the façade can justify the concentration of the cracks in this zone. Cracks also partially arise on roof and dome from 8 msec and 16 msec, respectively, but the intensity of the damage is not high, even by the end of the analysis.

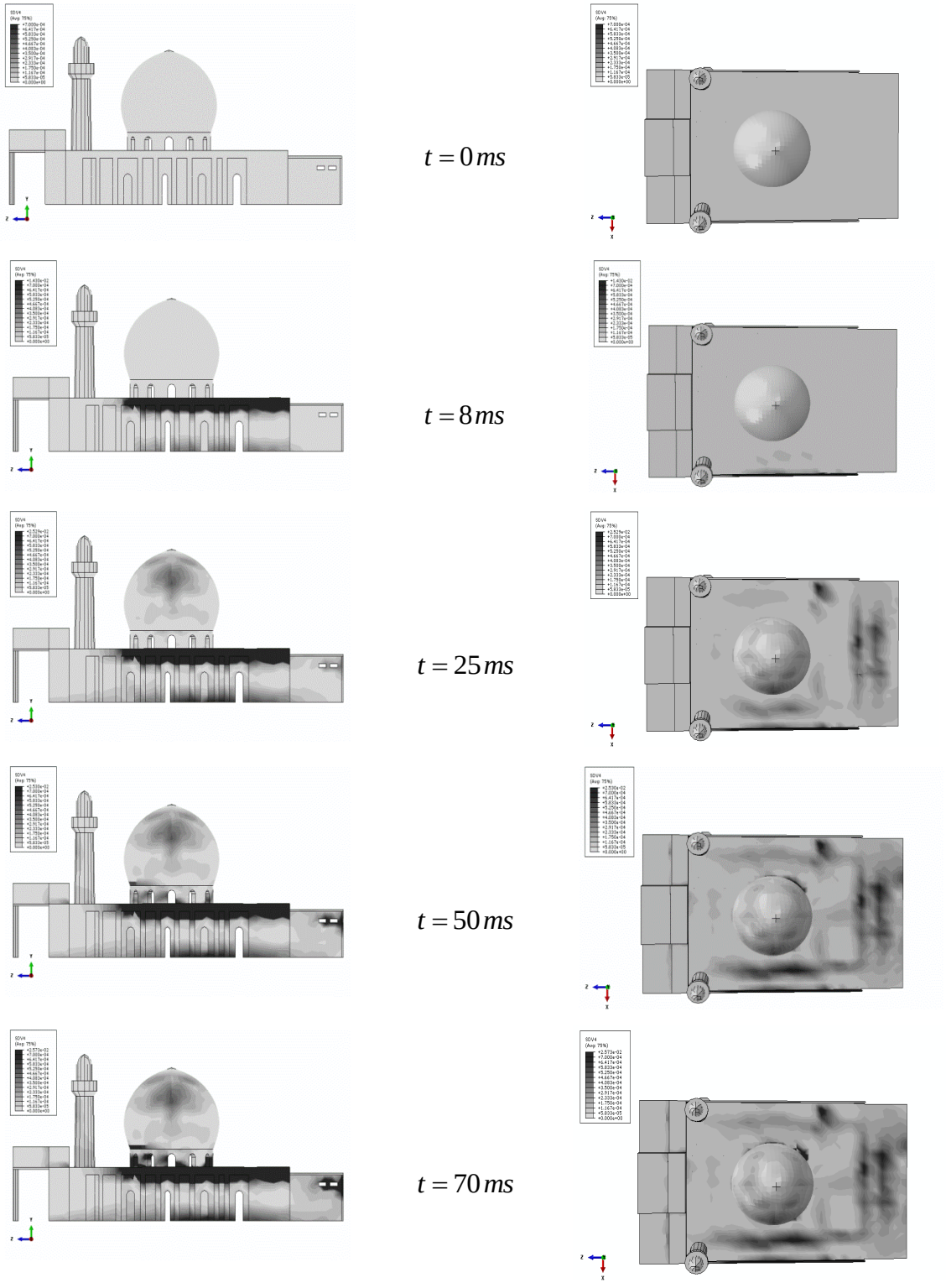

Fig. 6.20. Results of the analysis of the shrine – scenario B: time history of maximum principal plastic strain (a) West side view; (b) top view.

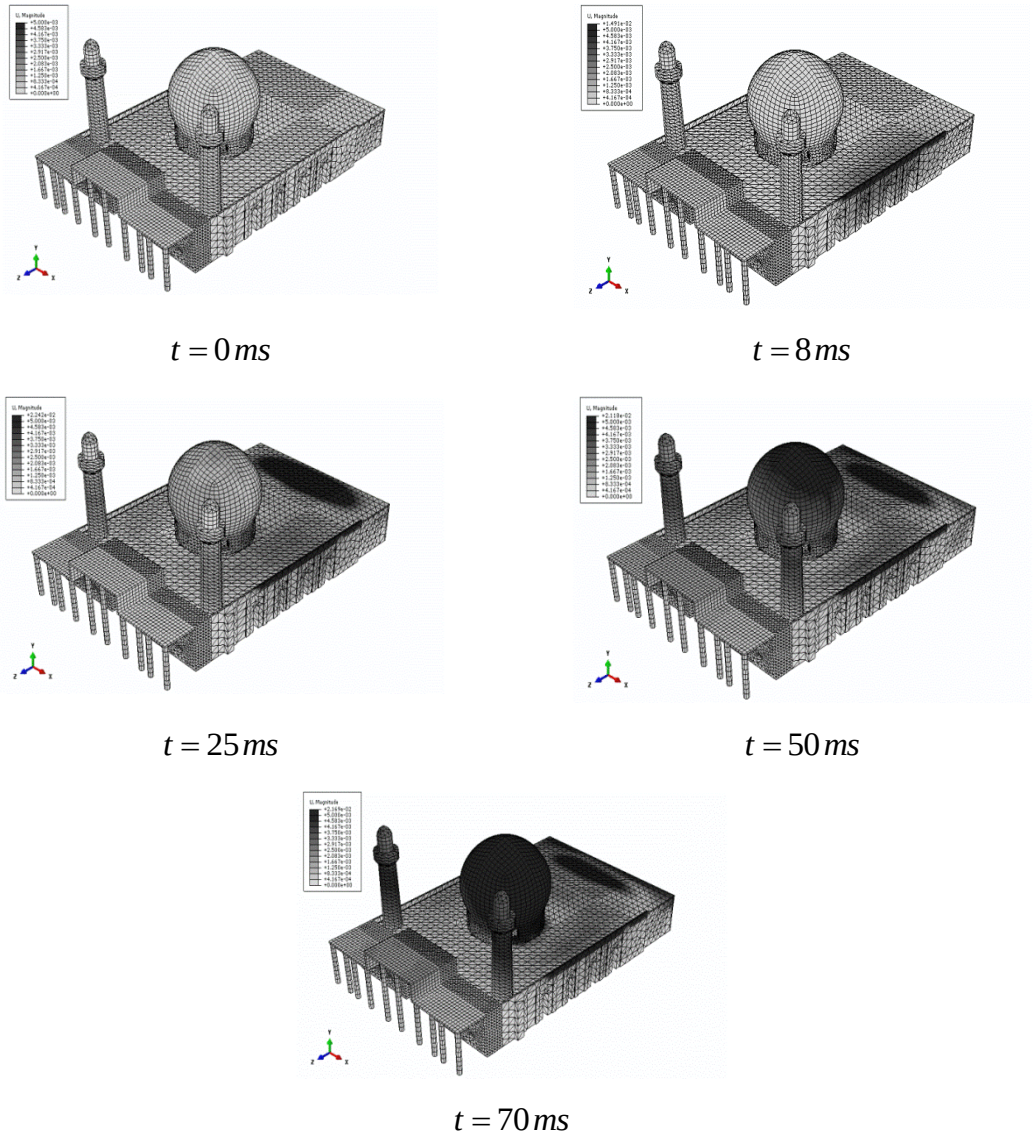

Fig. 6.21. Incremental deformed mesh for the shrine – scenario B.

The amount of explosive charge weight is not high enough to reach the material non-linearity in the majority of the structural parts and to lead to serious damages. Hence, most of the structural parts still remain elastic. Under the scenario B circumstances, from 8 msec, crack formation initiates on the West façade results in the slop changes in displacement vs. time responses, see Fig. 6.22(a). The maximum displacement of the façade occurs at point D1. At D1, the displacement in *x* direction moves immediately to reach the maximum displacement of 18.4 mm at 17 msec. As shown in Fig. 6.22(a), in the post-peak region, given the rocking back of the local sections, noticeable reductions are noted. These cause residual deflections of almost 75% of the maximum deflections at the end of the analysis. Analysis of the support rotations show that the maximum support rotation of 0.1^0 occurs at point R1 which is far from reaching the defined

damage levels. It is also noted that the structural responses, including the maximum displacement and rotation decrease by moving further from the location of the explosive charge, see Fig. 6.22(b).

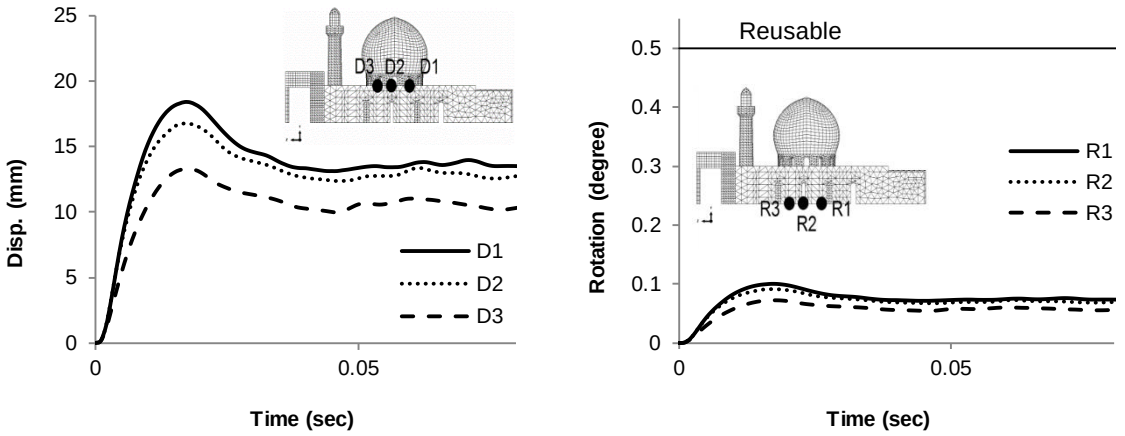

(*a*) (*b*)

Fig. 6.22. Results of the analysis of West façade – scenario B: (a) displacement vs. time response in x direction; (b) rotation at the support vs. time response around z direction.

Scenario C

In scenario C, an explosion is considered to occur with a car size IED with a high explosive charge weight of 500 kg TNT located at 5 m from the West side façade and at mid-length of it, see Fig. 6.7. The pressure profiles acting on the building are shown in Fig. 6.14. The explosion produces a huge amount of blast wave reflected over-pressure of nearly 8.4 MPa acting on the L1 zone of the shrine, almost 41 times more than the corresponding value in scenario B. The time history of the deformed mesh and crack distribution of the shrine are given in Fig. 6.23 and Fig. 6.24. As expected, the masonry material in most parts of the building changes its state to non-linear in a very short time interval. It is noted that in case of using higher amount of charge weight, the west side façade is seriously damaged. The cracks are extensively distributed over the entire length of the wall. Besides the West façade, explosion will extremely damage the roof. Also, external dome and minarets are partially damaged by explosion. Comparing with the results of scenario B, the cracks are severely and widely distributed in the damaged parts specially the façade and roof due to the significant material non-linearity of masonry in these parts.

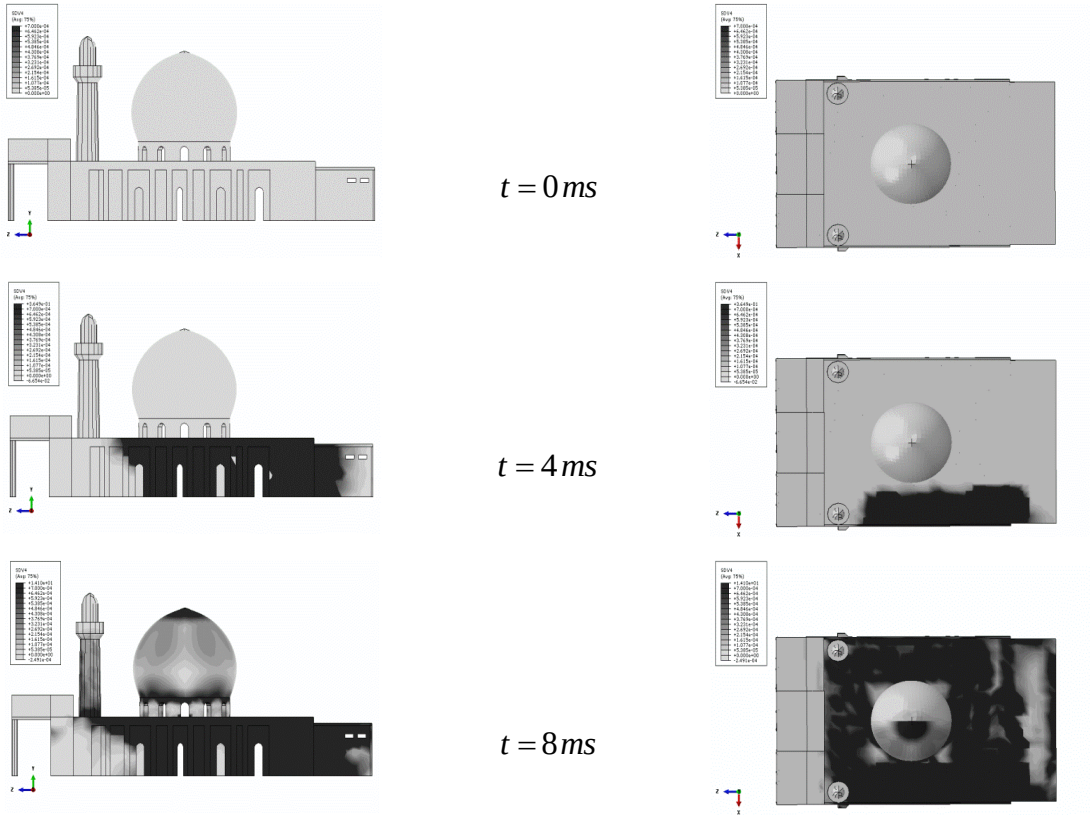

Fig. 6.23. Results of the analysis of the shrine – scenario C: time history of maximum principal plastic strain (a) West side view; (b) top view.

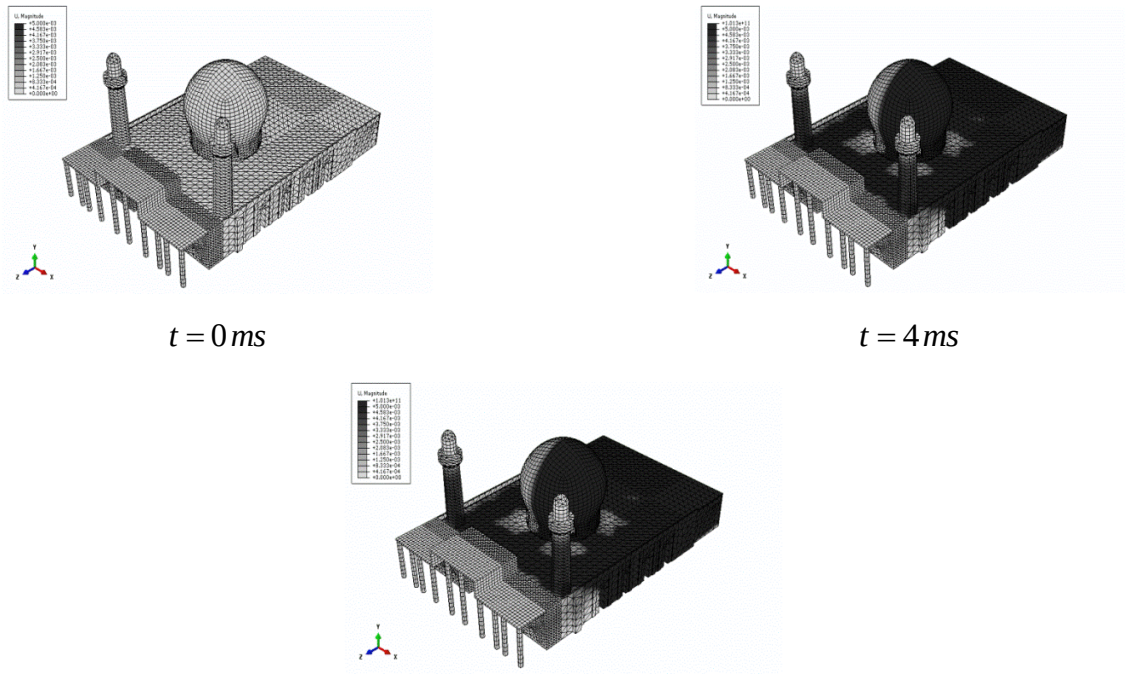

Fig. 6.24. Incremental deformed mesh for the shrine – scenario C.

As shown in Fig. 6.25(b), under scenario C loading condition, the maximum support rotation at point R1 instantly grows to violate the non-reusable limit and continue to impose irrecoverable devastation on the building in a short time interval, meaning that the West façade collapses at 5 msec. Moreover, the maximum displacement of the façade at point D1 also significantly rises to reach 700 mm at 8 msec. It means an extreme increase of 58 times at 8 msec compared with scenario B, see Fig. 6.26. It can be also noticed that the severity of the blast responses decreases by moving away from the explosion. Furthermore, it is worth mentioning that once the explosion happens, even if not considered in the modelling approach, large pieces of debris acting as projectiles would be precipitated to different directions, which results in intense devastation of other structural parts on their ways. This is therefore an unacceptable scenario for a loading action.

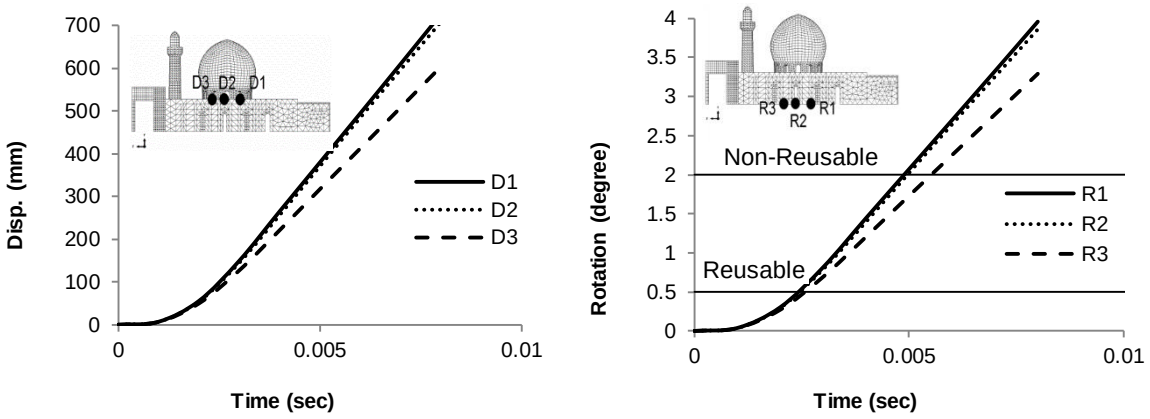

(*a*) (*b*)

Fig. 6.25. Results of the analysis of West façade – scenario C: (a) displacement vs. time response in x direction; (b) rotation at the support vs. time response around z direction.

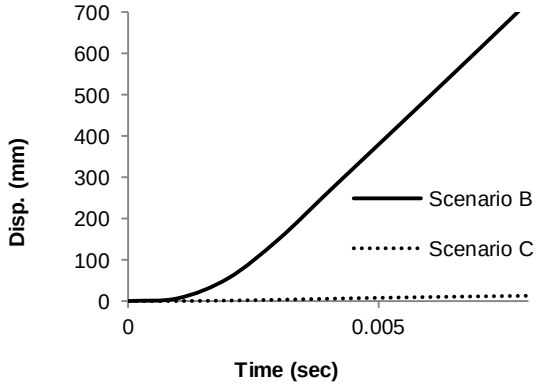

Fig. 6.26. Comparison between the displacement vs. time responses of D1 for scenarios B and C.

6.4 FINAL REMARKS

The present study is conducted to demonstrate the capacity of applying the new continuum plasticity model into an engineering application to solve a real problem. The full-scale numerical simulation of the blast response of Al-Askari holy shrine is considered here to discuss the difficulties in this application and to validate the model capability.

In order to model the blast loading, the structure is divided into different zones, allowing the blast pressure profile acting on each zone to be calculated using the given stand of distance and charge weight. According to scenario A, the shrine was subjected to a real explosion of 200 kg TNT at the top of the dome. Numerical simulation of the blast response of the structure is carried out. As noted, the numerical results including the failure of the dome and damage in the roof, minarets and side facades agree reasonably well with the observed damage. Collapse of external dome was clear from the results. The level of loading is also high enough to move further the West side facade and raise the support rotation to reach the reusable damage level.

Besides the real explosion, two different scenarios are also defined, namely B and C to estimate the most likely high strain rate response of the shrine under different explosions producing different pressure profiles. For scenarios B and C, the explosive charges are assumed to be located on the West side, 5 m to the façade and at the mid-length of it and the charge weights are estimated 20 and 500 kg TNT. As expected, using heavier charge results in severe cracking and widely distribution of the failure on different structural parts. In scenario B, the upper part of the West side façade and a limited part of the roof and dome are slightly damaged while, in scenario C, the cracks widely distribute along the length of the façade and the roof is partially damaged. As a result of using a greater charge, the explosion instantly moves the West side façade to reach maximum support rotation of 2^0 at 5 msec, meaning that the façade becomes non-reusable and collapses in a very short interval. This is an unacceptable loading scenario.

Chapter 7

7 SUMMARY AND CONCLUSIONS

The present study aims at providing dynamic constitutive material models as a set of reliable numerical tools that combine representation of accurate material behavior using mathematical theory of plasticity with robust solution approaches for numerical prediction of high strain rate response of unreinforced masonry structures to describe the post failure behavior of masonry structures in order to evaluate their safety and level of damage.

Implementing the proposed dynamic constitutive material models in FE code ABAQUS using Dynamic Explicit analysis method requires the development of FORTRAN user-defined subroutines. Through this process, material models are implemented by introducing multi-surface yield criteria, a return mapping algorithm, and a regular iterative Newton-Raphson method to solve the update of the state variables at the integration point level.

This study also briefly covers the topics dealing with blast loading and response of structures under such devastating loads. The mechanisms of blast wave propagation are

given in case of facing existing structures with different geometries along with a simulation method as pressure distribution over the time. The empirical expressions are also provided to predict the blast wave pressure parameters and blast scaling. The main results of each chapter are briefly discussed below.

7.1 SYNTHESIS AND RESULTS

In Chapter 3, a newly developed dynamic interface model accounting for strain rate effects is proposed. The rate-dependent composite yield surface is divided into three parts, namely tension cut-off mode, Coulomb friction mode, and elliptical compressive cap mode on the basis of the corresponding failure mechanisms. After implementing the material model into ABAQUS as a user subroutine, a micro approach is used for numerical modeling of masonry walls. The simplified micro modeling strategy considers masonry as a combination of individual units and zero-thickness interface elements as joints, where the composite interface model representing the inelastic behavior is lumped in weak joints. A comparison between numerical results and test data obtained by Gilbert et al. [4] is performed to evaluate the performance of the proposed material model and the accuracy of the simulation in predicting the impact response and damage of masonry walls. It can be inferred from the numerical results that the model can predict the maximum deflection and failure mode over the entire length of the walls, with good agreement. Moreover, conducting a sensitivity analysis to evaluate the influence of the material properties of the joint and wall thickness on response of the walls, it is concluded that the influence of tensile strength on the maximum displacement-time response of the walls is significant, much more than the cohesion. Also, it is noted that the use of a zero dilatancy in case of a localized impact load leads to localized failure with shear sliding between the blocks, making it not recommended for applications. A small dilatancy angle should be used instead. Moreover, it was found that the increasing the wall thickness can decrease the maximum deflection, as expected, but not in a way proportional to the elastic stiffness. Finally, study of the influence of strain rate dependency is conducted. It is noted that considering the same properties in all integration points results in a slight reduction in displacement vs. time response and negligible changes on failure mode for low strain rates. However, at higher strain rates, the changes are more intensified.

In Chapter 4, a rate dependent anisotropic continuum model is proposed for numerical simulation of the high strain rate response of masonry walls. The developed 3D material model benefits from the idea of combining a Rankine type yield criterion in tension and a Hill type yield criterion in compression, including three surfaces for tension and one ellipsoid shaped surface for compression. The continuum model, developed as a user-defined subroutine, is implemented into ABAQUS and attributed to 3D solid elements to simulate the masonry behavior. The macro approach is involved in the numerical modeling of masonry walls reported by Gilbert et al. [4] and Pereira [16], and is combined with a dynamic explicit method. The results obtained are compared with test data to evaluate the accuracy of the proposed material model to numerical predict the structural damage and response of masonry walls subjected to high strain rates. The numerical predictions accounting for the maximum deflection and crack patterns over the entire length of the wall are well predicted when compared with test data. A parametric study is also performed to study the effectiveness of the most likely main properties on impact response of a masonry parapet and blast response of a masonry infill wall. As noted, the influence of tensile strength on maximum deflection and crack patterns of the masonry wall is much more significant in y and z directions, but less in x direction. The *x*, *y*, *z* axes are along the horizontal, vertical and thickness directions of the wall, respectively. As expected, increasing the wall thickness decreases the maximum deflection and damage. Evaluating the influence of strain rate dependency, it is concluded that considering the same properties in all integration points causes a slight decrease in displacement vs. time evolution and imperceptible changes on crack distribution for low strain rates. Regarding the evaluation of the effectiveness of the uniaxial compressive strength and Young's modulus along each material axis on high strain rate response of masonry infills under blast over a specified range of scaled stand of distance, $Z = \frac{R}{W^{1/3}}$, reducing the parameter Z results in increasing the maximum displacement for all parameters. Its growth rate also rises significantly at lower amounts of Z, specially for $Z \leq 3$. The compressive strength and Young's modulus in y direction governs significantly the maximum displacement, much more than the x and z direction over the given range of Z. Finally, a mesh sensitivity analysis is conducted to study the sensitivity of the results with respect to the mesh, demonstrating that further refinement in the mesh along the thickness direction is not required.

In Chapter 5, P-I diagrams are introduced as simple tools for designers to use in preliminary design, the iso-damage curves are addressed for the tested masonry infill wall simulated in Chapter 4 along with the three different types of typical Portuguese masonry infill walls labeled A, B and C with three different thicknesses. The wall A is a solid wall with no openings, while the wall B has one opening, and the wall C has two openings. Thus, performing several analyses, the P-I diagrams are obtained for different masonry infills under different loading conditions. It is concluded that the panel with higher thickness is able to accommodate somewhat larger loading profiles and have the iso-damage curves further away. Additionally, for the wall type A, for each damage level, the differences between the P-I diagrams of wall thicknesses become clearer by increasing the wall thickness, and the differences is more significant in quasi-static loading than the dynamic loading and impulsive loading sections. For the walls type B and C, at lower thicknesses, increasing the wall thickness changes the damage levels slightly, while for higher thickness, it moves the damage levels further away. Also, it can be concluded that the changes between the iso-damage curves of three types of wall are significant for the wall thickness of 200 mm at non-reusable level, much more than the reusable level. Finally, performing multiple analyses, the pressure-impulse diagrams are obtained for the wall type A reinforced with two different reinforcement solutions under different loading conditions. As expected, involving the reinforcement solutions shifts damage levels further away from the origin for both solutions, but the results for the external reinforcement mesh solution are much better than the bed joint reinforcement, and excluding the price factor, the external reinforcement mesh is considered more preferable to reinforce the masonry infill walls in case of large impulsive loading.

In Chapter 6, full-scale numerical simulation of one prominent target, namely Al-Askari holy shrine, a world cultural heritage site located in Samarra, Iraq is carried out to present an engineering application of the continuum model developed. The structure is divided into different zones to model the blast loading, allowing the blast pressure profile acting on each zone to be calculated in terms of given stand of distance and charge weight. As noted, the numerical results including the failure of the dome and damage in the roof, minarets and side facades agree reasonably well with the observed damage. Collapse of external dome was clear from the results. The level of loading is also high enough to move further the West side facade and raise the support rotation to

violate the reusable limit. Besides the real explosion, two different scenarios are also defined, namely B and C to estimate the most likely high strain rate response of the shrine under different explosions producing different pressure profiles. For scenarios B and C, the explosive charges are assumed to be located on the West side, 5 m to the façade and at the mid-length of it and the charge weights are estimated 20 and 500 kg TNT. As expected, using heavier charge results in severe cracking and widely distribution of the failure on different structural parts. In scenario B, the upper part of the West side façade and a limited part of the roof and dome are slightly damaged while, in scenario C, the cracks widely distribute along the length of the façade and the roof is partially damaged. As a result of using a greater charge, the explosion instantly moves the West side façade to reach maximum support rotation of 2^0 at 5 msec, meaning that the façade becomes non-reusable and collapses in a very short interval. This is an unacceptable loading scenario.

7.2 FUTURE DEVELOPMENTS

All the objectives defined in chapter 1 are successfully accomplished in this work. However, there are also some areas to be addressed in future research, as they are outside the scope of this thesis.

In the scope of newly developed dynamic material models some aspects deserving further attention are highlighted:

- The present study suffers mostly from the lack of DIFs for tensile material properties of masonry. Besides the difficulties concerned to the experimentally derivation of the dynamic tensile mechanical characteristics, conducting a set of tests to characterize the masonry materials' behavior such as brick and mortar at high strain rates is highly recommended.
- It is of interest to numerically develop the empirical expressions for out of plane high strain rate behavior of masonry walls with different geometries by performing several numerical simulations and making a database including the dependent and independent parameters and applying mathematical operations.
- In spite of the complexities dealing with the definition of the consistent tangent stiffness matrix, a study is required to ugrade the newly developed anisotropic continuum plasticity model to use it for implicit analysis.
- Besides the simulation of masonry brick work structures carried out in present study, further simulations of masnory structures built with different masonry

construction materials such as stone are suggested for validation of proposed material models.

- The proposed material models are also suggested to use for different loading conditions well over a wide range of strain rate such as static, seismic, impact and blast.

In the scope of developing iso-damage curves for masonry infills some aspects deserving further attention are highlighted:

- In spite of three types of masonry infills involved in chapter 5, there are also a total of nine different types [51] distributed across the country. An investigation is required to achieve the iso-damage curves for them with different wall thicknesses and applying various reinforcement solutions thorough massive numerical analyses
- It is also suggested to derive the P-I curves of masonry infills addressed in chapter 5 by following the micro approach and compare with the available obtained curves.

In the scope of engineering application of the developed models some aspects deserving further attention are highlighted:

- A full-scale micro numerical simulation of the Al-Askari shrine under real explosion (scenario A) is required for a good representation of real damage (blowing of part of the bricks, while the rest remains).
- Considering the results addressed in chapters 5 and 6, conducting a study is suggested to choose applicable reinforcement solutions to apply on shrine to estimate the blast effects mitigation on structure.

REFERENCES

[1] Ngo T, Mendis P, Gupta A, Ramsay J. Blast loading and blast effects on structures–An overview. Electronic Journal of Structural Engineering. 2007;7:76-91.

[2] Lodygowski T, Sielicki P. Failure of the masonry structure under blast loading. Workshop on Dynamic Fracture and Damage of Brittle and Ductile Materials and its Industrial Applications. 2008. p. 46.

[3] Dewey JM. The shape of the blast wave: studies of the Friedlander equation. In Proc. of the 21st International Symposium on Military Aspects of Blast and Shock (MABS), Israel, 2010.

[4] Pandey AK, Kumar R, Paul DK, Trikha DN. Non-linear response of reinforced concrete containment structure under blast loading. Nuclear Engineering and Design. 2006;236:993-1002.

[5] Baylot JT, Bevins TL. Effect of responding and failing structural components on the airblast pressures and loads on and inside of the structure. Computers & Structures. 2007;85:891-910.

[6] Hopkinson B. British ordinance board minutes 13565. British Ordinance Office, London, UK; 1915.

[7] Brode HL. Numerical solutions of spherical blast waves. Journal of Applied Physics. 1955;26:766-75.

[8] Kinney GF, Graham KJ. Explosive shocks in air. Berlin and New York, Springer-Verlag, 1985, 282 p. 1985;1.

[9] Newmark N, Hansen R. Design of blast resistant structures. Shock and Vibration Handbook. 1961;3.

[10] Mills CA. The design of concrete structure to resist explosions and weapon effects. In Proc of the 1st International Conference on Concrete for Hazard Protections, Edinburgh, UK, 1987. p. 61-73.

[11] Bangash M, Bangash T. Explosion-resistant buildings: design, analysis, and case studies: Springer; 2006.

[12] Bounds WL. Design of blast-resistant buildings in petrochemical facilities. American Society of Civil Engineers; 2010.

[13] Shi Y, Hao H, Li ZX. Numerical derivation of pressure–impulse diagrams for prediction of RC column damage to blast loads. International Journal of Impact Engineering. 2008;35:1213-27.

[14] Oswald C, Wesevich J. Empirical based concrete masonry pressure-impulse diagrams for varying degrees of damage. American Society of Civil Engineers, Reston, New York, United States. 2005:2083-94.

[15] Hao H, Tarasov B. Experimental study of dynamic material properties of clay brick and mortar at different strain rates. Australian Journal of Structural Engineering. 2008;8:117.

[16] Pereira JM. Security evaluation and design of structures subjected to blast loading [PhD Dissertation]. Guimaraes, Portugal: University of Minho; 2014.

[17] Burnett S, Gilbert M, Molyneaux T, Tyas A, Hobbs B, Beattie G. The response of masonry joints to dynamic tensile loading. Materials and Structures. 2007;40:517-27.

[18] Asprone D, Cadoni E, Prota A, Manfredi G. Dynamic behavior of a Mediterranean natural stone under tensile loading. International Journal of Rock Mechanics and Mining Sciences. 2009;46:514-20.

[19] Comité Euro-International du Béton. CEB-FIP Model Code. Wiltshire, UK: Redwood Books; 1993.

[20] Malvar LJ, Ross CA. Review of strain rate effects for concrete in tension. ACI Materials Journal. 1998;95.

[21] Asprone D, Cadoni E, Prota A. Experimental analysis on tensile dynamic behavior of existing concrete under high strain rates. ACI Structural Journal. 2009;106:106-13.

[22] Ruiz G, Zhang X, Tarifa M, Yu RC, Camara M. Fracture energy of high-strength concrete under different loading rates. Anales de Mecánica de la Fractura 26. 2009;2.

[23] Malvar LJ. Review of static and dynamic properties of steel reinforcing bars. ACI Materials Journal. 1998;95.

[24] Wei X, Hao H. Numerical derivation of homogenized dynamic masonry material properties with strain rate effects. International Journal of Impact Engineering. 2009;36:522-36.

[25] Baylot JT, Bullock B, Slawson TR, Woodson SC. Blast response of lightly attached concrete masonry unit walls. Journal of Structural Engineering. 2005;131:1186-93.

[26] Dennis ST, Baylot JT, Woodson SC. Response of 1/4-scale concrete masonry unit (CMU) walls to blast. Journal of Engineering Mechanics. 2002;128:134-42.

[27] Eamon CD, Baylot JT, O'Daniel JL. Modeling concrete masonry walls subjected to explosive loads. Journal of Engineering Mechanics. 2004;130:1098-106.

[28] Gilbert M, Hobbs B, Molyneaux T. The performance of unreinforced masonry walls subjected to low-velocity impacts: experiments. International Journal of Impact Engineering. 2002;27:231-51.

[29] Muszynski LC, Purcell MR. Use of composite reinforcement to strengthen concrete and air-entrained concrete masonry walls against air blast. Journal of Composites for Construction. 2003;7:98-108.

[30] Myers JJ, Belarbi A, El-Domiaty KA. Blast resistance of FRP retrofitted un-reinforced masonry (URM) walls with and without arching action. The Masonry Society Journal. 2004;22:9-26.

[31] Davidson JS, Porter JR, Dinan RJ, Hammons MI, Connell JD. Explosive testing of polymer retrofit masonry walls. Journal of Performance of Constructed Facilities. 2004;18:100-6.

[32] UFC. Structures to resist the effects of accidental explosions. Department of Defense, Unified Facilities Criteria 3-340-02, Washington, DC, USA, 2008.

[33] Doherty K, Griffith MC, Lam N, Wilson J. Displacement-based seismic analysis for out-of-plane bending of unreinforced masonry walls. Earthquake Engineering & Structural Dynamics. 2002;31:833-50.

[34] US Army Corps of Engineers. Design and analysis of hardened structures for conventional weapons effects. 2002.

[35] Zapata BJ, Weggel DC. Collapse study of an unreinforced masonry bearing wall building subjected to internal blast loading. Journal of Performance of Constructed Facilities. 2008;22:92-100.

[36] Varma R, Tomar C, Parkash S, Sethi V. Damage to brick masonry panel walls under high explosive detonations. ASME-PUBLICATIONS-PVP. 1996;351:207-16.

[37] Lourenço PB. Computations on historic masonry structures. Progress in Structural Engineering and Materials. 2002;4:301-19.

[38] Marques R, Lourenço PB. Possibilities and comparison of structural component models for the seismic assessment of modern unreinforced masonry buildings. Computers & Structures. 2011;89:2079-91.

[39] Wei X, Stewart MG. Model validation and parametric study on the blast response of unreinforced brick masonry walls. International Journal of Impact Engineering. 2010;37:1150-9.

[40] Eamon CD. Reliability of concrete masonry unit walls subjected to explosive loads. Journal of Structural Engineering. 2007;133:935-44.

[41] Milani G, Lourenço PB. Blast analysis of enclosure masonry walls using homogenization approaches. International Journal for Multiscale Computational Engineering. 2009;7.

[42] Milani G, Lourenço PB, Tralli A. Homogenized rigid-plastic model for masonry walls subjected to impact. International Journal of Solids and Structures. 2009;46:4133-49.

[43] Lourenço PB. Computational strategies for masonry structures [PhD Dissertation]. Delft, The Netherlands: Delft University of Technology; 1996.

[44] Pluijm R. Material properties of masonry and its components under tension and shear. In Proc of the 6th Canadian Masonry Symposium, University of Saskatchevan, Saskatoon, Saskatchevan, Canada, 1992.

[45] Pluijm R. Shear behaviour of bed joints. In Proc of the 6th North American Masonry Conference, Drexel University, Philadelphia, Pennsylvania, USA1993. p. 125-36.

[46] Feenstra PH. Computational aspects of biaxial stress in plain and reinforced concrete [PhD Dissertation]. Delft, The Netherlands: Delft University of Technology; 1993.

[47] Rots JG. Computational modeling of concrete fracture [PhD Dissertation]. Delft, The Netherlands: Delft University of Technology; 1988.

[48] Rafsanjani SH, Lourenço P, Peixinho N. Dynamic interface model for masonry walls subjected to high strain rate out-of-plane loads. International Journal of Impact Engineering. 2015;76:28-37.

[49] Pereira MFP. Avaliação do desempenho das envolventes dos edifícios face à acção dos sismos [PhD Dissertation]. Guimaraes, Portugal: University of Minho; 2013.

[50] Hashemi Rafsanjani S, Bakhshi A, Ghannad MA, Yekrangnia M, Soumi F. Predictive Tri-Linear Benchmark Curve for In-Plane Behaviour of Adobe Walls. International Journal of Architectural Heritage. 2014.

[51] Furtado A, Costa C, Rodrigues H, Arêde A. Characterization of structural characteristics of Portuguese RC buildings with masonry infill walls stock. In Proc of the 9th International Masonry Conference, Guimarães, Portugal, 2014.

[52] NCC. Report on terrorism 2011 . Office of the Director of National Intelligence; USA; 2012.

[53] Northedge A. The historical topography of Samarra. 2005.

[54] Ashkan M, Ahmad Y. Discontinuous double-shell domes through Islamic eras in the Middle East and Central Asia: history, morphology, typologies, geometry, and construction. Nexus Network Journal. 2010;12:287-319.

[55] Group FP. UN warns of chaos in Iraq. Hamshahri. Tehran, Iran: Hamshahri; 2006.

[56] Elbanna A. The Al-Askariyyain shrine in Samarra-Iraq, restoration project. Cairo: Conservation Center of Archaeology, Faculty of Archaeology, Cairo University; 2009.

[57] Masaeli H. Study on mechanical characteristics and seismic behavior of adobework buildings using shaking table [MSc Dissertation]. Tehran, Iran: Sharif University of Technology; 2009.

[58] Tarque N, Camata G, Spacone E, Varum H, Blondet M. Numerical modelling of in-plane behaviour of adobe walls. In Proc of the 8th National Conference on Seismology and Earthquake Engineering – SÍSMICA 2010, University of Aveiro, Aveiro, Portugal, 2010.

[59] Cormie D, Mays GC, Smith PD. Blast effects on buildings, 2nd edition. England: Thomas Telford Publications; 2009.

ANNEXES

ANNEX 1

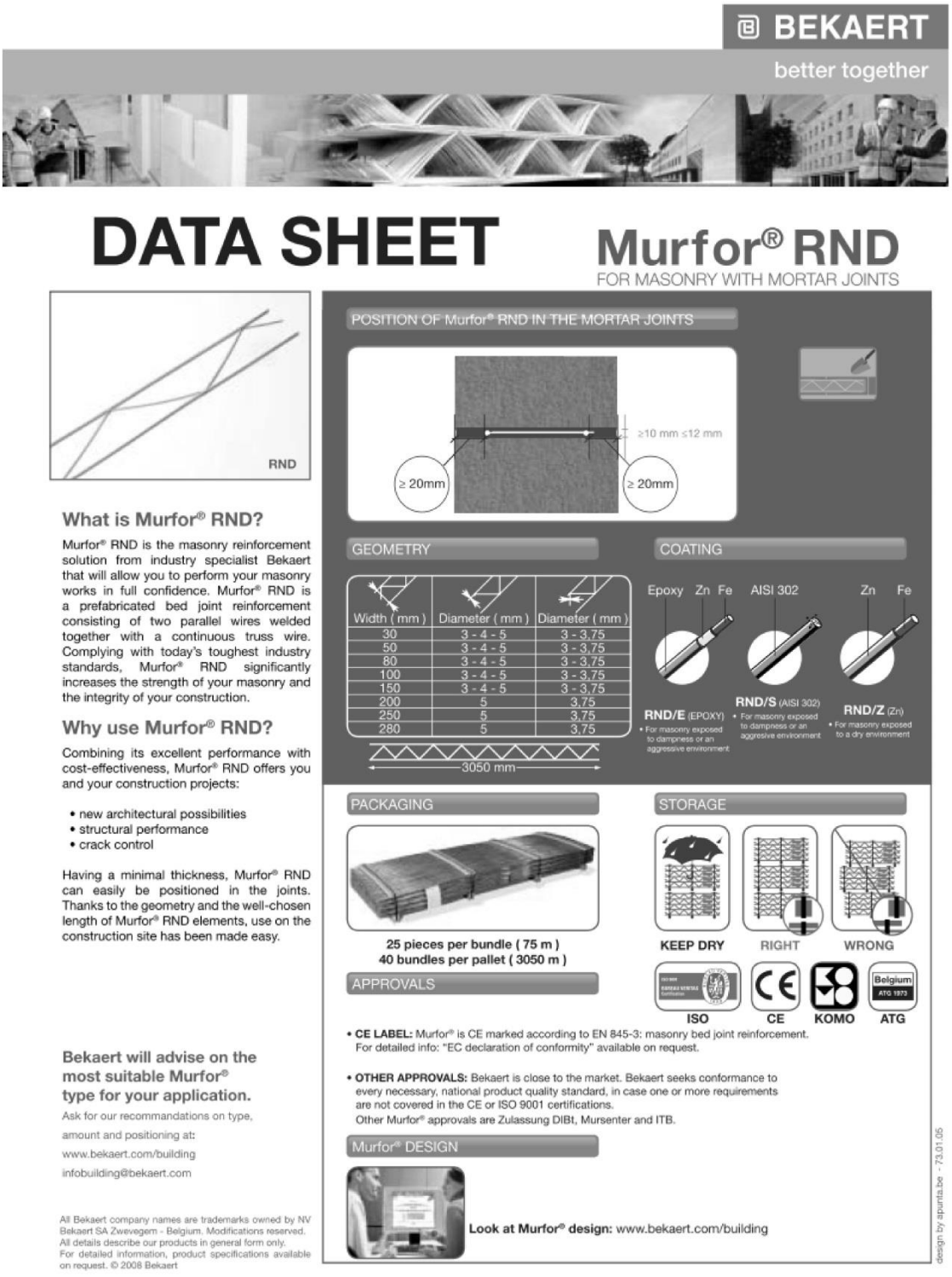

Fig. Annex.1. MURFOR RND Datasheet.

ANNEX 2

BEKAERT

better together

DATA SHEET Armanet®

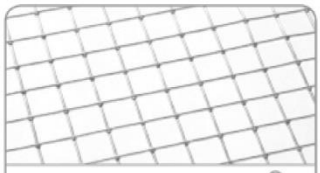

What is Armanet®?

Armanet® is a heavy galvanized welded mesh used for interior and exterior plastering and rendering.

Armanet® is used as reinforcing mesh for plastering in the renovation of cracked walls. It is also used as a plaster support for insulation systems.

Why use Armanet®:

- ☑ For renovation of walls
- ☑ For external insulation systems
- ☑ For the repair and reinforcement of cracked areas

Bekaert will advise on the most suitable Armanet® type for your application. Ask for our recommendations on type, amount and placing at:

www.bekaert.com/building
infobuilding@bekaert.com

TECHNICAL DATA: ROLLS

	M (mm)	ø (mm)	H (mm)	L (m)
welded and heavily galvanized mesh	12,7 x 12,7	0,65	1000	25
		0,80	500 + 1000	25
		1,05	1020	25
	19 x 19	1,05	1010	25
welded mesh with galvanized wires	19 x 19	0,70	250	50
			500	50
			1000	50
Stainless steel (on request)	16 x 16	1,00	1000	25

TECHNICAL DATA: PANELS

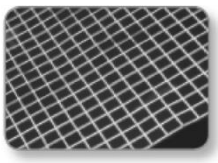

Armanet® Flat: Reinforced mesh
This panel has the same characteristics as the roll type, but can preferably be used for big surfaces of walls and ceilings as there is no bend to compensate. With suitable dowel parts, you can fix it with a distance to the subground. This panel is the right reinforcement and plaster carrier for new and renovation application in- and outside.

- Diameter: 1,05 mm
- Mesh size: 12,7 x 12,7 mm
- Zinc: min. 350 gr/m²
- Panel size: 1,02 x 2,50 m
- Package: 20 panels/bundle
- 200 panels/pallet

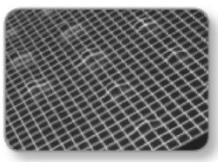

Armanet® Dista: Reinforcing mesh with spacer
Armanet® Dista is a heavily galvanized wire mesh panel with indentations at regular intervals. These indentations act as spacers. This panel is mainly used for cracked or painted walls.

- Diameter: 1,05 mm
- Mesh size: 16 x 16 mm
- Zinc: min. 350 gr/m²
- Profile depth: max. 10 mm
- Profile distance: 100 mm x 100 mm
- Packaging: 20 panels/bundle
- Panel size: 0,40 x 2,00 m (800 panels/pallet)
  0,60 x 2,00 m (800 panels/pallet)
  1,00 x 2,00 m (400 panels/pallet)

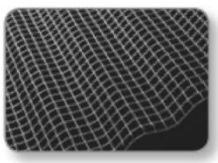

Armanet® Iso: Corrugated reinforced mesh
Armanet® Iso is a corrugated, galvanized and welded wire mesh panel, that can be used as a plaster support or as reinforcing mesh for insulation mortars.

- Diameter: 1,05 mm
- Mesh size: 16 x 16 mm
- Zinc: min. 350 gr/m²
- Packaging: 20 panels/bundle
  400 panels/pallet
- Panel size: 1,00 x 2,10 m
- Types: 20/90 and 30/125

Type 20/90 Armanet® Iso

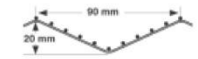

Type 30/125 Armanet® Iso

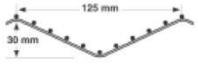

designed by BOA-inc.be - 73.07.05

Fig. Annex.2. ARMANET Datasheet